ISBM 2026

XVIIth Congress of the International Society of Bone Morphometry

July 4–7th, 2026

Queen Mary University of London, United Kingdom

SCANCO MEDICAL

REGENERON®

Wonderful Scientific

EVIDENT

LLS ROWIAK LaserLabSolutions

Table of Contents

Visit the meeting website for more information about ISBM 2026

https://www.bonemorphometry.org/isbm-2026/

The ISBM 2026 website includes:
Virtual Program and Abstract Booklet
Code of conduct

Welcome to ISBM 2026

Dear Colleagues,

It is our great pleasure to welcome you to the XVIIth Meeting of the International Society of Bone Morphometry (ISBM 2026). We gather together with esteemed colleagues from across the globe, united by a shared commitment to advance our understanding of bone biology, imaging, and morphometry.

ISBM has always been more than a scientific meeting. The forum is distinctive in that it brings together basic scientists, clinicians, engineers, and trainees to exchange ideas, challenge existing concepts, and establish new collaborations. We extend a warm welcome to both long-standing members of our community and those attending ISBM for the first time.

The program for this year is indicative of the remarkable breadth and innovation that is characteristic of our field. In the coming days, a series of keynote lectures, scientific sessions at the forefront of research, workshops, and poster presentations will be presented. We will explore topics ranging from osteocyte biology and mechanosensing to emerging approaches in spatial omics, artificial intelligence, computational imaging, and bone regeneration. We are privileged to welcome our keynote speaker, Dr. Christa Maes, and plenary speakers, Dr. Isidro Salusky and others, who continue to shape the future of skeletal research. They will showcase the latest advances in bone research and quantitative skeletal assessment. It is also particularly noteworthy that a significant number of early-career investigators are participating. Their enthusiasm and creativity continue to shape the future of bone morphometry.

We would like to express our sincere gratitude to our sponsors, partners, speakers, session chairs, and all participants whose support and contributions have made this meeting possible. We hope that ISBM 2026 will inspire new ideas, foster meaningful discussions, and create lasting connections. We wish you a productive, enjoyable, and memorable meeting.

Sincerely,

Michelle McDonald
University of Sydney
President of ISBM

Aline Bozec
Universitätsklinikum Erlangen
Program Organizing Chair for ISBM 2026

Stefaan Verbruggen
Queen Mary University
Local Organizing Chair for ISBM 2026

Saravana Ramasamy
NTU Singapore
Fundraising Chair for ISBM 2026

Lisbeth Thomsen
University of Saskatchewan
ECI Representative

Mathilde Palmier
University of Southern Denmark
ECI Representative

ISBM 2026 Sponsors

Gold Level Sponsors

SCANCO MEDICAL

REGENERON®

Silver Level Sponsors

Wonderful Scientific

LLS ROWIAK LaserLabSolutions

EVIDENT

Bronze Level Sponsors

MEDIMAPS
We understand bone health

BIOQUANT®
image analysis corporation

ascendis pharma

Lucid concepts

ISBM 2026 Awards

ASBMR Hartmut H. Malluche Early Career Investigator Award

Dr. Hartmut H. Malluche

Dr. Hartmut H. Malluche is a past president and founder of the ISBM. The purpose of this program is to promote the professional and technical development of exceptional early career basic, translational, and clinical researchers in skeletal biology. Support for this award was generously provided by the ASBMR and Dr. Hartmut Malluche.

2026 ASBMR Hartmut H. Malluche Early Career Investigator Awardees:

Alexandra Tits, Max Planck Institute of Colloids and Interface

Anushka Gerald Washington University in St. Louis

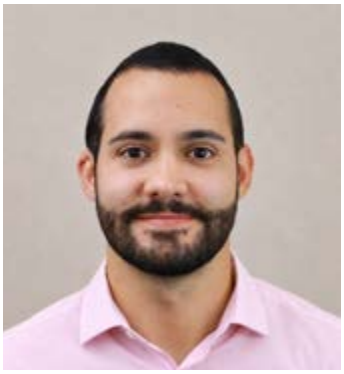

Carlos Urrego, University of Michigan

Jonathan Williams, University of Strathclyde

Kenna Brown, Montana State University

Lisbeth Thomsen, University of Southern Denmark

Martin Christensen, Aarhus University

Mathilde Palmier, University of Southern Denmark

Naomi Jung, University of British Columbia

Stine Katrine Rye Østergaard, Aarhus University

ISBM 2026 Awards

Juliet Compston Travel Award for Clinical Research in Morphometry

Dr. Juliet Compston

Dr. Juliet Compston is a physician scientist and the 9th President of the ISBM (1999-2002). Her work has substantially advanced our understanding of the pathophysiology and treatment of osteoporosis and metabolic bone disorders. This competitive award, created by Dr. Compston in partnership with the ISBM, honors talented early- to mid-career physicians that are actively pursuring clinical research related to bone morphometry avnd bone health.

2026 Juliet Compston Travel Award for Clinicical Research in Morphometry Awardees:

Julia Vaz
University of São Paulo

Patricia and David Dempster Rising Star Award for Excellence in Bone Metabolism Research

Dr. David Dempster and Patricia Dempster

Dr. David Dempster was the first non-clinician to serve as the President of the ISBM (1996-1999), ushering in an era of partnership between basic/ translational and clinical scientists. He and his wife Patti organized the 8th ISBM Congress in Arizona in 1999. They remain committed to supporting emerging leaders in the field and have created this award in partnership with the ISBM to honor rising stars in the field of bone morphometry that are actively contributing to the advancement of cutting-edge quantitative imaging techniques and training of new members of the field.

2026 Patricia & David Dempster Rising Star Award for Excellence in Bone Metabolism Research Awardees:

Dzenita Muratovic,
Adelaide University

Xiao-Hua Qin,
ETH Zürich

ISBM 2026 Awards

Webster S.S. Jee Travel Award for Research in Bone Histomorphometry

Dr. Webster S. S. Jee

Dr. Jee was a pioneer in bone histomorphometry, and as an inspirational mentor, instilled an enthusiasm for this important technique in graduate students, postdocs, and junior investigators who trained with him. This award was created in his name by ISBM Past President Dr. Tom Wronski (2009 to 2012) and Dr. Donald Kimmel to honor a member of the ISBM that exemplifies and continues this important mission.

2026 Webster S.S. Jee Travel Award for Research in Bone Histomorphometry Awardee:

Benjamin Sinder
UConn Health

About ISBM

ISBM originated from a series of workshops on bone morphometry, the first of which was held in Ottawa in 1973 and entitled '*First Workshop on Bone Morphometry*.' Since its founding, the society seeks to advance research, education, and clinical practice through the development and refinement of tools for quantitative imaging and analysis of bone. Indeed, the first workshops focused on radiological and histological aspects of bone morphometry. Today, the methodologies used to investigate bone morphometry span histological, tomographical, and other advanced imaging modalities for basic, translational, and clinical studies in skeletal tissues.

Our core mission has four elements:
1. Educate and train clinicians and scientists in all aspects of bone morphometry,
2. Provide a forum for experts to share and to develop their research,
3. Set standards within the field for skeletal imaging and morphometry, and
4. Advance novel therapies to support lifelong skeletal health.

Article on ISBM history

To find out more about the history of the society, read our article from 2024: *'Celebrating 50-years: the history and future of the International Society of Bone Morphometry*' in *JBMR Plus* (https://doi.org/10.1093/jbmrpl/ziae070).

As an attendee of ISBM 2026, **you are now a full member of ISBM** for the 2026-2028 cycle. We encourage you to get involved in the life of the society. Please visit bonemorphometry.org, keep up to date on our LinkedIn, or subscribe to our mailing list.

Enjoy ISBM 2026, the XVIIth Congress of the International Society of Bone Morphometry!

ISBM website:

ISBM Leadership

ISBM 2024 - 2026 Board of Directors

President
Michelle McDonald, PhD
University of Sydney

President Elect and Membership Oversight
Joel Boerckel, PhD
University of Pennsylvania

Working Group and Training Workshops Coordinator
Thomas L. Andersen, PhD
University of Southern Denmark

Treasurer
Frank Ko, PhD
Rush University

Historian
Elizabeth Zimmerman, PhD
McGill University

ISBM 2026 Program Organizing Committee Chair
Aline Bozec, PhD
Universitätsklinikum Erlangen

ISBM 2026 Fundraising Committee Chair
Saravana Ramasamy, PhD
NTU Singapore

ISBM Leadership

ISBM 2024 - 2026 Scientific Leadership Committee

Special thanks to the Scientific Leadership Committee, who in addition to the Board, scored the abstracts submitted to the conference. Thank you to all abstract reviewers for their time and contributions to the scientific programming of ISBM 2026.

Chair: Randee Hunter, The Ohio State University
Amirreza Haghighi, Brigham and Women's Hospital, Harvard Medical School
Farzin M. Takyar, The University of Minnesota
Karl Lewis, Cornell University
Chao Liu, Southern University of Science and Technology
Xiao-Hua Qin, ETH Zurich
Ali Ghasem-Zadeh, University of Melbourne
Miguel Castilho, Eindhoven University of Technology
Stefaan Verbruggen, Queen Mary University of London
Kathleen Becker, University of New England
Miryoung Lee, University of Texas Health Science Center at Houston
Mary Beth Cole, The Ohio State University
Marta Diaz del Castillo, University of Aarhus

ISBM 2024 - 2026 Early Career Investigator Committee

The Early Career Investigator (ECI) Committee was created in 2022. Over the past two years, the ECI Committee coordinated numerous virtual scientific seminars to engage ISBM members and create opportunities to discuss bone morphometry. Thank you for your contributions to the society.

Chair: Matthias Walle, University of Calgary
Co-Chair: Ankita Agrawal, Copenhagen University Hospital
Lejla Emini, University of Odense
Carlos Urrego, University of Michigan
Seyedmahdi Hosseinitabatabaei, McGill University
Lisbeth Thomsen, University of Southern Denmark
Koji Ishikawa, Duke University
Mohamed Hassan, Washington University in St. Louis
Mathilde Palmier, University of Southern Denmark
Anika Shimonty, Brigham and Women's Hospital, Harvard Medical School
Rachana Vaidya, Washington University in St. Louis

Scientific Leadership Committee (SLC)

SLC Chair
Randee L. Hunter, PhD
The Ohio State University

SLC Member
Amirreza Haghighi, MD
Brigham & Women's Hospital

SLC Member
Chao Liu, PhD
Southern University of Science Technology

SLC Member
Karl Lewis, PhD
Cornell University

SLC Member
Marta Diaz del Castillo, PhD
Aarhus University

SLC Member
Farzin M. Takyar, MD, PhD
The University of Minnesota

SLC Member
Stefaan Verbruggen, PhD
Queen Mary University of London

SLC Member
Ali Ghasem-Zadeh, PhD
The University of Melbourne

SLC Member
Xiao-Hua Qin, PhD
ETH Zurich

SLC Member
Kathleen Becker, PhD
University of New England

SLC Member
Miguel Castilho, PhD
Eindhoven University of Technology

SLC Member
Miryoung Lee, PhD
University of Texas Health Science Center at Houston

SLC Member
Mary Beth Cole, PhD
The Ohio State University

ISBM Early Career Investigators (ECI) Comittee

ECI Chair
Matthias Walle
University of Calgary

ECI Co-Chair
Ankita Agrawal
Copenhagen University Hospital

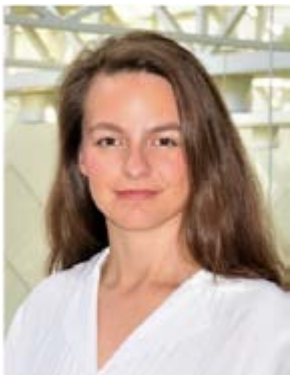

ECI Member
Lejla Emini
University of Odense

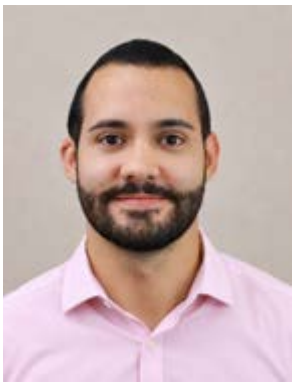

ECI Member
Carlos Urrego
University of Michigan

ECI Member
Seyedmadhi Hosseinitabatabaei
McGill University

ECI Member
Koji Ishikawa
Duke University

ECI Member
Mathilde Palmier
University of Southern Denmark

ECI Member
Anika Shimonty
Brigham & Women's Hospital

ECI Member
Rachana Vaidya
Washington University in St. Louis

ECI Member
Mohamed Hassan
Washington University in St. Louis

ECI Member
Lisbeth Thomsen
University of Southern Denmark

Invited Speakers

Inaugural Hartmut H. Malluche Memorial Lecture Speaker

Isidro Salusky, MD

Professor
Department of Pediatrics
Chief of Pediatric Nephrology
Director of Pediatric Dialysis Program
School of Medicine at University of California, Los Angeles

A Life in Bone: Honoring the Legacy of Dr. Hartmut H. Malluche

I believe that the best way to honor Dr. Malluche's journey is by understanding his lasting influence on bone and mineral metabolism in chronic kidney disease (CKD). His fascination with bone histology and meticulous morphometric analysis took shape in Heidelberg, Germany. During this period, he systematically characterized the features of renal osteodystrophy across the spectrum of CKD. His move to the United States marked the beginning of his most influential scientific period. Here, he built a world-renowned program, established bone biopsy and histomorphometry as indispensable research and clinical tools, and trained a generation of investigators. His work was supported for almost four decades with continuous NIH funding. Dr. Malluche bridged pathology and patient care, trained an inspired a generation of investigators and left a legacy that continues to guide the field.

Invited Speakers

Keynote Speaker

Christa Maes, PhD

Professor
Head of the Laboratory of Skeletal Cell Biology & Physiology
KU Leuven, Belgium

Seeing Stem wCells in Context: In Situ Visualization and Analysis of Tissue Function

Skeletal stem cells (SSCs) and progenitors for the osteoblast lineage, collectively termed skeletal stem/progenitor cells (SSPCs), are crucial for bone development, postnatal growth, adult bone homeostasis, hematopoietic support in the bone marrow, and for mediating fracture repair after trauma. SSPCs represent prime targets for bone regenerative strategies and new osteo-anabolic therapies, but much remains to be uncovered about their identity, heterogeneity, characteristics, and locations. Particularly the specific recognition of the various key SSPC subsets in their native skeletal environment remains challenging. Notwithstanding the technical difficulties associated with imaging and in situ analysis of bone tissue, tremendous progress has been made over the last decade in the identification and characterization of various SSPC populations with chondrogenic, osteogenic, hematopoiesis-supporting, and/or adipogenic capacity. This progress was powered by the implementation of lineage tracing methodologies and advanced technologies for high-resolution analyses at the single-cell level and using multiplexing, tissue-clearing and confocal imaging within the skeletal context. Such research is helping to elucidate the roles and regulation of SSPCs in the growth plate, within the reticular stroma and around blood vessels in the bone marrow cavity, and in the periosteum. Their behavior is being studied in the context of skeletal repair and regeneration, various diseases, and ageing. In this presentation, some of these advances and complexities will be discussed, offering an overview of the current knowledge and examples of ongoing research on the fates and functions of SSPC populations in bone homeostasis, disease, and regeneration.

Invited Speakers

Special Session: Bone Tumors

Alison Gartland, PhD

Professor
Bone and Cancer Biology
University of Sheffield, United Kingdom

Bone Cancers from Dinosaurs to Dogs: Seeing is Believing

While historically categorized as a modern affliction driven by post-industrial environmental factors, paleopathological evidence fundamentally refutes the notion that cancer is a relatively recent phenomenon. Initial archaeological surveys of thousands of Egyptian and Greek skeletal remains yielded negligible evidence of malignancy, as it simply wasn't seen, leading to the widespread assumption that cancer was exceedingly rare in antiquity. However, advanced non-destructive structural imaging has revolutionized our understanding of bone pathology across evolutionary history.

In 2016, high-resolution micro-computed tomography exposed the earliest known hominin malignancy: a distinct osteosarcoma lesion in a 1.7-million-year-old fifth metatarsal, proving that cancer literally has a foothold in antiquity. This deep evolutionary lineage was further underscored by the morphometric identification of an osteosarcoma in the fossilized leg bone of a 240-million-year-old Triassic stem turtle. Touché!

Today, primary bone cancers like osteosarcoma remain a devastating clinical reality. Predominantly affecting children and young adults, these tumors arise during windows of intense skeletal kinetics, where early diagnostic signs are frequently masked by the rapid remodeling of a growing skeleton. Despite the critical nature of the disease, therapeutic treatment options and outcomes have stagnated for over half a century, severely hindered by lack of research funding and poor primary care diagnostic pathways.

This presentation will address the profound challenges faced in the clinical and morphometric vdiagnosis of primary bone cancer, critically evaluate the structural pitfalls of current pre-clinical skeletal models, and demonstrate how comparative oncology, specifically utilizing naturally occurring osteosarcoma in our canine companions, can help accelerate therapeutic translation. It will also pose the question if seeing is believing – how can we see bone cancer clearly?

Invited Speakers

Session I: Osteoctyes, Lacunocanalicular Network and Mechanosensing

Tamara Alliston, PhD

Scientific Director
National Institute of Arthritis and Musculoskeletal and Skin Diseases (NIAMS), USA

Multiscale Modeling of Osteocyte Mechanosensing in Bone

Session II: Spatial Omics

Neashan Mathavan, PhD

Lecturer
Institute for Biomechanics
ETH Zürich, Switzerland

Forces and Function: Spatial Omics in Bone Mechanobiologyv

Robert Tower, PhD

Assistant Professor
The University of Texas Southwestern Medical Center
Dallas, Texas, USA

Spatial Omics Insights into Cellular Niches and Tissue Regeneration

Session III: Bone Vascularization and Microstructure

Anjali Kusumbe, PhD

Associate Professor
Nanyang Technological University, Singapore

Specialized Vascular Niches Regulating Bone Formation and Repair

Warren Grayson, PhD

Professor
John Hopkins University
Baltimore, Maryland, USA

Investigating the Neurovascular Contribution to Bone Healing

Invited Speakers

Session IV: Clinical Imaging Assessment in Inflammatory Diseases

Kathryn Stok, PhD

Professor
University of Melbourne
Melbourne, Australia

Advanced Imaging Approaches for Preclinical Assessment of Inflammatory Musculoskeletal Diseases

Session V: Computation AI Assessment of Bone Remodeling and Fracture

Steven Boyd, PhD

Professor
University of Calgary
Calgary, Alberta, Canada

Computational Imaging and AI-Based Analysis of Bone Fracture Risk

Nicolas Newell, PhD

Associate Professor
Imperial College London, United Kingdom

Towards in Vivo Quantification of Spinal Deformations and Strains Using MRI and CT-Based Digital Volume Correlation

Session VI: Emerging Paradigms in Bone Research

Chrissy Hammond, PhD

Professor
University of Bristol
Bristol, United Kingdom

Mechanical Regulation Of Bone Cell Fate: Emerging Paradigms in Skeletal Biology

Atsuhiko Hikita, PhD

Professor
University of Tokyo, Japan

Spatiotemporal Analysis of Cell and Matrix Dynamics During Bone Remodeling in an In Vitro Model

Invited Speakers

Session VII: Bone Marrow Microenvironments and Functions

Erica Scheller, PhD

Associate Professor
Washington University in St. Louis, USA

Marrow Adipocytes and Bone Homeostasis

Session VIII: Mechanoregulation of Bone Development & Regeneration

Niamh Nowlan, PhD

Professor
University College Dublin, Ireland

How Mechanical Forces Shape Skeletal Development

Workshop Descriptions

Workshop IA:
From Sample Processing to Bioinformatics: Practical Workflows in Spatial Omics (Wet and Dry Lab Perspectives)

Robert Towers, PhD, University of Texas Southwestern
Esther Wehrle, PhD, DVM, AO Research Institute Davos
Xenia Goldberg Dahl, PhD, University of Southern Denmark
Stine Katrine Rye Østergaard, MSc, Aarhus University

Location: Graduate Centre, Room 222

This workshop provides a comprehensive overview of spatial omics, bridging experimental design and computational analysis. We will first introduce key outcomes from the ISBM spatial omics working group, including community efforts, identified challenges, and emerging best practices.

The workshop is structures in two main parts. The wet lab session will cover critical aspects of sample preparation and experimental workflows, followed by platform-specific examples (GeoMx, Visium, Xenium). The dry lab session will introduce general data analysis principles and workflows in spatial transcriptomics, complemented by practical examples across technologies.

Throughout the sessions, participants will be engaged in live polling and discussions to share their backgrounds and identify key challenges in the field. The workshop aims to foster dialogue, provide actionable guidance, and support both newcomers and experienced researchers in designing and analyzing spatial omics experiments.

Learning Outcomes:

1. Understand key considerations in spatial omics experimental design, including sample preparation and platform selection.
2. Compare major spatial transcriptomics technologies (e.g. GeoMx, Visium, Xenium) and recognize their strengths and limitations.
3. Describe core computational workflows for analyzing spatial omics data, from preprocessing to biological interpretation.
4. Identify common challenges and best practices in both wet lab and dry lab settings.

Workshop Descriptions

Workshop IB:
Application of MicroCT Imaging in Musculoskeletal Research

Ali Ghasem Zadeh, PhD, University of Melbourne
Randee Hunter, PhD, The Ohio State University
Mathilde Palmier, PhD, University of Southern Denmark

Location: Graduate Centre, Room 203

This workshop is designed for first-time and novice users of microCT imaging in musculoskeletal research, offering a foundational overview of key concepts and techniques. Participants will be introduced to image acquisition methods, reconstruction and processing workflows, data output, and available analysis software solutions. The session will also highlight best practices for reporting microCT methodology and results in manuscripts. Attendees will explore practical examples demonstrating the application of microCT imaging to bone morphometry. The workshop will conclude with an open Q&A session, providing an opportunity to address questions on all fundamental aspects of microCT imaging.

Learning Outcomes:

1. Explain the basic principles of microCT imaging, including image acquisition
2. Identify appropriate acquisition settings and bone outcome variables and understand how to select them based on specific research objectives/questions
3. Describe common methods and tools used to analyze microCT data, and how these approaches are applied to assess bone morphometry

Workshop Descriptions

Workshop IC:
Basic Bone Histomorphometry

Thomas L. Anderson, PhD, University of Southern Denmark
Benjamin Sinder, PhD, University of Connecticut

Location: Graduate Centre, Room 202

The workshop will first focus on how to perform classical bone histomorphometry from tissue handling, processing and sectioning to staining and histomorphometry on both animal and human bones. Second, the workshop will focus on the classical and some non-classical static and dynamic histomorphometric parameters both from an analysis and interpretation perspective. Third, the workshop will provide examples of how the histomorphometric parameters may be affected and this change should be interpretated.

Learning Outcomes:

1. How to go from tissue to stained sections for bone histomorphometry
2. Stereological consideration when performing bone histomorphometry
3. Static and dynamic bone histomorphometry parameters – analysis and interpretation
4. Examples of how histomorphometry parameters may be affected and its interpretation

Workshop Descriptions

Workshop IIA:
Advanced Bone Histomorphometry

Thomas L. Anderson, PhD, University of Southern Denmark
Erica Scheller, DDS, PhD, Washington University in St. Louis

Location: Graduate Centre, Room 222

In this session, attendees will learn about advanced applications of histomorphometric principles to define the function of osteoblasts and osteoclasts within different skeletal compartments based on the quantification of the bone structural unit (BSU) composition of bone, the different bone formation modes (RBF, MBF, and oRBF) and RNA-based histomorphometry (40 minutes). Moreover, we will provide an overview of emerging ‘digital dynamic histomorphometry’ techniques for determination of bone formation and resorption using serial vivaCT and whole mount imaging (15 minutes). This will be followed by open discussion (20 minutes).

Learning Outcomes:

1. How to identify and quantify bone structural units and the major bone formation modes across compartments
2. How to successful perform RNA-based histomorphometry
3. Review protocols and considerations for digital dynamic histomorphometry

Workshop Descriptions

Workshop IIB:
Intravital Imaging of Bone: Opportunities, Challenges, and Emerging Applications

Karl Lewis, PhD, Cornell University

Location: Graduate Centre, Room 203

Advances in skeletal imaging have transformed our ability to visualize bone structure and remodeling across multiple spatial scales. While many imaging approaches provide exceptional structural and quantitative information, intravital multiphoton microscopy offers a complementary capability: direct observation of cellular behaviors and signaling events within living bone. These approaches enable investigators to study processes such as osteocyte mechanotransduction, bone remodeling, vascular dynamics, immune cell trafficking, and skeletal regeneration in their native physiological context.

This interactive workshop will provide an overview of intravital imaging methodologies used in skeletal research, with a particular focus on two-photon (2P) and three-photon (3P) microscopy. The session will cover fundamental imaging principles, experimental design considerations, current capabilities, and practical limitations associated with imaging mineralized tissues. Emphasis will be placed on the types of biological questions that can be addressed using intravital imaging and how these approaches complement established morphometric and ex vivo imaging methods. Following a brief overview, the majority of the session will be dedicated to an attendee-driven discussion focused on technical challenges, emerging applications, and opportunities for integrating intravital imaging into skeletal research programs.

Learning Outcomes:
1. Describe the fundamental principles and applications of two-photon and three-photon intravital microscopy in skeletal tissues.
2. Compare the capabilities, limitations, and experimental tradeoffs associated with 2P and 3P imaging approaches.
3. Identify biological questions that are uniquely suited to intravital imaging and understand how these methods complement traditional morphometric and ex vivo imaging techniques.
4. Discuss current challenges, emerging technologies, and future opportunities for applying intravital imaging in skeletal research.

Workshop IIC:
Micro-CT in Bone Research: From Core Principles to Advanced Applications

Arne Maes, Phd, Wonderful Scientific (Sponsor)

Location: Graduate Centre, Room 202

This workshop will guide you through the vast landscape of ex vivo micro-CT applications for bone research. Over the last few decades, micro-CT has revolutionized bone research by enabling non-destructive 3D visualization of the bone microstructure. Nowadays, micro-CT applications cover a wide range of scales and resolutions. To address these various needs, we at Neoscan have developed several micro- and nano-CT benchtop systems, each with its own specialty. Depending on the system type, imaging can range from scanning entire large-animal bones (e.g., sheep femurs) to resolving the finest details in the bone microstructure, such as osteocyte lacunae. This workshop aims to explore these diverse bone applications through case studies, acquired using the different Neoscan systems. Throughout the workshop, attendees will also gain insight into the key principles of acquiring a micro-CT scan. Finally, the workshop will cover essential 3D quantitative bone analyses and demonstrate how to execute these features using our license-free Neoscan software.

Learning Outcomes:

1. Brief introduction to micro-CT for bone research
2. Exploring the wide range of micro-CT applications for bone
3. Choosing the right Neoscan system for your specific application
4. Understanding the general concepts of acquiring a micro-CT scan
5. Extracting quantitative metrics from micro-CT data using Neoscan software

Workshop Descriptions

Workshop IIIA:
Automated Workflows for Reproducible Image Analysis with XamFlow

Tor Hildebrand, PhD, Lucid (Sponsor)

Location: Graduate Centre, Room 222

This workshop will introduce practical automated workflows for reproducible bone image analysis, with examples from micro-CT, HR-pQCT, and complementary modalities. We will demonstrate typical steps such as metadata handling, batch processing, automated VOI selection, segmentation, and quantitative morphometry. A simple machine learning example will show how labelled data can be used for training and applying segmentation models. The workshop will also discuss how workflow-based analysis can improve efficiency, transparency, and reproducibility in larger imaging studies.

Learning Outcomes:

1. Design image analysis workflows to improve reproducibility and efficiency in micro-CT and HR-pQCT studies.
2. Automate VOI selection and evaluation as batch processes in larger imaging studies.
3. Train machine learning models for segmentation, labelling training data, and applying pre-trained models.
4. Integrate complementary modalities such as histology or Raman data into correlative workflows.
5. Combine diverse tools including Scanco IPL, BoneJ, open-source ORMIR modules, ML models and other Python or R tools into cohesive automated pipelines without friction.

Workshop Descriptions

Workshop IIIB:
Tissue Clearing & Nerves in Bone

Daniel Coutu, PhD, The Ottawa Hospital
Erica Scheller, DDS, PhD, Washington University in St. Louis

Location: Graduate Centre, Room 203

This workshop will cover the basics of tissue clearing for musculoskeletal tissues, including adaptations for bone, immunostaining and signal amplification, and optical clearing and imaging (30 minutes). This will be followed by three case presentations from different labs regarding the successful use of tissue clearing to visualize nerves in and around bone (30 minutes). The session will end with 15 minutes reserved for discussion.

Learning Outcomes:

1. Understand basic tissue clearing concepts
2. Explore adaptation of tissue clearing for bone tissue
3. Review and discuss use cases to support successful experimental design

Workshop Descriptions

Workshop IIIC:
Multiplex Immunostaining & Lineage Tracing

Thomas L. Anderson, PhD, University of Southern Denmark
Anjali Kusumbe, PhD, Nanyang Technological University

Location: Graduate Centre, Room 202

The workshop will first focus on how to perform to successfully perform single- and multiplex immunostaining on bone tissue, including tissue handling and processing, staining protocols and tricks, downstream analysis using AI-assisted analysis, and the future of multiplex immunostaining using spatial proteomics (50 min including Q&A). Second, the workshop will focus on the lineage tracing, including study design, tissue handling and processing, analysis and interpretation (25 min including Q&A).

Learning outcomes:

1. How to perform single- and multiplex on bone tissue – tips and tricks
2. How to design a multiplex immunostaining protocol
3. How to optimize your analysis of multiplex staining using AI-assisted analysis
4. How to perform lineage tracing in bone – tips and tricks

Scientific Sessions Agenda

Agenda Summary - *XVIIth Congress of the International Society of Bone Morphometry* July 4th-7th • Queen Mary University of London, United Kingdom • Live times listed in BST – British Summer Time	
Saturday, July 4TH	
14:00 - 16:00	Early Career Investigator Meeting - *Graduate Centre, Room 701*
18:00 - 20:00	Registration Opens – *Graduate Centre Foyer*
19:00 - 20:00	Welcome Reception – *Graduate Centre Foyer*
20:00 - 21:25	Welcome and Inaugural Hartmut H. Malluche Memorial Lecture – *Graduate Centre* Moderator: **Michelle McDonald, PhD**, University of Sydney; **Joel Boerckel, PhD**, University of Pennsylvania ○ *Welcome and Highlights of ISBM 2026:* **Michelle McDonald, PhD,** University of Sydney ○ *Inaugural Hartmut H. Malluche Memorial Lecture:* **Isidro Salusky, MD**, University of California, Los Angelos *A Life in Bone: Honoring the Legacy of Dr. Hartmut H. Malluche* ○ *The ASBMR Hartmut H. Malluche Early Career Investigator Award Presentation:* **Dr. Sigrun Leonhart-Malluche**

Sunday, July 5th	
7:30 - 17:00	Registration Opens – *Graduate Centre Foyer*
7:30 - 8:30	Poster Setup – *The Octagon*
8:30 - 9:50	Session I: Osteocytes, Lacunocanalicular Network and Mechanosensing Moderators: **Anika Shimonty, PhD**, Brigham & Women's Hospital; **Chao Liu, PhD,** Southern University of Science and Technology Location: *Graduate Centre*
	8:30 - 8:50 ○ *Invited speaker:* **Tamara Alliston, PhD**, National Institutes of Health *Abstract S1-1: Multiscale Modeling Of Osteocyte Mechanosensing in Bone*
	8:50 - 9:10 ○ *Dempster Awardee:* **Xiao-Hua Qin, PhD**, ETH Zürich *Abstract S1-2: Image-Guided Biomimetic 3D Microprinting of Osteocyte Networks*
	9:10 - 9:20 ○ *Compston Awardee:* **Julia Vaz, MD,** University of São Paulo *Abstract S1-3: Distinct Osteocyte Protein Profiles Across Renal Osteodystrophy Subtypes With Mineralization Defects*
	9:20 - 9:30 ○ *Malluche Awardee:* **Alexandra Tits, PhD,** VieCuri Medical Max Planck Institute of Colloids and Interface Center *Abstract S1-4: Shape Matters: How is Lacunocanalicular Network Structure Correlated With Apposition Rate in Human Osteons?*
	9:30 - 9:40 ○ *Malluche Awardee:* **Naomi Jung,** University of British Columbia *Abstract S1-5: Now You See Me: Optimized Imaging And Connectomic Analysis Protocol Reveals Disrupted Lacunocanalicular Network Connectivity in Human Trabecular Bone Lesions of Prostate Cancer Bone Metastasis*
	9:40 - 9:50 ○ Short talks selected from abstracts: 1. **Eisha Farrukh Hashmi,** Queen Mary University of London, *Abstract S1-6: Investigating the Effect of Dendrite Removal on Osteocyte Mechanosensitivity in Breast And Prostate Cancer Patients*
9:50 - 10:10	Coffee and Tea Break - *The Octagon*
10:10 - 11:30	Poster Orals and Poster Session
	10:10 - 10:35 ○ **Poster Oral Session I (Even):** *Graduate Centre* *PO1 - PO14* Moderators: **Stine Katrine Rye Østergaard**, **MSc,** Aarhus University; **Carlos Urrego, PhD**, University of Michigan
	10:35 - 11:30 ○ **Poster Viewing Session I (Even):** *The Octagon* *P16-P34* Guides: **Frank Ko, PhD**, Rush University; **Mary Beth Cole, PhD**, The Ohio State University
11:30- 12:40	Session II: Spatial Omics Moderators: **Ryan Smith,** McMaster University; **Naomi Jung,** University of British Columbia Location: *Graduate Centre*
	11:30 - 11:50 ○ *Invited speaker:* **Neashan Mathavan, PhD**, ETH Zürich *Abstract S2-1: Forces and Function: Spatial Omics in Bone Mechanobiology*
	11:50 - 12:10 ○ *Invited speaker:* **Robert Tower, PhD**, University of Texas Southwestern *Abstract S2-2: Spatial Omics Insights into Cellular Niches and Tissue Regeneration*
	12:10 - 12:20 ○ *Malluche Awardee:* **Stine Katrine Rye Østergaard**, **MSc,** Aarhus University *Abstract S2-3: Evaluation of sample pre-treatment protocols for high throughput spatial profiling of formalin-fixed paraffin embedded human bone tissue*
	12:20 - 12:30 ○ *Malluche Awardee:* **Martin Christensen, MSc,** Aarhus University *Abstract S2-4: Innervation and pain experience in multiple myeloma: a spatially resolved histological study of human bone*
	12:30 - 12:40 ○ Short talks selected from abstracts: *1.* **Hiroyuki Okada, MD, PhD**, University of Tokyo, *Abstract S2-5: Quantitative osteocyte profiling powered by AI assisted bone deep spatial transcriptomics*
12:40 - 14:00	Lunch Break: *The Octagon*

Sunday, July 5th - Continued		
14:00 - 15:10	Session III: Bone Vascularization and Microstructure Moderators: **Kathryn Stok, PhD**, University of Melbourne; **Kenna Brown, MSc,** University of Southern Denmark Location: *Graduate Centre*	
	14:00 - 14:20	○ *Invited speaker:* **Anjali Kusumbe, PhD**, Nanyang Technological University *Abstract S3-1: Mutimodal Evidence for Bone Lymphatics and Reassessment of Skeletal Vasculature*
	14:20 - 14:40	○ *Invited speaker:* **Warren Grayson, PhD**, John Hopkins University *Abstract S3-2: Investigating the Neurovascular Contribution to Bone Healing*
	14:40 - 14:50	○ Short talks selected from abstracts: *1.* **Corinne Mahfouz, MEng**, CentraleSupélec, *Abstract S3-3: Multiscale rabbit bone structure: primary vs. secondary osteons*
	14:50 - 15:00	**2.** **Anne Marie Møller Faaborg, MSc,** Aarhus University, *Abstract S3-4: Microstructural heterogeneity in human bone affected by X-linked hypophosphatemia*
	15:00 - 15:10	3. **Ryan Smith**, McMaster University, *Abstract S3-5: 3D characterization of the cement line in human trabecular bone via micro-computed x-ray tomography*
15:10 - 15:30	15:10 - 15:30	○ Coffee and Tea Break: *The Octagon*
15:30 - 16:50	Session IV: Clinical Imaging Assessment in Inflammatory Diseases Moderators: **Neashan Mathavan, PhD**, ETH Zürich; **Xuan Wei, MA**, University of Saskatchewan Location: *Graduate Centre*	
	15:30 - 15:50	○ *Invited speaker:* **Kathryn Stok, PhD**, University of Melbourne *Abstract S4-1: Advanced Imaging Approaches for Preclinical Assessment of Inflammatory Musculoskeletal Diseases*
	15:50 - 16:00	○ *Malluche Awardee:* **Carlos Urrego, PhD**, University of Michigan *Abstract S4-2: Compromised bone architecture and strength in skeletally mature female mice with type 2 diabetes is associated with decreased endosteal bone formation and increased bone resorption*
	16:00 - 16:20	○ *Dempster Awardee:* **Dzenita Muratovic, PhD,** Adelaide University *Abstract S4-3: Single-stain quantitative histomorphometry of bone matrix and lacunocanalicular, network distinguishes septic from aseptic osteolysis*
	16:20 - 16:30	○ Short talks selected from abstracts: *1.* **Ali Ghasem-Zadeh, PhD,** University of Melbourne, *Abstract S4-4: P*atients with chronic kidney disease have accelerated microstructural bone deterioration.
	16:30 - 16:40	*2.* **Gerald Degenhart, MSc,** *Abstract S4-5: Quantitative HR-pQCT bone morphometry and composite score derivation as indicators of metabolic disease phenotypes—demonstrated in iron deficiency*
	16:40 - 16:50	*3.* **Corinna Modiz, MSc,** *Université Paris-Est Créteil Val de Marne, Abstract S4-6: Whole-bone-scale, high-resolution quantification of femoral bone mineral content using xct: A regional analysis across anatomical octants and radial compartments*
17:00 - 18:00	Keynote Speaker: **Christa Maes, PhD**, KU Leuven *Keynote Address: Seeing Stem Cells in Context: In Situ Visualization and Analysis of Tissue Function* Moderators: **Ali Ghasem-Zadeh, PhD,** University of Melbourne; **Randee Hunter, PhD**, The Ohio State University Location: *Graduate Centre*	
18:30 -	Social Event with Dinner (Paid for by ISBM): *The Morgan Arms (~15-minute walk)* Address: 43 Morgan Street Bow Greater London England E3 5AA	

Monday, July 6th		
7:30 - 8:30	Registration Opens - *Graduate Centre Foyer*	
8:30 - 9:50	Session V: Computation AI Assessment of Bone Remodeling and Fracture Moderators: **Niamh Nowlan, PhD**, University College Dublin; **Lisbeth Thomsen, PhD**, University of Southern Denmark Location: *Graduate Centre*	
	8:30 - 8:50	○ *Invited speaker:* **Steven Boyd, PhD,** University of Calgary *Abstract S5-1: Computational Imaging and AI-Based Analysis of Bone Fracture Risk*
	8:50 - 9:10	○ *Invited speaker:* **Nicolas Newell, PhD,** Imperial College London *Abstract S5-2: v*
	9:10 - 9:20	○ *Malluche Awardee:* **Kenna Brown, MSc,** Montana State University *Abstract S5-3: Applying Universal Kriging to correlate strain and osteocyte turnover in young-adult Wistar rats*
	9:20 - 9:30	○ Short talks selected from abstracts: *1.* **Zichu Ding**, **MSc,** Queen Mary University of London, *Abstract S5-4: Enhancing qct-based vertebral fracture prediction using physics-informed neural networks*
	9:30 - 9:40	*2.* **Atsuko Nakanishi-Kimura, PhD,** Hokkaido University, Abstract S5-5: Morphometric evaluation of teriparatide effects on bone remodeling in the parietal and mandibular bones of ovariectomized rats: an AI driven multiscale analysis
	9:40 - 9:50	*3.* **Melissa Bevers, PhD**, VieCuri Medical Center, *Abstract S5-6: Automatic periosteal and endosteal contouring and detection of indeterminate bone areas near the endosteal boundary on high-resolution CT scans using deep learning*
9:50 - 10:10	Coffee and Tea Break: *The Octagon*	
10:10 - 11:30	Poster Orals and Poster Session	
	10:10 - 10:35	○ **Poster Oral Session II (Odd):** *Graduate Centre* *PO1 – PO15* Moderators: **Jodi Dowthwaite, MPhil, PhD,** SUNY Upstate Medical University; **Martin Christensen**, **MSc,** Aarhus University
	10:35 - 11:30	○ **Poster Viewing Session II (Odd):** *The Octagon* *P17 – P33* Guides: **Karl Lewis, PhD**, Cornell University; **Esther Wehrle, PhD, DVM,** AO Research Institute Davos
11:30 - 13:00	Session VI: Emerging Paradigms in Bone Research Moderators: **Mary Beth Cole, PhD**, The Ohio State University; **Jonathan Williams, EngD**, University of Strathclyde Location: *Graduate Centre*	
	11:30 - 11:50	○ *Invited Speaker:* **Chrissy Hammond, PhD**, University of Bristol *Abstract S6-1: Mechanical Regulation Of Bone Cell Fate: Emerging Paradigms in Skeletal Biology*
	11:50 - 12:10	○ *Invited Speaker:* **Atsuhiko Hikita, PhD,** University of Tokyo *Abstract S6-2: Spatiotemporal Analysis of Cell and Matrix Dynamics During Bone Remodeling in an In Vitro Model*
	12:10 - 12:20	○ *Malluche Awardee:* **Lisbeth Koch Thomsen, PhD,** University of Southern Denmark *Abstract S6-3: Advancing the paradigm of PTH treatment: PTH rejuvenates the coupling mechanism, inducing the transition from eroded to formative bone surfaces*
	12:20 - 12:30	○ Short talks selected from abstracts: ○ **Birgitte Villadsen, PhD**, University of Southern Denmark, *Abstract S6-4: Alendronate increases early reversal cells in a rat model of bone remodeling*
	12:30 - 12:40	○ **Florence Lima, PhD**, University of Kentucky, *Abstract S6-5: Self-supervised dual domain segmentation for static and dynamic bone histomorphometry using LeJEPA*
	12:40 - 12:50	○ **Anika Shimonty, PhD**, Brigham & Women's Hospital, *Abstract S6-6: Mutation in CLCN7 alters tissue material properties in ADOII mice*
	12:50 - 13:00	○ **Yixia Xie, MA**, University of Missouri-Kansas City*, Abstract S6-7: Development of an immortalized osteogenic cell line stably expressing GFP-collagen and membrane-targeted TdTomato for live cell imaging of collagen assembly*
13:00 - 14:00	Lunch Break: *The Octagon*	

Monday, July 6th - Continued		
14:00 - 15:10	Session VII: Bone Marrow Microenvironments and Functions Moderators: **Atsuhiko Hikita, PhD,** University of Tokyo; **Anushka Gerald, PhD,** Washington University in St. Louis Location: *Graduate Centre*	
	14:00 - 14:20	○ *Invited speaker:* **Erica Scheller, DDS, PhD**, Washington University in St. Louis *Abstract S7-1: Marrow adipocytes and bone homeostasis*
	14:20 - 14:30	○ *Invited speaker:* **Peter Maye, PhD**, UConn Health *Abstract S7-2: Introducing the Rodent Open Science Skeletal Archive (ROSSA)*
	14:30 - 14:40	○ *Jee Awardee:* **Benjamin Sinder, PhD,** UConn Health *Abstract S7-3: Spatial Mapping of Periosteal and Endosteal Bone Formation During Growth*
	14:40 - 14:50	○ *Malluche Awardee:* **Mathilde Palmier, PhD**, University of Southern Denmark *Abstract S7-4: Defining the spatial phenotype of diet-induced individual bone marrow adipocytes in male mice*
	14:50 - 15:00	○ *Malluche Awardee:* **Jonathan Williams, EngD**, University of Strathclyde *Abstract S7-5: Metaphyseal trabecular separation is bimodal: separating intra-trabecular spacing from marrow-cavity expansion*
15:00 - 15:20	Coffee and Tea Break - *The Octagon*	
15:20 - 16:00	Special Session: Bone Tumors Moderators: **Stefaan Verbruggen, PhD,** Queen Mary University of London, **Xenia Goldberg Dahl, PhD,** University of Southern Denmark ○ Location: *Graduate Centre* ○ *Invited speaker:* **Alison Gartland, PhD**, University of Sheffield *Bone Cancers from Dinosaurs to Dogs: Seeing is Believing*	
16:10 - 17:20	Session VIII: Mechanoregulation of Bone Development & Regeneration Moderators: **Frank Ko, PhD,** Rush University; **Dzenita Muratovic, PhD,** Adelaide University; Location: *Graduate Centre*	
	16:10 - 16:30	○ *Invited speaker:* **Niamh Nowlan, PhD**, University College Dublin *Abstract S8-1: How Mechanical Forces Shape Skeletal Development*
	16:30 - 16:40	○ *Malluche Awardee:* **Anushka Gerald, PhD**, Washington University in St. Louis *Abstract S8-2: Schwann cell mapping and function in the regeneration of bone from different embryonic origins*
	16:40 - 16:50	○ Short talks selected from abstracts: *1.* **Martina Jolic, PhD**, University of Gothenburg, *Abstract S8-3: Multimodal characterisation of re-osseointegration after mechanical overload*
	16:50 - 17:00	*2.* **Tomer Stern, PhD,** University of Michigan, *Abstract S8-4: Linking Chondrocyte Activity to Cartilage Deformation by Pseudo-Cell Tracking*
	17:00 - 17:10	*3.* **Hajar Souhail, MSc**, University of Liege, *Abstract S8-5: Microstructural heterogeneity shapes mechanical variability in human trabecular*
	17:10 - 17:20	*4.* **Claire Acevedo, PhD,** University of California, San Diego, *Abstract S8-6: Spatial regulation of cochlear bone by osteocytes preserves mechanical gradients for healing*
18:30 -	Gala Dinner: *The Octagon*	

Open Science & Training Workshops

Tuesday, July 7th	
7:30 - 8:30	Registration Opens – *Graduate Centre Foyer*
8:30 - 9:45	Concurrent Training Workshops I ○ **Workshop IA: From Sample Processing to Bioinformatics: Practical Workflows in Spatial Omics (Wet and Dry Lab Perspectives)** Robert Towers, PhD, University of Texas Southwestern Esther Wehrle, PhD, DVM, AO Research Institute Davos Xenia Goldberg Dahl, PhD, University of Southern Denmark Stine Katrine Rye Østergaard, MSc, Aarhus University Location: *Graduate Centre, Room 222* ○ **Workshop IB: Application of MicroCT Imaging in Musculoskeletal Research** Ali Ghasem Zadeh, PhD, University of Melbourne Randee Hunter, PhD, The Ohio State University Mathilde Palmier, PhD, University of Southern Denmark Location: *Graduate Centre, Room 203* ○ **Workshop IC: Basic Bone Histomorphometry** Thomas L. Anderson, PhD, University of Southern Denmark Benjamin Sinder, PhD, University of Connecticut Location: *Graduate Centre, Room 202*
9:45 - 11:00	Concurrent Training Workshops II ○ **Workshop IIA: Advanced Bone Histomorphometry** Thomas L. Anderson, PhD, University of Southern Denmark Erica Scheller, DDS, PhD, Washington University in St. Louis Location: *Graduate Centre, Room 222* ○ **Workshop IIB: Intravital Imaging of Bone: Opportunities, Challenges, and Emerging Applications** Karl Lewis, PhD, Cornell University Location: *Graduate Centre, Room 203* ○ **Workshop IIC: Micro-CT in Bone Research: From Core Principles to Advanced Applications** Arne Maes, PhD, Wonderful Scientific (Sponsor) Location: *Graduate Centre, Room 202*
11:00 - 11:30	Coffee and Tea Break: *The Octagon*
11:30 - 12:45	Concurrent Training Workshops III ○ **Workshop IIIA: Automated Workflows for Reproducible Image Analysis with XamFlow** Tor Hildebrand, PhD, Lucid (Sponsor) Location: *Graduate Centre, Room 222* ○ **Workshop IIIB: Tissue Clearing & Nerves in Bone** Daniel Coutu, PhD, The Ottawa Hospital Erica Scheller, DDS, PhD, Washington University in St. Louis Location: *Graduate Centre, Room 203* ○ **Workshop IIIC: Multiplex Immunostaining & Lineage Tracing** Thomas L. Anderson, PhD, University of Southern Denmark Anjali Kusumbe, PhD, Nanyang Technological University Location: *Graduate Centre, Room 202*
12:50 - 13:00	Concluding Remarks: *Graduate Centre*

Poster Orals and Posters

POSTER ORALS (PO) AND POSTERS (P)

All even numbered posters are presented at Poster Session I (Sunday, July 5th). All odd numbered posters are presented at Poster Session II (Monday, July 6th). Poster Orals (PO) also give a three-minute oral presentation in the corresponding Poster Orals session.

Poster Number	Presenter Name, Affiliation, Poster title
PO-01	**Megi Ishmaku, MSc,** ETH Zürich, *Directed Formation of Bone Cell Networks in Micropatterned Hydrogels*
PO-02	**Edoardo Pedrinazzi, MSc**, University of Liège, *Three-dimensional morphological characterization of bone packets and osteocyte lacunae in human trabecular bone*
PO-03	**Julia Vaz, MD**, University of São Paulo, *New Insights into an Old Disease: Osteocyte Protein Expression in CKD-Associated Osteomalacia*
PO-04	**Ali Ghasem-Zadeh, PhD,** University of Melbourne, *Cortical Porosity Assessment of the Distal Radius and Tibia Using Phase-Contrast Synchrotron Radiation CT*
PO-05	**Junichiro Kazama, MD, PhD**, Fukushima Medical University, *Integrated Evaluation of Renal Bone Disease: Bone Histomorphometry Remains Fundamental but Must Be Complemented by Assessment of Bone Material Properties*
PO-06	**Jack Fenwick, MPhil,** Queensland University of Technology, *A Mathematical Model of Osteocyte Network Growth*
PO-07	**Xenia Goldberg Dahl**, **PhD,** University of Southern Denmark, *Spatial transcriptional changes in bone cell populations and bone microstructure across age in ADO2 and WT mice*
PO-08	**Madhumathi Rao, MD, PhD**, University of Kentucky, *Bone Biopsy Trends in a Metabolic Bone Disease Program*
PO-09	**Xuan Wei, MA**, University of Saskatchewan, *Elevated cortical bone remodeling and associated porosity induced by parathyroid hormone and glucocorticoids in male rabbits*
PO-10	**Jonathan Williams, EngD**, University of Strathclyde, *A tissue mineral density weighted polar moment for microCT cortical bone analysis*
PO-11	**Jonathan Williams**, **EngD,** University of Strathclyde, *Quantifying trabecular bone through simulated assembly: The Trabecular bone Assembly index (Tb.AI)*
PO-12	**Maja Østergaard**, **PhD,** Aarhus University, *Quantifying the lacuna-canalicular network in bone using high-resolution synchrotron X-ray imaging*
PO-13	**Jose Ignacio Aguirre, PhD**, University of Florida, *Differential tissue distribution of glyphosate: evidence of high skeletal affinity in sprague-dawley rates following a short-term exposure*
PO-14	**Cindy Cruz, MSc,** University of Florida, *Necroptosis Is the Dominant Cell Death Mechanism in Medication-Related Osteonecrosis of the Jaw (MRONJ), with Bone Necrosis Preceding Clinical Bone Exposure.*
PO-15	**Xiao-Hua Qin**, **PhD**, ETH Zürich, *The impact of pore architecture on cell physiology during invitro osteogenesis*
P-16	**Naoki Tsuji, PhD**, Hokkaido University, *Efferocytosis of apoptotic osteoclasts reawakens osteoblasts in functional bone organoids*
P-17	**Peter Maye**, **PhD,** UCONN Health**,** *Introducing the Rodent Open Science Skeletal Archive (ROSSA)*
P-18	**Keita Nagira, MD**, **PhD,** Tottori University, *Expansion of the Non-Osteocyte Layer of the Subchondral Bone Plate Suggests Endochondral Ossification and Is Associated with Osteoarthritis*
P-19	**Claire Acevedo, PhD,** University of California, San Diego, *From Collagen denaturation to mineral disorganization in dentinogenesis imperfecta*
P-20	**Fatma Younis**, University of Saskatchewan, *Bone Remodeling Dynamics Within Individual Glucocorticoid-Treated Basic Multicellular Units*
P-21	**Shahak Kuba**, **MSc**, Queensland University of Technology, *Geometric and mechanical regulation of osteoblast-osteocyte differentiation*

Poster Orals and Posters

Poster Number	Presenter Name, Affiliation, Poster title
P-22	**Ashlyn Soule**, **MSc,** Medical University of South Carolina, *Site specific and sex dependent effects of minocycline and docycycline on craniofacial and appendicular bone maturation in C57BL/6 mice*
P-23	**Josefin Ewerman**, **MSc,** University of Gothenburg, *Correlative EDX And Vibrational Spectroscopy: Toward More Realistic Measurements of Bone Mineral Elemental Composition*
P-24	**Chao Liu**, **PhD**, Southern University of Science and Technology, *Harnessing Macrophage Mechanobiology: New Therapeutic Strategies for Bone Regeneration*
P-25	**Krittikan Chanpaisaeng, PhD,** Chulalongkorn University, *Evaluation of nile tilapia derived biphasic calcium phosphate scaffolds for bone regeneration in a rate calvarial defect model*
P-26	**Jodi Dowthwaite, MPhil, PhD,** SUNY Upstate Medical University*, Height adjusted growth curves show advantages in radius periosteal and cortical bone geometry for female gymnasts vs non-gymnasts*
P-27	**Mimi Sammarco, PhD,** Mayo Clinic, *TrkA+ sensory nerve signaling is required to promote digit regeneration*
P-28	**Alexandra Armstrong, DVM, PhD,** University of Minnesota, *Digital Pathology of the Femoral Head: Using a Novel RGB-Trichrome Stain for Tissue Quantification using HALO©*
P-29	**Alexandra Armstrong**, **DVM, PhD,** University of Minnesota, *DV200 Values in Human and Porcine Formalin-Fixed Paraffin-Embedded (FFPE) Osteochondral Samples*
P-30	**Kaja Laursen**, Aarhus University, RNA integrity determination in formalin-fixed paraffiin-embedded human bone tissue for xenium spatial profiling
P-31	**Patricia Juarez Camacho, PhD**, CICESE, *Development of Bioactive Luminescent Apatites: A Combined In Vitro and In Vivo Study for Enhanced Osteogenesis and Bioimaging*
P-32	**Wanchai Grossrieder, MSc**, ETH Zürich, *Quantitative Analysis of Intercellular Connectivity in In Vitro Osteocyte-Like Networks*
P-33	**Sayaka Ono, DDS, PhD**, University of Tokyo, *Cysteine Protease Inhibition Disrupts Quantitative Coupling of Bone Resorption and Formation in a Bone Organoid Imaging System*
P-34	**Kalyan Nannuru, PhD,** Regeneron, *NPR2 gain-of-function of variants drive increased skeletal growth but causes tibial curvature in mice*

Speaker Abstracts

Session I: Osteocytes, Lacunocanalicular Network and Mechanosensing

S1-1: Tamara Alliston, PhD

Multiscale Modeling of Osteocyte Mechanosensing in Bone

Osteocyte structure and function is profoundly disrupted by aging. With aging, osteocyte dendritic networks degenerate, compromising mechanosensitivity and cell-cell communication. Impaired osteocytic coordination of osteoblast-mediated bone formation and osteoclast-driven bone resorption interferes with the homeostatic control of bone mineral density. In addition, suppression of osteocyte perilacunocanalicular remodeling (PLR) is responsible for age-related declines in bone matrix material properties. Given the central role of osteocytes in age related bone fragility, due to impaired bone quantity and quality, this seminar will examine potential strategies to stimulate osteocyte PLR with the goal of restoring bone mechanical homeostasis in aging.

Session I: Osteocytes, Lacunocanalicular Network and Mechanosensing

S1-2: Xiao-Hua Qin, PhD

Image-Guided Biomimetic 3D Microprinting of Osteocyte Networks

Margherita Bernero, Megi Ishmaku, Wanwan Qiu, Xianjun Yang, Ralph Müller, Xiao-Hua Qin* Institute for Biomechanics, ETH Zurich, Zurich, Switzerland

PURPOSE: A long-standing challenge in bone tissue engineering is to reconstruct inter-connected, living 3D osteocyte networks in vitro. While conventional hydrogels are extensively used in studying osteocyte biology, current techniques lack the precision to manipulate the complex pericellular environ¬ment of osteocytes – the lacuno-canalicular network (LCN). Here, we report a biomimetic 3D microprinting approach that enables image-guided direct laser writing of LCN microstructures in hydrogels, enabling user-dictated creation of geometrically defined living cellular networks in vitro.

MATERIALS & METHODS: By analyzing the FIB-SEM data of mouse femur, topologies of the LCN were extracted. A series of artificial LCN models with varying number of canaliculi and lacunar shape were generated. These models were microprinted in cell-compatible hydrogel substrates (Fig. 1a). Optimal printing parameters were evaluated by systematic screenings of laser power, scanning speed, layer height and line distance. Print fidelity was assessed by perfusion with FITC-dextran tracers. Finally, different cell types were seeded atop the patterned hydrogels and cultured for up to 28 days to assess cell morphology, osteogenic differentiation, and mechanosensitivity.

RESULTS: We developed biomimetic computer-aided design (CAD) models inspired by native LCN that allow independent control over osteocyte network density and intercellular connectivity. Only by individually tuning the printing parameters for bulk and linear structures, reliable subtractive microprinting of complex geometries was achieved at high writing speeds up to 300 mm/s. Good print fidelity was confirmed by perfusing the structures with FITC-dextran tracers and confocal microscopy (Fig. 1b). Human dermal fibroblasts seeded atop migrated into the structures within three days and formed interconnected networks after two weeks (Fig. 1c). Preliminary osteogenic cultures with human osteoblasts and murine IDG-SW3 osteoblasts demonstrated similar network formation with functional cell-cell connections by fluorescence recovery after photobleaching (FRAP), as well as the expression of osteogenic differentiation markers. Additionally, live-cell calcium imaging was applied to study transient Ca2+-signaling in living cellular networks in response to fluid flow on chip.

Session I: Osteocytes, Lacunocanalicular Network and Mechanosensing

S1-2: Xiao-Hua Qin, PhD

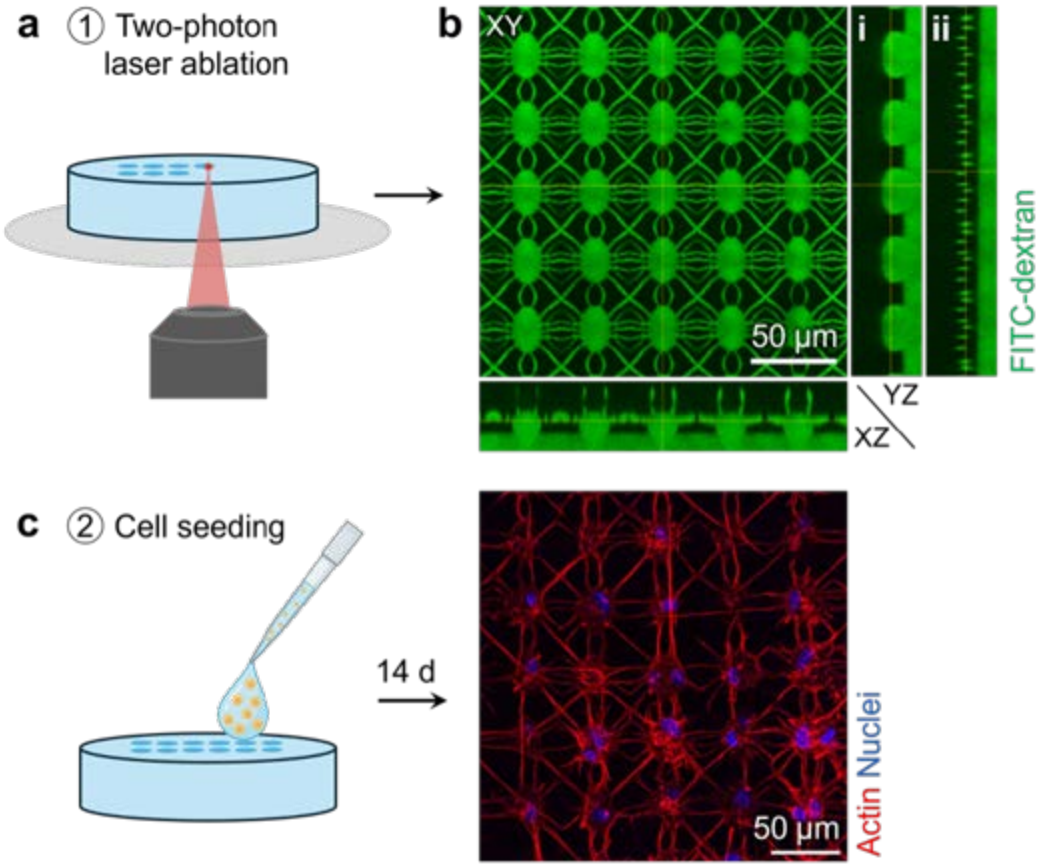

Fig. 1: **a** Artificial LCN models were subtractively printed into soft cell-compatible hydrogels. **b** Optimized printing parameters ensured the accessibility of the lacunae (i) and canaliculi (ii). The structures are visualized by FITC-dextran perfusion. **c** Guided cell morpho¬genesis and network formation of human dermal fibroblasts is observed within the micro¬structures after 14 days.

CONCLUSIONS: The disclosed image-guided approach for engineering in vitro cell networks allows the design of increasingly complex cell-scale architectures without exposing the cells to harmful laser irradiation. Collectively, this platform seeks to establish biomimetic osteocyte networks with predefined morphologies and functions, enabling systematic in vitro studies of bone tissue morphogenesis and osteocyte-mediated bone mechano-adaptation.

ACKNOWLEDGEMENTS: This work was supported by a SERI-funded ERC Starting Grant and ETH ALIVE initiative.

Session I: Osteocytes, Lacunocanalicular Network and Mechanosensing

S1-3: Julia Vaz, MD

Distinct Osteocyte Protein Profiles Across Renal Osteodystrophy Subtypes With Mineralization Defects

J.Vaz*, J. Chaer, A. de Deus, C. Da Silva, I. Oliveira, W. Dominguez1, R. Moyses, L. Dos Reis*, V. Jorgetti* 1.LIM 16, Laboratório de Fisiopatologia Renal, Hospital das Clínicas HCFMUSP, São Paulo, Brasil * Presenting Author

Purpose: Renal osteodystrophy (ROD) comprises heterogeneous bone disorders characterized by alterations in bone turnover, mineralization, and volume. Osteomalacia (OM), mixed uremic osteodystrophy (MUO), and adynamic bone disease (ABD) may all present impaired mineralization, however the mechanisms distinguishing these subtypes remain incompletely understood, particularly with regard to osteocyte proteins. Therefore, we aimed to compare clinical characteristics, histomorphometric parameters, and osteocyte protein expression profiles among patients with OM, DM, and ABD in order to identify distinguishing features of ROD subtypes associated with mineralization defects.

Materials and Methods: This retrospective study analyzed bone biopsies collected between 2000 and 2024 from a bone biopsy bank. Adult hemodialysis patients (>18 years, ≥6 months on HD) with histologically confirmed CKD-associated OM (n=15), ABD (n=20), and MUO (n=27) were included. Clinical, biochemical, histomorphometric, and immunohistochemistry (IHC) analyses were compared. Osteocyte stained cells were quantified in trabecular bone for dentin matrix protein-1 (DMP1), matrix extracellular phosphoglycoprotein (MEPE), fibroblast growth factor 23 (FGF23), osteoprotegerin (OPG), receptor activator of nuclear factor kappa-B ligand (RANKL), sclerostin (Scl), Dickkopf-1 (DKK1), CD44 and E11, as well as apoptotic cells and normalized to total trabecular osteocytes.

Results: Patients with ABD were older than those with OM and MUO (61.5, 28-79 vs 48, 19-69 and vs 56, 34-76 years; p=0.001). The proportion of men was 46.7%, 68%, and 66.6% in OM, ABD, and MUO patients, respectively (p=0.2277). Mean time in hemodialysis was longer in OM compared with ABD and MUO (60,6-168 vs 24, 6-108 and vs 51, 12-216 months; p=0.0016), and fractures were more frequent in OM (50%) than in ABD (20%) and MUO (5%), (p=0.0036), Figure 1a. Phosphorus, alkaline phosphatase, and parathyroid hormone levels differed significantly among groups (p≤0.0005).

Session I: Osteocytes, Lacunocanalicular Network and Mechanosensing

S1-3: Julia Vaz, MD

Histomorphometry analysis showed distinct patterns of ROD subtypes. OM was characterized by increased osteoid parameters (OV/BV, O.Th and OS/BS), ABD by low bone formation (OV/BV, OS/BS, BFR/BS) and MUO by higher bone turnover (OV/BV, OS/BS, Ob.S/BS, Oc.S/BS and Fb.V/TV). Osteocyte protein expression also differed among groups. Scl and FGF-23 expression were higher in ABD (10.53% and 5.6%) accompanied by a greater proportion of apoptotic osteocytes (4.62%) whereas OPG and CD44 expression were higher in OM (8.5% and 37.22%), Figure 1b.

Conclusion: ROD subtypes associated with mineralization defects exhibit distinct clinical, histomorphometric and osteocyte protein expression profiles.

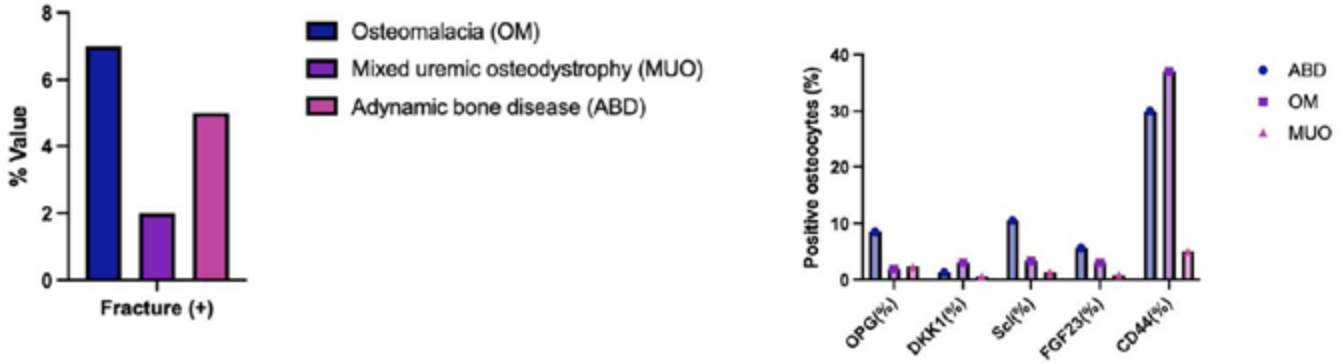

a. Prevalence of fracture according to renal osteodystrophy subtype

b.Significant differences in osteocyte protein expression among renal osteodystrophy subtypes

Figure 1. Prevalence of fracture and osteocyte protein expression differences among renal osteodystrophy subtypes. (a) Prevalence of fracture according to renal osteodystrophy subtype. Fractures were more frequent in patients with osteomalacia (OM) compared with mixed uremic osteodystrophy (MUO) and adynamic bone disease (ABD). Values are expressed as percentage. (b) Significant differences in osteocyte protein expression among renal osteodystrophy subtypes. The percentage of osteocytes positive for OPG, DKK1, SOST, FGF23, and CD44 is shown for each group (ABD, OM, and MUO). Higher SOST and FGF23 expression were observed in ABD, whereas OPG and CD44 expression were higher in OM.

Session I: Osteocytes, Lacunocanalicular Network and Mechanosensing

S1-4: Alexandra Tits, PhD

Shape Matters: How is Lacunocanalicular Network Structure Correlated With Apposition Rate in Human Osteons?

Alexandra Tits*, Shahak Kuba, Tarang Janawalkar, Ahmed Lakhel, Davide Ruffoni, Pascal Buenzli, Richard Weinkamer

Department of Biomaterials, Max Planck Institute of Colloids and Interfaces, Potsdam, Germany
Max Planck Queensland Centre for the Materials Science of Extracellular Matrices, Brisbane and Potsdam
School of Mathematical Sciences, Queensland University of Technology (QUT), Brisbane, Queensland, Australia
Mechanics of Biological and Bioinspired Materials Laboratory, University of Liege, Liege, Belgium * Presenting author

Introduction: New osteon formation is initiated by osteoclasts resorbing old or damaged bone, creating a resorption cavity delineated by a distinctive cement line. This cavity is then progressively filled by osteoblasts, which deposit layers of bone lamellae until a central Haversian canal remains open. During the infilling of the cavity, some osteoblasts are buried in osteoid and differentiate into osteocytes, thereby forming the lacunocanalicular network (LCN). Lacunae accommodate the osteocyte cell bodies, while dendritic processes extend through canaliculi, narrow channels connecting lacunae.

In human cortical bone, circular osteons with a central Haversian canal are rare. Instead, osteons exhibit diverse morphologies (e.g., roughly circular, asymmetric or elliptical) with angular variation of wall thickness that reflect differences in the bone apposition rate. These different morphologies affect the architecture of the osteocyte or lacunocanalicular network, which in turn may influence several regulatory mechanisms (such as mechanosensation or mineralization). To understand how strongly network architecture is influenced by osteon morphology, we quantify the LCN architecture in differently shaped osteons and characterize the influence of the bone formation rate on the resulting network architecture.

Materials and Methods: We have developed an experimental and computational workflow that allows us to image the threedimensional architecture of the LCN using confocal laser scanning microscopy and to segment these images into a spatial network of nodes (lacunae, junctions) and edges (canaliculi). Using the custombuilt software TINA [1], we quantify the network architecture in terms of density and spatial heterogeneity in human osteons of diverse shapes: ordinary, elliptical, and asymmetric.

Session I: Osteocytes, Lacunocanalicular Network and Mechanosensing

S1-4: Alexandra Tits, PhD

We combine this approach with second harmonic imaging (SHI) of collagen to visualize the bone lamellae and with mathematical modelling to generate pseudo-lamellae using Euclidean distance maps between the cement line and the Haversian canal boundaries.

Results: In a pre-analysis, SHI is used to confirm that variation in osteon shape is not due to sample preparation artifacts. Quantification of the LCN revealed a positive spatial correlation between bone deposition rate and density: the network is denser where wall thickness is greater, that is, where the bone was deposited faster (Figure 1). Three-dimensional experimental reconstruction of bone lamellae and comparison with mathematical pseudo-lamellae provide insights into the osteon formation process, including the direction along the axis of the long bone in which bone was formed.

Conclusions: Our analysis suggests that osteoblasts carry positional information during their embedment, enabling them to locally adapt the network structure to ensure sufficient connectivity to the Haversian canal (and hence the nutrient source). These findings indicate a strong dynamic interplay between the LCN architecture and bone growth.

[1] Repp, F., Kollmannsberger, …, Wagermaier, W. and Weinkamer, R., 2017, Bone Reports 6, 101

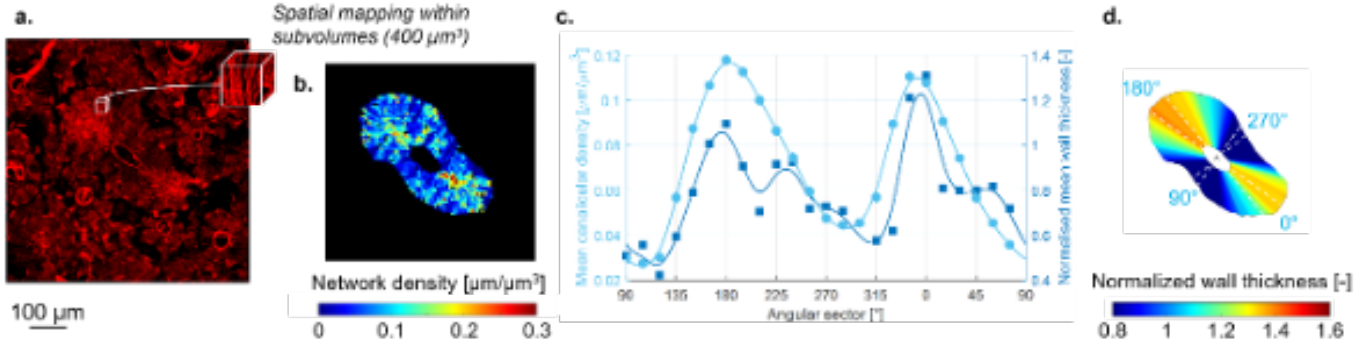

Figure 1: a. Projection of a raw confocal laser scanning microscopy image stack of an elliptical osteon; b-d. Corresponding spatial correlation within angular sectors (c) between mean canalicular density (b) and normalized mean wall thickness (d).

Session I: Osteocytes, Lacunocanalicular Network and Mechanosensing

S1-5: Naomi Jung

Now You See Me: Optimized Imaging And Connectomic Analysis Protocol Reveals Disrupted Lacunocanalicular Network Connectivity in Human Trabecular Bone Lesions of Prostate Cancer Bone Metastasis

Naomi Jung1,2, Grace Harms1,2, Erica Anderson3, Mika Radisic Hoang4, Robyn Birch5,7, Jihyeung Lim1,2, Qiong Wang5, Doris Liang6,7, Marina Eckermann8, Samuel Xu1,2, Peter Cloetens9, Eva Corey10, Colm M. Morrissey10, Lawrence D. True11, Kathryn Grandfield4, Rizhi Wang5,6,7, Michael E. Cox1,2, Felipe Eltit1,2

1 Department of Urologic Sciences, University of British Columbia, Vancouver, Canada. 2 Vancouver Prostate Centre, Vancouver, Canada. 3 School of Biomedical Engineering, McMaster University, Hamilton, Canada. 4 Department of Materials Science and Engineering, McMaster University, Hamilton, Canada. 5 Department of Materials Engineering, University of British Columbia, Vancouver, Canada. 6 School of Biomedical Engineering, University of British Columbia, Vancouver, Canada. 7 Centre for Aging SMART at VCH, Vancouver, BC, Canada. 8 Institute of Applied Physics, University of Bern, Switzerland 9 European Synchrotron Radiation Facility, Grenoble, France 10 Department of Urology, University of Washington, Seattle, USA. 11 Department of Pathology and Laboratory Medicine, University of Washington, Seattle, USA.

Purpose: With 1.5 million diagnoses annually, prostate cancer (PC) is the second mostcommon male malignancy. One fifth of patients progress to incurable metastatic disease and 90% of them develop PC bone metastases (PCBMs). PCBMs disrupt bone remodeling and produce osteolytic, mixed, and osteosclerotic lesions. The lacunocanalicular network (LCN) may contribute to this dysregulation, yet structural alterations in PCBM remain undefined. Despite advances in LCN connectomics, imaging protocols are inconsistently reported and segmentations often lack ground-truth validation, limiting reproducibility. We hypothesize that standardized imaging and validated segmentation will enable characterization of LCN connectivity in healthy and PCBM trabecular bone and reveal disease-associated disruption.

Methods: Human vertebral trabecular bone cores were imaged using synchrotron X-ray nano-holotomography (ESRF ID16A; 50–120 nm voxels; 2 control, 4 PCBM) and rhodamine-6G confocal microscopy (Nikon A1R; 25×; 124×124×375 nm voxels; 2 control, 6 PCBM). A confocal protocol was developed by modeling depth-dependent fluorescence attenuation and dynamically adjusting laser power to maintain signal uniformity. LCN segmentation was performed in the Tool for Image and Network Analysis (TINA; PMID: 28377989) using 26 parameters.

S1-5: Naomi Jung

Manual ground-truth segmentations (16 images; 3 ROIs/image; 15 slices) were used for Bayesian optimization of these parameters with 4-fold cross-validation across 200 trials (1–DICE loss). Group differences were assessed using t-tests and ANOVA.

Results: Laser adjustment stabilized fluorescence intensity across 50 μm depth, reducing coefficient of variation from 40% to 29% (Fig 1A-B). Bayesian optimization improved DICE scores by 24% for lacunae and 12% for canaliculi (Fig 1C). Both modalities showed increased lacunar and canalicular density in osteosclerotic PCBM bone (Fig 1D-F,I). Synchrotron imaging additionally revealed increased lacunar degree (Fig 1H). While trends were consistent, confocal measured larger lacunar volumes (Fig 1G).

Discussion: We established a validated pipeline for confocal LCN imaging in human trabecular bone. Synchrotron and confocal imaging showed similar trends in lacunar metrics; however, short, small-diameter canaliculi near the lacunar surface in osteosclerotic bone were not detected by confocal, indicating confocal alone misses fine canalicular features. Fluorescence imaging overestimates lacunar volume due to signal spreading, making synchrotron more suitable for absolute volumetric measurements. Osteosclerotic PCBM bone showed increased lacunar and canalicular density, suggesting greater void volume fraction and disrupted osteocyte mechanosignaling. These findings provide the first connectomic characterization of the LCN in PCBM and establish standards for reproducible quantitative LCN analysis.

Session I: Osteocytes, Lacunocanalicular Network and Mechanosensing

S1-5: Naomi Jung

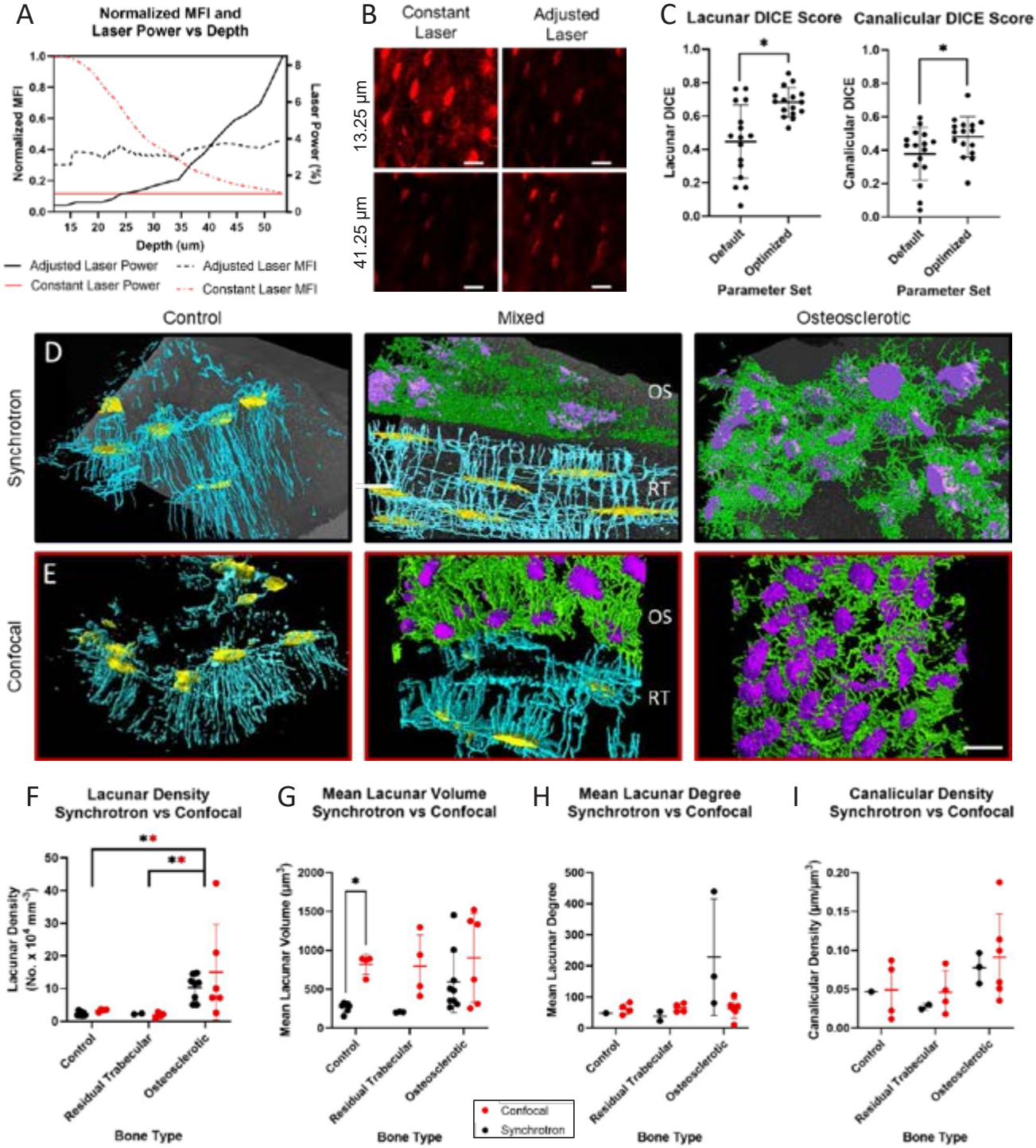

Figure 1. Optimized confocal imaging and analysis of the LCN in vertebral trabecular bone. A) Representative graph of rhodamine 6G-stained confocal imaging region of interest with the mean fluorescence intensity (MFI) for adjusted and constant laser settings. B) Confocal image demonstrating greater visibility of the rhodamine stained LCN with adjusted laser power at two depths (scale bar = 10 µm). C) Lacunar and canalicular DICE score for optimized segmentation parameters. LCN segmentations renders (thickness 30 µm) from D) confocal and E) synchrotron imaging of control (column 1), PCBM mixed osteolytic-osteosclerotic (column 2), and PCBM osteosclerotic (column 3) cadaveric vertebral trabecular bone samples (scale bar = 20 µm) Lacunae shown in yellow and canaliculi in blue in control and residual trabecular (RT) bone. Lacunae shown in purple and canaliculi in green in osteosclerotic (OS) bone. F)-H) comparison of synchrotron and confocal lacunar quantifications from 16 synchrotron images at 50-70 nm isotropic voxel size and 14 confocal images at 124 x 124 x 375 nm voxel size. I) comparison of synchrotron and confocal canalicular density from 4 synchrotron images at 50-70 nm isotropic voxel size and 14 confocal images at 124 x 124 x 375 nm voxel size. * = p-value <0.05

Session I: Osteocytes, Lacunocanalicular Network and Mechanosensing

S1-5: Eisha Farrukh Hashmi

Investigating the Effect of Dendrite Removal on Osteocyte Mechanosensitivity in Breast And Prostate Cancer Patients

Eisha F. Hashmi 1, Stefaan W. Verbruggen 1 2

School of Engineering and Materials Science,Queen Mary University of London,London,E1 4NS,United Kingdom 1. INSIGNEO Institute for in silico Medicine and Department of Mechanical Engineering, University of Sheffield, United Kingdom 2.

Purpose: Bone metastasis is a major cause of pain in advanced breast and prostate cancer. Although interactions between metastatic cells and the bone microenvironment are well established [1], the role of osteocytes—the most abundant bone cells and primary mechanosensors—remains underexplored. Osteocytes regulate their local mechanical environment through peri-lacunar remodelling, a process that may be disrupted in cancer [2] and influence osteocyte mechanics. Metastatic disease is also associated with dendritic degradation and reduced lacuna-canalicular connectivity [2]. Since dendrites serve as primary mechanosensory structures [3], we hypothesise that their gradual loss disrupts mechanotransductive signalling in cancer-affected bone.

Materials and Methods: Idealised multiphysics models were developed in which the osteocyte and lacuna were represented as ellipsoids (7.5×13.5 µm and 9×15 µm respectively), while dendritic processes and canaliculi were modelled as branching channels (Ø=0.44µm and Ø=0.6µm respectively) – reduced by symmetry to the layout in Fig1A-B. The osteocyte body was defined as a linear elastic solid (E_{cell}=4.47 kPa; ν_{cell}=0.3), and the surrounding pericellular matrix (PCM) was treated as a viscous fluid (µ=0.000855kg/m·s; ρ=997kg/m³) [4]. Progressive metastatic deterioration was simulated by removing individual, paired, triple, or all dendritic processes, with the resulting voids filled by PCM. Interstitial fluid flow of 60 µm/s was applied, and the mechanical response of the system was evaluated using a one-way fluid-structure interaction approach. To generate physiological geometries, confocal laser scanning microscopy was performed using a Lecia DMi8 (Leica Microsystems) microscope on fixed samples of C57BL/6 mouse bone. Osteocytes were visualised with hydrophobic lipophilic membrane dye DiI (Thermo Fisher), and DAPI to identify cell nuclei, with geometries reconstructed using MIMICS (Materialise) [5].

S1-5: Eisha Farrukh Hashmi

Results: Membrane shear stress (Fig.1D) remained approximately 3-4 Pa when some processes were removed but decreased to ~1.5 Pa when all processes were eliminated. Maximum cellular strain (Fig.1E) declined from ~40,000 to ~30,000 με following the removal of a single process, with only minor additional decreases until complete process loss, which reduced strain to nearly zero.

Conclusion: These findings indicate that dendritic process loss primarily affects strain transmission while having minimal impact on membrane shear stress experienced by osteocytes. Shear-driven mechanotransduction remained largely maintained—even after complete process removal—since osteogenic responses can occur at shear levels of ~0.8 Pa [6]. In contrast, strain-related signalling was significantly reduced, indicating that dendrites may play a greater role in amplifying strain than in sensing shear. This suggests that osteocytes may retain some mechanosensory capability despite structural degradation. Future work will incorporate more realistic osteocyte geometries and two-way fluid–structure interaction modelling including the extracellular matrix to better predict thresholds of mechanosensory failure in metastatic bone (Fig.1C).

References:

[1] James Stinson, Med Hypotheses, 1975
[2] Haniyeh Hemmatian et al., Bone, 2021
[3] Sirisha Burra et al., Proc Natl Acad Sci U S A, 2010
[4] Stefaan Verbruggen et al., Biomech Model Mechanobiol, 2014
[5] Charles Schurman et al., Proc Natl Acad Schi U S A, 2021
[6] Neal Chen, Am J Physiol Cell Physiol, 2000

Session I: Osteocytes, Lacunocanalicular Network and Mechanosensing

S1-5: Eisha Farrukh Hashmi

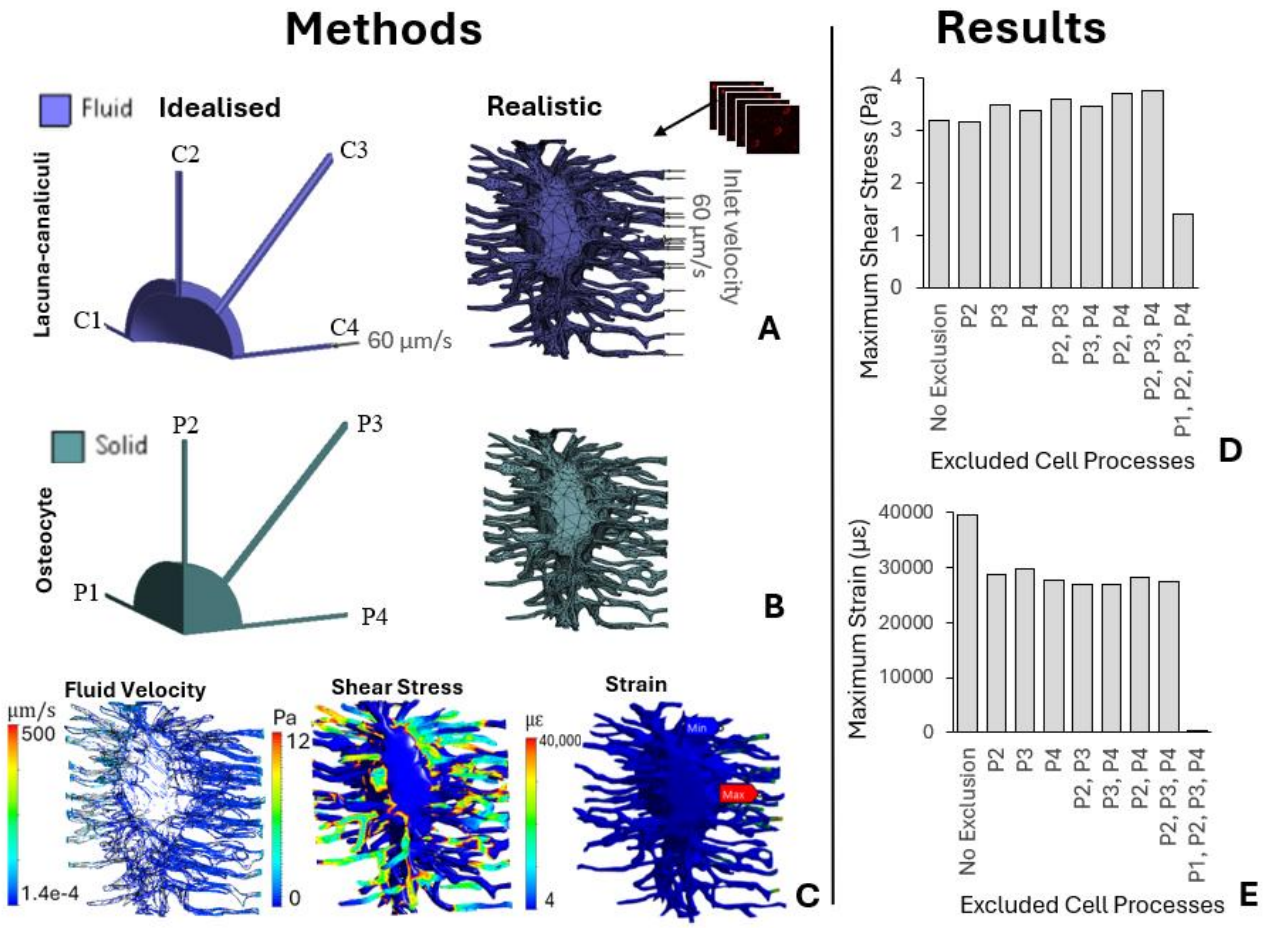

***Figure 1*. Modelling osteocyte mechanobiology and the impact of dendritic process removal.**
(A) Idealised and imaging-derived lacunar-canalicular geometries representing the osteocyte microenvironment, and (B) the corresponding osteocyte morphologies with processes. These components are coupled through a fluid-structure interaction framework to evaluate the mechanical response of the osteocyte and surrounding pericellular matrix under interstitial fluid flow. (C) Representative simulation outputs showing spatial distributions of fluid velocity, membrane shear stress, and cellular strain. (D) Maximum membrane shear stress and (E) maximum cellular strain for different process-removal scenarios, where individual or multiple dendritic processes (P1-P4) are sequentially excluded from the idealised model.

Session II: Spatial Omics

S2-1: Neashan Mathavan, PhD

Forces and Function: Spatial Omics in Bone Mechanobiology

Spatial omics represent a transformative advancement in cellular profiling technologies, enabling high-resolution characterization of cellular function within its native spatial context. In bone, these technologies present new opportunities to dissect the molecular and cellular processes that underpin tissue homeostasis, adaptation, and disease. To leverage this potential, we have developed an integrated framework combining spatial multi-omics, time-lapsed micro-CT imaging and micro-finite element modelling, allowing cellular function to be investigated across local mechanical and structural landscapes and their associated micro-environments.

Applying this framework across models of bone adaptation and regeneration, we can explore how spatially distinct tissue and mechanical environments drive divergent cellular and molecular programs. In doing so, we illustrate the potential of our framework to provide new insights into the regulatory mechanisms governing skeletal biology and to identify novel targets for therapeutic intervention in bone disease.

S2-2: Robert Tower, PhD

Spatial Omics Insights into Cellular Niches and Tissue Regeneration

Spatial transcriptomics is a powerful technology that facilitates the measurement of gene expression levels within the native tissue architecture. Spatial-omics applications have proven crucial in elucidating aspects of cellular heterogeneity, molecular mechanisms underlying injury, and gene expression patterning in tissue homeostasis and disease across numerous fields. However, turning raw data into biological insight from spatial transcriptomics experiments remains a substantial bottleneck in the application and utilization of spatial data. Here, we present some of the emerging analysis tools being applied to spatial transcriptomics data to extract new biological insight.

S2-3: Stine Katrine Rye Østergaard, MSc

Evaluation of sample pre-treatement protocols for high throughput spatial profiling of formalin-fixed paraffin embedded human bone tissue

Stine Katrine Rye Østergaard,1 Maja Hinge,6 Thomas Lund,5,6,9 Hanne E. H. Møller,3 Morten Nørgaard Andersen,8,10 Kasper Thorsen,8 Thomas Levin Andersen,1,2,3,4 Therese Standal,7 Marta Diaz-delCastillo.1,2
1Dept. of Forensic Medicine, Aarhus University, Aarhus, Denmark. 2Danish Spatial Imaging Consortium, University of Southern Denmark, Odense, Denmark. 3Dept. of Pathology, Odense University Hospital, Odense, Denmark. 4Molecular Bone Histology Team, Dept. of Clinical Research, University of Southern Denmark, Odense, Denmark. 5Department of Hematology, Odense University Hospital, Odense, Denmark.6Department of Hematology, Lillebaelt Hospital, Vejle, Denmark. 7Dept. of Clinical and Molecular Medicine, Norwegian University of Science and Technology (NTNU), Trondheim, Norway. 8Dept. of Clinical Medicine - Department of Molecular Medicine (MOMA), Aarhus University, Aarhus, Denmark. 9Centre for Innovative Medical Technology, Odense University Hospital, Odense, Denmark. 10Dept. of Hematology, Aarhus University Hospital, Aarhus, Denmark.

Spatial profiling with platforms like the Xenium In Situ and CosMx Spatial Molecular Imager (CosMx SMI) enables high-throughput single-molecule mapping at subcellular resolution in intact tissue slides. Current pretreatment protocols for formalin-fixed, paraffin-embedded (FFPE) bone tissue are often suboptimal, limiting transcript detection. Therefore, optimizing these protocols is crucial for maximizing the efficiency of spatial profiling of human bone marrow.

We have developed an optimized protocol for pretreatment of FFPE clinical bone marrow biopsies for spatial profiling by Xenium In Situ and CosMx SMI. We compared our optimized protocol (modified pretreatment enzyme, temperature, and incubation time) with the vendor protocols for Xenium In Situ and CosMx SMI using archival trephine iliac crest biopsies from patients with monoclonal gammopathies (n = 9). Spatial profiling was performed with the following panels: Xenium RNA v1 Human Immuno-Oncology Panel (380 genes + 100 custom bone-specific targets), Xenium Prime 5K Human Pan Tissue & Pathways Panel (5001 targets), and CosMx Human RNA Universal Cell Characterization panel (1000 targets). Raw data were benchmarked in R, followed by cell type clustering using a Seurat-based pipeline.

S2-3: Stine Katrine Rye Østergaard, MSc

Application of our pretreatment protocol increased mean counts per cell in serial sections from the same patient biopsies across all platforms, compared to the vendor protocols. For Xenium V1, mean counts per cell increased from 173.4 (SD 146.9) to 184.0 (SD 142.9). Both Xenium Prime and CosMx showed an approximately threefold increase in mean counts (Prime: 11.57 [SD 13.57] to 29.34 [SD 23.55]; CosMx: 40.72 [SD 49.07] to 116.92 [SD 102.16]). Xenium V1 demonstrated a significantly higher sample-level signal-to-noise ratio (SNR) than Xenium Prime under the vendor protocols ($p = 0.008$), with no significant differences between pretreatments within either platform (Prime: optimized 162.63 [SD 31.04] vs. vendor 145.64 [SD 93.91]; V1: optimized 713.38 [SD 394.21] vs. vendor 543.40 [SD 158.73]). In contrast, CosMx showed an almost threefold increase in SNR with the optimized pretreatment (23.53 vs. 60.13; single sample, no SD). Bone tissue was lost in CosMx, partially preserved in Xenium Prime, and best preserved in Xenium V1, where lamellar structures remained clearly visible. This structural preservation enabled detection of osteoblast and osteoclast populations in the endosteal niche and detection of osteocyte-specific gene expression in cells embedded within the mineralized matrix.

Our optimized pretreatment protocol improved transcript detection across all platforms and enabled spatial mapping of osteoblasts, osteoclasts, and osteocytes. These findings demonstrate that optimized pretreatment may enhance both data quality and biological interpretability in spatial profiling of FFPE bone.

S2-4: Martin Christensen, MSc

Innervation and pain experience in multiple myeloma: a spatially resolved histological study of human bone

Martin S J Christensen1, Rebecca E Andrews2, 3, Aritri Mandal3, Andrew D Chantry2,3, Vera Lund-Rasmussen4, Thomas L Andersen1,5,6,7, Anne-Marie Heegaard8, Marta Diaz-delCastillo1,2,3,7

1Dept. of Forensic Medicine, Aarhus University, Aarhus, DK. 2Sheffield Myeloma Research Team, School of Medicine and Population Health, and Mellanby Centre for Musculoskeletal Research, University of Sheffield Medical School, Sheffield, UK. 3Dept. of Haematology, Sheffield Teaching Hospitals NHS Foundation Trust, Royal Hallamshire Hospital, Sheffield, UK. 4Rigshospitalet, Afdeling for Røntgen og Skanning DIA, Copenhagen, DK. 5Dept. of Clinical Research, University of Southern Denmark, Odense, DK. 6Dept. of Clinical Pathology, Odense University Hospital, Odense, DK. 7The Danish Spatial Imaging Consortium (DanSIC). 8Dept. of Drug Design and Pharmacology, University of Copenhagen, Copenhagen, DK.

Background: Multiple myeloma (MM) is a plasma cell cancer preceded by the pre-malignant (PMG) stages monoclonal gammopathy of undetermined significance and smouldering multiple myeloma. Pain is among the main symptoms experienced by patients with MM; however, the underlying mechanisms remain unknown.

Aim: To investigate the relation between self-reported pain scores and neuronal remodelling in the bone marrow microenvironment of patients with PMG or MM.

Methods: A cohort of 17 PMG and 20 MM patients attending Sheffield Teaching Hospital for a diagnostic trephine iliac crest biopsy answered the Brief Pain Inventory (BPI) and the European Organisation for Research and Treatment of Cancer (EORTC) C-30 questionnaires to investigate pain and quality of life (QoL), respectively (approval REC19/YH/0319). Diagnostic whole-body MRI imaging was evaluated by an experienced radiologist blinded to patient identity. Formalin fixed, paraffin embedded biopsies were sectioned at 3µm thickness and immunostained for CD138 (plasma cells), CD34 (blood vessels) and either PGP9.5 (pan-neural marker) or TH (sympathetic nerves) on serial sections. Histological spatial analysis was performed using AI-assisted histology; a cohort of 7 healthy controls (approval S-20110112) was similarly evaluated.

S2-4: Martin Christensen, MSc

Results: BPI pain intensity was comparable across patients with PMG and MM, while interference with daily activities was significantly higher in patients with MM. EORTC-QLQ C030 revealed significantly lower QoL in patients with MM compared to PMG ($p<0.05$). Notably, MRI imaging of 16 patients with MM showed that 76% of bone lesions do not colocalise with self-reported pain location. Bone biopsies from patients with MM presented, as expected, a significantly higher density of CD138+ plasma cells compared to PMG. Both PMG and MM patients presented an increased density of CD34+ blood vessels compared to controls. A non-significant decrease in PGP9.5+ nerve profile density was observed in both PMG and MM patients compared to controls. Interestingly, the frequency of nerve profiles located within 25µm of CD34+ blood vessels decreased with progression from control to PMG or MM ($p<0.05$, $p<0.001$). PGP9.5+ and TH+ nerve profile density was decreased in the peritrabecular niche within 100µm of bone surfaces vs the hematopoietic niche (>100 µm) in MM patients compared to PMG. Surprisingly, PGP9.5+ nerve profile density, but not lesion burden, was significantly correlated with pain and QoL.

Conclusion: This is the first evaluation of bone marrow innervation in patients with PMG and MM. Our data suggest that disease progression causes profound reorganisation of the bone marrow microenvironment, including angiogenesis and nerve remodelling, and that systemic cancer-driven loss of innervation, rather than bone lesion development, may contribute to bone pain in MM.

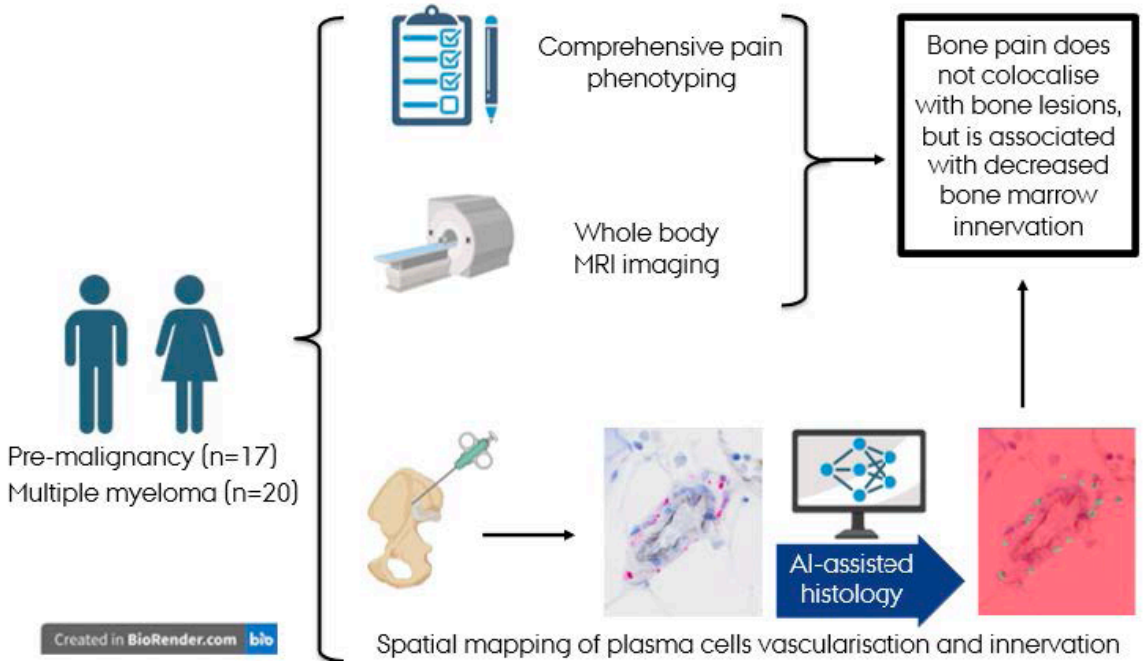

Figure – Study overview and conclusion

S2-5: Hiroyuki Okada, PhD

Quantitative osteocyte profiling powered by AI assisted bone deep spatial transcriptomics

Hiroyuki Okada1,2,3,*, Fumiko Yano4, Asuka Terashima5, Sanshiro Kanazawa6, Yasunori Omata2,5, Francesca Gori3, Taku Saito2, Shigeto Seno7, Junichi Kikuta8, Roland Baron3, Ung-il Chung1,9, Sakae Tanaka2, Hironori Hojo1,9,10”

1. Center for Disease Biology and Integrative Medicine, the University of Tokyo 2. Department of Orthopaedic Surgery, the University of Tokyo 3. Department of Oral Medicine, Infection, and Immunity, Harvard School of Dental Medicine 4. Showa Medical University Research Administration Center 5. Bone and Cartilage Regenerative Medicine, the University of Tokyo Hospital 6. Department of Oral and Maxillofacial Surgery, Graduate School of Medicine, the University of Tokyo 7. Department of Bioinformatic Engineering, Graduate School of Information Science and Technology, the University of Osaka 8. Division of Immunology, Department of Future Medical Sciences, Graduate School of Medicine, Kobe University 9. Department of Bioengineering, Graduate School of Engineering, the University of Tokyo 10. Department of Bioinformatics, Graduate School of Dental Medicine, the University of Osaka

Purpose: Current spatial transcriptomics platforms such as the 10x Genomics Xenium system segment cells by expanding nuclear masks derived from DAPI without incorporating histological images. While adequate for homogeneous, cell-dense tissues, this approach fails in bone, where osteocytes are sparsely embedded in mineralized matrix alongside empty lacunae and diverse tissue types. Here, we devel-oped an original cell segmentation and label transfer framework that integrates H&E images co-registered to DAPI, enabling quantitative osteocyte profiling across whole murine femora.

Materials and Methods: FFPE femoral sections from wild-type (n = 3) and ovariectomized (OVX, n = 3) mice were decalcified for 72 h and analyzed on the Xenium In Situ platform. H&E images were co-registered to DAPI and mapped to the Xenium coordinate system. Our pipeline leverages classical histomorphometric features from H&E—lacunar morphology, tissue texture, and staining patterns—to guide tailored cell segmentation algorithms across bone, cartilage, marrow, muscle, and fibrous tissue. An optimal transport–based, tissue-constrained label transfer method assigned cell identities using a mouse bone and marrow scRNA-seq reference atlas.

S2-5: Hiroyuki Okada, PhD

Results: Our pipeline segmented >110k cells per femur across six biological samples (>790k cells total), assigning >85% of transcripts to cells, compared with ~17k cells per femur and ~30% transcript assignment by default Xenium segmentation. Existing tools (Baysor, Cellpose3) proved ineffective in bone, yielding fewer morphologically plausible cells. Gene expression profiling of >10k osteocytes per section enabled classification into mineralizing and remodeling subtypes by the expression level of Tnfsf11. In OVX mice, preliminary morphometric analysis indicated reduced bone volume and a trend toward increased empty lacunae. This framework enables simultaneous quantification of tissue architecture, osteocyte occupancy, and functional subtype distribution, linking classical histomorphometry with spatial transcriptomics within a single coordinate system.

Conclusions: This study provides, to our knowledge, the first comprehensive spatial transcriptomic assessment of >10k osteocytes per femoral section, validated across six biological samples totaling ~800k cells. Classical histomorphometric knowledge—long the foundation of bone biology—proved essential for accurate AI-driven cell segmentation in mineralized tissue. Starting from the most segmentationresistant tissue, our approach offers a transferable strategy for spatial transcriptomics in calcified and heterogeneous tissues, bridging decades of histological expertise with modern molecular profiling.

S2-5: Hiroyuki Okada, PhD

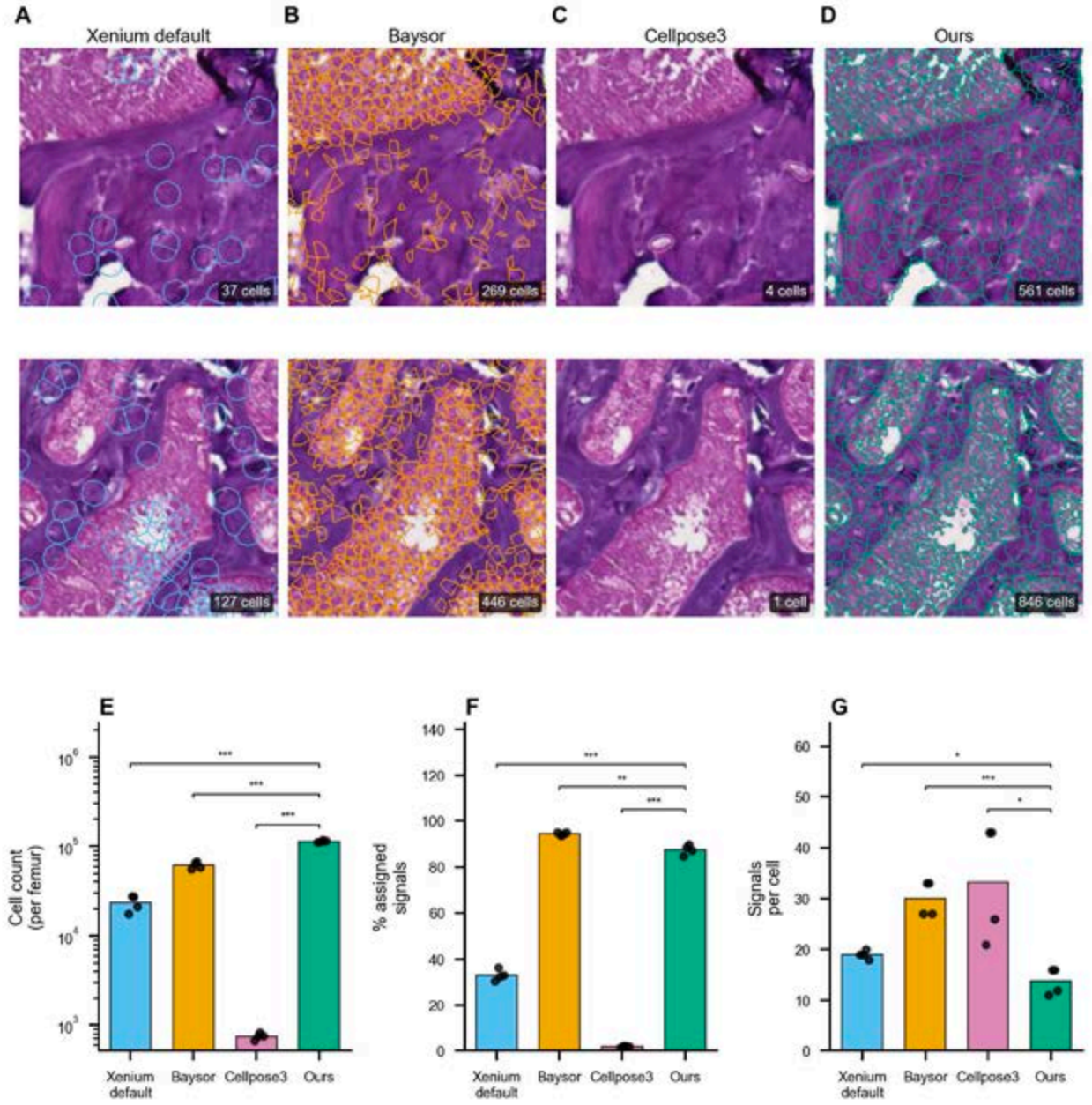

Figure 1. H&E-guided cell segmentation enables quantitative osteocyte profiling in murine femora. (A–D) Two representative bone fields of view showing cell segmentation boundaries overlaid on H&E for four methods: (A) Xenium default, (B) Baysor, (C) Cellpose3, and (D) our pipeline. (E) Cell count per femur (log scale; n = 4 biological samples, individual data points shown). (F) Percentage of Xenium transcripts assigned to segmented cells. (G) Median number of transcripts per cell. Welch's t-test: *p < 0.05, **p < 0.01, ***p < 0.001.

Session III: Bone Vascularization and Microstructure

S3-1: Anjali Kusumbe, PhD

Multimodal Evidence for Bone Lymphatics and Reassessment of Skeletal Vasculature

Bone lymphatic endothelial cells (LECs) have emerged as a previously unrecognized component of the skeletal microenvironment, with important implications for bone biology, regeneration, and disease. In this presentation, we integrate multimodal approaches, including spatial transcriptomics, single-cell RNA sequencing, and advanced three-dimensional imaging, to define the identity, localization, and function of skeletal LECs across murine and human bone. Spatial transcriptomic analyses reveal Prox1-positive endothelial populations embedded within bone, while reanalysis of multiple independent single-cell RNA sequencing datasets demonstrates the reproducible presence of bone LECs across diverse skeletal sites. We further highlight the importance of appropriate tissue sampling, sensitive genetic tools, and validated imaging strategies for accurately identifying rare endothelial populations within mineralized tissues. Finally, we discuss how integrative reanalysis of publicly available datasets provides new insights into skeletal vascular organization, endothelial heterogeneity, and age-associated vascular remodeling. Together, these findings establish bone LECs as an integral component of the skeletal vascular niche and provide a framework for future studies investigating their roles in skeletal homeostasis, ageing, regeneration, and disease.

Session III: Bone Vascularization and Microstructure

S3-2: Warren Grayson, PhD

Investigating the Neurovascular Contribution to Bone Healing

Bone injuries demonstrate rapid peripheral nerve ingrowth followed by nerve pruning as healing ensues. However, in non-healing bone injuries, peripheral innervation remains elevated, the implications of which remain unknown. Therefore, we investigated the neuroskeletal microenvironment in subcritical- and critical-sized calvarial defects using quantitative 3D fluorescence imaging. We identified elevated densities of peripheral nerves and Osterix positive (Osx+) osteoprogenitors in critical-sized defects, while osteogenic differentiation markers were severely diminished. Moreover, Osx+ osteoprogenitors in critical-sized defects exhibited enhanced proximity to peripheral nerves, which in turn was associated with increased osteoprogenitor cell proliferation. Using retrograde tracing in conjunction with single cell RNA-sequencing of sensory nerves from the innervating trigeminal ganglia, we identified a sensorineural-skeletal signaling interaction elevated in critical-sized defects that can be leveraged as a potential therapeutic target for enhancing bone healing. These studies reveal insights into the kinetics and distribution of nerves in non-healing injuries that may provide insights for the design of biomaterials used to treat these injuries.

Session III: Bone Vascularization and Microstructure

S3-3: Corinne Mahfouz, MEng

Multiscale rabbit bone structure: primary vs. secondary osteons

Corinne Mahfouz *a,c, Thomas Reissa, Patrick Aimedieub , Benjamin Smaniottoa, Elsa Vennata, Sophie LeCannc
a LMPS, Université Paris-Saclay, CentraleSupélec,
Gif-sur-Yvette, France
b Navier, CNRS, ENPC, UGE, Champs-sur-Marne,
France
c MSME, CNRS, UPEC, Créteil, France
*Corresponding author:
corinne.mahfouz@centralesupelec.fr

1. Purpose: The mechanical behavior of bone is conditioned by its multiscale, hierarchical structure starting from the nanoscale (Buss et al. 2022). Assessing bone quality requires investigating smaller scales with high-resolution imaging which is often limited to either small volumes of interests or 2D. Multiscale and multimodal correlative workflows integrate 3D information with 2D high resolution detail, which is particularly relevant given the heterogenous and anisotropic nature of bone. Moreover, species- and site-specific variations, should be accounted for when using animal models. The aim of this work is to gain a deeper understanding of the microstructural organization of healthy rabbit bone, a common animal model, underexplored at small scales, with a focus on
primary and secondary osteons.

2. Methods:

2.1 X-ray micro-computed tomography (micro-CT) Samples of 4 x 1 x 4 mm3 were sectioned from the middle shaft of three rabbit tibiae and scanned with high resolution (Ultratom, RX Solutions, isotropic voxel size 2 µm).

2.2 Scanning electron microscopy (SEM)
The same samples were prepared (dehydration in graded ethanol, embedding, polishing) and visualized with a SEM (Gemini, Zeiss) in backscattered electrons (BSE) mode.

2.3 Transmission electron microscopy (TEM) Ultrathin sections of primary and secondary osteonal lamellae zones were lifted-out in-situ by focused ion beam (FIB) (Helios Nanolab, Thermo Fisher Scientific) and observed in TEM (Titan3, Thermo Fisher Scientific).

S3-3: Corinne Mahfouz, MEng

2.4 Image processing and analysis
Segmentation and analyses were done in Dragonfly.
For micro-CT, cortical porosity was isolated from the mineralized bone tissue using Otsu threshold. For SEM, deep-learning aided segmentation was used to segment bone, porosities and exclude cracks. Volume and surface criteriums were applied to distinguish vascular canals from osteocyte lacunae in micro-CT and SEM.

3. Results and discussion: Structural features in healthy rabbit bone were quantified at different scales. The 3D arrangement of the canal network appeared site-specific (Figure 1), consistently with literature (Pazzaglia et al. 2008). Canals and osteocyte lacunae were quantified in 3D. Local mineralization heterogeneities (cement lines, mineralized islands) and smaller scale porosities (canaliculi) were seen in SEM images (unresolved in micro-CT), allowing the distinction between canal types (primary, secondary and periosteal). 620 canals and 7500 osteocyte lacunae were measured. Canals of secondary osteons had higher 2D areas on average than primary osteons and periosteal bone, osteocyte lacunae 2D area followed the same pattern. TEM images revealed alternating collagen fibril orientation and variable mineral orientation in adjacent lamellae.

4. Conclusions and perspectives: Healthy rabbit bone structure was analyzed through a multiscale and multimodal approach. While site-specific differences in osteon types were previously established, similar analysis on osteocyte lacunae has not been done to our knowledge. These findings support further extended 3D analyses of osteocyte lacunae in different osteon types and in larger populations, helping to clarify osteocyte function in bone remodeling in rabbits.

Acknowledgements: This work was funded by the ANR MuBIA (23-CE51-0018), Paris Ile-de-France Region (DIM “Respore”) and the CNRS (MITI interdisciplinary program).

References:
Buss, D. J., Kr ̈oger, R., McKee, M. D., and Reznikov, N. (2021). Hierarchical organization of bone in three dimensions: A twist of twists. Journal of Structural Biology: X,6:100057
Pazzaglia, U. E., Bonaspetti, G., Ranchetti, F., and Bettinsoli, P. (2008). Amodel of the intracortical vascular system of long bones and of its organization: an experimentalstudy in rabbit femur and tibia. Journal of Anatomy, 213(2):183–193.
Dragonfly 3D World, Comet Technologies Canada Inc., Montreal, Canada.

S3-3: Corinne Mahfouz, MEng

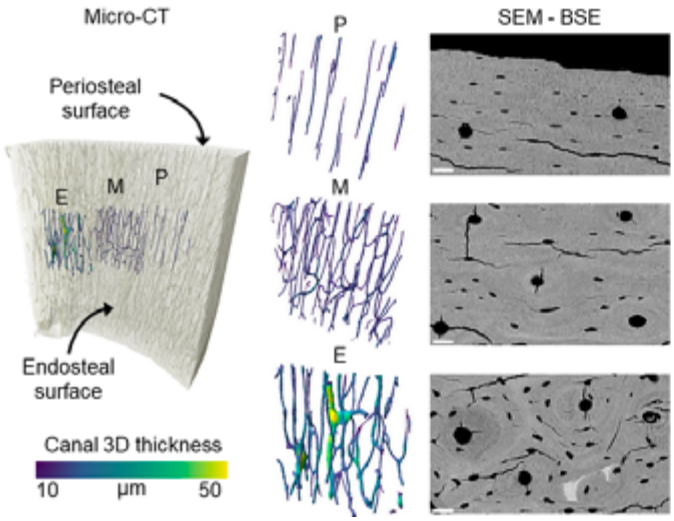

Parameters	Secondary Osteon	Primary Osteon	Periosteal Bone
Canals Porosity (%)	4.21 ± 0.15	1.72 ± 0.13	1.39 ± 0.49
Canal Minimum 2D Diameter (µm)	16.68 ± 1.10	11.32 ± 0.34	11.63 ± 0.76
Lacunae Porosity (%)	2.94 ± 0.016	2.10 ± 0.35	1.55 ± 0.27
Lacuna Minimum 2D Diameter (µm)	3.77 ± 0.051	3.21 ± 0.11	2.61 ± 0.20

Figure 1: Site-specific differences in rabbit bone. Micro-CT: endosteal (E), mid-cortex (M) and periosteal (P) regions present different porosity and structural 3D arrangement. SEM – BSE: cross-sectional view of canals and osteocyte lacunae. Data shown in table are expressed as mean ± standard deviation.

Session III: Bone Vascularization and Microstructure

S3-4: Anne Marie Møller Faaborg, MSc

Microstructural heterogeneity in human bone affected by X-linked hypophosphatemia

Anne Marie M. Faaborg,1 Marta D. del Castillo,2 Kaja S. Laursen,2 Maja Østergaard,1 Peter A. S. Vibe,1 Richard Deyhle Jr.,1 Marius Didziokas,1 Jesper S. Thomsen,3 Signe S. Beck-Nielsen,4 Lars Rejnmark,4 Thomas L. Andersen,2,5 Henrik Birkedal1

1Dept. of Chemistry & iNANO, Aarhus University (AU), Aarhus, Denmark, 2Dept. of Forensic Medicine, AU, Denmark, 3Dept. of Biomedicine, AU, Aarhus, Denmark, 4Dept. of Clinical Medicine, Aarhus University Hospital, Aarhus, Denmark, 5Dept. of Clinical Research, University of Southern Denmark, Odense, Denmark

Purpose: X-linked hypophosphatemia (XLH) is a rare, bone impairing disease caused by mutation in the gene PHEX. Clinical bone manifestations include osteomalacia, skeletal deformations, and pain1. At a microstructural level, XLH is characterised by hypomineralised lesions as well as a highly heterogeneous mineralization pattern2. These manifestations are believed to be linked to elevated levels of fibroblast growth factor 23 (FGF23) and local accumulation of mineralisation-inhibiting osteopontin (OPN)3,4. However, a large-scale comparative investigation of the microstructural manifestations in human bone with correlation to biochemical markers has, to our knowledge, never been conducted and will provide contrast to model studies in mice5, contribute to our understanding of the disease as well as of general bone microstructure.

Materials and methods: Investigations are conducted on iliac crest biopsies from 22 XLH patients and 12 healthy controls of different ages and sexes. The microarchitecture of the trabecular and cortical compartments is analysed using X-ray microcomputed tomography (μCT) with a linear voxel size of 10 μm. Microstructure, including quantification of osteocyte lacunae, is analysed using high-resolution synchrotron X-ray CT with a linear voxel size of 0.55 μm. Osteoid and remodelling is assessed using histomorphometry.

Results: The manifestations of XLH are shown to vary in severity across the investigated length scales. Microarchitectural manifestations are mainly observed in the cortical compartment as increased cortical porosity and are more severe in men than in women consistent with hemizygosity.

Session III: Bone Vascularization and Microstructure

S3-4: Anne Marie Møller Faaborg, MSc

The microstructural mineralisation pattern in XLH-bone is highly heterogeneous in comparison to healthy bone, and observations include hypomineralised lesions associated with Haversian canals, osteocyte lacunae, and cement lines as well as irregular remodelling motifs (osteons, cement lines) (see figure). Histomorphometry reveals a varying degree of osteomalacia in XLH-bone, with osteoid surface ratios reaching >90% in the most severe cases.

Conclusion: The study shows that the expression of XLH is highly varied. The most severe cases are characterised by heterogeneous and irregular mineralisation patterns and lesions as well as pervasive osteomalacia and increased cortical porosity.

1. Carpenter TO. et al. J. Bone Miner. Res. 26 (2011) 1381-1388. doi:10.1002/jbmr.340
2. Fratzl-Zelman N. et al. J. Struct. Biol. 211 (2020) 107556. doi:10.1016/j.jsb.2020.107556
3. Boukpessi T. et al Bone 95 (2017) 151-161. doi:10.1016/j.bone.2016.11.019
4. Beck-Nielsen SS. et al. Orphanet J. of Rare Dis. 14 (2019) 58. doi:10.1186/s13023-019-1014-8
5. Hoac B. et al. J. Bone Miner. Res. 35 (2020) 2032. doi:10.1002/jbmr.4101

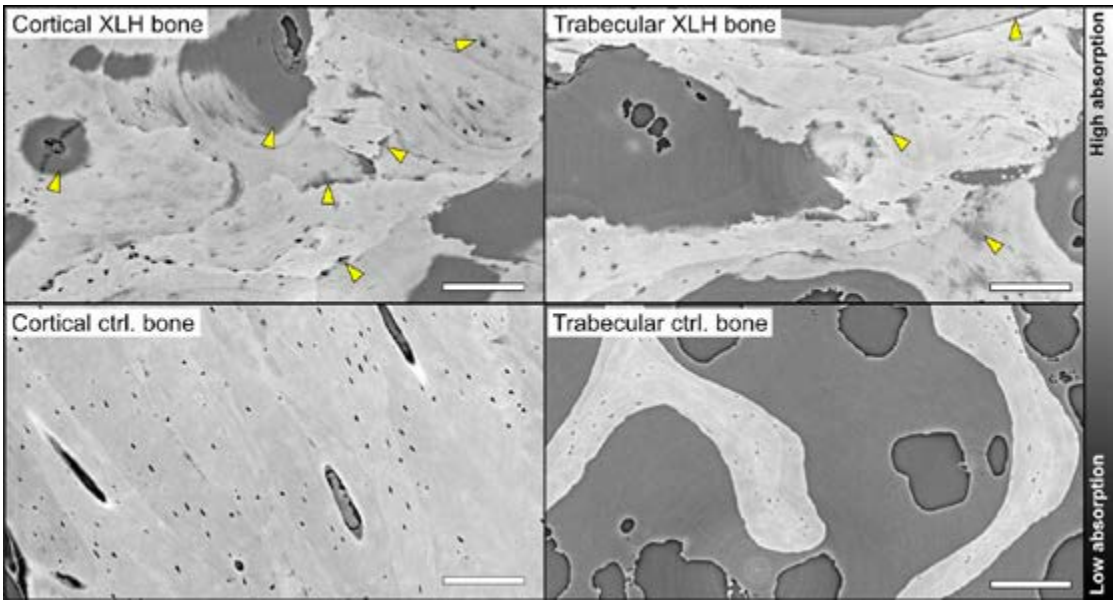

Figure: Tomographic slices from the synchrotron X-ray CT dataset showing the microstructure of a bone severely affected by XLH and a healthy control (ctrl.) bone. The mineralisation pattern in XLH bone is observed to be heterogeneous and irregular in comparison with healthy bone. Examples of non-mineralised lesions associated with Haversian canals, osteocyte lacunae, and cement lines are indicated in the XLH bone with yellow arrowheads.

Session III: Bone Vascularization and Microstructure

S3-5: Ryan Smith

3D characterization of the cement line in human trabecular bone via micro-computed x-ray tomography

Ryan Smith1, and W. Brent Lievers2*, Kathryn Grandfield1*

1 Materials Science and Engineering, McMaster University, Hamilton, Ontario, Canada 2 School of Engineering and Computer Science, Laurentian University, Sudbury, Ontario, Canada
*Shared senior authorship

Introduction: Cement line is created during bone remodeling and acts as the interface between existing tissue and newly created bone structural units (BSU) [1]. Its distinct composition and mechanical behavior relative to the BSU makes it a preferential pathway for microcrack initiation and propagation [2], [3]. The proportion of cement line is known to increase with age, which is thought to contribute to increased fracture risk in the elderly, and those with osteoporosis, by increasing the number of potential crack pathways. The ability to quantify the volumetric distribution of these interfaces could better illuminate the role of the cement line in skeletal fragility; unfortunately, existing 3-D characterization methods are time consuming and destructive. Micro-computed X-ray tomography (μCT) may offer a non-destructive and suitably scalable alternative. The goal of this work is to identify an effective workflow for μCT characterization of the cement line in human trabecular bone.

Methods: Samples for μCT were dissected from a previously fixed bulk section of a human femoral head. Using a Dremel rotary saw, several samples were dissected from the bulk section and dehydrated via ethanol series. Finished samples were mounted and scanned with a Zeiss Xradia 630 Versa X-ray microscope. Initial μCT trials were conducted to identify optimal scanning parameters for resolving the cement line: voltage, pixel size, and scan time. Resultant tomographs were reconstructed and converted into grayscale image stacks for 3-D image analysis in Dragonfly. When necessary, raw images were filtered with contrast limited adaptive histogram equalization and Gaussian smoothing filters to improve clarity. Image segmentation was performed utilizing trained U-Net regression models for the cement line. Watershed transforms bordered by the cement line allowed for identification of BSU.

Session III: Bone Vascularization and Microstructure

S3-5: Ryan Smith

Results: From initial trials, it was determined that μCT parameters of 50kV and 0.25μm pixel size produced the clearest image of the cement line, with a total scan-time of ~70-90 hours. Seen in Figure 1a, the cement line may be easily identified for manual training of a U-Net model for segmentation. 2-D examples of U-Net segmented cement line and subsequent watershed-identified BSU are shown in Figures 1b-c. Further μCT data was collected using these scanning parameters to demonstrate the capabilities of the method and acquire data related to BSU and cement line morphology.

Conclusions: A suitable μCT method for volumetric cement line characterization has been identified that allows the user to analyze the trabecular microstructure. Morphological observations from this method have been shown to agree qualitatively with the only previous study of 3-D trabecular BSU analyses [4]. Future work is planned to independently verify the accuracy of features seen in μCT through SEM imaging of previously scanned ROIs.

References:
[1] A. M. Parfitt, “The physiologic and clinical significance of bone histomorphometric data,” in Bone Histomorphometry: Techniques and Interpretation, Recker, 1983, pp. 143–223.
[2] K. Choi and S. A. Goldstein, “A comparison of the fatigue behavior of human trabecular and cortical bone tissue,” J. Biomech., vol. 25, no. 12, pp. 1371–1381, Dec. 1992, doi: 10.1016/0021-9290(92)90051-2.
[3] J. G. Skedros, J. L. Holmes, E. G. Vajda, and R. D. Bloebaum, “Cement lines of secondary osteons in human bone are not mineral-deficient: New data in a historical perspective,” Anat. Rec. A. Discov. Mol. Cell. Evol. Biol., vol. 286A, no. 1, pp. 781–803, 2005, doi: 10.1002/ar.a.20214.
[4] J. Kragstrup and F. Melsen, “Three-dimensional morphology of trabecular bone osteons reconstructed from serial sections,” Metab. Bone Dis. Relat. Res., vol. 5, no. 3, pp. 127–130, Jan. 1983, doi: 10.1016/0221-8747(83)90013-9.

Session III: Bone Vascularization and Microstructure

S3-5: Ryan Smith

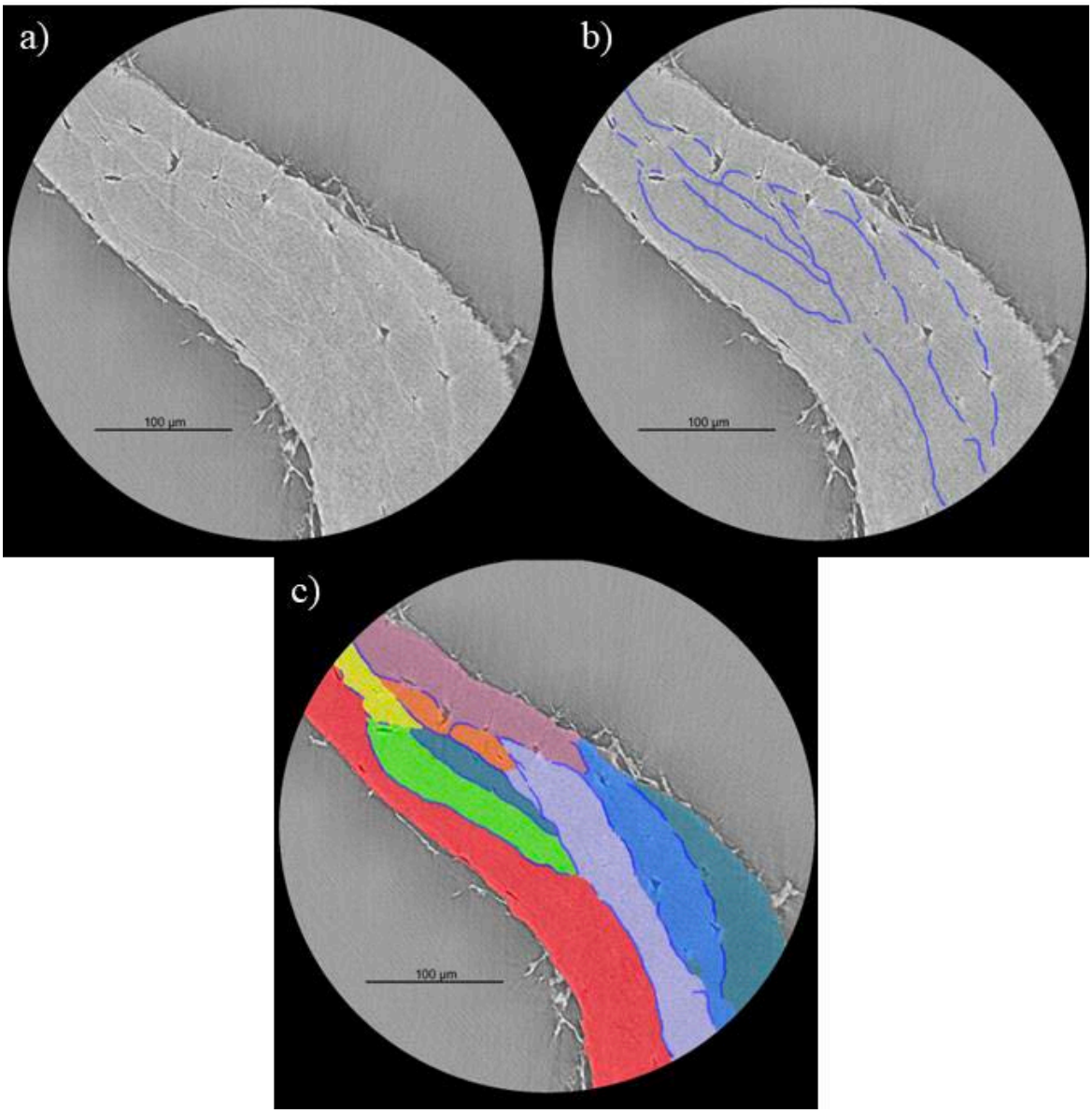

Figure 1: 2-D µCT images acquired at 50kv and 0.25µm. a) raw 2-D reconstruction of µCT data, b) U-Net segmented cement line interfaces (blue), c) watershed transform identified BSU (various colours).

Session IV: Clinical Imaging Assessment in Inflammatory Diseases

S4-1: Kathryn Stok, PhD

Advanced Imaging Approaches for Preclinical Assessment of Inflammatory Musculoskeletal Diseases

High-resolution, multi-scale, longitudinal characterisation of joint pathology can transform preclinical assessment of inflammatory musculoskeletal diseases. This presentation will describe protocols and findings for contrast-enhanced micro-computed tomography (microCT) studies of murine osteoarthritis models. High-temporal-resolution ex vivo microCT reveals subchondral bone microstructure deterioration that occurs as early as one-week post-disease induction, with a critical non-linear transition within three weeks. Extending this into longitudinal in vivo studies enables simultaneous tracking of whole-joint, microstructural, and dynamic remodelling analyses, demonstrating early osteoclastic activity preceding joint malalignment. Contrast-enhanced microCT provides quantitative insight into cartilage degeneration alongside bone adaptation, uncovering temporal fluctuations and mechanically driven changes across the 8-week timeline. Together, these approaches establish that early disease progression is rapid, non-linear, and multi-factorial, underscoring the importance of frequent, longitudinal imaging. This supports research towards identification of sensitive biomarkers and facilitates the development and evaluation of targeted interventions.

Session IV: Clinical Imaging Assessment in Inflammatory Diseases

S4-2: Carlos Urrego, PhD

Compromised bone architecture and strength in skeletally mature female mice with type 2 diabetes is associated with decreased endosteal bone formation and increased bone resorption

“Carlos A. Urrego1, Juan Pablo Raigosa1, Abigail G. Quint1, Savannah W. Jomaa1, Benjamin S. Sexton,1,2, Ingrid L. Rosko1, Clifford J. Rosen3 & David H. Kohn1,2 University of Michigan Dept. of Biomedical Engineering1, Dept of. Biological and Material Sciences2, Maine Health Institute for Research3

Women with type 2 diabetes (T2D) have a higher risk of fracture compared to diabetic men, but the underlying mechanism by which T2D compromises female bone quality remains unknown. We previously developed a T2D C57BL/6J mouse model and discovered that the effect of T2D on bone quality was driven by reduced cortical total volume (Ct.TV) and bone volume (Ct.BV). This study aimed to determine the role of bone formation and resorption as key determinants in diabetic bone architecture. We recreated our T2D mouse model using a combination of high-fat diet (HFD) and Streptozotocin (STZ). Healthy controls were fed a low-fat diet (LFD) and received sham injections (VEH). Diet-only (HFD+VEH) and STZ-only (LFD+STZ) control groups were also included. T2D was induced at 18 weeks, and all mice were euthanized at 30 weeks of age (n = 18–20). Bone architecture was assessed by micro-computed tomography; mechanical properties by four-point bending; bone formation and resorption by serum assays and dynamic histomorphometry; and bone marrow adiposity by histology with H&E staining. We demonstrated that the combination of HFD and STZ was required to induce diabetes. Only the HFD+STZ group developed and maintained diabetes for 12 weeks (blood glucose >250 mg/dL). The other groups remained euglycemic, proving that HFD or STZ alone were not sufficient to induce T2D in female mice. Consistent with the diabetic state, the combination of HFD and STZ was required to decrease total volume and bone volume. Compared with healthy controls (LFD+VEH), the HFD+STZ group showed a 5.4% reduction in Ct.TV (P=0.0028) and a 7.6% reduction in Ct.BV (P=0.0005) at the mid-diaphysis. These changes in architecture with T2D led to a 10.7% (P=0.002) decrease in the femoral ultimate load while preserving tissue-level properties. Furthermore, T2D decreased the mineral apposition rate by 21.1% (P=0.0164) and the bone formation rate (BFR) by 26.2% (P=0.0029) in the endocortical region. In addition, serum markers indicated a 97.9% (P=0.0002) increase in bone resorption with T2D. BFR was significantly correlated with Ct.TV (r=0.36) and Ct.BV (r=0.39).

Session IV: Clinical Imaging Assessment in Inflammatory Diseases

S4-2: Carlos Urrego, PhD

Lastly, T2D increased bone marrow adiposity by enlarging the average adipocyte size by 18.5% (P=0.0188), without altering adipocyte number. In summary, our findings demonstrate that reduced bone volume in T2D is associated with decreased bone formation and increased bone resorption, highlighting impaired bone metabolism as a key driver of the diabetic bone phenotype. This study shows that the combination of HFD and STZ is required to induce T2D in skeletally mature female mice, validates the reproducibility of our T2D animal model, and further supports the hypothesis that T2D's impact on bone quality is structure-driven. Our findings contribute to the understanding of the biomechanical mechanisms by which T2D compromises
women's skeletal health."

ISBM 2026 Abstract Figure - Carlos A. Urrego

A. The combination of a high-fat diet and streptozotocin induces type-2 diabetes (T2D) in female C57Bl6J mice. **B–C.** T2D female mice display spatially compromised femoral architecture. **D–E.** T2D compromises load-bearing capacity while preserving tissue-level material properties. **F–G.** Compared with healthy controls, the T2D group shows decreased mineral apposition rate and bone formation rate. **H–J.** Consistent with the observed architectural and histomorphometric changes, T2D alters circulating levels of bone formation and resorption markers, ultimately decreasing the expression of the bone formation-to-resorption ratio. **K–L.** T2D increases marrow adiposity by increasing adipocyte size while preserving the number of adipocytes.

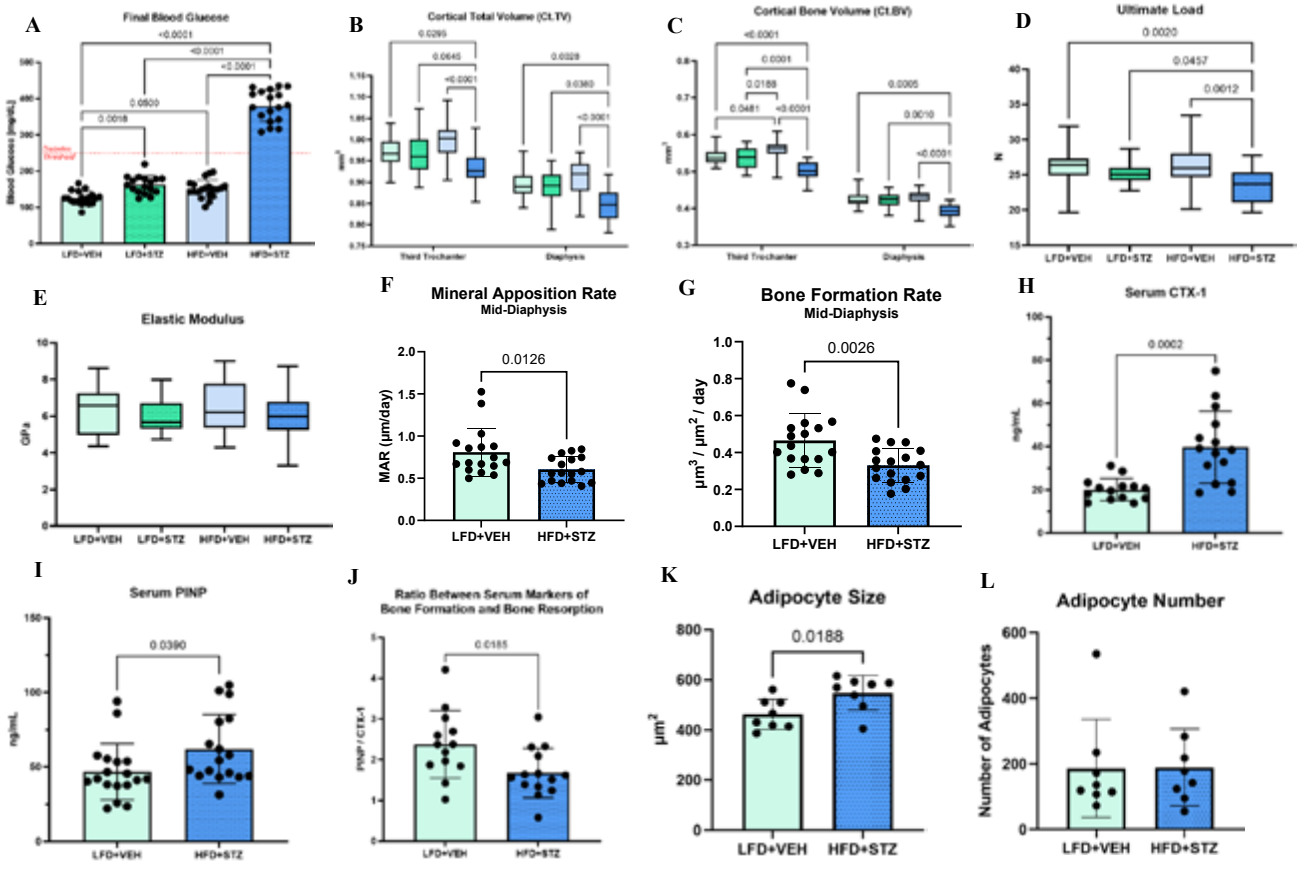

Session IV: Clinical Imaging Assessment in Inflammatory Diseases

S4-3: Dzenita Muratovic, PhD

Single-stain quantitative histomorphometry of bone matrix and lacunocanalicular, network distinguishes septic from aseptic osteolysis

Dzenita Muratovic 1, Dongqing Yang 1, Ryan D. Quarrington 1, Renjy Nelson 2, Boopalan Ramasamy 1,3, Lucian B. Solomon 1 3, Gerald J. Atkins1
1 School of Medicine, College of Health, Adelaide University, Adelaide, SA Australia
2 Department of Infectious Diseases, Central Adelaide Local Health Network, Adelaide, SA, Australia
3 Department of Orthopaedics and Trauma, Royal Adelaide Hospital, Adelaide, SA, Australia.

Introduction: Diagnosing periprosthetic joint infection (PJI) and distinguishing it from aseptic osteolysis (AO) remains a major challenge in revision arthroplasty. Current diagnostics rely predominantly on inflammatory cell thresholds and microbiological findings, with limited evaluation of deep bone matrix integrity or osteocyte lacunocanalicular network (LCN) pathology. In this study we developed and validated a novel single-stain quantitative histomorphometric platform enabling simultaneous assessment of bone matrix degradation and osteocyte LCN architecture within a single tissue section.

Methodology:Bone specimens from 41 patients undergoing revision arthroplasty were stratified into three groups: AO (n = 16), PJI (n = 16), and primary hip arthroplasty controls (n = 9). Following standardized fixation, decalcification, and paraffin embedding, RGB trichrome staining was validated as a single-section alternative to conventional multi-stain workflows (Masson's trichrome and Ploton's silver). Quantitative histomorphometry was then performed to identify structural and cellular parameters distinguishing AO from PJI.

Results: RGB trichrome provided superior simultaneous visualization of matrix and LCN architecture. PJI specimens exhibited marked type I collagen degradation relative to controls and AO ($p < 0.001$), enlarged and more circular lacunae ($p < 0.001$), reduced canalicular density ($p < 0.001$ vs AO; $p < 0.05$ vs controls), and shorter, narrower canaliculi (all $p \leq 0.005$). A distinctive perilacunar collagen "collar" was observed exclusively in PJI. In contrast, AO demonstrated relatively preserved collagen integrity but increased canalicular density compared with controls ($p < 0.05$) and PJI ($p < 0.0005$), producing a characteristic mottled matrix pattern (Figure 1). ROC analysis confirmed strong diagnostic performance, with lacunar circularity distinguishing PJI (AUROC = 0.935) and canalicular density discriminating both PJI (0.862) and AO (0.826).

S4-3: Dzenita Muratovic, PhD

Conclusions: This study establishes the osteocyte LCN as a histomorphometric signature of infection-driven bone destruction and introduces a scalable single-section workflow suitable for translational and intraoperative application. By shifting diagnostic emphasis from surface inflammation to deep structural integrity, this platform advances bone morphometry toward clinically actionable precision diagnostics.vv

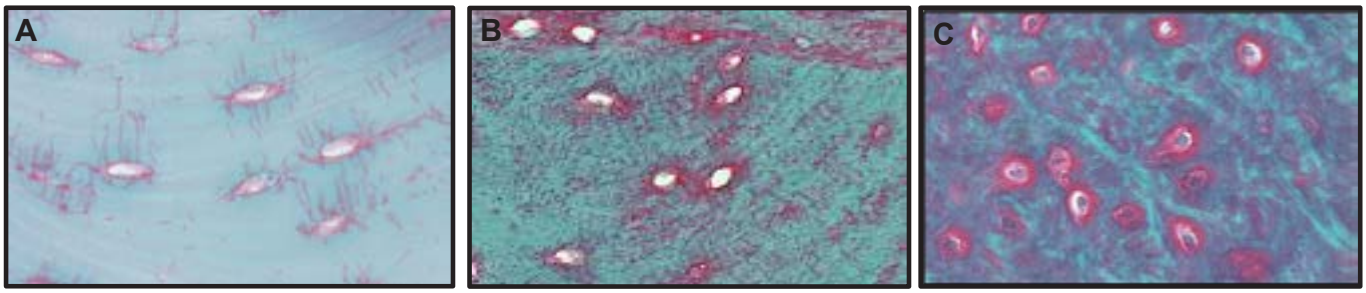

Figure 1. *RGB trichrome reveals distinct matrix and lacunocanalicular alterations across groups. A) Control: preserved matrix and LCN. (B) AO: increased canalicular density with mottled matrix. (C) PJI: collagen degradation, rounded lacunae, reduced canaliculi, and perilacunar collars.*

Session IV: Clinical Imaging Assessment in Inflammatory Diseases

S4-4: Ali Ghasem-Zadeh, PhD

Patients with chronic kidney disease have accelerated microstructural bone deterioration

Ali Ghasem-Zadeh1, Vanitha Nagarajah2, Cherie Chiang1, Nigel Toussaint3, Peter F Mount2 and Ego Seeman1

1- Department of Medicine, Austin Health, The University of Melbourne, Victoria, Australia
2. Department of Nephrology, Austin Health, The University of Melbourne, Victoria, Australia
3. Department of Nephrology, The Royal Melbourne Hospital, Victoria, Australia

Aim: To quantify the microstructural basis of bone fragility in patients with chronic kidney disease (CKD)

Background: Unbalanced remodelling upon intracortical and medullary canal surfaces of cortical bone enlarge these surfaces facilitating more frequent unbalanced remodelling events that erode the ever-decreasing cortical bone volume. By contrast, unbalanced remodelling upon surfaces of trabecular plates perforates and remove them with their surfaces. We therefore hypothesized that CKD accelerates cortical bone loss, but trabecular bone loss eventually ceases as trabeculae disappear; particularly in postmenopausal women.

Methods: Distal radius microarchitecture was quantified using serial High Resolution peripheral Computed Tomography scans in patients with CKD (24F, age 62.0 [52.6-68.8]), (26M, age 54.8[53.2-58.1]) followed for a median of 4.6(2.9–7.2) years, and controls (67F, 45M) followed for 3.7(1.4–7.9) years.

Results: Respective changes (%/yr) in microarchitecture relative to changes in controls were: in women, cortical area decreased faster (-3.4[-5.9 to -1.4] vs -0.99[2.0 to -0.46], p=0.0005); change in cortical volumetric bone mineral density (vBMD) (-1.38[1.29] vs -1.06[0.69] was not significant (p=0.14). Inner trabecular vBMD was unchanged (0.0[-0.1 to 0.05) vs 0.68[-0.19 to 1.2], p=0.08). In men, greater decreases in cortical area (-1.6[-4.9 to 1.1] vs -0.56[-3.5 to 0.29] did not achieve significance (p=0.31) but cortical vBMD decreased (-0.96[-1.4 to -0.04] vs 0.06[-0.82 to 1.6], p=0.024). However, unlike in women, there was a greater decrease in inner trabecular vBMD relative to controls (-0.35[-1.85 to 0.43] vs. 0.72[0-0.1to 2.5], p=0.03).

S4-4: Ali Ghasem-Zadeh, PhD

Conclusion: Within the constraints imposed by the small sample, we infer that microarchitectural deterioration is severe in CKD and continues, particularly in cortical bone, signaling the need for
antiresorptive therapy to slow bone loss and anabolic therapy to reconstruct the skeleton.

Session IV: Clinical Imaging Assessment in Inflammatory Diseases

S4-5: Gerald Degenhart, MSc

Quantitative HR-pQCT bone morphometry and composite score derivation as indicators of metabolic disease phenotypes—demonstrated in iron deficiency

Johannes Bereiter-Payr 1,2, Thomas Ausserer2, Sonja Wagner 3,4, Kerstin Stock 5, Benjamin Dejakumr 6, Martina Saretto3,4, Heinz Zoller 3,4, and Gerald Degenhart 2,†
1VASCage – Centre on Clinical Stroke Research, Data Science
2Medical University of Innsbruck, University Clinic for Radiology, Core Facility MicroCT 3Medical University of Innsbruck, Department of Medicine I – Gastroenterology – Hepatology and Endocrinology
4Medical University of Innsbruck, Christian Doppler Laboratory on Iron and Phosphate Biology
5Medical University of Innsbruck, University Clinic for Orthopedics and Traumatology
6Medical University of Innsbruck, Department of Neurology
†Presenting author

Background: Metabolic disorders may induce compartment-specific skeletal alterations that are not ade-quately captured by areal bone mineral density (aBMD). High-resolution peripheral quantitative CT (HR-pQCT) enables detailed assessment of trabecular and cortical bone morphometry; how-ever, interpretation commonly remains parameter-based and descriptive. We aimed to transform multidimensional HR-pQCT morphometric data into a composite structural metric by deriving a bone score directly from normalized morphometric parameters. This score is intended to en-able identification of metabolic disease–associated bone phenotypes rather than to represent a phenotype itself. Iron deficiency served as an exemplary metabolic model.

Methods: A total of 192 patients from two clinical cohorts underwent HR-pQCT imaging of the distal radius (XCT-2, Scanco Medical AG), with 4–6 scans per patient over 12 months. Standard trabecular (number, thickness, separation, volumetric density) and cortical (thickness, area, porosity) morphometric parameters were extracted and averaged per individual. Age- and sex-adjusted normalization was performed using established statistical models. Principal component analysis (PCA) identified dominant axes of structural variance, followed by fuzzy c-means clus-tering (FCM) to detect reproducible demineralization patterns. Morphometric findings were compared with areal BMD obtained by DXA, where available, or with projected mineral density derived from HR-pQCT. Based on PCA and compartment-specific parameter contributions, a composite bone score was mathematically derived directly from the normalized morphometric variables, providing continuous quantification of structural deviation.

S4-5: Gerald Degenhart, MSc

Results:

Three structural patterns were identified:
1. generalized trabecular and cortical impairment,
2. predominant trabecular deterioration with relative cortical preservation, and
3. selective cortical thinning with comparatively preserved trabecular structure.

The composite score differentiated these patterns independently of aBMD classification and provided continuous assessment of compartment-specific skeletal alteration. Patients with iron deficiency predominantly exhibited the trabecular-predominant pattern (2), characterized by reduced trabecular number and volumetric density without marked cortical compromise.

Conclusion: We present a novel framework that converts multidimensional HR-pQCT bone morphome-try into a composite score derived directly from normalized parameters. This metric enables compartment-sensitive structural assessment beyond conventional densitometry and may facili-tate the identification of metabolic disease phenotypes, as demonstrated in iron deficiency.

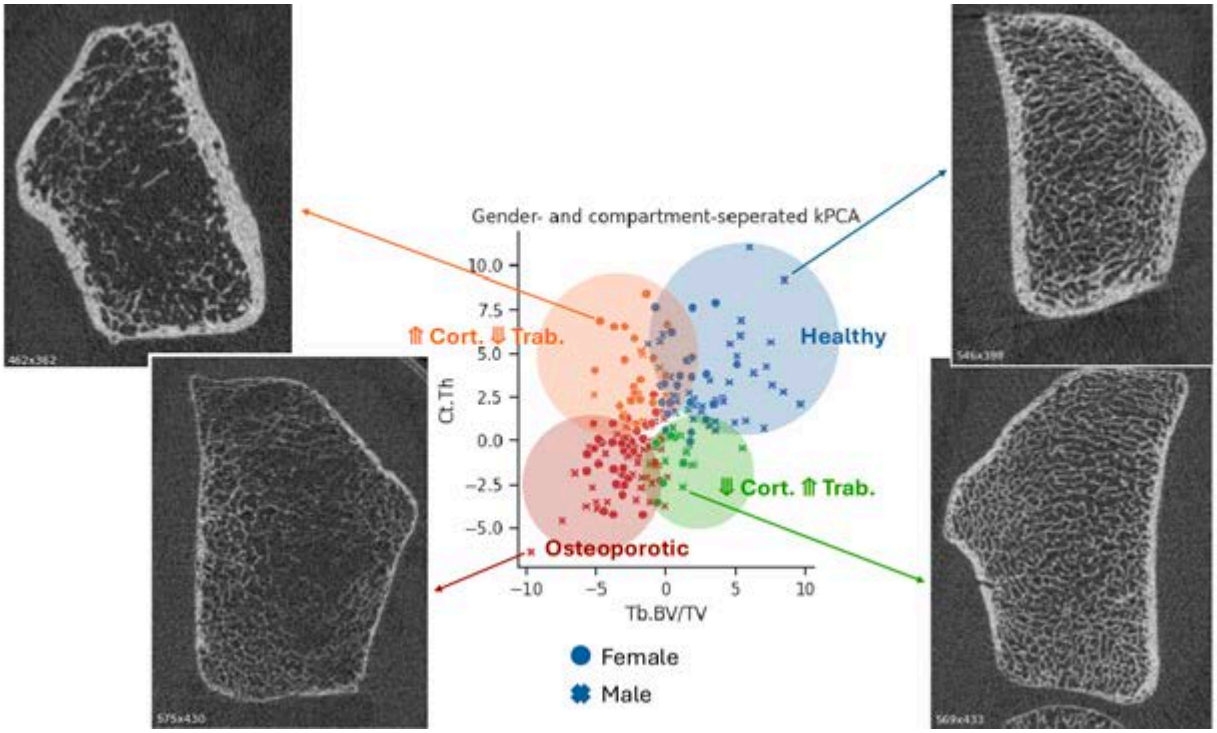

Figure 1: Results of clustering on a sample set of HR-pQCT measurements, showing different demineralization patterns.Top left shows the identified iron deficiency phenotype

Session IV: Clinical Imaging Assessment in Inflammatory Diseases

S4-6: Corinna Modiz, MSc

Whole-bone-scale, high-resolution quantification of femoral bone mineral content using xct: A regional analysis across anatomical octants and radial compartments

Corinna Modiz a,d, Natalia M. Castoldi b, Carl Yangc, Vittorio Sansaloned, Andrew Kingstonc, Peter Pivonkaa
a Queensland University of Technology (QUT), Brisbane, Australia | bTechnische Hochschule Nürnberg, Germany | cAustralian National University, Canberra, Australia | dUniv Paris Est Creteil / Univ Gustave Eiffel, CNRS, UMR 8208, MSME, Créteil, France

Tissue mineral content is a key determinant of bone mechanical properties, and spatial variations across anatomical regions are critical for accurate computational bone adaptation modeling. Quantitative backscattered electron imaging provides high-resolution mineral quantification but is restricted to small fields of view, capturing local rather than regional patterns. We quantify mineral volume fraction (MVF) across entire femoral midshaft cortical cross-sections using micro computed tomography (XCT), enabling simultaneous characterization of circumferential and radial heterogeneity at the whole-bone scale.

A physics-based pipeline converts XCT grey values to linear attenuation coefficients and subsequently to MVF using a polychromatic beam model with effective attenuation coefficients computed per material (hydroxyapatite, water, organic matrix). Bone segmentation uses multi-Otsu thresholding with morphological refinement and in-plane erosion to mitigate partial volume effects. Regional analysis includes eight anatomical octants and three radial compartments, defined via distance-transform normalised position maps applied across the full 3D volume (~1000 slices) at 11□□ resolution. Estimation statistics with bootstrap confidence intervals assess octant-wise differences. Samples were imaged at 60 keV peak energy with 0.5 mm Cu filtration; an Al phantom below each sample enabled beam-hardening correction (BHC, exponent 1.2) and signal-to-noise assessment. To assess sex and age differences in MVF patterns, four cadaveric femur midsections (male/female; young/old) from the Melbourne Femur Research Collection were imaged. Figure 1 shows results for an 81-year-old female donor.”

Session IV: Clinical Imaging Assessment in Inflammatory Diseases

S4-6: Corinna Modiz, MSc

Figure 1. Binary segmentation mask after morphological refinement and erosion; MVF map; octant classification map; radial compartment map; and radial boundary contours superimposed on octant labels (shown at 25%, 50% and 75% of stack depth).

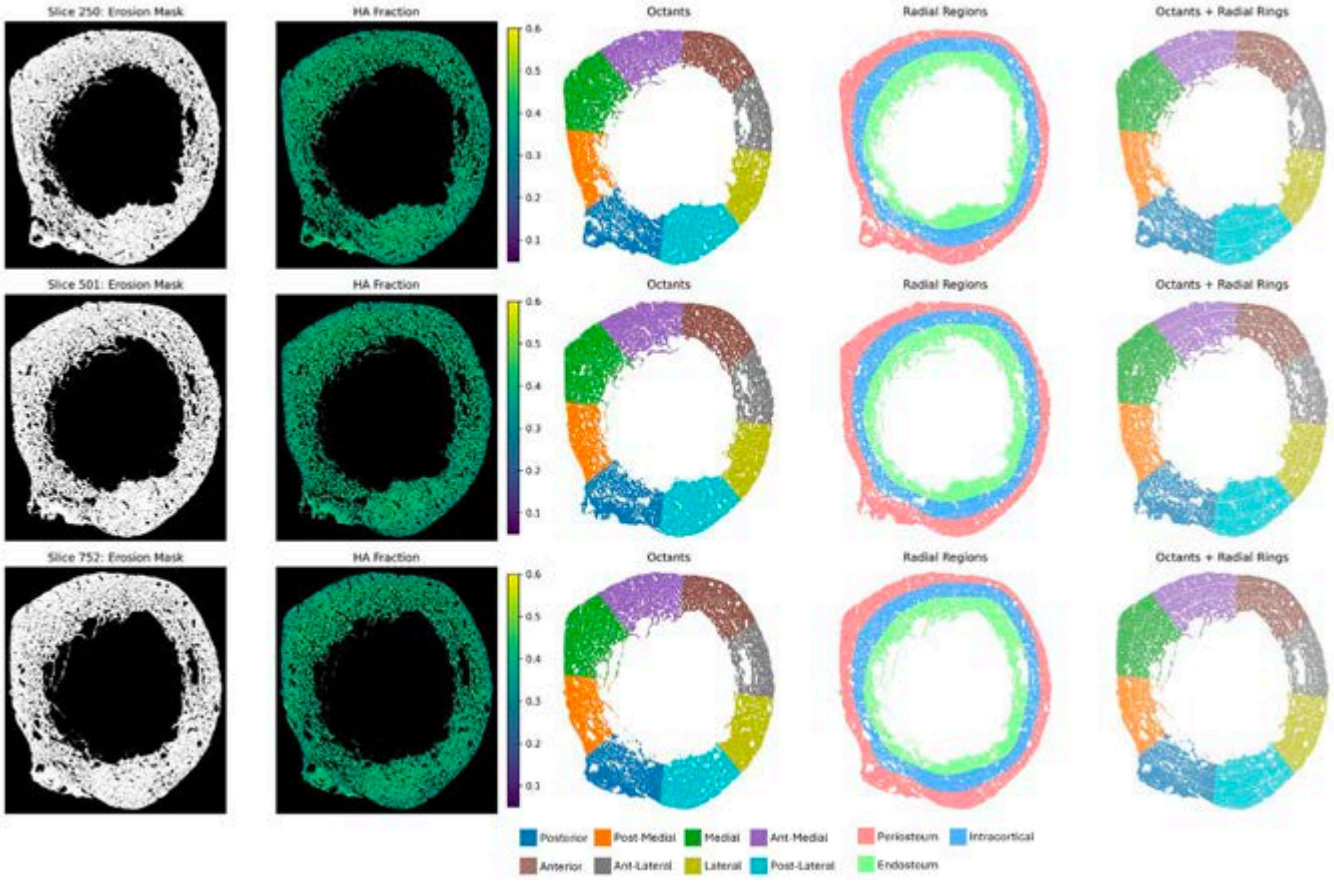

Mean MVF ranged from 0.367 to 0.408 across octant–radial region combinations. Intracortical compartments consistently showed higher MVF than periosteal and endosteal regions. Medial and ant-medial octants exhibited the highest intracortical MVF (0.408 and 0.406, respectively), while the lateral octant showed the lowest periosteal MVF (0.367). All pairwise comparisons versus the posterior octant were statistically significant (bootstrap 95% CI), with modest mean differences (range: -0.0055 to +0.0089), suggesting anatomically relevant but subtle spatial heterogeneity. Hypermineralisation in the posterior region may reflect adaptation to habitual loading and muscle/ligament insertion forces.

Our analysis reveals statistically significant but modest regional MVF variations, with highest mineralisation in the posterior periosteal region, consistent with adaptation to habitual loading.

Session V: Computation AI Assessment of Bone Remodeling and Fracture

S5-1: Steven Boyd, PhD

Computational Imaging and AI-Based Analysis of Bone Fracture Risk

Medical imaging provides a rich source of data for quantitative analysis of musculoskeletal structure and function. Traditionally, image analysis has relied on custom computational methods, including image-based finite element analysis and specialized techniques for quantifying structural features such as cortical thickness. More recently, advances in artificial intelligence (AI) have created new opportunities to analyze the large-scale datasets commonly generated in medical imaging studies. Deep learning–based segmentation methods are now widely used and form a key component of automated pipelines for feature extraction and fracture prediction. Machine learning approaches can also support clinical decision-making by integrating complex imaging and clinical data for osteoporosis fracture risk assessment. Emerging AI applications further enable characterization of bone architecture and estimation of chronological age from imaging data. The implementation of these approaches is increasingly accessible through open-science initiatives that provide trained models and model weights. In addition, online platforms are making advanced AI-based image analysis tools available to non-expert users, broadening access to state-of-the-art quantitative imaging methods.

Session V: Computation AI Assessment of Bone Remodeling and Fracture

S5-2: Nicolas Newell, PhD

Towards in vivo quantification of spinal deformations and strains using MRI and CT-based Digital Volume Correlation

Patients with severe spinal pathologies routinely undergo clinical imaging such as X ray, MRI, or occasionally CT. While these modalities provide valuable anatomical information, they offer little insight into how hard and soft tissues respond to load. Recent advances now allow non invasive quantification of internal three dimensional strains, creating new opportunities to inform prevention and treatment strategies. This talk covers a series of research studies designed to incrementally build confidence in the use of MRI-based Digital Volume Correlation (MRI-DVC) for characterizing the biomechanical response of the spine to loading.

Session V: Computation AI Assessment of Bone Remodeling and Fracture

S5-3: Kenna Brown, MSc

Applying Universal Kriging to correlate strain and osteocyte turnover in young-adult Wistar rats

Kenna Brown1, Jacob Swenson1, Colette Niglio1, Beatriz Bermudez2,3, Ana Ferreira Ruble3, Cheryl Ackert-Bicknell3, Dana Carpenter2, Chelsea Heveran1
1Montana State University, Bozeman, MT, 2University of Colorado – Denver, Denver, CO, 3University of Colorado – Anschutz Medical Campus, Aurora, CO

Purpose: Osteocytes are mechanosensitive cells essential for maintaining bone health but the roles of the osteocyte lacunar canalicular system (LCS) are debated. Labeling studies demonstrate osteocytes engage in perilacunar mineral turnover and that there may be site-specific differences, indicating a potential role of tissue strain. However, it is uncertain if strain has a role in LCS turnover. Osteocytes also demonstrate sex-dependent activity. Finite element analysis (FEA) has suggested that there are sex differences in human tibia strain distributions, but a similar analysis has not been performed on the femoral midshaft. Here we apply FEA and Universal Kriging (UK) to create a strain map for co-registration with microscopy data to determine if LCS turnover is associated with strain. We hypothesized that females will not have larger strain magnitudes along the loading axes compared to males and that LCS mineralization correlates with local strain differently between sexes.

Materials & methods: All animal procedures were approved by the University IACUC. Young-adult (9-months old) Wistar rats of both sexes (n = 12/sex) were injected with calcein 2 days before euthanasia. Left femora were scanned by μCT for FEA and imaged by confocal scanning laser microscopy (CSLM). The μCT data was used to create models for FEA. Material properties were assigned to the model by converting density to modulus using an established relationship. The models were loaded in ABAQUS to a displacement of 0.5% of the femoral length (Fig.1A). Strain values of a cross section near the midshaft were interpolated between using UK. The UK map was overlayed on the CSLM data (Fig. 1B). Spatial correlation and statistics are ongoing at ROIs defined as the 200 μm to either side of the loading axes (Fig. 1C).

Results: UK can be applied with FEA results to obtain interpolated maps with a resolution comparable to osteocyte lacunae (Fig. 1B&C). When mineral density is accounted for, female (F) and male (M) young-adult rat femurs do not have significantly different strain value averages over the ROIs ($p > 0.05$ for all).

Session V: Computation AI Assessment of Bone Remodeling and Fracture

S5-3: Kenna Brown, MSc

The medial and lateral ROIs had the highest strain magnitudes, with the medial ROI being in compression (F = -2271 ± 357 με, M = -1997 ± 447 με) and the lateral being in tension (F = +1425 ± 131 με, M = +1368 ± 241 με). The lateral ROIs had the highest variability by standard deviation (F = 635 ± 143 με, M = 648 ± 143 με) while the posterior ROI had the lowest (F = 292 ± 41 με, M = 236 ± 63 με). Spatial analysis along with co-registration with the CSLM images is ongoing.
Conclusions: For the first time, high-resolution maps of femoral midshaft strain that account for mineral distribution were produced. UK maps can be co-registered with microscopy images of osteocyte mineralization. Together these will advance the understanding of the prevalence and spatial distribution of osteocyte-mediated LCS turnover in healthy bones in both sexes.

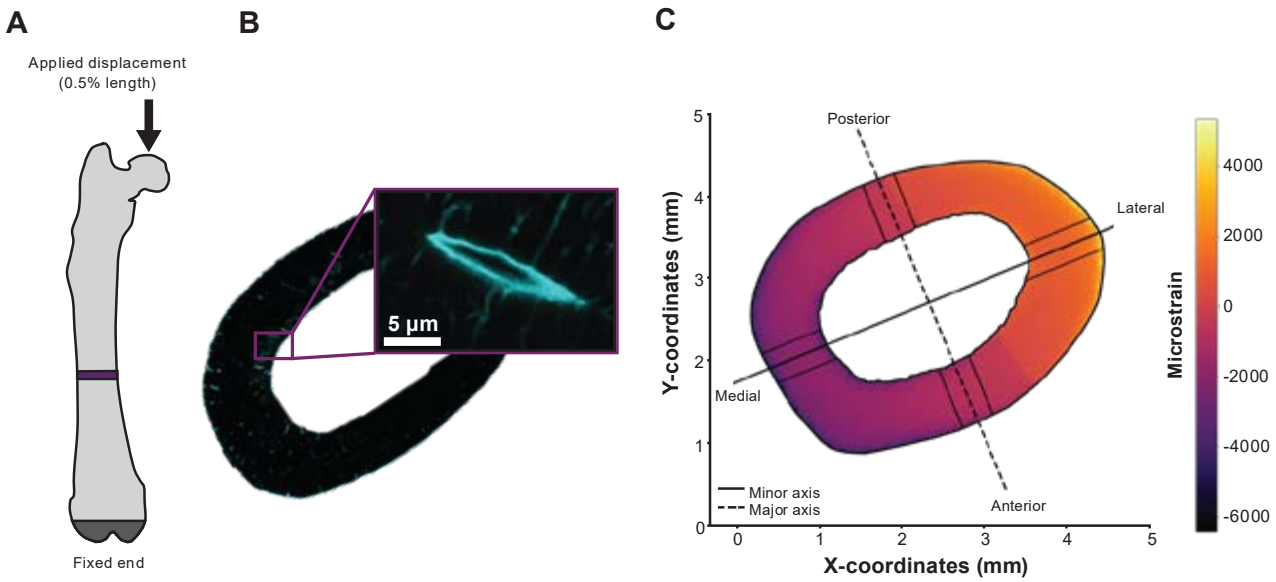

Figure 1 (A) An illustration of the finite element analysis (FEA) simulation parameters on 3D models generated from µCT scans where the modulus was assigned based on mineral density (n = 12/sex). The highlighted purple midsection represents the location of imaging with confocal scanning laser microscopy (CSLM) and where cross-sections from the FEA results were taken for applying Universal Kriging (UK). (B) An example of the CSLM images taken at the highlighted cross-section in (A). Quantification of mineralizing lacunae in the ROIs around the loading axes shown in (C) is ongoing. The window shows the resolution of an individual mineralizing lacunae taken with a 10x magnification and digital zoom. (C) An example of the strain distribution after applying UK to the FEA results near the mid-shaft where each pixel is ~5 µm. The minor loading axis is along the medial-lateral direction, and the major axis is along the anterior-posterior direction. ROIs were defined as the 200 µm to either side of the loading axes calculated by principal component analysis. UK results co-registration with the CSLM images is ongoing.

Session V: Computation AI Assessment of Bone Remodeling and Fracture

S5-4: Zichu Ding, MSc

Enhancing qct-based vertebral fracture prediction using physics-informed neural networks

Zichu Ding*1, Stefaan W. Verbruggen1,2

1Centre for Bioengineering, School of Engineering and Materials Science, Queen Mary University of London, London, United Kingdom
2Digital Environment Research Institute, Queen Mary University of London, London, United Kingdom

Purpose: While quantitative computed tomography (qCT) is a standard clinical tool for assessing bone mineral density (BMD) and thus inferring fracture risk, accurate fracture prediction requires information about bone geometry and quality. To this end, researchers have long deployed finite element analysis (FEA) as a widely used method to evaluate vertebral biomechanics. However, FEA remains a computationally expensive and time-consuming tool for patient-specific or clinical applications [1]. Physics-informed neural networks (PINNs), a class of machine learning algorithms, can provide a fast surrogate, combining standard computer vision with training on real-life physics [2]. The aim of this study was to develop a geometry-feature-enhanced physics-informed surrogate model to rapidly predict vertebral strain and von Mises stress from qCT.

Materials and Methods: Patient-specific 3D vertebral models were reconstructed from qCT scans of 20 healthy volunteers collected as part of the ANTELOPE clinical trial. Nonlinear FEA was performed in ANSYS for each vertebra under 1.9% compressive displacement applied to the superior endplate [3]. To standardise volumetric representation, 80,000 internal points were sampled from each specimen. Input features combined spatial coordinates, qCT-derived heterogeneous material properties, and Laplacian eigenvectors to encode both local mechanical heterogeneity and global morphology [1]. The network was trained as a geometry-aware physics-informed surrogate using FEA-derived displacement fields and von Mises stress distributions. Model outputs were the displacements along the X, Y, and Z axes and the corresponding von
Mises stress field (Fig. 1A).”

Results: The model produced stable full-field predictions of vertebral mechanical response. Predicted displacements successfully reproduced the superior–inferior deformation gradient observed in FEA (Fig. 1B, 1D).

S5-4: Zichu Ding, MSc

For von Mises stress, the model captured the overall distribution trend (Fig. 1C) but showed moderate agreement with FEA in the vertebral core region (Pearson r = 0.68, R^2 = 0.43) (Fig. 1E). Stress predictions showed substantial scatter and reduced accuracy in higher-stress regions, indicating that the current framework is more reliable for displacement reconstruction than for precise local stress quantification, and thus requires further training.

Conclusions: Integrating qCT-based material mapping and geometric features improves physics-informed modeling of vertebral mechanics. The proposed framework enables rapid prediction of displacement and stress fields and provides a foundation for future development of more accurate patient-specific vertebral fracture risk models [4,5]. This work provides the intriguing prospect of bedside stress and fracture risk prediction, bringing robust fracture mechanics to the clinic using imaging techniques.

References:
[1] Zhang Y, Zhang J, Li H, Wang Q. EPINN-GF: An enhanced physics-informed neural network integrating geometric features for stress prediction in complex spinal geometries. Comput Methods Programs Biomed 2025;271. https://doi.org/10.1016/j.cmpb.2025.109044.
[2] Sunil P, Sills RB. FE-PINNs: finite-element-based physics-informed neural networks for surrogate modeling 2024.
[3] Gibson FG, Paggiosi MA, Handforth C, Brown JE, Li X, Dall'Ara E, et al. Altered vertebral biomechanical properties in prostate cancer patients following androgen deprivation therapy. Bone 2025;195. https://doi.org/10.1016/j.bone.2025.117465.
[4] Caforio F, Regazzoni F, Pagani S, Karabelas E, Augustin C, Haase G, et al. Physics-informed neural network estimation of material properties in soft tissue nonlinear biomechanical models. Comput Mech 2025;75:487–513. https://doi.org/10.1007/s00466-024-02516-x.
[5] Zhang M, Gong H, Zhang K, Zhang M. Prediction of lumbar vertebral strength of elderly men based on quantitative computed tomography images using machine learning. Osteoporosis International 2019;30:2271–82. https://doi.org/10.1007/s00198-019-05117-0.

Session V: Computation AI Assessment of Bone Remodeling and Fracture

S5-4: Zichu Ding, MSc

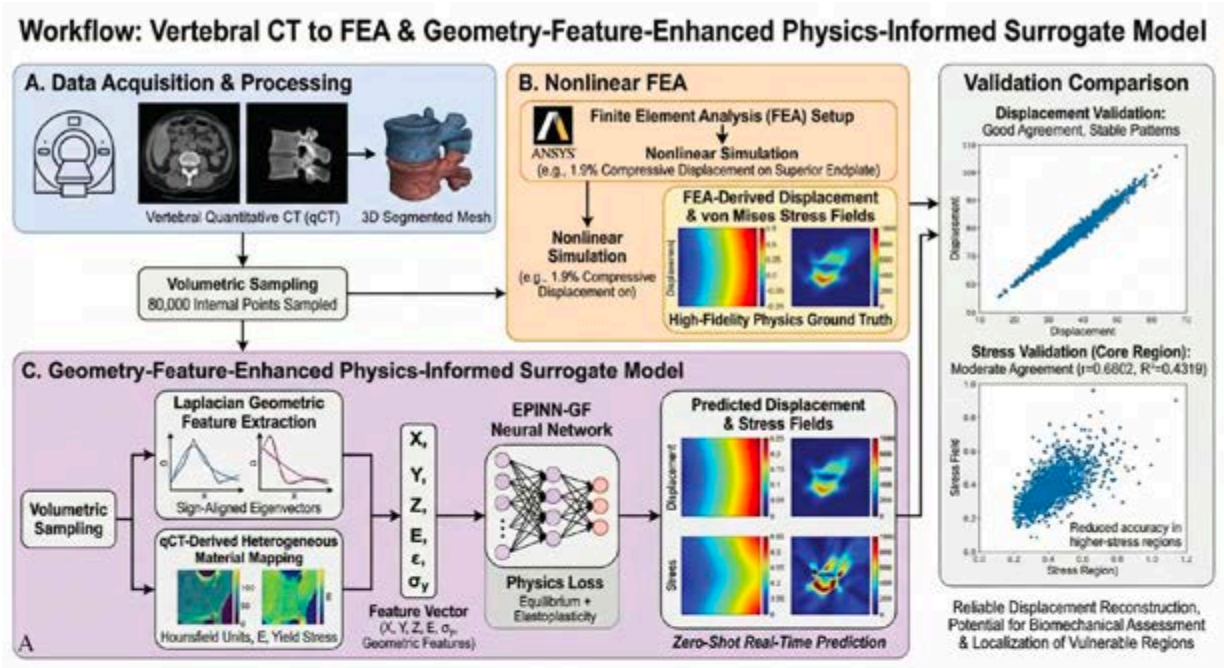

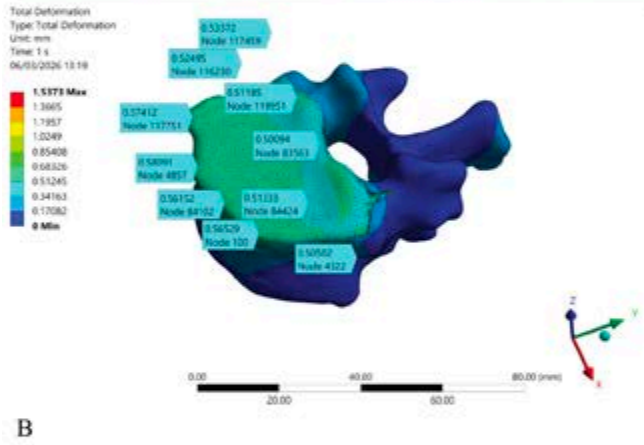

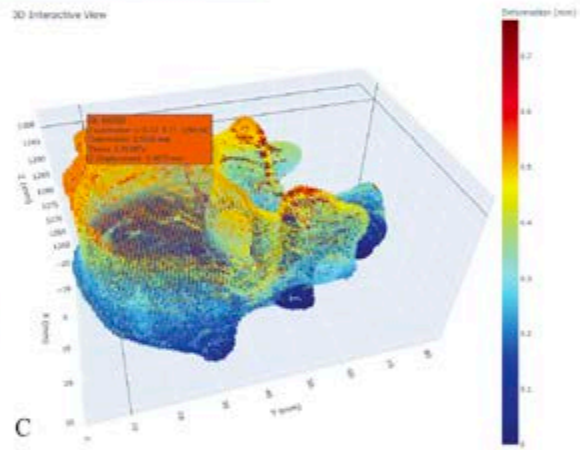

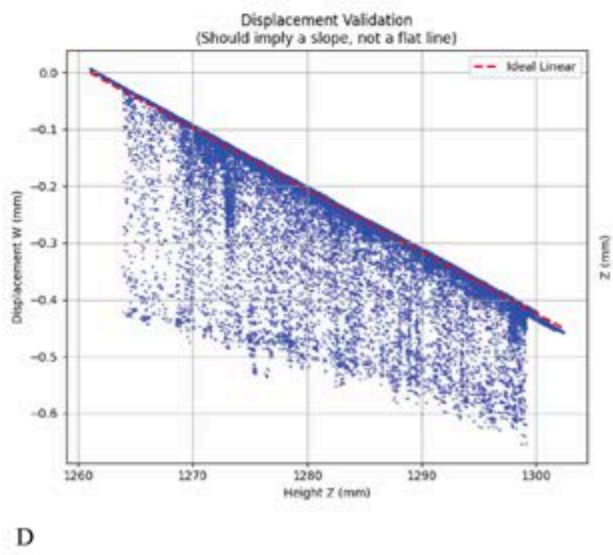

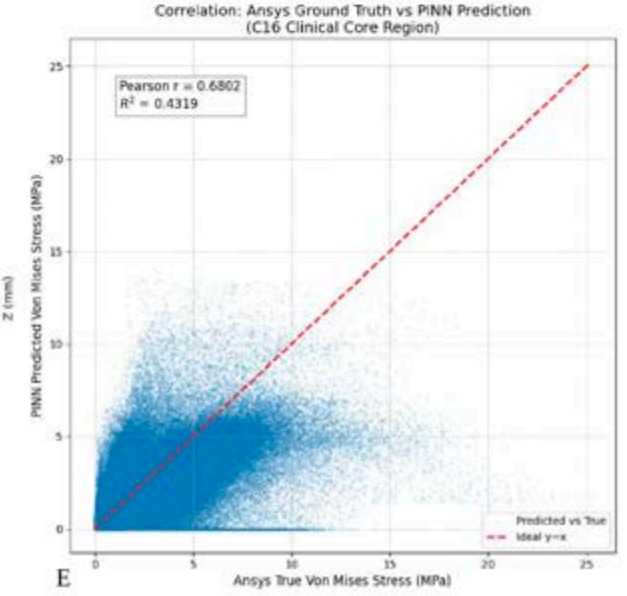

Session V: Computation AI Assessment of Bone Remodeling and Fracture

S5-4: Zichu Ding, MSc

Figure 1. A) Workflow of the qCT-based geometry-feature-enhanced physics-informed surrogate model for vertebral displacement and stress prediction. B) Total deformation obtained from nonlinear ANSYS simulation. C) Predicted displacement and von Mises stress fields generated by the surrogate model. D) Surrogate-model-predicted displacement and von Mises stress fields. D, Relationship between predicted displacement and vertebral height, showing the compressive displacement gradient. E) Scatter comparison between PINN-predicted and ANSYS ground-truth von Mises stress values in the vertebral core region.

Session V: Computation AI Assessment of Bone Remodeling and Fracture

S5-5: Atsuko Nakanishi-Kimura, PhD

Morphometric evaluation of teriparatide effects on bone remodeling in the parietal and mandibular bones of ovariectomized rats: an AI driven multiscale analysis

Full Author List: Atsuko Nakanishi-Kimura1,2), Aya Takakura3), Marie Hoshi-Numahata1,2),
Haruhisa Watanabe1,4), Yoshiaki Sato2), Ryoko Takao-Kawabata3), Tadahiro Iimura1)

List of Author affiliations and country:
1) Department of Pharmacology, Faculty and Graduate School of Dental Medicine, Hokkaido
University, Japan
2) Department of Orthodontics, Faculty and Graduate School of Dental Medicine, Hokkaido
University, Japan
3) Pharmaceuticals Research Center, Asahi Kasei Pharma Corporation, Japan
4) Department of Oral Medicine and Diagnostics, Faculty and Graduate School of Dental
Medicine, Hokkaido University, Japan

Purpose: Teriparatide (hPTH1-34) is an anti-osteoporotic drug with bone anabolic effects. Clinical and preclinical studies have indicated that TPTD has value in oral and maxillofacial bone therapies, including jawbone regeneration, periodontal tissue repair, and the treatment of medication-related osteonecrosis of the jaw. However, it is unclear whether the craniofacial bones respond to TPTD similarly to the axial and appendicular bones. Recent studies showed that TPTD acts on both osteocytes and osteoblasts. This study aimed to characterize distinct craniofacial bone sites, with a focus on morphometric changes in osteocytic lacunae in ovariectomized rats receiving TPTD.

Material and method: Rats at 12 weeks of age were subjected to sham surgery or ovariectomy, and each group were injected 30 μg/kg of TPTD or saline three times weekly for 4 weeks. (Total 4 groups, n=5 per group.) Conventional bone histomorphometric analyses of mandibular and parietal bone sections were conducted. High-resolution confocal imaging-based three-dimensional fluorescence morphometric analyses of osteocytic lacunae in distinct mandibular and parietal bone sites were conducted. The morphology of osteocytic lacunae and perivascular spaces was quantified using an AI based bone morphometric recognition system.

S5-5: Atsuko Nakanishi-Kimura, PhD

Result: In the mandibular bone, the volume and surface area of osteocytic lacunae in the buccal and alveolar bone significantly increased in the OVX-Vehicle group compared to the Sham-Vehicle group, while these parameters significantly decreased in the OVX-TPTD group compared to the OVX-Vehicle group. Conversely, no regular significant differences were observed in the morphology of the perivascular spaces in the buccal mandible across all groups. Furthermore, morphometric analysis of osteocytic lacunae in the parietal bone revealed no significant differences among any groups at any of the sites evaluated.

Conclusion: These results indicate that dynamic changes in the morphometric characteristics of osteocytic lacunae in the alveolar bone and other mandibular sites occur in response to estrogen deficiency and TPTD administration, and these effects are more pronounced in the perilacunar region than on the bone surface or in perivascular spaces. These findings suggest that osteocytes in the mandibular bone (specifically, the alveolar bone) have unique functional characteristics for the dynamic regulation of osteocytic perilacunar remodeling, whose characteristics are less obvious in other bones.

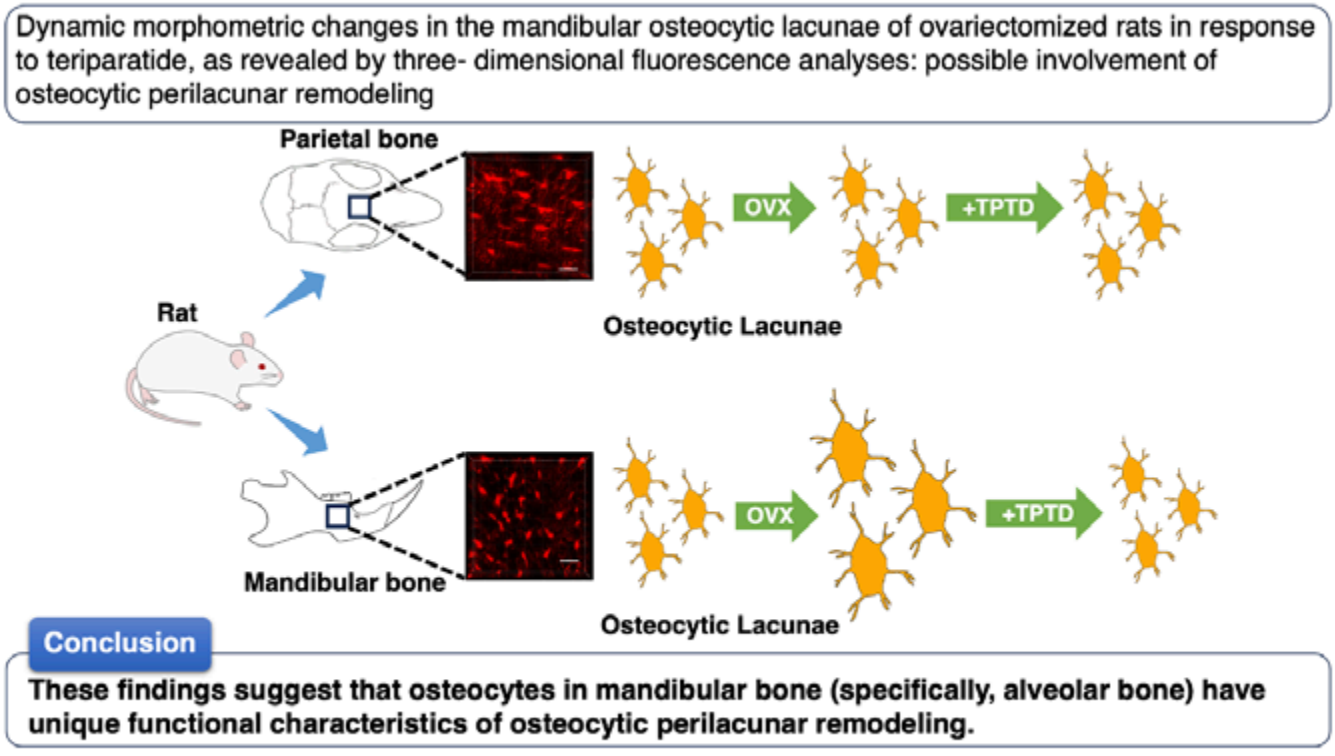

Ref. Nakanishi-Kimura A. et al., J Oral Biosci. 2024 Mar;66(1):49-60. doi: 10.1016/j.job.2023.11.010. Epub 2023 Dec 3. PMID: 38048848.

Session V: Computation AI Assessment of Bone Remodeling and Fracture

S5-6: Melissa Bevers, PhD

Automatic periosteal and endosteal contouring and detection of indeterminate bone areas near the endosteal boundary on high-resolution CT scans using deep learning

Author list: Freek J.P.N. van den Bergh1, Bert van Rietbergen2,3, Joop P. van den Bergh1,4,5, Caroline E. Wyers1,4,5, Melissa S.A.M. Bevers1,2,4

Affiliations:
1Department of Internal Medicine, VieCuri Medical Center, Venlo, The Netherlands 2Department of Biomedical Engineering, Eindhoven University of Technology, Eindhoven, The Netherlands
3Department of Orthopedic Surgery, Maastricht University Medical Center, Maastricht, The Netherlands
4NUTRIM Institute of Nutrition and Translational Research In Metabolism, Maastricht University, Maastricht, The Netherlands
5Department of Rheumatology, Maastricht University Medical Center, Maastricht, Maastricht, The Netherlands

Purpose: High-resolution peripheral quantitative CT (HR-pQCT) enables in-vivo assessment of cortical and trabecular microarchitecture at the distal radius and tibia. To separate the cortical and trabecular bone, typically automatic HR-pQCT contouring software is used to which manual correction may be applied. Yet, particularly the endosteal contour can be difficult to judge and correct –even more in distinct microarchitectural phenotypes such as osteogenesis imperfecta (OI). Here, we assessed the performance of a recently developed deep learning (DL) model for automatic contouring on HR-pQCT on an external validation dataset and an OI dataset. Then, by using Monte Carlo (MC) simulations, we quantified the model's uncertainty in trabecular/cortical separation in both datasets.

Materials and Methods: 600 HR-pQCT scans were available: 393 external validation scans (elderly with a recent fracture, 'FX data') and 207 OI scans. Contours were generated with a recently published DL model [Neeteson et al. Sci Rep 2023] and compared with reference contours (automatic with manual periosteal contour correction). Contour comparison was quantified using Dice (DSC) and Jaccard similarity coefficient (JSC), average symmetric surface distance (ASSD), and Hausdorff distance (HD). To quantify the model's contouring uncertainty in both datasets, MC dropout was used to generate 60 model versions where a random 10% of each model's weights was excluded. The per-voxel probabilities for belonging to background, cortical bone, and trabecular bone from all models were averaged.

S5-6: Melissa Bevers, PhD

The resulting mean was used to compute a per-voxel total indeterminate bone area (TIBA) score as the minimum of the cortical and trabecular probabilities minus the background probability. Thresholds for the TIBA score between 0.01 and 0.25 were evaluated to visualize and size TIBA along the endosteal boundary region and to compute the difference in cortical thickness (Ct.Th) between DL contours with TIBA in- and exclusion.

Results: Median DSC and JSC in both datasets were >0.91 and median ASSD and HD <1.15 mm. Contouring differences were mostly seen in distinct microarchitectural patterns (Fig. 1a). TIBA volume relative to total volume at a 0.01 threshold was 6.6% (IQR: 2.3, min-max: 3.4-15.8) in the FX data and 5.9% (2.2, 3.5-13.7) in the OI data and decreased with increasing threshold (Fig. 1b). Ct.Th was 14.9% (4.9, 8.3-33.9; FX) and 13.7% (4.3, 6.1-30.8; OI) lower with exclusion of TIBA at a 0.01 threshold than with TIBA inclusion, with decreasing difference for higher thresholds. TIBIA examples are shown in Fig. 1c.

Conclusion: The DL model generates periosteal and endosteal contours generally consistent with our reference contours in both FX and OI scans, which highly reduces the need for manual correction. Indeterminate bone areas, identified using the model's contouring uncertainty, can largely influence Ct.Th outcomes.

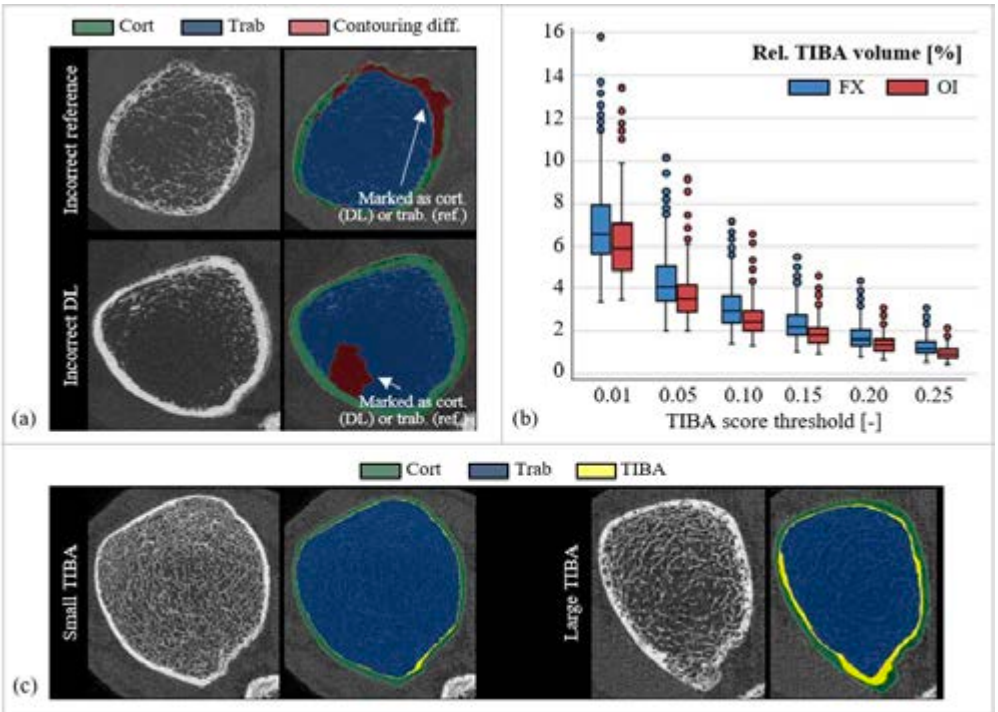

Fig. 1 (a) Examples of differences (in red) between DL and reference contours in OI tibia scans. (b) TIBA volume relative to total volume for evaluated thresholds for the TIBA score in FX and OI scans. (c) Examples of FX tibia scans with low and high relative TIBA volume (in yellow) at a 0.05 threshold.

Session VI: Emerging Paradigms in Bone Research

S6-1: Chrissy Hammond, PhD

Mechanical Regulation Of Bone Cell Fate: Emerging Paradigms in Skeletal Biology

Bones are remarkable organs. Throughout life they adapt to changing mechanical demands, repair injury, and maintain their structure despite continual turnover. These processes depend on skeletal cells making appropriate fate decisions in response to genetic, molecular and physical cues. Yet how mechanical information influences these decisions across the lifespan remains incompletely understood. In this talk, I will explore how zebrafish models are helping us understand the role of mechanics in shaping skeletal cell behaviour from evolution to ageing. I will discuss how variation in mechanical environments contributes to skeletal form and function, drawing on recent work in evolutionary morphology, computational phenotyping and developmental mechanobiology. I will examine how physical cues influence skeletal regeneration and repair, highlighting emerging evidence that local tissue architecture and mechanics help direct cellular responses to injury.

Finally, I will present new work investigating how ageing alters the relationship between mechanics and cell fate. Combining single-cell genomics, imaging and biomechanical analyses, we find that aged skeletal tissues exhibit disrupted organisation, altered material properties and changes in cellular identity that are associated with reduced regenerative capacity.

Together, these studies suggest that mechanical information may act as a unifying regulator of skeletal cell behaviour across diverse biological contexts. Understanding how cells interpret, and eventually misinterpret, these cues may provide new insights into musculoskeletal ageing and disease.

Session VI: Emerging Paradigms in Bone Research

S6-2: Atsuhiko Hikita, PhD

Spatiotemporal Analysis of Cell and Matrix Dynamics During Bone Remodeling in an In Vitro Model

Understanding bone remodeling, including the spatiotemporal coupling of bone resorption and formation, has been hindered by a lack of suitable analytical methods. To address this limitation, our group established a novel in vitro bone organoid system that enables longitudinal tracking of cellular and matrix dynamics at identical sites. This platform utilizes osteoblast-derived mineralized nodules that closely mimic native bone architecture, featuring bone-lining-like cells on the surface and embedded osteocyte-like cells. Co-culturing these nodules with bone marrow macrophages successfully induces osteoclastogenesis and subsequent matrix resorption. Furthermore, switching back to an osteoblast differentiation medium reactivates osteoblasts, leading to targeted refilling of the resorption pits with newly formed matrix. This organoid serves as a robust tool to evaluate how various therapeutics affect bone remodeling. For instance, we identified distinct remodeling profiles between zoledronic acid and the cathepsin K inhibitor E-64, and confirmed that varying the frequency of intermittent parathyroid hormone (PTH) administration alters matrix outcomes. Ultimately, this bone organoid offers a powerful platform for bone research, as further evidence continues to be accumulated.

Session VI: Emerging Paradigms in Bone Research

S6-3: Lisbeth Koch Thomsen, PhD

Advancing the paradigm of PTH treatment: PTH rejuvenates the coupling mechanism, inducing the transition from eroded to formative bone surfaces

“Lisbeth Koch Thomsen,1 Galina Pronina,1 Niyosha Ghalibaf,1 Tanja Sikjaer,2,3 Bente Langdahl,3,4 Christina Møller Andreasen,1,5 Jesper Skovhus Thomsen,6 Lars Rejnmark,3,4 Thomas Levin Andersen,1,5,7,8
1Molecular Bone Histology Lab, Research Unit of Pathology, Department of Clinical Research, University of Southern Denmark, Odense, Denmark, 2Department of Internal Medicine, Gødstrup Regional Hospital, Herning, Denmark, 3Department of Endocrinology and Internal medicine, Aarhus University Hospital, Aarhus, Denmark, 4Department of Clinical Medicine, Aarhus University, Aarhus, Denmark, 5Department of Pathology, Odense University Hospital, Odense, Denmark, 6Department of Biomedicine, Aarhus University, Aarhus, Denmark, 7Department of Forensic Medicine, Aarhus University, Aarhus, Denmark, 8Danish Spatial Imaging Consortium (DanSIC), University of Southern Denmark and Aarhus University, Denmark

Previously, it was thought that the rapid increase in bone formation induced by daily parathyroid hormone (PTH) injections was mediated by modeling-based bone formation. However, we have recently demonstrated that PTH treatment mainly induce osteoclast-initiated bone formation modes. Therefore, a new explanation for the reported rapid increase in PTH-induced bone formation is required. Previous studies have linked aging- and osteoporosis-induced bone loss to an inadequate transition from erosion to formation, suggesting an impaired coupling mechanism in these conditions. Here, we investigate whether PTH treatment can rejuvenate the coupling mechanism, thereby improve transition from eroded to formative surfaces, and increase the activation frequency of bone formation.

We applied histomorphometric analyses to trabecular bone surfaces in Masson Goldner trichrome-stained sections from 48 iliac crest biopsies previously obtained in a clinical trial, where patients with hypoparathyroidism (n=48) were randomized to receive either placebo (PLB; n=24) or 100 µg rhPTH(1-84) (PTH; n=24) once daily as add-on to conventional therapy for 6 months. We determined classical histomorphometric parameters and whether eroded bone surfaces were adjacent to formative surface (active eroded) or not (arrested eroded) (fig 1).

We identified a low activation frequency of bone formation in conventionally treated hypoparathyroidism (0.02/year ± 0.04), resulting in an accumulation of arrested eroded trabecular bone surfaces without adjacent osteoid-covered bone surfaces (48% ± 10%) – more than 10-fold higher than previously reported. In the PTH-treated group, eroded surfaces were reactivated and rapidly transitioned into bone forming surfaces, while simultaneously generating new coupled bone remodeling events.

S6-3: Lisbeth Koch Thomsen, PhD

This lowered the proportion of eroded surfaces from 55% ± 10% to 31% ± 17% ($p < 0.001$) while the proportion of osteoid-covered surfaces rose from 1% ± 2% to 33% ± 21% ($p< 0.001$), thereby reducing the ratio of eroded and bone forming surfaces ($p < 0.001$). The activation frequency of bone formation was 15-fold higher in the PTH-group (0.31/year ± 0.30) compared with the PLB-group ($p < 0.001$). Similarly, PTH treatment resulted in a 16-fold increase in the ratio of active to arrested eroded surfaces ($p < 0.001$). Bone formation activity parameters (formation period, wall thickness and mineral apposition rate) were unchanged by PTH treatment. Supplementary active vitamin D-dosage correlated negatively with osteoid surfaces and positively with eroded surfaces and arrested eroded surfaces during PTH treatment.

Collectively, in patients with hypoparathyroidism, PTH treatment increase the initiation of bone formation by reactivating previously accumulated arrested eroded surfaces and rejuvenating the transition from eroded to bone forming surfaces, thereby restoring the coupling mechanism”

Fig. 1 - Bone remodeling during hypoparathyroidism and PTH treated hypoparathyroidism

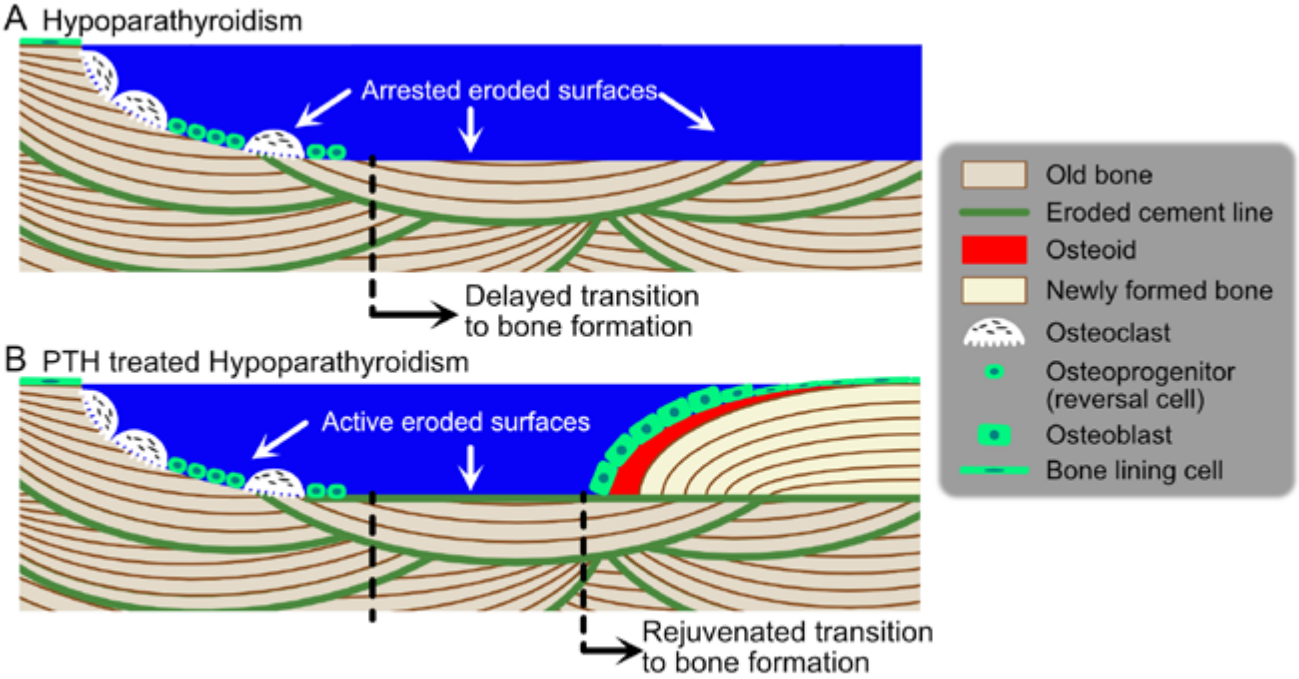

Figure 1 - Schematics illustrating (A) arrested eroded surfaces - eroded surfaces with no adjacent formative surfaces - in conventionally/placebo treated hypoparathyroidism. (B) In PTH treatment eroded surfaces are reactived to active eroded surfaces - eroded surfaces with adjacent formative surfaces - through a rejuvenation of the coupling mechanism ensuring transition to bone formation.

Session VI: Emerging Paradigms in Bone Research

S6-4: Birgitte Villadsen, PhD

Alendronate increases early reversal cells in a rat model of bone remodeling

“B. Villadsen1, W. Yassin1, P. Shitole4, D. Sumner4, J. Wallace5, F. Ko4, R.D. Ross4*, T.L. Andersen1,2,3,6*
1 Molecular Bone Histology Lab, Dept. of Clinical Research, University of Southern Denmark, Odense, Denmark
2 Danish Spatial Imaging Consortium (DanSIC), University of Southern Denmark, Odense, Denmark
3 Dept. of Pathology, Odense University Hospital, Odense, Denmark
4 Dept. of Anatomy and Cell Biology, Rush University, Chicago, US
5 Weldon School of Biomedical Engineering, Purdue University, West Lafayette, US
6 Dept. of Forensic Medicine, Aarhus University, Aarhus, Denmark

Background: Bisphosphonates (BPs) are widely used to treat osteoporosis, but their effects on the coupling between bone resorption and formation during cortical and trabecular remodeling remain incompletely understood. We previously showed that short-term alendronate treatment in rats in-creases the proportion of eroded pores and reduces formative pores in cortical bone, indicating a prolonged reversal–resorption phase. Because cortical bone represents only part of the skeleton, we now extend our analyses to the trabecular compartment.

Aim: To determine how bisphosphonate treatment influences trabecular bone remodeling dynamics in a rat model of induced bone resorption.
Methods: Lactating Sprague Dawley rats on a low-calcium diet (0.01% Ca) received alendronate (28 µg/kg, 2×/week) or vehicle for 7 days (n = 7–8/group). Femurs were fixed, EDTA-decalcified, paraffin-embedded, and analyzed by multiplex RNAscope FISH for Ctsk, Mmp13, and Col1a1. Trabecular regions in the proximal femur and femoral head were quantified from whole-slide im-ages using HALO/HALO AI with validated classifiers for bone, osteoclasts, and nuclei. Cell pheno-types were assigned using 99.99th-percentile negative-control–derived thresholds, and spatial distri-butions were mapped relative to trabecular surfaces (0–10, 10–30, 30–100 µm) and neighboring os-teoclasts. Statistics were performed on rat-level means using Box–Cox transformation, assumption testing, and two-tailed t-tests or Mann–Whitney tests to assess treatment effects. Two-way ANOVA was used to evaluate whether treatment, together with distance and intensity effects, influenced the outcomes ($\alpha = 0.05$; trends at $p < 0.08$).

S6-4: Birgitte Villadsen, PhD

Results: Alendronate significantly increased the proportion of osteoclasts among surface cells (6.6± 1.7% vs. 2.7 ± 1.2% in controls, $p<0.01$), as well as osteoclast size (190 ± 34 μm² vs. 116 ± 20 μm², $p<0.0001$) and nuclei number (2.8 ± 0.36 nuclei vs. 2.0 ± 0.26 nuclei, $p<0.01$), indicating en-hanced fusion. The proportion of early reversal cells among surface cells (Mmp13+/Col1a1-) was also significantly increased during alendronate treatment (7.0 ± 2.6% vs. 3.4 ± 1.6%, $p<0.05$), in a region-dependent manner.

Conclusion: Bisphosphonate treatment rapidly alters remodeling dynamics by prolonging the re-versal–resorption phase and increasing osteoclast size and multinucleation. The observed rise in early reversal cells further suggests that bisphosphonates affect the earliest remodeling highlighting the need for cell and site-specific evaluation of treatment outcomes.

Session VI: Emerging Paradigms in Bone Research

S6-5: Florence Lima, PhD

Self-supervised dual domain segmentation for static and dynamic bone histomorphometry using LeJEPA

Authors: 1.M. Gokmen1, M. Rao2, E. Collier1, C. Bumgardner1, F. Lima2
Affiliations: Center for Applied AI, University of Kentucky1; Division of Nephrology, Bone and Mineral Metabolism, University of Kentucky2

Purpose: Quantitative bone histomorphometry relies on accurate segmentation of bone tissue components, including mineralized bone, osteoid, and active mineralization, yet manual annotation of whole-slide images (WSI) is labor-intensive. Automated segmentation has reduced this burden, but existing approaches are modality-specific. We present a self-supervised learning pipeline that trains a single foundational encoder on both fluorescence microscopy and Masson's Trichrome brightfield images, routing tiles to modality-specific segmentation heads, establishing a foundation for scalable quantitative analysis from limited labeled data.

Methods: A dataset of 16,732 image tiles (224×224 pixels) was derived from 108 fluorescence and 415 brightfield region of interest (ROI) images. Each 448×448 region yielded four non-overlapping quadrant tiles and one center crop to ensure boundary regions were adequately represented. Tiles were used to pretrain a Vision Transformer (ViT) encoder with register tokens via Latent Joint-Embedding Predictive Architecture (LeJEPA), a self-supervised objective that learns spatially rich representations without pixel-level annotations. The pretrained feature space exhibits a natural separation between imaging domains, exploited by a lightweight linear classifier that routes each tile to a domain-specific segmentation head.
The fluorescence head performs three-class segmentation of bone, osteoid, and active mineralization fronts, where the region between tetracycline double-labels is filled to delineate the interlabel area representing new bone formation, the key substrate for dynamic histomorphometric parameters such as Mineral Apposition Rate (MAR). The brightfield head delineates mineralized bone from osteoid tissue which delineates tissue perimeter and area. Both heads employ a progressive CNN decoder fusing ViT patch token embeddings with multi-head attention maps. At inference, ROI images are tiled, independently segmented, and reconstructed into full-resolution segmentation maps.

Session VI: Emerging Paradigms in Bone Research

S6-5: Florence Lima, PhD

Evaluation: Evaluated on held-out test sets, the fluorescence model achieves a Dice score of 0.9436 (IoU: 0.8944) and the brightfield model achieves 0.8420 (IoU: 0.7560), with detection F1-scores exceeding 0.975 in both modalities. This level of performance suggests the approach is reliable for downstream histomorphometric quantification, such as mineralized bone and unmineralized osteoid areas and Mineral Apposition Rate (MAR).

Conclusion: These results demonstrate that self-supervised pretraining with LeJEPA on a modest, domain-specific ROI image collection enables robust and scalable segmentation of complex bone tissue architecture across heterogeneous imaging modalities, offering a practical path toward automated histomorphometry in clinical and research settings where large, annotated datasets are unavailable.

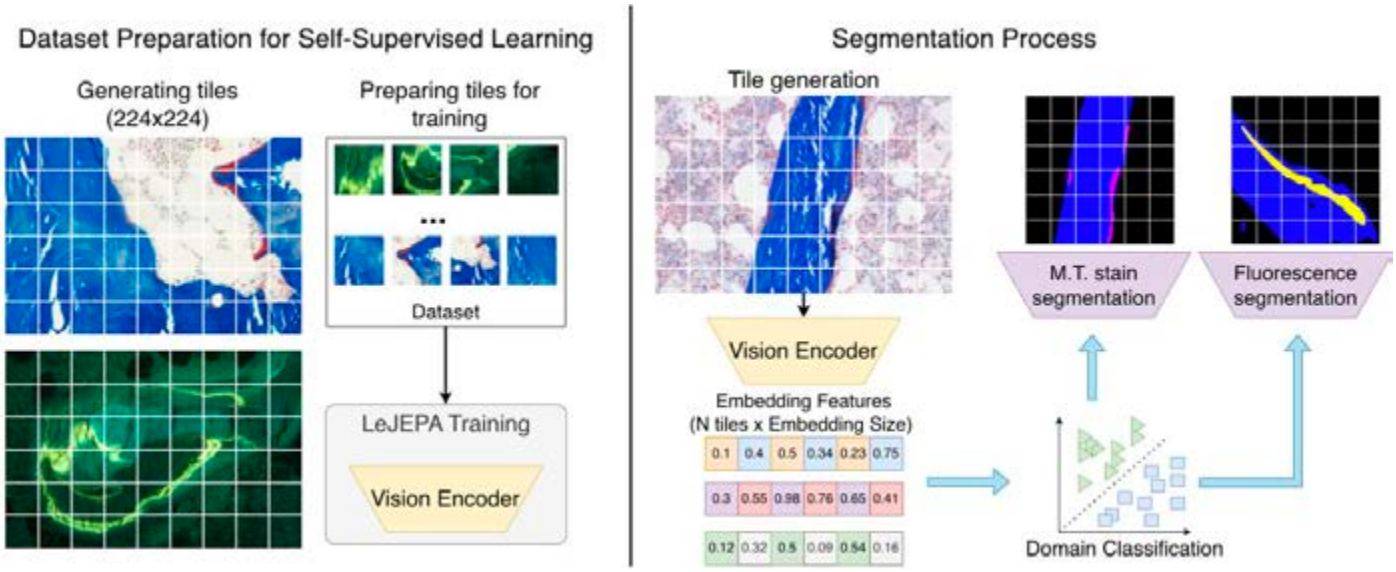

FIGURE CAPTION: Self-supervised learning pipeline with LeJEPA that trains a single foundational encoder on both fluorescence microscopy and Masson's Trichrome brightfield images, routing tiles to modality-specific segmentation heads for static and dynamic histomorphometric quantification.

Session VI: Emerging Paradigms in Bone Research

S6-6: Anika Shimonty, PhD

Mutation in CLCN7 alters tissue material properties in ADOII mice

Anika Shimonty,1 Xenia Goldberg Dahl,2 Mustafa Unal,3 Dyann M Segvich,4 Elissa Zboinski,1 Malene H Nielsen,2 Emily McDonald,1 Mary Bouxein,3 Joey Wallace,4 Thomas L. Andersen,2 Julia F Charles1
1Brigham and Women's Hospital; Harvard Medical School, Boston, MA, USA, 2Dept. of Clinical Research, University of Southern Denmark; Odense University Hospital, Odense, Denmark 3Beth Israel Deaconess Medical Center; Harvard Medical School, Boston, MA, USA 4Weldon School of Biomedical engineering, Purdue University, Indianapolis, IN, USA

Background: Autosomal Dominant Osteopetrosis Type II (ADOII) is a rare inheritable condition primarily caused by mutations in the CLCN7 gene, encoding a Cl-/H+ exchanger necessary for osteoclastic bone resorption. ADOII patients have high bone mass, yet are susceptible to fracture, suggesting impaired bone tissue quality.

Aim: To investigate how mutation in Clcn7 may modulate bone material properties resulting in increased susceptibility to fracture.

Hypothesis: Altered bone material properties result from disrupted osteoclast–osteocyte coupling and/or a previously unrecognized role of Clcn7 in osteocytes

Methods: Mice with Clcn7 G213R heterozygous mutation (G213R/+), analogous to a mutation reported in ADOII patients were used. We compared 12-week-old female C57BL/6 G213R/+ (ADO) mice bones to WT littermate controls by employing μCT, 3-point bending test, fracture toughness test, Raman spectroscopy, phalloidin staining, and spatial transcriptomics.

Results: ADO mice had higher femoral trabecular bone (12% vs 14% BV/TV, n=15, p= 0.01) compared to WT. 3-point-bending tests showed reduced toughness in ADO mice, with no significant change in other parameters. Similarly, fracture toughness test did not show any significant difference between WT and ADO mice. By Raman spectroscopy, ADO mice femurs had similar mineral quality and crystallinity to WT mice (n=10). Consistent with reduced remodeling due to osteoclast functional deficit, ADO mice had a higher mineral-to-matrix ratio (phosphate/amide I, phosphate/amide III, and phosphate/proline, $p<0.01$), reflecting increased tissue mineralization.

S6-6: Anika Shimonty, PhD

Unexpectedly, ADO mice also had higher immature collagen content and different crosslinking compared to WT littermates (lower hypoproline/ proline, 1670/1640, and 1670/1690 ratio in ADO, $p<0.05$). As enzymatic collagen crosslinking is primarily a function of osteoblastic and osteocytic cells, this suggests altered osteoblast or osteocyte function in ADO mice. Matrix relevant genes (Lox, Plod1, Gja (Cx43), and Postn) had lower expression levels in ADO mice ($p<0.05$) compared to WTs. As we have previously found that osteocytes express Clcn7, we compared WT and ADO osteocytes. Preliminary data from spatial transcriptomics shows differentially expressed genes in WT and ADO mice osteocytes. Additionally, differences in osteocyte lacunocanalicular network in ADO mice compared to WT were detected by phalloidin staining.

Conclusion: Our findings suggest that the combined activity of ADOII osteoclasts, osteoblasts, and osteocytes forms bone with different material properties, which may contribute to the bone fragility observed in ADOII.

Session VI: Emerging Paradigms in Bone Research

S6-7: Yixia Xie, MA

Development of an immortalized osteogenic cell line stably expressing GFP-collagen and membrane-targeted TdTomato for live cell imaging of collagen assembly

Yixia Xie1, Kun Wang1, Michael Grillo2, Yongbo Lu1,3, Mikayla Mwanzia, Sarah L. Dallas1,
1 - University of Missouri Kansas City, Kansas City MO
2 - Pennsylvania State University, Hershey, PA
3 - Texas A&M University College of Dentistry, Dallas, TX.

Type I collagen is a heterotrimer of two α1(I) chains and one α2(I) chain, encoded by the COL1A1 & COL1A2 genes. Although the collagen biosynthetic pathway is well understood, the dynamic process for collagen assembly into bone matrix is less well defined. To address this, we previously generated transgenic mice expressing GFP-tagged α2(I) collagen and have now developed an osteogenic cell line from these GFP-collagen transgenic mice crossed with mice expressing a membrane-targeted TdTomato (mT) reporter. Characterization of this cell line, named ColGFP-mT, showed stable GFP-collagen and mT expression up to at least 25 passages. Osteogenic differentiation of the cell line was confirmed by alkaline phosphatase and alizarin red staining in long term cultures up to 28 days. Mineralizing bone nodules contained extensive GFP-collagen fibers in a highly structured bone-like organization with osteocyte lacunae. Immunofluorescent staining showed constitutive expression of osteocyte marker E11/gp38. Expression of Dmp1 was seen at 14-28 days in mineralizing nodules, and sclerostin was expressed in mature osteocytes by 21-28 days. Live cell imaging of colGFP-mT cells in a scoreline wounding model showed directional cell migration into the wounded area and cell density-dependent assembly of repair collagen. The collagen assembly process was highly dynamic, with fibers being stretched, contracted and reshaped by cell-derived forces during their assembly. To image collagen deposited by individual cells, the ColGFP-mT cells were parachuted at low density onto a layer of WT (non-fluorescent) osteoblasts. Live cell imaging showed collagen localized in intracellular vesicle-like structures with rapid intracellular motion and deposition of GFP-collagen “”packets”” onto forming fibers. Finer fibers appeared to be formed on fine cell projections at the periphery of the cell membrane, often at the leading edge of cells, with thicker fibrils formed by deposition of larger collagen “packets” from the main cell body. Individual migrating cells added collagen onto existing fiber networks.

S6-7: Yixia Xie, MA

When ColGFP-mT cells underwent cell division, the collagen distribution became punctate and the cell remained tethered to the cell layer by numerous fine membrane projections. Collagen was split equally between daughter cells, which moved in opposite directions, tearing their collagen matrix as they moved apart. These data show the power of the colGFP-mT cells for live cell imaging of collagen matrix and cell membrane dynamics and suggest that collagen assembly involves movement of collagen-containing vesicles to the cell periphery and main cell body and is driven by local cell motions and cell-generated forces.

Session VII: Bone Marrow Microenvironments and Functions

S7-1: Erica Scheller, DDS, PhD

Marrow adipocytes and bone homeostasis

In adult humans, ~70% of the skeleton is filled with bone marrow adipose tissue (BMAT). There are two types of BMAT – regulated and constitutive, creating two distinct regulatory niches in bone. Regulated bone marrow adipocytes (rBMAds) are found in red bone marrow and, like peripheral adipocytes, are responsive to metabolic demand. Regulated BMAds increase at osteoporotic fracture sites and are inversely correlated with bone mass and hematopoiesis. Unlike rBMAds, constitutive BMAds (cBMAds) fill yellow marrow during development at sites of high bone mass and strength. Constitutive BMAds are uncoupled from day-to-day metabolic needs, making this the largest known depot of “stable adipocytes” in the body. Constitutive BMAd-filled bones are also relatively protected against fragility fractures in osteoporosis. While many projects have focused on mechanisms of rBMAd expansion, very little is known about the regulation and function of mature BMAds. In this talk, we will leverage the unique properties of cBMAT to reconsider the classical assumption that BMAT is bad for bone.

Session VII: Bone Marrow Microenvironments and Functions

S7-2: Peter Maye, PhD

Introducing the Rodent Open Science Skeletal Archive (ROSSA)

Peter Maye1, Brian Kelleher2, William Shostak2, Aaron Mark2, Natalie Lacroix2, Benjamin Sinder3, Je-Yong Choi4, Viktoria Bonne Kofod5, Ching-Hsin Huang5, Joel Salisbury2, Dong-Guk Shin6, Thomas L Andersen5,7, David W Rowe1
v
1. Regenerative Medicine and Skeletal Development, School of Dental Medicine, University of Connecticut Health, Farmington, CT 06030
2. Institutional Insights & Innovation (I3), University of Connecticut, Storrs, CT 06269,
3. Musculoskeletal Institute, School of Medicine, University of Connecticut Health, Farmington, CT 06030
4. Department of Biochemistry and Cell Biology, Skeletal Diseases Analysis Center, School of Medicine, Kyungpook National University, Daegu 41944, Republic of Korea
5. Molecular Bone Histology Lab (MBH), University of Southern Denmark & Odense University Hospital, 5230 Odense, Denmark
6. Computer Science & Engineering, School of Computing, University of Connecticut, Storrs, CT 06269
7. Dept. of Forensic Medicine, Aarhus University, 8200 Aarhus, Denmark

Over the last 40 years, a vast range of rodent skeletal phenotyping studies have been conducted to understand the mechanisms of human skeletal disease. To ensure that this knowledge is preserved and accessible to the broader research community, we are developing ROSSA: the Rodent Open Science Skeletal Archive (rossa.uchc.edu), an NIH-funded open-access repository for rodent skeletal phenotyping data.

ROSSA is designed as a centralized platform where researchers can both contribute their own skeletal phenotyping datasets and explore studies conducted by others. To achieve this, ROSSA features two core components: a robust data submission form and a dynamic data center offering multiple ways to view, analyze, and access archived data. As the repository grows, we anticipate it will become an essential resource for advancing our understanding of skeletal disease mechanisms.

Here we announce the completion and launch of Version 1 of our web-based data submission form, capable of capturing a wide range of experimental paradigms used in rodent skeletal research. Supported experimental approaches include genetically modified animal models, pharmacological interventions, and gonadectomy procedures, which are frequently used in combination. Alongside metadata collection, the form supports ingestion of quantitative phenotyping data generated through standard analytical techniques, including Dual-Energy X-ray Absorptiometry (DEXA), Microcomputed Tomography (μCT), Bone Histomorphometry, Mechanical Strength Testing, and biomarker assays from serum, plasma, and urine.

S7-2: Peter Maye, PhD

Submitted data is preserved in its original form to ensure authenticity and is also parsed into a relational database to facilitate advanced search functionality and programmatic access via API.

Ultimately, ROSSA aims to transform how preclinical bone research is shared and utilized; enabling the construction of phenotype-associated regulatory networks and laying the groundwork for AI-driven models that will advance the diagnosis and treatment of skeletal
disease.

Session VII: Bone Marrow Microenvironments and Functions

S7-3: Benjamin Sinder, PhD

Spatial Mapping of Periosteal and Endosteal Bone Formation During Growth

Anthony Zuo1, Jennifer Alaska1, Danielle Rux1, Benjamin Sinder1 1Department of Orthopedic Surgery, UConn Health, Farmington, CT

Cortical bone accounts for roughly 80% of total bone mass and is the principal determinant of whole-bone strength. Defining when, where, and how cortical bone forms is essential for interpreting nearly any skeletal phenotype. A commonly held paradigm regarding bone modeling is that the periosteal surface is a site of bone formation and the endosteal surface is a site of resorptvion, likely resulting from the observation that bones increase in width and marrow cavity size during growth.

The purpose of this study was to map the contribution of periosteal and endosteal bone formation to cortical bone mass during a key formative period of bone mass accrual. A total of 16 mineral labels (calcein, alizarin, and demeclocycline) were given weekly to mice from 4weeks of age through 16weeks of age. The mineral label order was designed such that each label could be uniquely identified. At 16weeks of age, femur and tibia were embedded in plastic and transverse sections were exhaustively taken every ~750 microns throughout the entire length of the bone (~15-20 sections per bone). Sections were imaged and quantified.

At the distal portion of the femur with sections located in the distal ~30% of the bone length, we found that cortical bone formation was exclusively located on the endosteal surface with no detectable periosteal bone formation. At this distal location in the femur, the rate of endosteal bone formation is such that bone located on the periosteal surface at 16 weeks of age (study endpoint) was formed on the endosteal surface only 6-8weeks prior. This same observation indirectly highlights the rapid rate of periosteal bone resorption. Near the mid-diaphysis of the femur, both periosteal and endosteal bone formation were observed with a clear pattern cortical drift - showing bone formation on complementary posterior periosteal, and anterior endosteal, surfaces. In the proximal ~1/3 of the femur, formation was mostly periosteal with a smaller, but present, endosteal component. The tibia was similarly analyzed to the femur and while the pattern was not identical, the overall trend was generally conserved. However, the tibia bone formation pattern was inverted in the proximal/distal dimension relative to the femur, such that the overall femur-tibia patterns were symmetric about the knee.

S7-3: Benjamin Sinder, PhD

In conclusion, this work comprehensively mapped the contribution of periosteal and endosteal bone formation to long bone cortical bone mass during growth and provides a rational framework to guide interpretation of a wide variety of genetic, pharmacological, and cellular skeletal phenotypes.

Session VII: Bone Marrow Microenvironments and Functions

S7-4: Mathilde Palmier, PhD

Defining the spatial phenotype of diet-induced individual bone marrow adipocytes in male mice

Mathilde Palmier1,2, Marc Petersen Harford1,2, Dalia Ayesh Hafez Ali1, Greet Kerckhofs3, Grzegorz Pyka3, Alexander Rauch1,2
1 Molecular Endocrinology Laboratory (KMEB), Department of Endocrinology, Odense University Hospital, Odense C, Denmark
2 Department of Clinical Research, Faculty of Health Sciences, University of Southern Denmark, Odense M, Denmark
3 Biomechanics lab, Institute of Mechanics, Materials, and Civil Engineering, UCLouvain, Belgium

While obesity and anorexia nervosa have opposite effects on peripheral fat, both conditions are associated with increased bone marrow adipose tissue (BMAT) and fracture risk. Therefore, we hypothesized bone marrow adipocytes (BMAds) to obtain a context-specific function impacting bone quality. Our aim was to investigate the effects of dietary exposure on bone structure and spatial characteristics at the individual BMAd level within calcified bone.

Ten-week-old male C57BL/6J mice were placed on control diet (Normal Diet – ND, ad libitum), Caloric Restriction (CR, 70% of ND), High Fat Diet (HFD, ad libitum) for 6 and 12 weeks, with dietary switch after 6 weeks (n=8 per group). Diet efficiency was monitored through body weight. Fixed tibiae were stained ex vivo with polyoxometalate followed by microCT scanning of the proximal tibia at 11 and 2 µm resolution. Using Xamflow software (Lucid), we created a workflow enabling the quantification of bone and single BMAd parameters through the combination of interactive and automated tasks with a machine-learning model for image segmentation.

Mice in the HFD group gradually gained weight throughout the 12-week diet, whereas mice in the CR group lost most of their weight during the first 6 weeks. When CR preceded the diet switch, both ND and HFD restored body weight to a similar extent. When mice initially fed HFD were switched to ND, body weight returned to control level, whereas switching to CR led to a greater weight reduction. After 6 weeks, animals in the HFD and CR groups had lower BV/TV than those in the ND group. After 12 weeks, trabecular and cortical thicknesses were significantly smaller in animals under CR compared to ND (-0.02 ± 0.00 mm and - 0.06 ± 0.01 mm) or HFD (-0.02 ± 0.01 mm and -0.03 ± 0.02 mm). As for HFD, the trabecular number was lower (-1.91 ± 0.29 mm-1 vs. CR and -1.41± 0.52 mm-1 vs. ND), highlighting the differential effects of CR and HFD on trabecular bone.

S7-4: Mathilde Palmier, PhD

While the CR-induced bone phenotype was not improved by switching to ND or HFD, switching from HFD to ND led to a phenotype similar to control. Regarding BMAd, CR alone or following HFD resulted in a higher density compared to ND (+3726 ± 1146 and +3184 ± 1023 BMAds/VOI). Once exposed to CR, marrow adiposity could not be reversed by ND (+2233 ± 810 BMAds/VOI vs. ND alone). In contrast, mice switched from HFD to ND showed a lower BMAd density than mice maintained on HFD or switched to CR (-1697 ± 1117 and -2664 ± 1076 BMAds/VOI). Despite the changes in body weight, these data suggest that CR drives a more persistent increase in marrow adiposity and a more detrimental bone phenotype than HFD.

We observed diet-specific effects on bone parameters and BMAd density both in their skeletal targets and temporal responses. Future analyses will aim at combining the spatial phenotype with molecular profiles in male and female. This will provide valuable insights into the onset of BMAT expansion and ways to target it to preserve bone health.

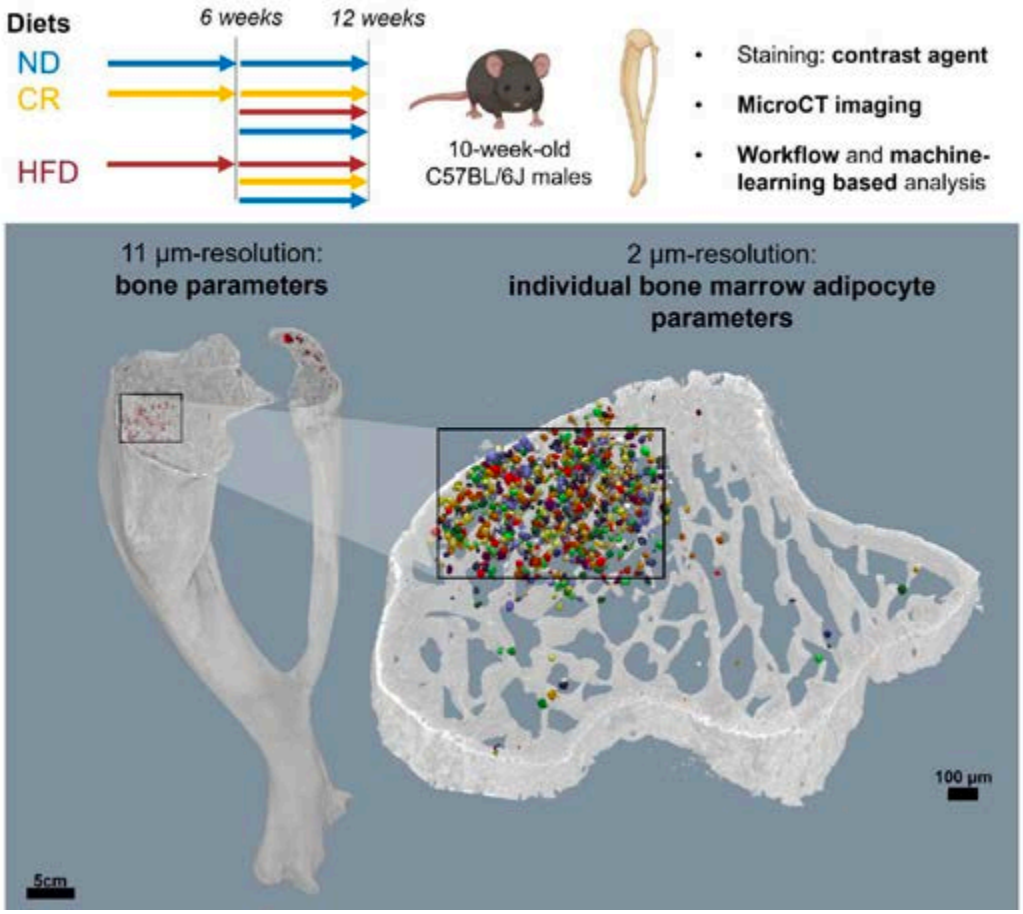

Graphical representation of the project methods.

Session VII: Bone Marrow Microenvironments and Functions

S7-5: Jonathan Williams, EngD

Metaphyseal trabecular separation is bimodal: separating intra-trabecular spacing from marrow-cavity expansion

Carmen Huesaa, John C. Lockhartb, Carl S. Goodyeara, Jonathan A. Williamsc
aSchool of Infection and Immunity, College of Medical, Veterinary and Life Sciences, University of Glasgow, G12 8QQ, UK
bInstitute of Biomedical and Environmental Health Research, University of the West of Scotland
cDepartment of Biomedical Engineering, Wolfson Building, University of Strathclyde, Glasgow, G4 0NW, UK *presenting and corresponding author

Purpose: Trabecular separation (Tb.Sp) from maximal sphere-fitting is routinely reported as a single mean for metaphyseal trabecular bone. Yet metaphyseal marrow space contains both (i) intra-trabecular spacing and (ii) larger central cavities that can form from loss of centrally located trabeculae. In long-bone metaphyseal VOIs, mean Tb.Sp is not meaningful in isolation because it conflates local spacing with VOI-dependent marrow-cavity expansion. We test whether metaphyseal Tb.Sp distributions are bimodal and present an update that reports two components: Tb.Sp1 (intra-trabecular spacing) and Tb.Sp2 (marrow-cavity expansion). The approach is designed as a lightweight add-on to standard Tb.Sp outputs, requiring no changes to the VOI definition and fits naturally into existing morphometry workflows.

Materials & Methods: Tb.Sp was analysed in standardised long-bone metaphyseal VOIs (proximal tibia) across 3 osteoporosis models: rat spinal cord injury (SCI), mouse ovariectomy (OVX), and mouse ageing. We extracted the Tb.Sp histogram and voxel-wise Tb.Sp map, computed distribution descriptors (SD, skewness, kurtosis), thresholded the map to separate low- and high-diameter compartments (automated (Otsu), and fixed global threshold), and re-computed Tb.Sp within each compartment VOI to obtain Tb.Sp1 and Tb.Sp2. Colour Tb.Sp maps visualised spatial localisation.

Results: For the age-induced osteoporosis datasets (14-, 36- and 62-week-old), a monotonic decrease in BV/TV and Tb.N, and an increase in Tb.Sp was observed ($p < 0.01$), confirming age-induced osteoporosis. Tb.Sp histograms were multimodal (Figure 1A). Segmenting the Tb.Sp dataset based on sphere diameter enabled the distinction of effects due to intra-trabecular thinning (first peak) captured by Tb.Sp1, from those due to the complete resorption of centrally-located trabeculae, which widens the metaphyseal marrow cavity, captured by Tb.Sp2 (Figure 1C).

S7-5: Jonathan Williams, EngD

All 3 types of Tb.Sp were different ($p<0.01$), indicating that both trabecular thinning/thickening and marrow cavity expansion contribute to Tb.Sp. In the 62-weeks-old dataset Tb.Sp2 became dominant (Figure 1B). Similar results were observed for ovariectomy and spinal cord injury models.

Conclusions: Metaphyseal Tb.Sp is not well represented by a single mean. Reporting Tb.Sp1 and Tb.Sp2 supports mechanistic interpretation (trabecular thinning/thickening vs central cavity expansion). We propose reporting metaphyseal Tb.Sp as (Tb.Sp1, Tb.Sp2) alongside conventional summary statistics. We envisage that this methodological update should enable a more sensitive distinction of skeletal phenotypes.

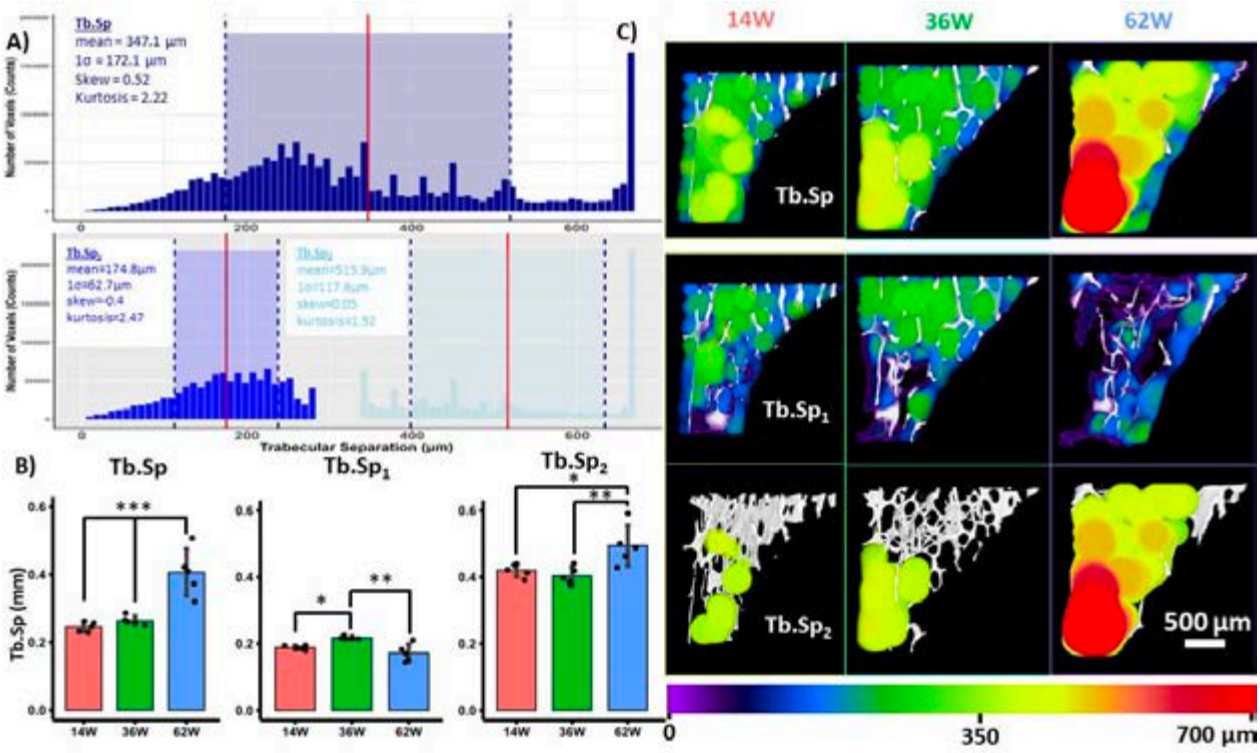

Figure 1. Trabecular separation (Tb.Sp) results for proximal tibial metaphyseal trabecular bone in the mouse ageing model. A) Representative osteoporotic Tb.Sp histogram with statistics, followed by Tb.Sp1 and Tb.Sp2, which provides information on intra-trabecular thinning and metaphyseal marrow cavity expansion. B) Tb.Sp morphometric analyses. C) Tb.Sp colour thickness maps illustrating the three types of Tb.Sp.

Session VIII: Mechanoregulation of Bone Development & Regeneration

S8-1: Niamh Nowlan, PhD

How Mechanical Forces Shape Skeletal Development

Mechanical loading plays a critical role in the postnatal development of all aspects of the musculoskeletal system, as we have learned from conditions affecting children's bones (such as cerebral palsy and Blount's disease) and also from animal models of altered loading (including tail or hindlimb suspension, exercise programs or local paralysis using botulinum toxin). However, there is a paucity of large animal models with altered mechanical loading on a scale that is translatable to human children. Furthermore, we lack a model system which creates simultaneous under-loading and overloading in an immature skeleton that facilitates teasing out the mechanisms underlying postnatal adaptation of different skeletal tissues over postnatal development. We have developed a novel caprine claw removal model in which removal of one digit from the forelimb of neonatal goats creates three distinct loading conditions within a single animal: underloaded and overloaded digits in one forelimb, and normally loaded digits in the contralateral forelimb. Surgery is well-tolerated, with animals displaying normal locomotor behavior within 24 hours. Pilot data confirm robust and consistent differences in bone morphometry and associated musculoskeletal tissues between loading conditions. This model offers a new translational platform for investigating load-mediated musculoskeletal development with relevance to paediatric orthopaedics, osteoporosis, osteoarthritis and space research.

Session VIII: Mechanoregulation of Bone Development & Regeneration

S8-2: Anushka Gerald, PhD

Schwann cell mapping and function in the regeneration of bone from different embryonic origins

Anushka Gerald,1 Quentin Meslier,2,3 Mohamed Hassan,2,3 Isabella Rastegar,4 Erica L Scheller1,2,3,5
1- Department of Biomedical Engineering, Washington University, Saint Louis, MO, USA.
2- Division of Bone and Mineral Diseases, Department of Medicine, Washington University School of Medicine, St. Louis, MO, USA.
3- Center of Regenerative Medicine, Washington University, St. Louis, MO, USA.
4- Department of Biology, Washington University, St. Louis, MO, USA.
5- Department of Cell Biology and Physiology, Washington University, Saint Louis, MO, USA.

Purpose: Schwann cells (SCs) are a neural crest lineage that provides trophic and structural support for nerve axons throughout the body and have unique plasticity in states of local injury. Despite their emerging importance for nerve signaling and tissue repair in bone, the morphology, distribution, and function of SCs in skeletal tissues remains largely undefined. We hypothesized that SCs would be prevalent in bone and, upon injury, transition into a repair state with potential to enhance osteogenesis and neurogenesis to promote healing.

Materials and Methods: We performed whole mount calvarial imaging and tissue clearing of limb and vertebral bones to visualize and quantify nerve-lining Schwann cells in skeletal tissues. This included triple mutant “Schwann Mapper” mice (MPZ-Cre+/-;TdT+/+;p75-eGFP+/+) that express eGFP in non-myelinating SCs and TdTomato in myelinating SCs and a new CRISPR-generated “p75 Tracer” mouse that labels non-myelinating SCs after tamoxifen treatment (P75-CreERT2+/-;ZsGreen1+/+). The p75 Tracer model was also used to map p75+ lineage derivatives during craniofacial regeneration and for FACS purification and RNAseq of traced populations.

Results: MPZ and p75-NGFR labeled myelinating and non-myelinating SCs, respectively, with broad distribution in all skeletal tissues examined. SCs in bone co-stained with S100B and demonstrated a classic “bead on a string” morphology overlying TUBB3+ peripheral nerves. Nerve-lining SCs were already present in periosteum at birth. Both MPZ+ and p75-NGFR+ SCs formed delicate, intricately branched structures within the periosteum and bone marrow. We also identified new MPZ+ and p75-NGFR+ fibroblast-like cells interspersed between adjacent periosteal nerves with the appearance of Schwann cell precursors (SCPs).

Session VIII: Mechanoregulation of Bone Development & Regeneration

S8-2: Anushka Gerald, PhD

Quantification of SCs and candidate SCPs revealed enhanced presence of SCs in neural crest-derived bone, a site of accelerated skeletal healing. To define the contributions of p75-lineage cells, we created paired calvarial defects in the neural crest-derived frontal and mesoderm-derived parietal bones. Imaging at 3, 14, and 28-days demonstrated remarkable differences – with dramatic expansion of fibroblastic p75 lineage cells within the center of the frontal defect. By RNAseq, traced cells had high expression of both SC and osteolineage markers. By contrast, p75 lineage cells within the parietal defect quickly re-associated with invading TUBB3+ neurons to re-establish the periosteal neural net. By RNAseq, SC markers and nerve recruitment factors were concurrently upregulated.

Conclusions: Our work shows that nerves within bone are covered by a robust network of MPZ+ or p75-NGFR+ SCs. Further, we reveal exceptional plasticity of p75 lineage SCs after skeletal injury that is closely associated with accelerated osteogenesis and neurogenesis in neural crest- and mesoderm-derived bone, respectively.

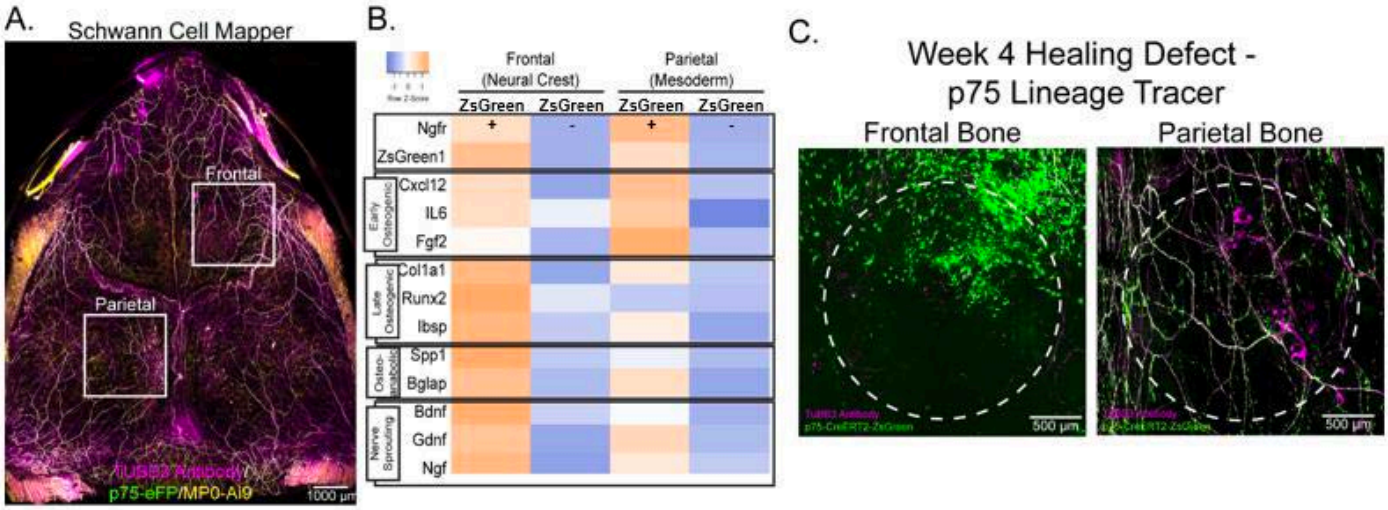

Figure. A) Maximum intensity projection (MIP) of whole mount 4x spinning disk confocal images of Schwann Mapper mouse calvaria. Scale bar is 1000µm. Magenta = TUBB3 antibody, Green = p75-eGFP reporter, Yellow = MP0-Ai9 reporter. (B) Heat map of bulk RNA sequencing of FACs sorted cells isolated from the regenerating calvaria at week 2 post injury. The groups are ZsGreen+ cells and ZsGreen- cells from both the frontal and parietal bones. (C) MIP of whole mount 10x spinning disk confocal images of p75 Lineage Tracer mouse showing the frontal and parietal bones. Dotted white circle represents original defect area. Magenta = TUBB3 antibody, Green = p75-CreERT2-ZsGreen reporter

Session VIII: Mechanoregulation of Bone Development & Regeneration

S8-3: Martina Jolic, PhD

Multimodal characterisation of re-osseointegration after mechanical overload

M. Jolic*, L. Emanuelsson, B. Norlindh, F.A. Shah, P. Thomsen, A. Palmquist
Department of Biomaterials, Institute of Clinical Sciences, Sahlgrenska Academy, University of Gothenburg, Sweden *presenting author

Successful long-term osseointegration of metal implants depends on a direct structural and functional connection between bone and implant 1. Despite high clinical success rates, implant failures can still occur following mechanical overload. While re-osseointegration after interface disruption has been demonstrated 2,3, the underlying biological and biomechanical responses remain poorly defined. Here we used our newly established preclinical model 3 to investigate the temporal biomechanical, tissue, cellular, and molecular patterns in the re-osseointegration process.

One screw-shaped titanium implant was inserted into each rat tibia. After 28 days of unloaded healing, mechanical overload was induced by snap-rotating selected implants 90° counterclockwise, immediately followed by 90° clockwise rotation. Control implants were exposed but not rotated. Animals were sacrificed immediately or at 3, 7, or 28 days post-disruption (n=16/group). Biomechanical stability was assessed by removal torque testing. A multimodal imaging approach including micro-computed tomography, histomorphometry, histology, and electron microscopy, was combined with compartment-specific RNA sequencing of peri-implant bone and implant-adherent interface tissue.

Mechanical disruption significantly reduced biomechanical stability and bone–implant contact ($p < 0.05$, Fig. 1A). Electron microscopy and histomorphometric analyses revealed region specific structural damage to peri-implant bone immediately following overload (Fig. 1C). A staged regenerative response was observed: provisional connective tissue matrix and strong pro-osteogenic response at 3 days post-disruption, extensive new bone formation within the peri-implant space at 7 days, and complete structural remodelling by 28 days. By this time point, biomechanical stability was fully recovered and exceeded disruption-time controls with an increase in peri-implant bone area (Fig. 1A-B). Preliminary transcriptomic analysis of peri-implant bone demonstrated transient upregulation of osteogenic and mineralisation pathways at early time points, with no differentially expressed genes detected at 28 days. In contrast, the implant-adherent tissue compartment exhibited sustained differential gene expression across all time points, indicating that the implant surface represents a dynamically evolving environment rather than a passive structural boundary.

S8-3: Martina Jolic, PhD

These findings demonstrate that re-osseointegration of mechanically disrupted titanium implants can occur in vivo under non-pathological conditions. Mechanical overload triggered a coordinated regenerative and adaptive response that restored bone–implant contact, enhanced bone formation, and biomechanical competence. This highlights re-osseointegration as a dynamic, biologically driven process with implications for improving implant longevity.

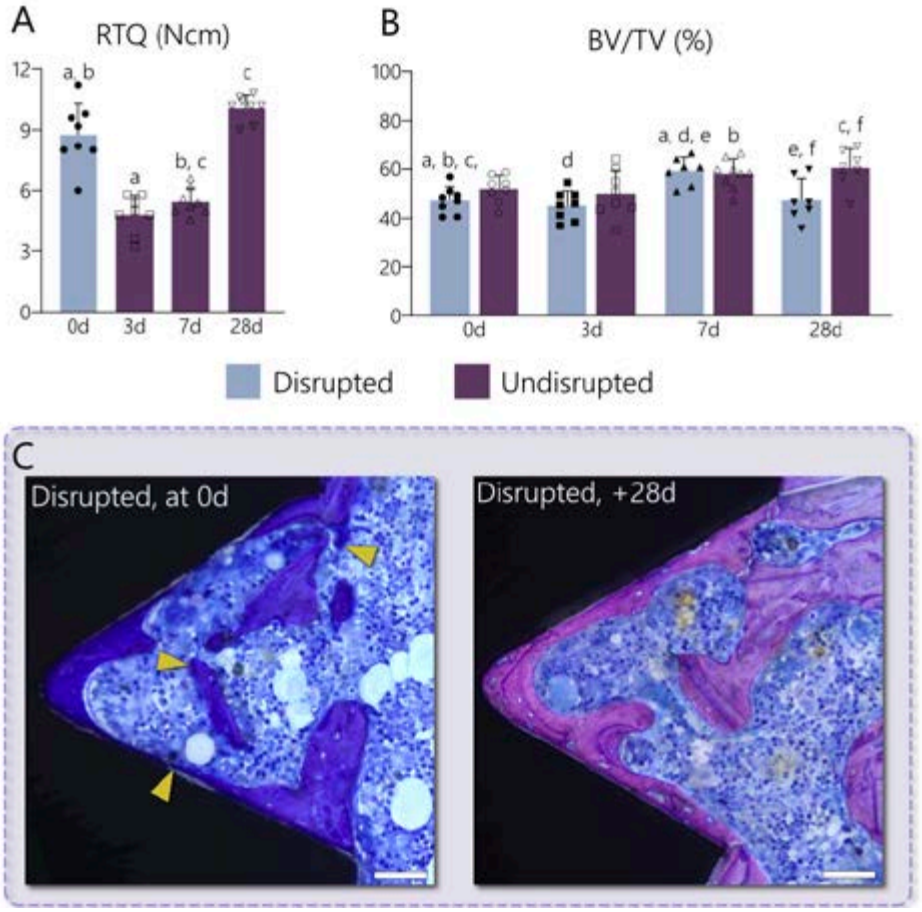

Fig. 1 A) Biomechanical stability measured with RTQ. B) Bone volume within total volume of implant threads (BV/TV). C) Representative undecalcified, basic fuchsin-toluidine blue micrographs showing damage to peri-implant bone following disruption (left) and complete re-osseointegration by 28 days post-disruption (right). Yellow arrowheads point to disruption damage in peri-implant bone. Data are presented as mean ± standard deviation. The same letters indicate statistical difference ($p < 0.05$). Scale bars = 50 μm.

References: 1F.A. Shah et al (2018) Acta Biomater, 84:1-
15. 2C-J. Ivanoff et al (1997) Int J Oral Maxillofac Implants, 26(4):310-5. 3M. Jolic et al (2025) Biomater Sci, PMID: 41111326.

Session VIII: Mechanoregulation of Bone Development & Regeneration

S8-4: Tomer Stern, PhD

Linking Chondrocyte Activity to Cartilage Deformation by Pseudo-Cell Tracking

Meng-Jia Lian1, Mou-Chi Cheng2, Celia Flory1, Maggie Wang3, Dana Akkal3, Jonathan Wong3, Lydia Glowney1, Haichun Pan1, Kristina Zheng1, Yuji Mishina1, Dawen Cai2, Tomer Stern1, *
1University of Michigan School of Dentistry,
2University of Michigan Medical School,
3University of Michigan College of Literature, Science, and the Arts
* Presenting author

Purpose: The epiphyseal cartilage prefigures the developing bone and drives its elongation, yet the quantitative relationship between chondrocyte activity and tissue morphogenesis remains unresolved. While cell division, hypertrophy, and matrix deposition are recognized contributors, the growth plate is a spatially heterogeneous structure where distinct zones deform through unique combinations of cellular processes. Because live-imaging deep 3D cartilage is technically challenging, these dynamics have not been directly reconstructed at a tissue scale. This gap limits our fundamental understanding of bone elongation and 3D shape formation, constraining mechanistic insight into skeletal dysplasias. To bridge this, we developed a computational framework for pseudo-cell tracking that reconstructs growth plate dynamics from sequential fixed 3D images at cellular resolution. This enables tissue-wide quantification of cell activities, extraction of deformation tensors, and direct association of cellular processes with local morphogenesis.

Materials and Methods: We utilized optical clearing and light-sheet fluorescence microscopy to image intact embryonic mouse growth plates expressing a membrane-localized reporter at high resolution. Deep-learning segmentation was used to map the 3D shape and position of up to 140,000 chondrocytes per tissue. To reconstruct cell movements across developmental time points, we adapted a statistical geometry framework for matching cells in sequential fixed samples while accounting for cell division and loss. This strategy enabled tissue-wide quantification of chondrocyte behaviors—including changes in cell volume, cell shape, and extracellular matrix deposition—alongside spatially resolved measurement of the direction and magnitude of local tissue deformation.

S8-4: Tomer Stern, PhD

Results: Focusing on axial elongation, our tissue-wide analysis identified the transition from the prehypertrophic to the hypertrophic zone as the principal region of elongation, exhibiting substantially higher local longitudinal strain than elsewhere. In this region, increases in cell volume and changes in cell aspect ratio emerged as the strongest candidate cellular contributors to local tissue deformation. Other regions displayed distinct deformation profiles and differing combinations of cell behaviors, highlighting the spatial complexity of the growth plate.

Conclusions: Pseudo-cell tracking enables the quantification of cellular activities and tissue deformations across scales using sequential fixed samples. This opens new opportunities for studying cartilage morphogenesis in both normal and pathological bone development. Furthermore, because it relies on minimal tissue-specific assumptions, pseudo-cell tracking offers a versatile strategy for reconstructing developmental dynamics in various other organ systems.

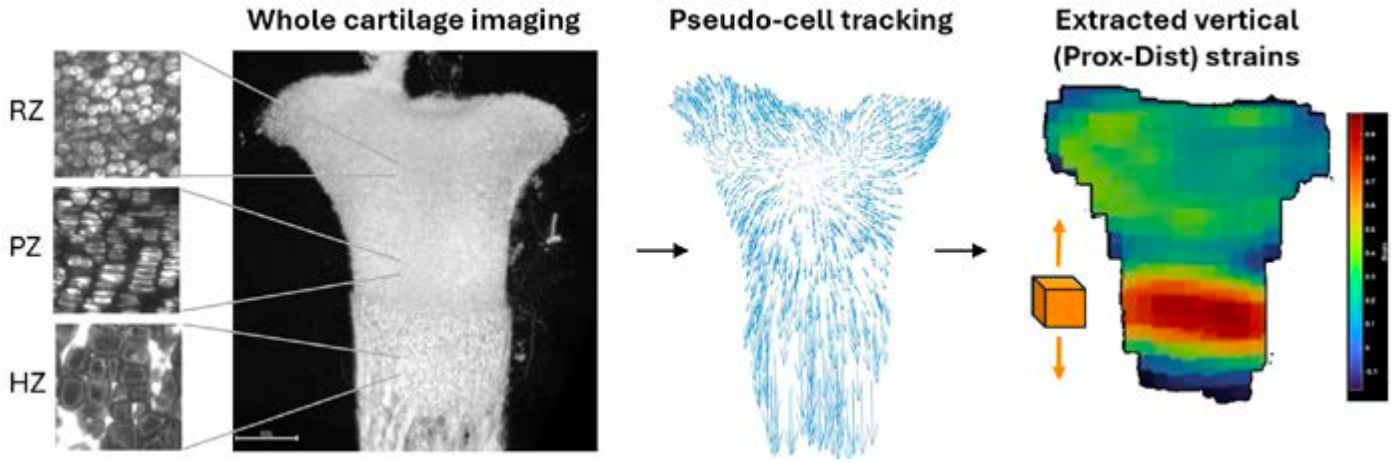

Graphic Abstract: Whole-cartilage light-sheet imaging, pseudo-cell tracking, and extraction of local proximodistal strain in the mouse proximal tibia between E16.5 and E17.5. Left, cleared intact E16.5 cartilage with representative resting zone (RZ), proliferative zone (PZ), and hypertrophic zone (HZ) morphology. Middle, reconstructed cell displacement field inferred between the two time points. Right, extracted proximodistal strain map showing a localized band of elevated elongation in the prehypertrophic region.

Session VIII: Mechanoregulation of Bone Development & Regeneration

S8-5: Hajar Souhail, MSc

Microstructural heterogeneity shapes mechanical variability in human trabecular

Hajar Souhail1, Luca 2*, Elisa Zamengo3*, Stéphane Blouin3, Pasquale Vena2, Andrea Berzlanovich4, Markus A. Hartmann3, Davide Ruffoni1
1. Mechanics of Biological and Bioinspired Materials Laboratory, University of Liège, Liège, Belgium;
2. Laboratory of Biological Structure Mechanics, Politecnico di Milano, Milan, Italy;
3. Ludwig Boltzmann Institute of Osteology, Vienna, Austria.
4. Center of Forensics Medicine, Vienna, Austria.
* equal contribution

Purpose: characterizing microstructural and mechanical behaviour of trabecular bone is fundamental not only for understanding bone strength in aged and diseased individuals but also for improving fracture fixation devices and scaffolds for bone defects. While microstructure–mechanics relationship has been extensively investigated, the role of spatial variations in trabecular microstructure and the mechanical implications, even within the same bone, are less explored. This work focuses on the microstructural variability of trabecular bone in human radii, aiming to evaluate how local microstructure variations translate in changes in mechanical properties.

Materials and Methods: in the trabecular compartment of 14 distal radii (age range 75 ± 14 years) 9 cubic ROIs per sample (5 mm side length) were chosen along the lateral–medial axis and the anterior-posterior axis on micro-computed tomography scans (µCT 50, SCANCO, 24 µm resolution) (Fig. 1A). The trabecular network was characterized by bone volume fraction (BV/TV), trabecular thickness (Tb.Th) and trabecular spacing (Tb.Sp). Micro-structural finite element analysis (micro-FE) was performed to compute the effective elastic modulus of each ROIs, for a total of 126 cubes. Spearman correlations were used to analyse the relationship between BV/TV and microstructural parameters (Tb.Th, Tb.Sp) in regions of low and high bone mass defined based on the median BV/TV. The relative variability of microstructure and mechanical properties was quantified by the coefficient of variation (CV).

S8-5: Hajar Souhail, MSc

Results and Discussion: Spearman correlations revealed distinct microstructural patterns (Fig. 1B): in regions of low bone mass, variations of BV/TV were predominantly thickness-driven, whereas in regions of higher bone mass, BV/TV correlated mainly with Tb.Sp. The variability analysis revealed that variations in mechanical properties are much stronger than those in bone volume fraction and microstructure alone (Fig. 1C): the global coefficient of variation evaluated over all 9 ROIs for elastic modulus was nearly double that of BV/TV and at least four times that of the microstructural parameters. These global patterns obtained considering all samples, were also observed locally across spatial ROIs positions (Fig. 1D).

Conclusions: we performed a spatially resolved analysis of trabecular microstructure and mechanics showing how regional variations in microstructure are amplified into mechanical changes. Such quantification shall provide a better understanding of the heterogenous mechanical behavior of trabecular bone.

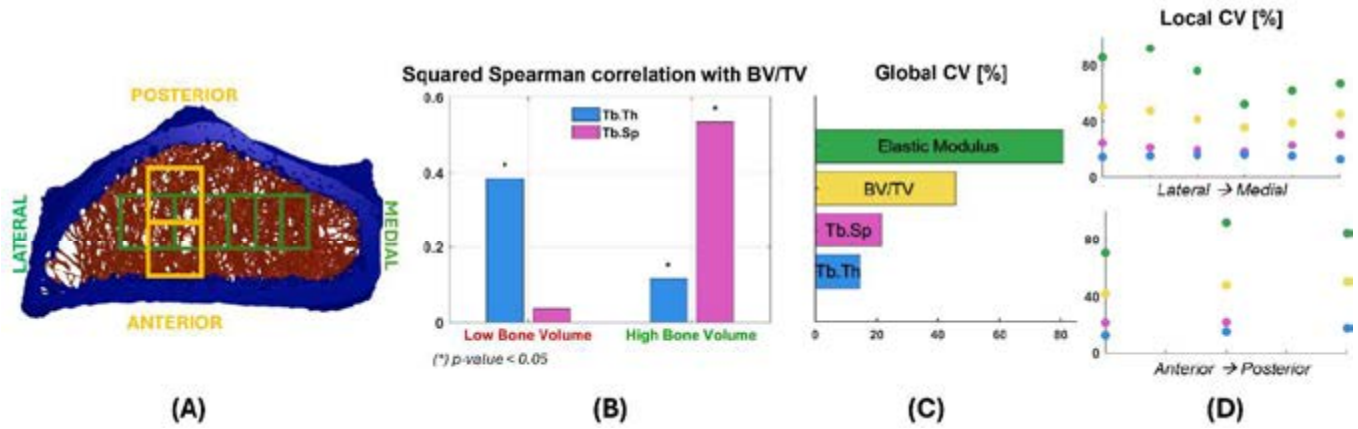

Figure 1: (A) micro-CT reconstruction of a transvers cross section of the distal radius, highlighting the positions of the extracted 5-mm trabecular cubes, arranged along the lateral–medial (green) and anterior–posterior (orange) axes. (B) Bar plots showing the Spearman's correlation coefficients between BV/TV and trabecular parameters (Tb.Th and Tb.Sp) for regions of low and high bone volume. (C) Pie chart and (D) scatter plots showing the global and local coefficient of variation (CV) for Tb.Th, Tb.Sp, BV/TV, and elastic moduli.

Session VIII: Mechanoregulation of Bone Development & Regeneration

S8-6: Claire Acevedo, PhD

Spatial regulation of cochlear bone by osteocytes preserves mechanical gradients for healing

Yoshihiro Obata[1], Christoforos Meliadis[2], Pupa Gilbert[3], Tamara Alliston[2], Claire Acevedo*[1]
[1]Department of Mechanical and Aerospace Engineering, University of California San Diego, USA
[2]Department of Orthopaedic Surgery, University of California San Francisco, USA
[3]Department of Physics, University of Wisconsin–Madison, USA
*Presenting author

Purpose: The cochlea relies on the mechanical properties of its surrounding bone to transmit sound frequencies through a spatially organized (tonotopic) system. Unlike most skeletal tissues, cochlear bone maintains exceptional stiffness throughout life despite the absence of osteoblast- and osteoclast-driven remodeling, yet it contains abundant osteocytes. These cells may therefore play a key role in regulating matrix quality through perilacunar remodeling. This study investigates whether spatial variations in mineralization and osteocyte lacunar morphology contribute to the mechanical specialization of cochlear bone that supports auditory function.

Materials and Methods: Cochlear bones from 16-week-old female C57BL/6 mice (N=10) were analyzed using Synchrotron Radiation micro-Computed Tomography (SRμCT) at 1.6 μm resolution (ALS beamline 8.3.2). Volumetric tissue mineral density (vTMD) and osteocyte lacunar morphology were quantified across cochlear turns (apex, middle, base) and across radial regions (inner and outer cortex). Image segmentation was performed to isolate cochlear subregions, allowing measurement of lacunar density, volume, and aspect ratio in relation to mineralization gradients.

Results: Significant spatial heterogeneity was observed in cochlear bone mineralization. The basal region exhibited the highest vTMD compared with the middle and apical turns, indicating increased stiffness in the region associated with high-frequency sound transmission. Radially, the inner cortical layer showed significantly greater mineral density than the outer cortex across all turns. Osteocyte lacunar morphology also varied spatially: lacunae were smaller and more spherical in the basal region and inner cortex, while the outer regions displayed more elongated lacunae. These patterns suggest region-specific osteocyte activity associated with gradients in matrix mineralization.

S8-6: Claire Acevedo, PhD

Conclusions: Cochlear bone exhibits pronounced spatial heterogeneity in both mineralization and osteocyte lacunar morphology. The association between regional mineral density gradients and osteocyte morphology supports the hypothesis that osteocytes actively regulate cochlear bone quality through spatially distinct perilacunar remodeling. These findings challenge the view of cochlear bone as a passive structural element and instead suggest a coordinated matrix-cell mechanism that preserves the mechanical properties
required for auditory function.

Poster Abstracts

PO-01 Megi Ishmaku, MSc

Directed Formation of Bone Cell Networks in Micropatterned Hydrogels

M. Ishmaku[1], M. Bernero[1], X. Yang[1], W. Qiu[1], X.-H. Qin[1]

[1]*Institute for Biomechanics, ETH Zurich, Zurich, CH*

PURPOSE: Bone is a dynamic tissue that undergoes continuous remodeling to maintain mineral homeostasis and structural integrity. Osteocytes, as mechanosensory and endocrine cells, are the major contributors to this process, coordinating load-induced mechano-adaptation by regulating other bone cell types through their lacuno-canalicular network (LCN). Accurately modeling osteocyte formation and differentiation *in vitro* remains difficult. In this study, we aim to investigate 3D cell network formation and osteogenic differentiation in micropatterned hydrogels.

METHODS: Semi-synthetic computer-aided design (CAD) models of LCNs were made based on FIB-SEM imaging data from murine osteocytes. Bone-mimicking microstructures were fabricated using two-photon subtractive microprinting and high-resolution topographical features were achieved via precise two-photon ablation of gelatin methacryloyl (GelMA) hydrogels. To enhance ablation efficiency, a water-soluble two-photon photosensitizer (P2CK) was added to GelMA hydrogels before printing. Murine osteocyte-like IDG-SW3 cells were seeded onto the structures and cultured under osteogenic differentiation conditions for up to 5 weeks. Two seeding strategies were compared: 2D pre-differentiated cell seeding and in situ differentiation (Fig. 1a). Cell morphology was assessed by actin and nuclear staining, functional maturation by immunostaining, and cell connectivity by fluorescence recovery after photobleaching (FRAP).

RESULTS: Early osteocyte differentiation was confirmed by a significant increase in GFP-Dmp1 expression observed as early as two weeks after osteogenic induction in 2D culture (Fig. 1b). By day 14 post-seeding, directed cell network formation within the hydrogels was evident, as visualized through actin and nuclear staining (Fig. 1c). Comparative analysis of Dmp1-GFP expression between the two seeding strategies was conducted during network development. In the microprinted constructs, immunofluorescence analysis showed distinct, colocalized expression of connexin 43 (Cx43), a key marker of gap junctions with the cell morphology. Functional connectivity was further demonstrated by live-cell FRAP imaging, confirming active intercellular communication via gap junctions.

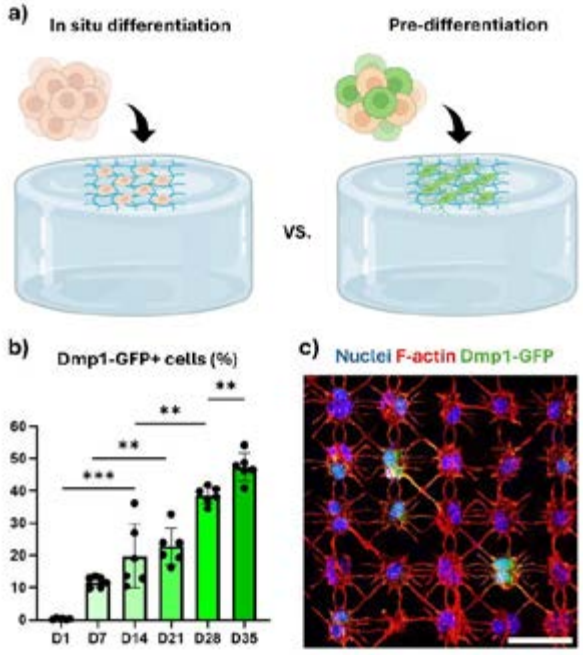

Fig. 1: Two-photon patterned microstructures for IDG-SW3 network formation. ***a)*** *IDG-SW3 seeding on micropatterned GelMA substrates via two approaches.* ***b)*** *Dmp1-GFP+ cell % in 2D culture.* ***c)*** *IDG-SW3 network after 14 days osteogenic differentiation in situ (scale bar: 50 µm).*

DISCUSSION & CONCLUSIONS: This study highlighted the utility of precise two-photon hydrogel patterning to generate instructive biomaterials for cell culture and tissue engineering. The patterned GelMA hydrogels effectively supported both morphogenesis and functional differentiation of osteocyte-like cells, as evidenced by network formation, and gap junction activity. These findings emphasize the potential of high-resolution hydrogel patterning for engineering physiologically relevant bone tissue models.

ACKNOWLEDGEMENTS: This work was supported by the SERI-funded European Research Council starting grant.

PO-02 Edoardo Pedrinazzi, MSc

Three-dimensional morphological characterization of bone packets and osteocyte lacunae in human trabecular bone

E. Pedrinazzi 1,2, S. Blouin 3, A. Tits 4, A. Simar 2, E. Zamengo 3, A. Berzlanovich 5, J. Perrin 6, T. Weitkamp 6, R. Weinkamer 4, M.A. Hartmann 3, D. Ruffoni 1
1. University of Liège, Belgium
2. Catholic University of Louvain, Belgium
3. Ludwig Boltzmann Institute of Osteology, Vienna, Austria
4. Max Planck Institute of Colloids and Interfaces, Postdam, Germany
5. Institute of Forensic Medicine, Vienna, Austria
6. Synchrotron SOLEIL, Saint-Aubin, France

PURPOSES: Trabecular bone is a porous, hierarchically organized tissue with a multiscale structure, consisting of a three-dimensional (3D) network of trabeculae, each formed by multiple bone packets (BP) that differ in shape and mineral content. This pattern arises from a continuous remodeling process regulated by osteocytes, the primary mechanosensory cells of bone, residing in lacunae. Data on BP morphology is sparse and often limited to two-dimensional (2D) analysis [1], as BP are usually not visible with desktop micro-computed tomography, the most used approach for trabecular microstructure. Prior analyses of 3D trabecular architecture did not directly focus on BP geometry [2, 3]. This study provides a morphological analysis of trabecular bone, investigating the relationship between trabecular architecture, BP properties, and osteocyte lacunae. The aim is to understand the interplay between bone remodeling and BP characteristics and, on the long run, the impact of BP on the mechanical behavior of single trabeculae.

MATERIALS AND METHODS: Trabecular bone specimens (cylinders, 6 mm diameter) were harvested from the femoral neck of 10 healthy donors aged 53–93 years. Samples were imaged by phase-contrast synchrotron radiation micro–computed tomography at 0.65 μm isotropic voxel size at Synchrotron SOLEIL (France). Trabeculae and osteocyte lacunae were automatically segmented using a deep learning model trained on manually annotated slices (Dragonfly) while BP were segmented manually following the visible cement lines. Key morphological parameters were extracted, considering also the BP mineral content and distinguishing between rod-like and plate-like trabeculae.

RESULTS AND DISCUSSION: Our 3D analysis revealed a complex BP morphology, non detectable by conventional 2D imaging. BP exhibit protrusions, cavities, and intertwined shapes (Fig. 1A). They vary widely in volume and length, frequently extending over the entire trabecula and, in some cases, even propagating from rod-like to adjacent plate-like trabeculae. Osteocyte lacunae showed smaller volumes in highly mineralized (older) BP than in lowly mineralized (younger) ones, possibly reflecting reduced cellular activity [4]. Moreover, older BP feature a higher fraction of lacunae filled by mineral deposits, an indication of micropetrosis [5, 6].

PO-02 Edoardo Pedrinazzi, MSc

Three-dimensional morphological characterization of bone packets and osteocyte lacunae in human trabecular bone

Lacunae had an ellipsoidal shape with the main axis aligned along the longitudinal direction of rod-like trabeculae, whereas no preferential lacunar alignment was found in plate-like trabeculae (Fig. 1B). These findings provide morphological insights into the organization of individual
trabeculae.

REFERENCES:
[1] Lamarche et al., Bone 160, 116399, 2022
[2] Goff et al., Bone 51, 28–37, 2012
[3] Tang et al., Sci Rep. 14, 21604, 2024
[4] Oda et al., Biogerontology 8, 345–352, 2007
[5] Jones et al., Acta Biomater. 209, 493–503, 2026
[6] Carpentier et al., Bone 50, 688–694, 2012

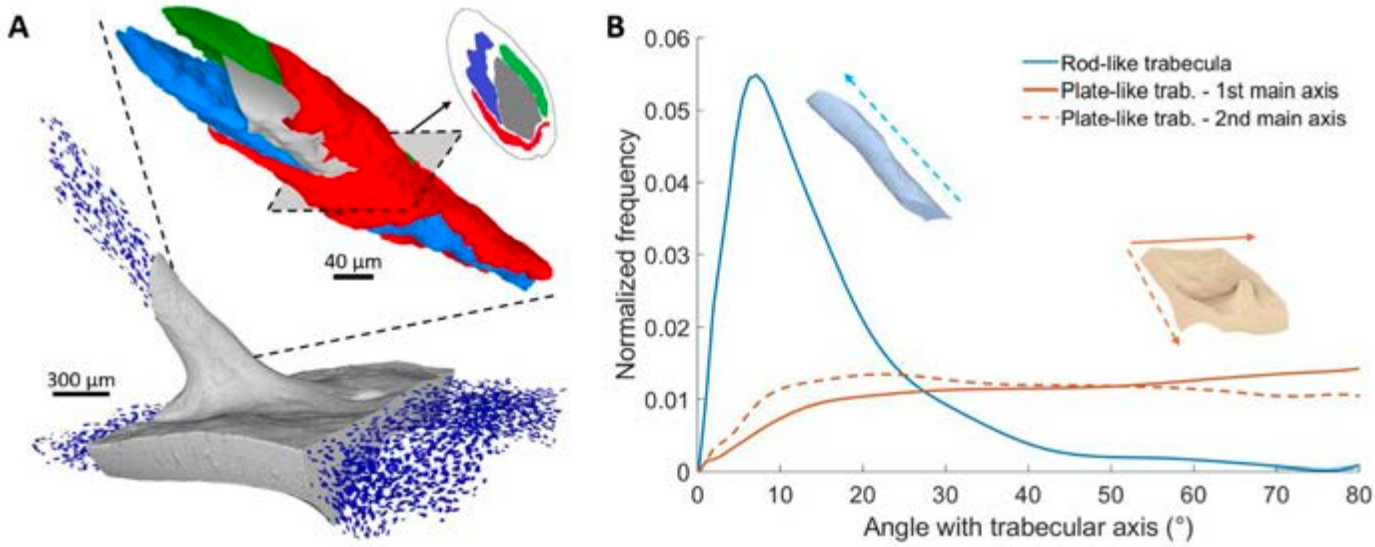

Figure 1: A) 3D rendering of four individual bone packets (BP) highlighted in different colors (top), extracted from a rod-like trabecula, emanating from a plate-like one (bottom). The inset shows a classical 2D view of the BP. The segmented osteocytes lacunae are shown in blue. B) Frequency distribution of lacunar orientation with respect to the main trabecular axes (shown on the plot), the rod-like trabecula was characterized by its main longitudinal axis, while the plate-like trabecula was characterized by its two in-plane main axes.

PO-03 Julia Vaz, MD

New Insights into an Old Disease: Osteocyte Protein Expression in CKD-Associated Osteomalacia

“J.vaz1*, C. Da Silva1, I. Oliveira1, W. Dominguez1, R. Moyses1, L. Dos reis1*, V. Jorgetti1*
1.LIM 16, Laboratório de Fisiopatologia Renal, Hospital das Clínicas HCFMUSP, São Paulo, Brasil
* Presenting Author

Purpose: Osteomalacia (OM) is a severe mineralization defect characterized by excessive osteoid accumulation and delayed mineral apposition. In chronic kidney disease (CKD), particularly in patients on hemodialysis (HD), disturbances in mineral metabolism impair bone mineralization, and aluminum (Al) deposition has historically been implicated as a modifier of CKD-associated OM. However, it remains unclear whether OM with and without Al represent distinct phenotypes. This study aimed to compare clinical, biochemical, histomorphometric, and osteocytic protein profiles in HD patients with OM with and without Al deposition.

Materials and Methods: This retrospective study analyzed bone biopsies collected between 2000 and 2024 from a bone biopsy bank. Adult HD patients (>18 years, ≥6 months on HD) with histological CKD-associated OM were included: OM-CKD (n=15) and OM-CKD-Al (n=12), defined by the presence of Al deposition at the mineralization front. Clinical, biochemical, histomorphometric, and immunohistochemistry (IHC) analyses were compared. Positive IHC osteocytes for dentin matrix protein-1 (DMP1), matrix extracellular phosphoglycoprotein (MEPE), fibroblast growth factor 23 (FGF23), osteopontin (OPN), osteoprotegerin (OPG), receptor activator of nuclear factor kappa-B ligand (RANKL), sclerostin (Scl), Dickkopf-1 (DKK1), CD44 and E11, as well as apoptotic osteocytes, were quantified and normalized to total trabecular osteocytes.

Results: Twenty-seven HD patients were included. Age (45.7±14.9 vs 50.8±13.4 years), male (n=14) and female (n=13), OM-CKD (46.7%), OM-CKD-Al (58.3%), dialysis vintage (66 [6–168] vs 72 [12–180] months), and fracture prevalence (50% vs 45%) were similar between OM-CKD and OM-CKD-Al. OM-CKD-Al patients had lower PTH (47.7 vs 287 pg/mL; p=0.012) and alkaline phosphatase (120 vs 220 U/L; p=0.015), and higher phosphate levels (p=0.034). Histomorphometry showed greater osteoid volume (p=0.021) and fibrosis (p=0.025) in OM-CKD. Differences were predominantly observed in osteoid, where OM-CKD showed higher FGF23 (p=0.033), MEPE (p=0.011), CD44 (p=0.021), and E11 (p=0.042). In mineralized bone, only CD44 remained higher (p<0.0001). Osteocyte apoptosis did not differ.

Conclusion: Aluminum-associated OM is characterized by suppressed turnover and lower osteocytic activation, whereas non-Al OM shows a more different protein profile, particularly in osteoid, suggesting divergent pathogenic pathways.

PO-04 Ali Ghasem-Zadeh, PhD

Cortical Porosity Assessment of the Distal Radius and Tibia Using Phase-Contrast Synchrotron Radiation CT

Ali Ghasem-Zadeh 1, Chris Hall 2, Duncan Butler2, Ego Seeman1 1-Department of Medicine, Austin Health, The University of Melbourne, Victoria, Australia
2- Imaging and Medical BeamLine, Australian Synchrotron Radiation, Clayton, Victoria, Australia

Introduction: High-Resolution peripheral Quantitative Computed Tomography (HR-pQCT, 82 μm isotropic voxel size) provides non-invasive, in vivo assessment of bone microarchitecture, offering insights into skeletal fragility by quantifying trabecular and cortical compartments. Cortical porosity is a key determinant of bone strength and a strong predictor of fragility fractures, as even small increases disproportionately weaken cortical stiffness and bending strength by concentrating stress and facilitating crack propagation. However, accurate quantification of cortical porosity with HR-pQCT is limited by image resolution, segmentation errors, beam hardening from poly-energetic photons, and blurred edges. These technical issues can lead to underestimation of fracture risk and misclassification of individuals at high risk. To assess cortical porosity accurately, we scanned post-mortem human radii and tibiae using synchrotron radiation tomography with phase-retrieval reconstruction at 9.6 μm voxel resolution. We hypothesised that cortical porosity arising from smaller pores would be quantifiable with HR-pQCT and could be validated against synchrotron-derived attenuation and phase-contrast images.

Methods: Thirty-two post-mortem human radii and tibiae, fresh and dry specimens, were imaged at the Australian Synchrotron Radiation-Imaging and Medical Beamline (IMBL), using 60 kV monochromatic x-ray-based tomography. Silicon amorphous detectors with voxel sizes of 9.6 and 14.6 microns have been used to create x-ray photons attenuation and phase-contrast based tomographic images.

Results: Preliminary comparison of axial images demonstrated greater visibility of small pores and Haversian canals in the phase-contrast–based images. Compared with the Scanco method, cortical porosity of the distal radius was substantially higher when measured using synchrotron imaging (21.0% vs. 8.5%, respectively).

Conclusion: We infer that cortical porosity analysis based on Synchrotron Radiation will enable more accurate estimation of cortical porosity from HR-pQCT and will improve the prediction of risk of fragility fracture.

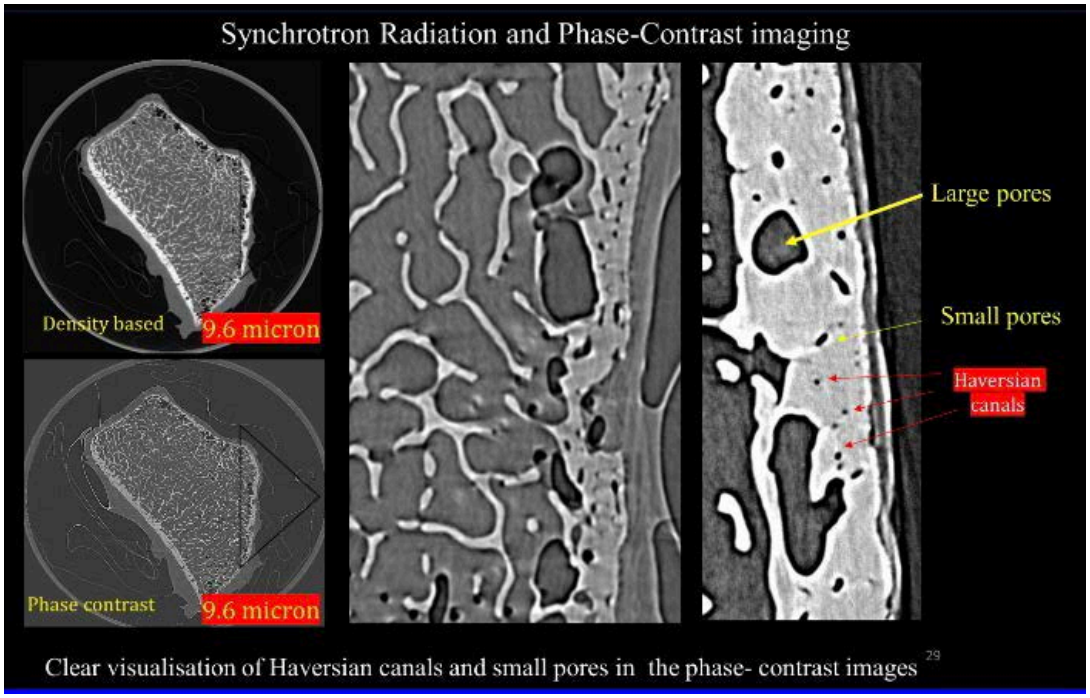

Clear visualisation of Haversian Canals and small pores of distal radius in the phase-contrast

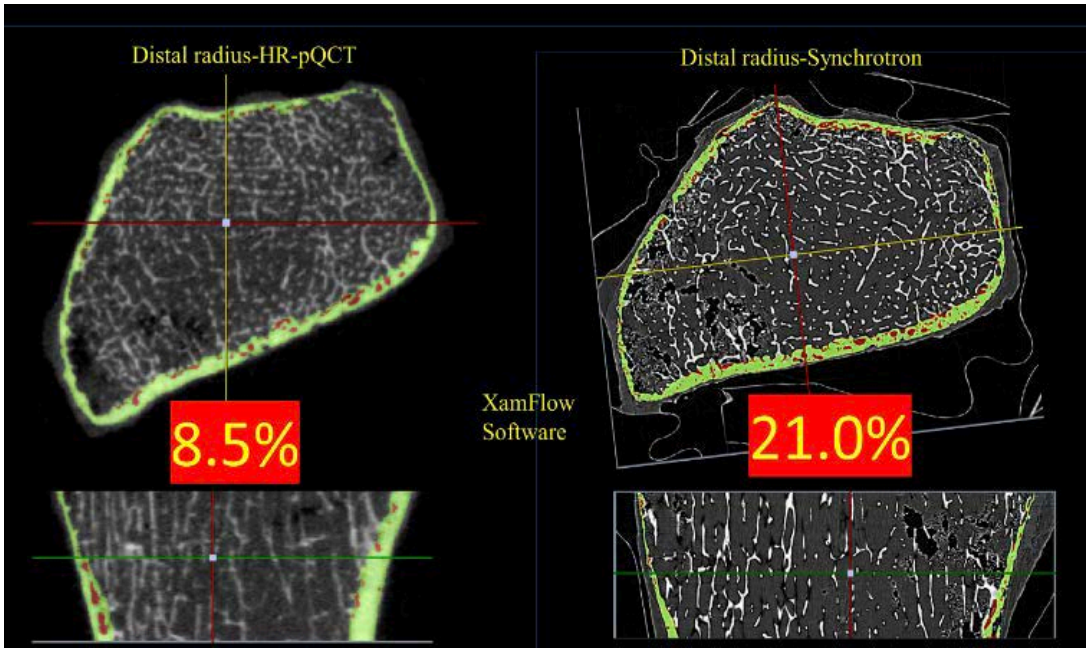

Cortical porosity of the distal radius assessed using HR-pQCT and Synchrotron Radiation

PO-05 Junichiro Kazama, MD, PhD

Integrated Evaluation of Renal Bone Disease: Bone Histomorphometry Remains Fundamental but Must Be Complemented by Assessment of Bone Material Properties

Affiliation
Department of Nephrology and Hypertension, Fukushima Medical University
1-Hikarigaoka
Fukushima-City, Fukushima 960-1295 JAPAN TEL: +81-24-547-1206
E-mail: jjkaz@fmu.ac.jp

Background: Renal bone disease in chronic kidney disease has traditionally been defined by abnormalities of bone turnover and mineralization caused by disturbances in calcium, phosphate, parathyroid hormone, and vitamin D metabolism. On this basis, tetracycline-based bone histomorphometry has been established as the gold standard for skeletal evaluation. However, accumulating evidence indicates that oxidative stress, an intrinsic feature of the uremic milieu, impairs bone matrix material properties independently of turnover abnormalities and contributes to skeletal fragility. 4-Methylthio-phenylthio-methane bisphosphonate (MPMBP), at low doses, scavenges reactive oxygen species within bone without significantly altering bone formation or resorption. We therefore examined its effects in an experimental model of renal impairment.

Methods: Thirty-two 8-week-old male Sprague-Dawley rats were assigned to four groups: normal diet; 0.2% adenine diet; adenine diet plus MPMBP 0.6 mg/kg; and adenine diet plus MPMBP 1.2 mg/kg. After 8 weeks, biochemical parameters, bone histomorphometry, mechanical testing, Raman spectroscopy, micro–X-ray diffraction, and oxidative stress markers were analyzed.

Results: All adenine-fed groups developed renal dysfunction and secondary hyperparathyroidism. Histomorphometric analysis demonstrated increased bone resorption and elevated empty lacunae counts; the latter was dose-dependently suppressed by MPMBP. Bone mineral density showed only modest reduction. In contrast, elastic properties of the femoral mid-diaphysis were markedly impaired. Raman spectroscopy revealed decreased hydroxyapatite crystallinity and increased carboxymethyl-lysine/matrix and pentosidine/matrix ratios. Micro–X-ray diffraction demonstrated disrupted apatite orientation. Tibial malondialdehyde levels were elevated. These alterations in matrix quality and oxidative stress were dose-dependently mitigated by MPMBP despite limited changes in conventional histomorphometric indices.

Conclusion: Low-dose MPMBP did not substantially modify classical histomorphometric parameters, yet it preserved bone material properties and mechanical integrity, likely through attenuation of oxidative stress. These findings do not diminish the central role of bone histomorphometry. Rather, they indicate that histomorphometry remains indispensable for defining turnover and mineralization, but must be complemented by assessment of matrix material properties to fully characterize skeletal status in renal bone disease. The gold standard has not been replaced; it has evolved into a more comprehensive framework.

PO-06 Jack Fenwick, MPhil

A Mathematical Model of Osteocyte Network Growth

Authors: Jack R Fenwick1, Alexandra Tits2, Vivien J Challis1, Richard Weinkamer2, Pascal R Buenzli1
1. School of Mathematical Sciences, Queensland University of Technology, Brisbane, Australia.
2. Department of Biomaterials, Max Planck Institute of Colloids and Interfaces, Potsdam, Ger-many.

Purpose: The osteocyte network plays an important role in the regulation of bone tissue adaptation, repair, and mineral homeostasis. While the architecture of the network is thought to influence how the network functions, little remains known about how this architecture is determined during bone formation. It has been suggested that osteoblast embedment during bone formation may be controlled by connections between osteoblasts and the existing osteocyte network. In this contribution, we develop a mathematical model of osteocyte network growth to explore how the regulation of osteoblast embedment by the existing osteocyte network may affect the developing architecture of the osteocyte network.

Materials and methods: We develop a novel, two dimensional agent-based model of osteocyte network growth for both planar and osteonal lamellar bone tissues. In this model, each osteocyte produces dendritic processes that connect to the bone surface and generate embedment signals to the osteoblasts. Embedding osteoblasts differentiate into osteocytes, thereby expanding the osteocyte network. We analyse the osteocyte networks produced by this model to understand how embedment signals affect the architecture of the network, including when and where osteocytes are generated, canalicular density, and network properties such as betweenness centrality.

Results: We find that network architecture depends strongly on the type of embedment signals received by osteoblasts. Inhibitory embedment signals consistently produced qualitatively realistic osteo-cyte networks that have cells distributed throughout the bone matrix in locally staggered and columnar arrangements, similar to arrangements of lacunae observed in lacuno-canalicular net-work cross-sections. In contrast, excitatory embedment signals produce networks with clusters of osteocytes.

PO-06 Jack Fenwick, MPhil

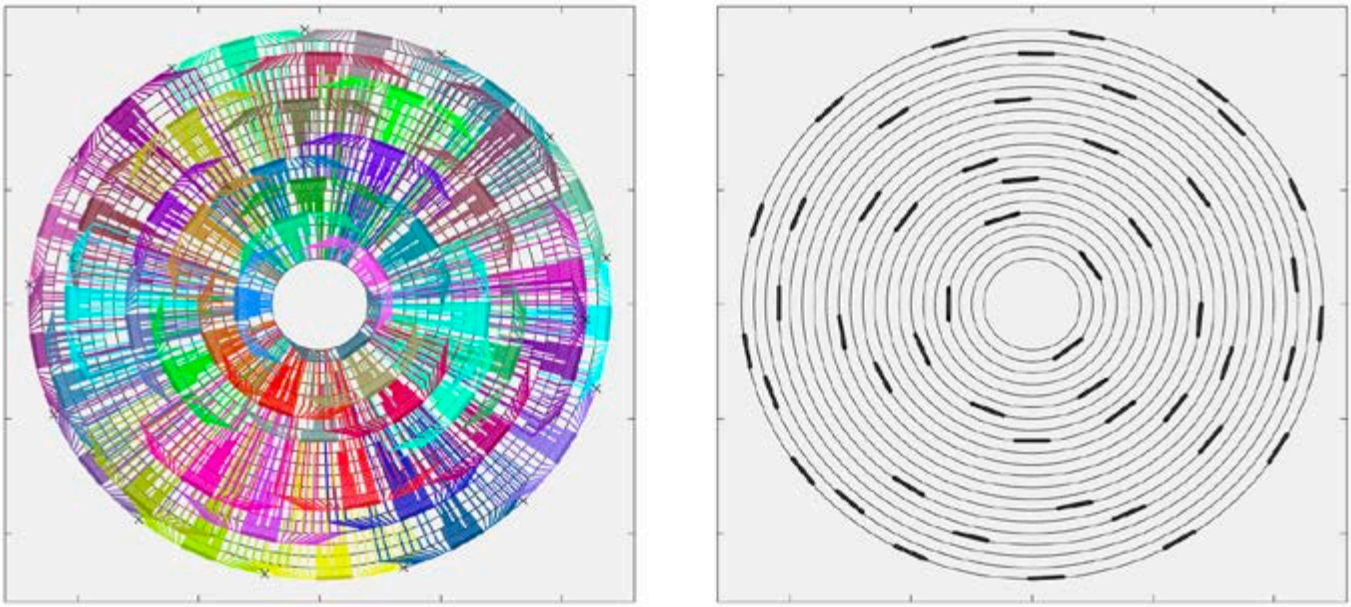

Figure 1: Left: A typical osteocyte network generated with the network growth model in the case of inhibitory embedment signals. This class of network is well connected across physical space and has proximity to all of the bone matrix in the osteon. Right: The osteocyte cell bodies of the left network highlighted in black. Inhibitory embedment signals cause osteoblasts to embed evenly throughout the domain.

Conclusion: Our model explores for the first time the hypothesis that regulation of osteoblast embedment by the existing osteocyte network can lead to realistic network growth patterns under some param-eter regimes. Features of the osteocyte network which are difficult to determine experimentally are readily accessible using this model, such as the cell-cell connections, making the model well suited for studying the development of network architecture.

PO-07 Xenia Goldberg Dahl, PhD

Spatial transcriptional changes in bone cell populations and bone microstructure across age in ADO2 and WT mice

Xenia Goldberg Dahl1,2,3, Anika Shimonty3, Malene Hykkelbjerg Nielsen1,4, Elissa Zboinsky3, Julia F. Charles3, Thomas L. Andersen1,4,5
1Molecular Bone Histology Team, Research Unit of Pathology, Dept. of Clinical Research, University of Southern Denmark, Odense, Denmark 2Dept. of Pathology, Odense University Hospital, Odense, Denmark 3Brigham & Women's Hospital, Harvard Medical School, Boston, MA, US 4Danish Spatial Imaging Consortium (DanSIC), Denmark 5Dept. Of Forensic Medicine, Aarhus University, Aarhus, Denmark

Introduction: Autosomal dominant osteopetrosis type II (ADO2) is a rare genetic disorder caused by mutations in the CLCN7 gene encoding a Cl-/H+ exchanger in osteoclasts. ADO2-patients have high bone mass with many (poorly resorbing) osteoclasts.

Purpose: To investigate the bone structure and cells of transgenic male mice with a Clcn7F318L/+ heterozygous mutation mimicking a human mutation versus wildtype (WT) across aging.

Materials and methods: We collected vertebrae at 12-weeks (Clcn7F318L/+ n=13, WT n=12), 24-weeks (Clcn7F318L/+ n=15, WT n=15), and 52-weeks (Clcn7F318L/+ n=17, WT n=15). Bone samples were fixed and µCT-scanned before being decalcified and paraffin-embedded. Embedded samples from 12-weeks (Clcn7F318L/+ n=3, WT n=4) and 52-weeks (Clcn7F318L/+ n=4, WT n=3) were analyzed by GeoMxTM digital spatial profiling (DSP) using the Mouse Whole Transcriptome Atlas. ROI-selection in the GeoMx software was guided by a TRAcP/Osteopontin immunofluorescent staining to select ROIs of eroded surfaces with osteoclasts and osteoprogenitors, marrow cells, osteoblasts, and osteocytes.
Results: As expected, Clcn7F318L/+-mice had a significantly higher BV/TV than WT across ages. Furthermore, BV/TV of WT mice was significantly decreased at 52-weeks compared to both 12- and 24-weeks (p=0.02 and p=0.0007). Surprisingly, vertebral BV/TV of 52-weeks Clcn7F318L/+ was maintained compared to both 12- and 24-weeks (p=1.0). GeoMx DSP analysis showed that aging not genotype was the main driver of transcriptional differences with components of senescence-associated secretory phenotype (SASP) changing with age in both genotypes. When comparing cell populations from 12- and 52-week mice a total of 126 differentially expressed transcripts were identified. Differentially expressed transcripts included Cyfip2 and Spp1 in osteoblasts, Epha3, Mmp13, and Ddx51 on eroded surfaces, and Vim and Tmsb4x in osteocytes. However, each genotype displayed distinct transcriptional changes with aging. To validate this, more samples are being added to the GeoMx-experiments.

Conclusion: Preliminary findings indicate that aging affects F318L mice differently than WT

PO-08 Madhumathi Rao, MD, PhD

Bone Biopsy Trends in a Metabolic Bone Disease Program

Authors: 1. E Schneider1, F Lima2, A Quinonez2, M Rao2
1. Presenting Author

Affiliations: MD Class of 2028, University of Kentucky College of Medicine1; Division of Nephrology, Bone and Mineral Metabolism, University of Kentucky2

Purpose: While undecalcified bone biopsy with fluorochrome labelling remains the gold standard for bone turnover and mineralization, there are few centers today with this expertise. Earlier reports (1980 to 2010) focused on renal osteodystrophy, but the spectrum of metabolic bone disease creates wider needs and indications. We conducted a single center study of clinical indications for bone histology and time trends over a 7-year period, that also coincided with expansion to a specialized metabolic bone center.

Methods: Retrospective study of all anterior iliac crest bone biopsies between 2019-2025 at the Division of Nephrology, Bone and Mineral Metabolism, University of Kentucky, to analyze time trends in age, sex, stated clinical indications for bone biopsy, including fracture history, bone density (BMD) decline, clinical contexts of advanced chronic kidney disease/dialysis (CKD/ESRD), organ transplant, genetic or rare bone disease, secondary osteoporosis and trends in histological diagnosis patterns.

Results: Between 2019-2025 a total of 347 bone biopsies were performed including 14 repeat biopsies (4%). The median (IQR) age was 58 (46-65) years; 33% were male. Osteoporosis was present in 55%; 45% had osteopenia or normal BMD; fractures prompted biopsy in 80% and were equally distributed across BMD categories. Other clinical settings for biopsy included advanced CKD/ESRD (14%), solid organ and stem cell transplant (10%), genetic and rare bone disease (RBD) (7%) and prior osteoporosis treatment (8%). Other stated indications were elevated ALP/BSAP (4%) and hyperparathyroid states (10%). Secondary osteoporosis indicated biopsy in 65%. While there were no changing time trends in age, osteoporosis or fractures, the frequency of male patients increased from 26 to 53% ($p=0.02$), secondary osteoporosis from 53 to 90%, ($p<0.01$), genetic or rare bone disease from 1.2 to 13% ($p<0.01$) and those with suboptimal response to prior osteoporosis treatment from 2.4 to 30% ($p<0.01$). The relative proportion of patients with organ transplants increased from 7 to 17% while advanced CKD/ESRD declined from 19 to 10% (p for linear association respectively <0.01 and 0.03). Histological diagnosis patterns predominantly reflected turnover status, with 62% in the low turnover spectrum; 11% showed defective mineralization. There were no significant time trends in histological patterns.

Conclusions: Although undecalcified bone histology has established value for characterizing renal osteodystrophy, it is less commonly performed than indicated. Our observations highlight the value of bone biopsy in a wider range of metabolic bone disease conditions that potentially reflect changing epidemiology, referral and practice patterns, and increasing awareness of secondary osteoporosis. Bone biopsy should be integrated as a critical tool into metabolic bone clinics.

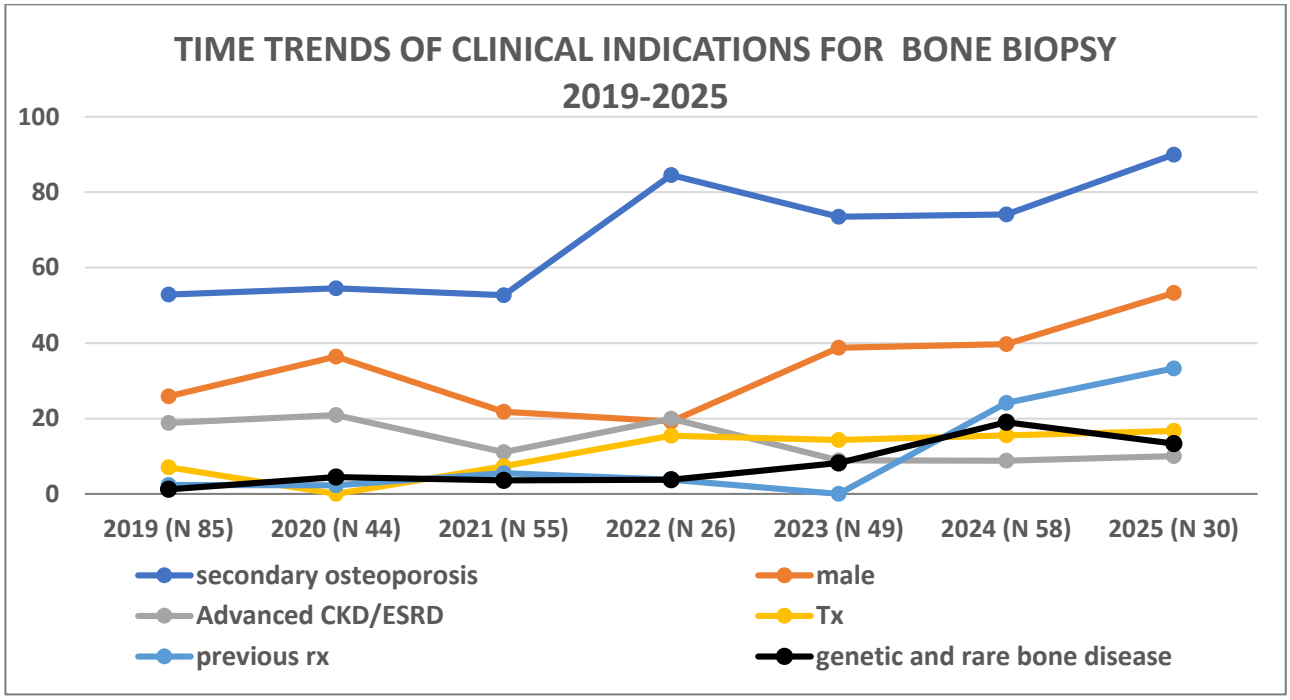

PO-09 Xuan Wei, MA

Elevated cortical bone remodeling and associated porosity induced by parathyroid hormone and glucocorticoids in male rabbits

Authors: Xuan Wei* (presenting author), Kim Harrison, Fatma Younis, David Cooper
Affiliation: Department of Anatomy, Physiology and Pharmacology, College of Medicine, University of Saskatchewan, Saskatoon, Saskatchewan, Canada

Purpose: Osteoporosis (OP) disproportionally affects postmenopausal women, however, it has been recognized that as life expectancy extends, OP also affects older men, often with more severe post-fracture mortality outcomes, possibly due to more advanced age and comorbidity. Additionally, secondary OP can affect men of all ages. Imbalance and/or uncoupling between bone resorption and formation during cortical remodeling leads to increased cortical porosity and bone loss, which is a main factor in increased fracture risk.

With a novel in vivo imaging platform, our group has thus far focused on cortical remodeling in female rabbit models, this is our first exploration into males. We sought to establish models of elevated cortical remodeling using human parathyroid hormone (PTH) and glucocorticoids (GC), two pharmaceutical agents with different underlying mechanisms in inducing cortical porosity. We hypothesized that, similar to females, PTH would increase cortical remodeling with net anabolic effects, while GC would elevate cortical porosity through remodeling space expansion, decreased formation, and endosteal resorption, leading to bone loss.

Materials and methods: Six-month-old male New Zealand White rabbits (n=18) were randomly assigned to 3 groups (n=6) and treated for 28 days with PTH, GC or saline (Controls), respectively. Fluorochrome labels were administered on days 0, 7, 14, and 28. The distal right tibial diaphyses were imaged ex vivo using micro-CT to extract cortical parameters. Cross sections were taken at 5mm proximal to the scanned area and at the corresponding location from the left side. Histomorphometric parameters were assessed from confocal microscopy images.

Results: Both GC and PTH elevated cortical porosity compared to Control ($p= 0.032$, $p< 0.001$). Osteonal mineral apposition sharply decreased in GC group during day 7-14 compared to Control and PTH groups ($p = 0.02$, $p<0.001$), and virtually ceased after 14 days. Activation frequency in the PTH group was higher than Control and GC groups ($p = 0.033$, 0.024). PTH group also had larger endosteal and periosteal mineralizing surfaces than GC group ($p=0.001$), reflecting their respective anabolic and catabolic effects. Morphologically, the PTH group showed increased coalescing, branching and merging of remodeling spaces, while in the GC group, remodeling spaces lost the classical morphology and instead exhibited radial expansion.

Conclusions: This study was the first to establish models of elevated remodeling in male rabbits focused on cortical bone microarchitecture. We demonstrated that PTH and GC induce patterns of microstructural change similar to those observed in female rabbit studies: while both effectively increased cortical porosity, PTH showed an overall anabolic effect, and GC caused considerable bone loss. Future studies will build on these models to explore how different OP treatment regimens affect in vivo cortical bone remodeling dynamics.

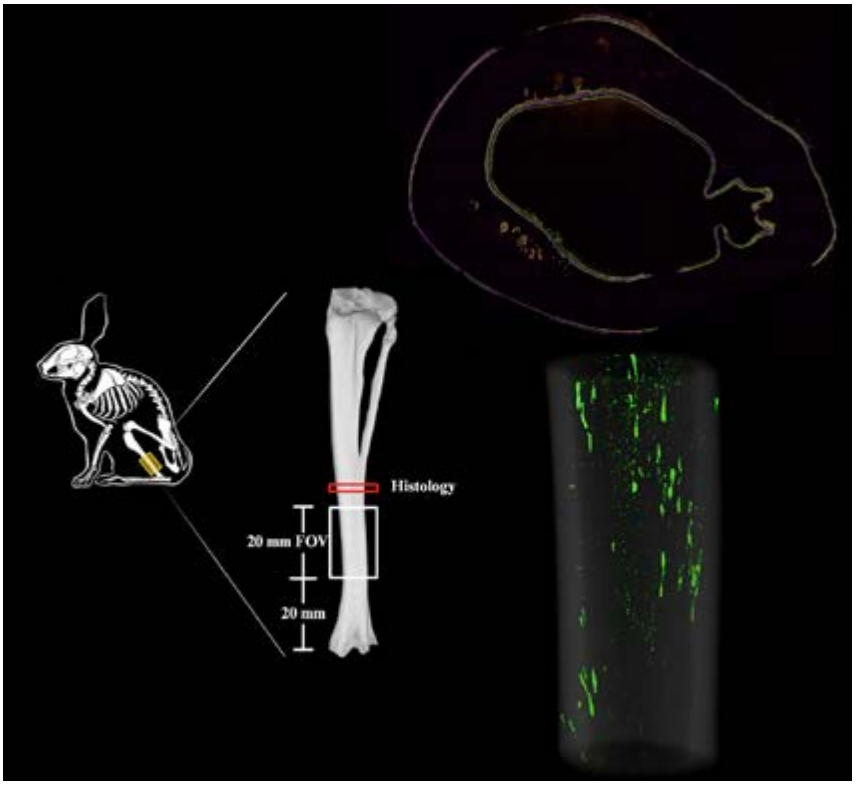

Figure showing the methodology of this study. A 20 mm long micro-CT field of view (FOV) was taken 20mm proximal to the distal end of the tibia. A cross section was taken 5mm above the FOV for histomorphometric measures. Lower right shows a 3D rendering of the FOV with cortical remodeling spaces in green. Upper right shows a confocal microscopy image of the cross section with fluorochrome labels indicating intracortical, endosteal and periosteal bone formation throughout the experimental period.

PO-10 Jonathan Williams, EngD

A tissue mineral density weighted polar moment for microCT cortical bone analysis

Arlo Feechana, Hussain Jafferyb, Natalie A. Simsc,d,e, Michael Doubef, Jonathan A. Williamsa,*
a. Department of Biomedical Engineering, Wolfson Centre, University of Strathclyde, Glasgow, G4 0NW, United Kingdom.
b. Centre for the Cellular Microenvironment, Institute of Molecular, Cell and Systems Biology, and Life Sciences, University of Glasgow, Glasgow G12 8QQ, United Kingdom.
c. Bone Cell Biology & Disease Unit, St. Vincent's Institute of Medical Research, Fitzroy, VIC 3065, Australia.
d. Department of Medicine at St. Vincent's Hospital, The University of Melbourne, Australia.
e. Mary Mackillop Institute for Health Research, Australian Catholic University, Melbourne, Australia.
f. bonej.org, Tannay, Switzerland
*presenting and corresponding author

Purpose: MicroCT cortical bone analyses frequently report a "polar moment of inertia" (pMOI) despite computing a geometric polar second moment of area (pMOA) from binary segmentation, leading to widespread terminological and methodological ambiguity in the field. Because cortical bone exhibits spatial variation in tissue mineral density (TMD), a true density-weighted polar moment (pMOI) may capture differences missed by geometry alone. We developed, mathematically formalised, and validated an open-source framework, now implemented in BoneJ (forthcoming release), that computes both pMOA and a rigorously defined TMD-weighted polar moment (pMOI) directly from calibrated microCT cross-sections, enabling density-aware analysis within standard workflows

Materials & Methods: Polar moments were computed slice-by-slice from segmented cortical cross-sections. Grayscale values were converted to TMD using hydroxyapatite phantom calibration and incorporated as pixel-wise weights within the moment integrals. Visualisation functionality generates slice-wise density-weighted moment maps and comparative pMOA/pMOI overlays (Fig. 1). The method was validated on synthetic datasets with identical geometry but controlled spatial TMD distributions and applied to three preclinical models: spinal cord injury (SCI; geometry change, uniform TMD), PI3K overactivation (geometry and TMD increase), and BCL3 deletion (geometry and TMD partially decoupled)."

Results: In synthetic datasets, pMOA was invariant to spatial TMD heterogeneity, whereas pMOI diverged between peripheral and central mineral distributions. In SCI, TMD was unchanged, and pMOA and pMOI decreased similarly (−42% and −40%; $p<0.001$). In PI3K, Ct.Ar and TMD increased (65% and 6%), with larger increases in pMOI than pMOA (79% vs 69%; $p<0.001$). In BCL3 deletion, mean TMD did not differ, and pMOA showed only a non-significant trend ($p=0.058$), while pMOI was significantly increased ($p=0.039$), indicating sensitivity to density redistribution not captured by geometry.

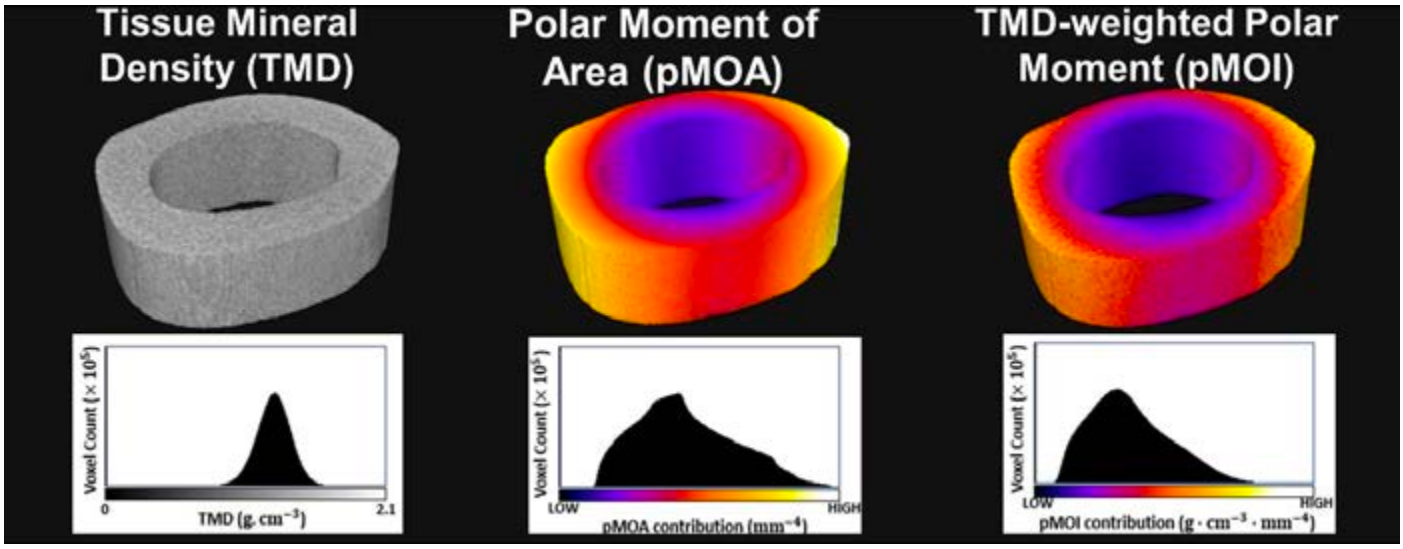

Figure 1. Graphical abstract illustrating the distinction between geometric pMOA (binary-weighted) and TMD-weighted pMOI (pixel-wise density-weighted) and their convergence or divergence depending on mineral distribution.

PO-11 Jonathan Williams, EngD

Quantifying trabecular bone through simulated assembly: The Trabecular bone Assembly index (Tb.AI)

Jonathan A. Williamsa
aDepartment of Biomedical Engineering, Wolfson Building, University of Strathclyde, Glasgow, G4 0NW, UK
*presenting and corresponding author

Purpose: Trabecular bone reflects the dynamic (im)balance between formation and resorption. Conventional morphometric parameters such as trabecular thickness (Tb.Th), separation (Tb.Sp), and connectivity density (Conn.D) provide valuable insights into bone microarchitecture but provide limited insight into the coordinated spatial organisation of the trabecular network. Here, I introduce the Trabecular Bone Assembly Index (Tb.AI), a process-based metric that simulates bone formation (or resorption) as a voxel-wise assembly (or disassembly) process. Tb.AI quantifies the number of discrete steps required to reconstruct the network. It offers a dynamic, spatially resolved measure of organisational complexity from microCT data.

Materials and Methods: Tb.AI begins from the skeletonised network (1-voxel-thick topology-preserved medial axis). Using iterative 3D flood-fill propagation (6-connectivity), each bone voxel is assigned an integer assembly step reflecting its order of incorporation during outward growth. This step value represents how early or late that voxel is “assembled” as the structure grows outward. The mean assembly step defines the global index. The algorithm was validated using synthetic binary datasets with analytically predictable assembly behaviour, confirming expected scaling with geometry and connectivity. Tb.AI exhibits distinct and predictable behaviour for canonical rod-, plate-, and fractal-like geometries (Figure 1E). Tb.AI is implemented within BoneJ and will be released in an upcoming update, providing immediate accessibility to the ISBM community. The method is here applied to microCT datasets of distal femoral metaphyseal trabecular bone from adult male Sprague–Dawley rats (SHAM and spinal cord injury-induced osteoporosis (SCI), n=8/group). Outputs include voxel-wise assembly maps and cumulative growth curves describing stepwise structural integration. Conventional morphometric parameters were computed for comparison (Figure 1A).

Results: Tb.AI significantly differentiated SHAM and SCI trabecular bone ($p<0.01$), with SHAM exhibiting higher mean assembly steps (Figure 1C). Colour-coded 3D maps revealed coordinated radial integration in SHAM bone, whereas SCI samples showed heterogeneous and truncated propagation. Growth curves demonstrated reduced assembly efficiency in SCI (Figure 1B). Tb.AI correlated with Tb.Th ($r=0.90$, $p<0.01$) yet captured network-level organisation beyond local thickness measures (Figure 1D).

Conclusions: Tb.AI is a validated morphometric/topologic parameter implemented in BoneJ that quantifies and visualises trabecular organisation through simulated structural assembly. It complements established microCT metrics by integrating hierarchical connectivity and spatial organisation within a reproducible, open-source workflow.

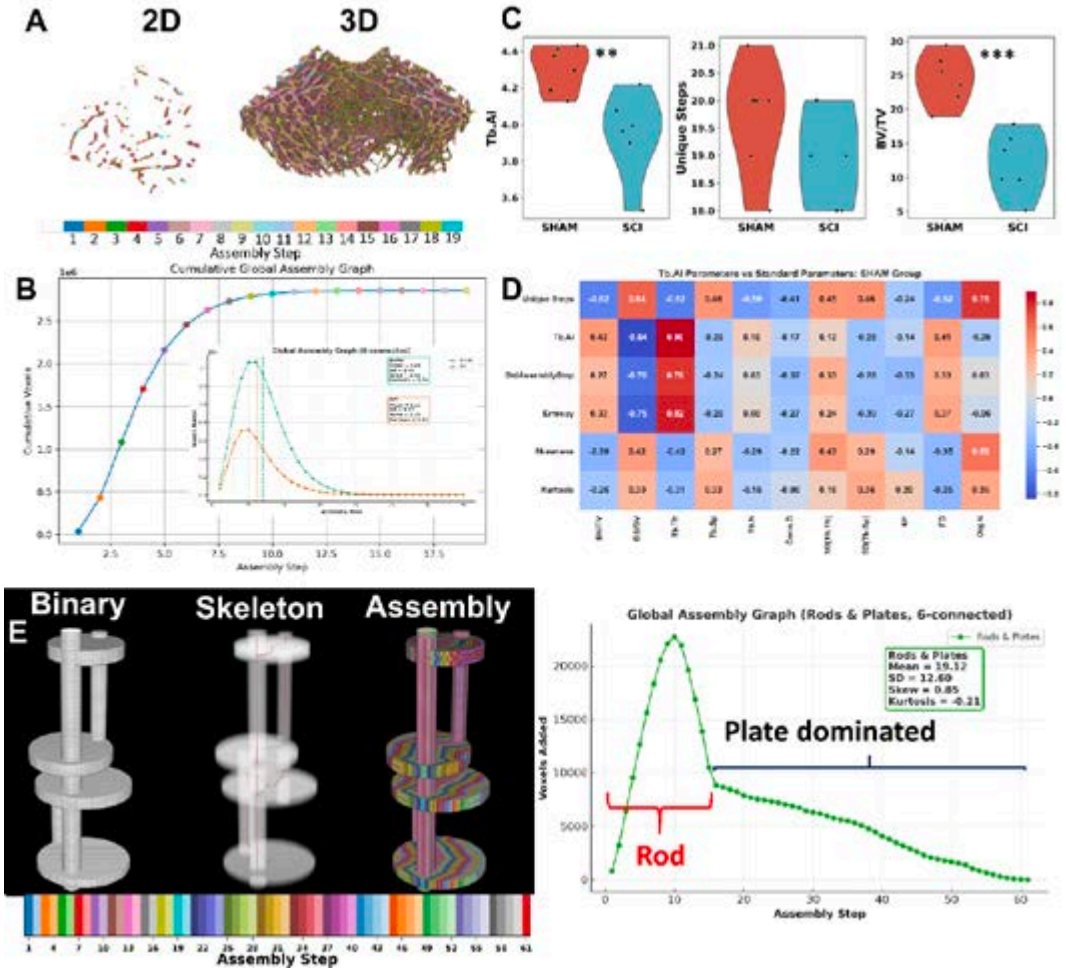

Figure 1. An introduction to trabecular bone assembly index (Tb.AI). A) Representative 2D and 3D trabecular Tb.AI maps showing voxel-wise assembly step assignment, with each discrete assembly step displayed as a distinct colour. B) Representative global assembly curves shown in cumulative and stepwise forms, derived from voxel-wise assembly progression. C) Violin plots comparing SHAM and SCI group metaphyseal trabecular bone for Tb.AI, number of unique assembly steps, and BV/TV. Statistical significance indicated by asterisks. D) Correlation heatmap (SHAM group) of Pearson coefficients between Tb.AI-derived parameters and standard trabecular morphometric measures. Cell values indicate the strength and direction of correlation. Synthetic composite geometry containing rod-and plate-dominated regions. Binary structure, skeleton, and voxel-wise Tb.AI assembly map are shown (each colour representing a discrete assembly step). The corresponding instantaneous global assembly graph (voxels added per step) demonstrates separable rod- and plate-dominated growth regimes."

PO-12 Maja Østergaard, PhD

Quantifying the lacuna-canalicular network in bone using high-resolution synchrotron X-ray imaging

Maja Østergaard,1 Anastasiia Sadetskaia,1 Lucie Burc,1 Nina K. Langdal,1 Manuel Guizar-Sicairos,2,3 Alexandra Pacureanu,4 Tanja T. Sikjær,5,6 Lars Rejnmark,5 Henrik Birkedal1
1: Dept. of Chemistry and iNANO, Aarhus University, Aarhus, Denmark
2: Center for Photon Science, Paul Scherrer Institute, Villigen, Switzerland
3: Institute of Physics, École Polytechnique Fédérale de Lausanne (EPFL), Lausanne, Switzerland
4: ESRF, The European Synchrotron, Grenoble, France
5: Dept. of Endocrinology and Internal Medicine, Aarhus University Hospital, Aarhus, Denmark 6: Dept. of Clinical Medicine, Aarhus University, Aarhus, Denmark

Bone is replete with both blood vessels and cells, the latter being situated in lacunae and interconnected by canaliculi only a few hundred nm in diameter. The cells play a vital role in bone health, as they are thought to be the orchestrators of the remodeling process. Thus, accurate characterization of the 3D morphology of the osteocyte lacunae and their signaling interconnections is crucial when investigating osteocyte function. It remains challenging, however, since the lacuno-canalicular network (LCN) is situated deeply within the mineralized bone matrix. With the emergence of fourth-generation synchrotrons, high-resolution synchrotron X-ray imaging, like nano-CT and ptychography, that allows for 3D investigations at resolutions sufficient to visualize even canalicular structure, will be more readily available.

Mapping and quantifying the morphology of the LCN is very important for understanding the network1 and how it forms2. But also to gain more insights into the canalicular fluid flow, since it has been shown that the LCN design strongly influences fluid flow in osteons1,2.

We investigated the LCN in human iliac crest biopsy samples from hypoparathyroidism patients treated with PTH(1-84) for 6 months. PTH treatment leads to renewed bone formation, hence we captured lacunae and their protruding canaliculi in regions of different stages of bone mineralization. Control samples were also studied. Nano-CT was performed in a holotomographical manner1 using a 50 nm isotropic voxel size at the ID16A beamline at the European Synchrotron Radiation Facility. Ptychography was conducted at the cSAXS beamline at the Swiss Light Source resulting in 3D resolutions of 55-112 nm as determined by Fourier shell correlation.

PO-12 Maja Østergaard, PhD

We quantify the LCN in human bone based on high-resolution synchrotron X-ray imaging and observe canaliculi that are strongly heterogenous in shape, see figure 1. This is the case at already recognized canalicular features such as the funnel-shaped openings toward the lacunar spaces or the enlarged junctions at places where several canaliculi cross1. Additionally, we also observe a heterogenous channel diameter along the canaliculi – a new and important finding that could influence future LCN fluid flow investigations.

1. NK. Wittig, et al. ACS Nano 13 (2019) 6421-6430. doi: 10.1021/acsnano.8b08478
2. S. Anuth et al. Materials Today Bio 37 (2026) 102813. doi:10.1016/j.mtbio.2026.102813.
3. AF. van Tol, et al. Biomech Model Mechanobiol 19, 823–840 (2020). doi: 10.1007/s10237-019-01250-1

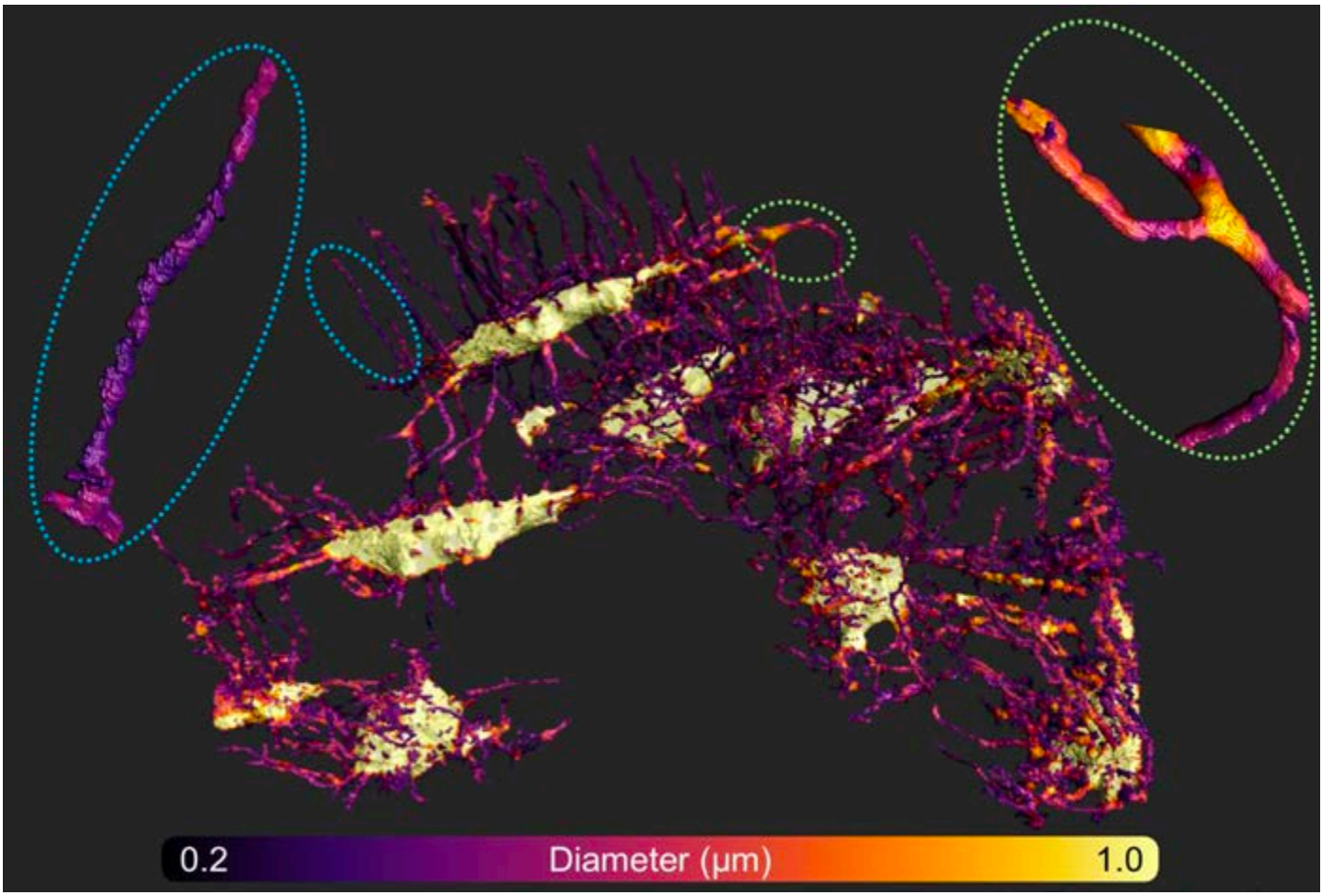

Figure 1: 3D rendering of a few lacunae and their associated canaliculi all colored by diameter. Two very different canaliculi are inserted as zoom-ins to illustrate the varying channel diameter along the canaliculi.

PO-13 Jose Ignacio Aguirre, PhD

Differential tissue distribution of glyphosate: evidence of high skeletal affinity in sprague-dawley rates following a short-term exposure

TL Frota Gomes1, CJ Cruz1, DK Goodger1, KJ Kroll1,2 SE Bisesi1,2, ND Denslow1,2, JI Aguirre1*
1Department of Physiological Sciences, University of Florida (UF), Gainesville, FL.
2The Center for Environmental and Human Toxicology, University of Florida (UF), Gainesville, FL.
*Presenting author

Introduction: Glyphosate (GLY), the world's most widely used herbicide, particularly in North and South America and Asia, is a ubiquitous contaminant of freshwater and food supplies linked to various adverse health outcomes, including cancer. Although GLY is generally cleared rapidly by the kidneys, emerging evidence indicates a high affinity for hydroxyapatite, suggesting that the skeleton may act as a long-term reservoir. This study investigated: (1) the presence and distribution of GLY in bone and other tissues, and (2) its short-term effects on BMD and mechanical properties.

Methods: Sprague-Dawley rats (n=8/group) were administered glyphosate (GLY) via drinking water for 2 weeks at the WHO/FAO Acceptable Daily Intake (ADI; 1.0 mg/kg bw/day), a 100-fold ADI dose representing very high agricultural residue levels (100 mg/kg bw/day), or a no-added-GLY control. After euthanasia, GLY concentrations in organs, serum, and bone (tibia and lumbar vertebrae [LV]) were quantified by ELISA, with bone levels further validated by liquid chromatography-tandem mass spectrometry (LC-MS/MS). Bone health was assessed via peripheral quantitative computed tomography (pQCT) for bone mineral density (BMD) and biomechanical testing for strength.

Results: Two-way ANOVA showed that GLY accumulation differed significantly by dose ($P<0.0001$) and tissue ($P<0.0001$), with a significant dose×tissue interaction ($P<0.0001$). At the ADI×100 dose, GLY levels were markedly elevated compared to both VEH and ADI rat groups in the kidney, LV, tibia, serum, and brain (all $P<0.0001$), and in the liver ($P<0.05$). No differences were observed between the ADI and VEH groups. The VEH:ADI: ADI×100 GLY level ratios were: kidney 1:1.8:190; vertebra 1:1.2:35; tibia 1:1:32; serum 1:0.98:15; liver 1:1.8:9.4; brain 1:1.5:16, with the overall concentration hierarchy: kidney > vertebra > tibia > serum > liver > brain. Comparable GLY levels were corroborated in femurs by LC MS/MS across the 3 groups. Despite substantial skeletal accumulation at the ADI×100 dose, no significant changes were detected in pQCT parameters or femoral mechanical properties over 2 weeks.

Conclusion: Short-term exposure to GLY at 100× the ADI dose induces pronounced accumulation in kidney, bone, serum, and brain, and confirms that GLY can cross the blood–brain barrier at high levels. This very high dose is relevant since extreme residue levels (up to 100 mg/kg) have been reported in genetically modified soy crops in South America, representing a plausible high-exposure scenario in intensive agricultural regions. Moreover, elevated concentrations in tibia and LV after a short, high-dose exposure support the role of bone as a reservoir for GLY and suggest that skeletal stores may be mobilized during bone remodeling, potentially sustaining circulating GLY levels and prolonging exposure of organs and tissues even after external intake has ceased.

PO-14 Cindy Cruz, MSc

Necroptosis Is the Dominant Cell Death Mechanism in Medication-Related Osteonecrosis of the Jaw (MRONJ), with Bone Necrosis Preceding Clinical Bone Exposure.

CJ Cruz1*, DG Freehill1, CM Castillo1, JF Yarrow2, EJ Castillo1, I Bhattacharyya3, DB Kimmel1, JI Aguirre1
*Presenting author
1Department of Physiological Sciences, University of Florida (UF), Gainesville, FL. 2VA Medical Center, Research Service, VAMC, Gainesville, FL. 3Department of Oral & Maxillofacial Diagnostic Sciences, College of Dentistry, UF, Gainesville, FL.

Introduction: Medication-related osteonecrosis of the jaw (MRONJ) is a serious, debilitating condition in patients taking antiresorptives like zoledronic acid (ZOL), who are affected by local risk factors such as periodontitis (PD) or tooth extraction. While the condition is defined by necrotic bone, the specific mechanisms of cellular death, particularly in osteocytes, and their timing relative to clinical onset, remain poorly understood. Given MRONJ's inflammatory nature, we hypothesized that necroptosis, a pro-inflammatory caspase-independent form of regulated cell death, rather than apoptosis, plays a key role in MRONJ pathophysiology. We aimed to identify the predominant cell death form and determine if osteocyte death precedes clinical bone exposure during the prodrome.

Methods: 108 rice rats were assigned to either a PD-inducing or PD-protective diet, then treated monthly with an oncologic dose of ZOL (80 µg/kg) or saline (VEH). This formed four groups: PD/VEH, PD/ZOL, No-PD/VEH, and No-PD/ZOL. Oral exams and in vivo MicroCT were performed every 3 weeks. Euthanasia was performed at weeks 0, 3, 6, 9, and 12 for histopathology and immunohistochemistry. Tissue markers of necroptosis (phosphorylated mixed lineage kinase domain-like protein, pMLKL) and apoptosis (cleaved caspase-3, CC3) were quantified in maxillary alveolar bone osteocytes, gingival keratinocytes, and periodontal ligament cells. For statistical analysis, we used the Kruskal–Wallis or one-way ANOVA tests to compare group differences.

Results: MRONJ developed only in PD/ZOL rats, with prevalence increasing from 25% at 6 weeks to 67% by 12 weeks. pMLKL expression in osteocytes and keratinocytes in PD/ZOL and PD/VEH rats was significantly higher than CC3 expression. More pMLKL-positive osteocytes were detected in PD/ZOL rats during the prodromal phase, well before the occurrence of overt clinical bone exposure or gingival ulceration. While necroptosis was highly expressed in PD/VEH and PD/ZOL rats, ZOL independently increased pMLKL in gingival keratinocytes in PD/ZOL and No-PD rats, suggesting that ZOL exerts a direct effect on necroptotic signaling. CC3 levels remained generally low, indicating that apoptosis plays only a minor role in this MRONJ model.

Discussion: Necroptosis is the dominant cell death mechanism driving MRONJ onset and progression. Our data suggest that osteocyte necroptosis is an early event in the MRONJ prodromal phase, directly preceding bone exposure and gingival ulceration. Our data also suggests that inflammation (PD) and ZOL synergistically enhance this pathway. Targeting necroptosis with specific pharmacological inhibitors in “At-risk” patients for MRONJ could emerge as a novel preventive strategy. This provides a critical window for cellular-level
intervention, potentially preventing underlying tissue damage that occurs before overt clinical symptoms.

The Impact of Pore Architecture on Cell Physiology during *In Vitro* Osteogenesis

M. Horrer[1], D. Zauchner[1], P. J. Lim[2], M. Rohrbach[2], C. Giunta[2], R. Müller[1], X.-H. Qin[1]

[1]ETH Zürich, Institute for Biomechanics, Zürich, Switzerland, [2] University Children's Hospital, Division of Metabolism and Children's Research Centre, Zürich, Switzerland

PURPOSE: During osteogenesis cells sense their extracellular environment which regulates their morphology, differentiation, and extracellular matrix production. Currently, *in vitro* bone models often build on animal-derived hydrogels like Matrigel. These matrices limit a mechanistic understanding over how different matrix properties influence cell physiology. Using a synthetic microporous hydrogel, we study the impact of pore architecture on cell physiology in an *in vitro* model of bone development (**Fig. 1A**).

METHODS: These microporous hydrogels [1] were formed through polymerization-induced phase separation between PEG and dextran. The PEG precursor was crosslinked via Michael addition with a matrix metalloproteinase (MMP)-sensitive crosslinker.
The pore architecture was controlled by varying the dextran concentrations (0%, 0.25% and 1%) and visualized by confocal microscopy. Pore size, porosity and pore connectivity were quantified accordingly. Human primary osteoblasts (hOB) were embedded within these hydrogels and cultivated for up to 21 days in osteogenic media. YAP subcellular localization was assessed by immunofluorescence staining and following confocal microscopy. Osteogenic differentiation was evaluated by qPCR normalized to *GAPDH*.

RESULTS: After encapsulation, cells adapted their morphology to pore architectures. After 7 days, cells in the 1% dextran hydrogels showed increased cell spreading as evidenced by confocal microscopy. Compared to the small pore group, higher viability was seen in 0.25% and 1% dextran hydrogels. On day 3, YAP was predominantly cytoplasmic across all pore sizes. Preliminary data shows increased *ALPL* and *PDPN* gene expression in smallest pores (0% dextran) after 21 days of osteogenic culture **(Fig. 1B)**, suggesting that the spatial confinement in hydrogels influences hOB osteogenic differentiation.

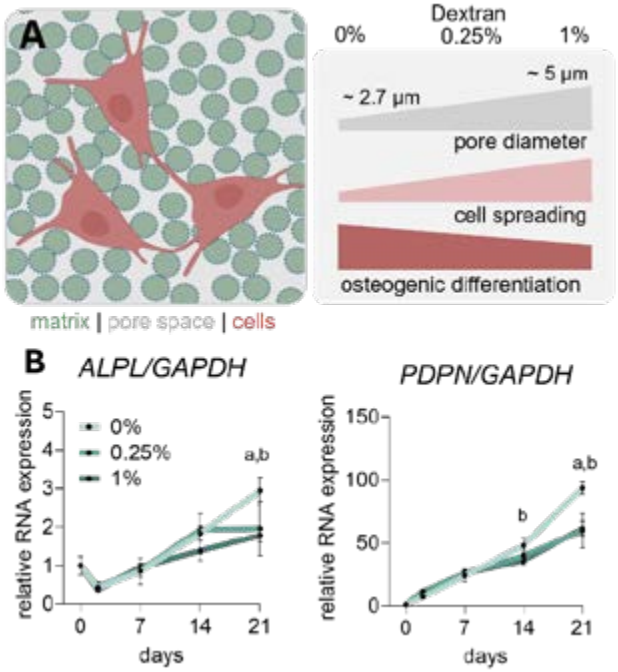

Figure 1: ***(A)*** *Schematic illustration of an embedded cell within the microporous hydrogel. Created with Biorender.com.* ***(B)*** *Relative RNA expression of ALPL and PDPN of hOBs within 21 days of osteogenic differentiation. $p < 0.05$: a) 0% vs. 0.25%, b) 0% vs. 1%.*

DISCUSSION & CONCLUSIONS: This synthetic microporous PEG hydrogel platform allows investigation of pore geometry effects on cell physiology during osteogenesis, offering new insights for bone tissue engineering and disease modeling applications.

ACKNOWLEDGEMENTS: This work was supported by the Swiss National Science Foundation (nos. 206501, 207542).

REFERENCE: [1] D. Zauchner *et al.*, *Nat. Commun.*, 2024, doi: 10.1038/s41467-024-49280-3.

P-16 Naoki Tsuji, PhD

Efferocytosis of apoptotic osteoclasts reawakens osteoblasts in functional bone organoids

Naoki Tsuji1,2, Tomoaki Sakamoto1, Haruhisa Watanabe3, Takashi Nakamura4, Kazuto Hoshi2, Tadahiro Iimura3, Atsuhiko Hikita1,2
1. Department of Clinical Stem Cell Biology, The University of Tokyo Hospital, Tokyo, Japan.
2. Department of Sensory and Motor System Medicine, Graduate School of Medicine, The University of Tokyo, Tokyo, Japan.
3. Department of Pharmacology, Hokkaido University, Faculty and Graduate School of Dental Medicine, Sapporo, Japan.
4. Oral Health Science Center, Tokyo Dental College, Tokyo, Japan

The human body generates billions of apoptotic cells each day, which are rapidly cleared by professional and non-professional phagocytes through efferocytosis to maintain tissue homeostasis. However, whether and how apoptotic osteoclasts are cleared within the bone remodeling microenvironment remains unknown, and their functional roles in bone remodeling have not been elucidated.

To analyze cell–cell interactions during the remodeling cycle which spans weeks to months, longitudinal observations of the same site are required. However, this is unattainable with conventional methods. Furthermore, intravital imaging suffers from poor vertical resolution when observing bone marrow through opaque and mineralized bone tissue. To address this limitation, we developed Functional Bone Organoids (FBOs), an in vitro system that recapitulates osteoclast-mediated resorption followed by osteoblast-driven bone formation in the same microenvironment. Primary osteoblasts isolated from CAG-EGFP mice were cultured in osteogenic medium to form mineralized bone nodules and co-cultured with bone marrow macrophages (BMMs) derived from Ctsk- or RANK-Cre; Rosa26-tdTomato mice to generate osteoclasts. By modulating culture conditions, we established distinct bone resorption and formation phases, and matrix remodeling and cellular dynamics were visualized using two-photon microscopy.

This system reproduced key structural and cellular features of bone remodeling, including dendritic connections between osteoblasts and osteocytes and site-specific bone formation within osteoclast-generated resorption pits. Using this platform, we investigated how osteoblasts sense resorption pits and what triggers their reactivation during the formation phase. We observed that osteoclasts undergo apoptosis after bone resorption and that apoptotic fragments are engulfed by osteoblasts adjacent to resorption pits. Based on this observation, we hypothesized that osteoclast-derived apoptotic bodies enhance osteoblast reactivation and functionally tested this mechanism. Consistent with this hypothesis, the addition of apoptotic bodies to quiescent osteoblast cultures induced morphological changes indicating reactivation, increased cellular motility, and enhanced bone formation, whereas inhibition of apoptosis by a pan caspase inhibitor impaired pit refilling.

Furthermore, co-culture of FBOs with DiI-labeled BMMs enabled visualization of labeled cell fragments incorporated within refilling resorption pits, highlighting active interactions during remodeling. These findings indicate that efferocytosis of apoptotic osteoclasts reactivates osteoblasts and serves as a key mechanism driving the coupling of bone resorption and formation. Together, our study reveals a previously unrecognized cellular mechanism underlying pit refilling during bone remodeling.

P-17 Peter Maye, PhD

Introducing the Rodent Open Science Skeletal Archive (ROSSA)

Peter Maye1, Brian Kelleher2, William Shostak2, Aaron Mark2, Natalie Lacroix2, Benjamin Sinder3, Je-Yong Choi4, Viktoria Bonne Kofod5, Ching-Hsin Huang5, Joel Salisbury2, Dong-Guk Shin6, Thomas L Andersen5,7, David W Rowe1
v
1. Regenerative Medicine and Skeletal Development, School of Dental Medicine, University of Connecticut Health, Farmington, CT 06030
2. Institutional Insights & Innovation (I3), University of Connecticut, Storrs, CT 06269,
3. Musculoskeletal Institute, School of Medicine, University of Connecticut Health, Farmington, CT 06030
4. Department of Biochemistry and Cell Biology, Skeletal Diseases Analysis Center, School of Medicine, Kyungpook National University, Daegu 41944, Republic of Korea
5. Molecular Bone Histology Lab (MBH), University of Southern Denmark & Odense University Hospital, 5230 Odense, Denmark
6. Computer Science & Engineering, School of Computing, University of Connecticut, Storrs, CT 06269
7. Dept. of Forensic Medicine, Aarhus University, 8200 Aarhus, Denmark

Over the last 40 years, a vast range of rodent skeletal phenotyping studies have been conducted to understand the mechanisms of human skeletal disease. To ensure that this knowledge is preserved and accessible to the broader research community, we are developing ROSSA: the Rodent Open Science Skeletal Archive (rossa.uchc.edu), an NIH-funded open-access repository for rodent skeletal phenotyping data.

ROSSA is designed as a centralized platform where researchers can both contribute their own skeletal phenotyping datasets and explore studies conducted by others. To achieve this, ROSSA features two core components: a robust data submission form and a dynamic data center offering multiple ways to view, analyze, and access archived data. As the repository grows, we anticipate it will become an essential resource for advancing our understanding of skeletal disease mechanisms.

Here we announce the completion and launch of Version 1 of our web-based data submission form, capable of capturing a wide range of experimental paradigms used in rodent skeletal research. Supported experimental approaches include genetically modified animal models, pharmacological interventions, and gonadectomy procedures, which are frequently used in combination. Alongside metadata collection, the form supports ingestion of quantitative phenotyping data generated through standard analytical techniques, including Dual-Energy X-ray Absorptiometry (DEXA), Microcomputed Tomography (μCT), Bone Histomorphometry, Mechanical Strength Testing, and biomarker assays from serum, plasma, and urine.

P-17 Peter Maye, PhD

Submitted data is preserved in its original form to ensure authenticity and is also parsed into a relational database to facilitate advanced search functionality and programmatic access via API.

Ultimately, ROSSA aims to transform how preclinical bone research is shared and utilized; enabling the construction of phenotype-associated regulatory networks and laying the groundwork for AI-driven models that will advance the diagnosis and treatment of skeletal
disease.

P-18 Keita Nagira, MD

Expansion of the Non-Osteocyte Layer of the Subchondral Bone Plate Suggests Endochondral Ossification and Is Associated with Osteoarthritis

First author: Keita Nagira, MD, PhD1
Co-author:
Hiroshi Hagino, MD, PhD1, 2, Hideki Nagashima, MD, PhD1
Affiliation:
1 Department of Orthopedic Surgery, Faculty of Medicine, Tottori University, Tottori, Japan
2 Department of Rehabilitation, Sanin Rosai Hospital, Yonago, Japan.
Presenting author: Keita Nagira

Background: In non-decalcified specimens of aged rat knees, we previously identified that the subchondral bone plate (Subcho.BP) can be divided into two distinct layers: an osteocyte-containing layer and a non-osteocyte layer. The non-osteocyte layer contains columnar arrangements of chondrocytes that appear continuous with the articular cartilage. However, how this unique structure forms during aging and how it relates to the development and progression of osteoarthritis (OA) remains unclear.

Hypothesis: Articular cartilage becomes thinner through age-related endochondral ossification, leading to expansion of the non-osteocyte layer of the Subcho.BP and contributing to the development and progression of OA.

Purpose: To clarify the mechanism of articular cartilage degeneration and thinning in OA by morphometric analysis of the osteochondral unit and to evaluate the relationship between Subcho.BP structure and radiographic sclerosis.

Methods: Non-decalcified histological specimens of the knee joint were prepared from Sprague–Dawley rats aged 1.5–18 months. The thickness of the articular cartilage and each layer of the Subcho.BP was quantitatively measured. Age-related changes were analyzed separately during the growth phase (1.5–6 months) and the aging phase (6–18 months). Correlations between Subcho.BP thickness and radiographic sclerosis were evaluated. Cartilage morphometry, angiogenesis, and bone morphometry of the subchondral regions were also analyzed.

Results: During the growth phase (1.5–6 months), both the osteocyte layer and the non-osteocyte layer of the Subcho.BP gradually increased in thickness. During the aging phase (6–18 months), articular cartilage thickness decreased while the Subcho.BP expanded. This expansion was mainly due to thickening of the osteocyte layer; however, the non-osteocyte layer also expanded, accompanied by osteocyte apoptosis, progression of chondrocyte differentiation, suppression of cartilage hypertrophy signaling, and increased angiogenesis. Radiographic sclerosis showed a positive correlation with Subcho.BP thickness, with a particularly strong correlation with the thickness of the non-osteocyte layer (r = 0.765). These findings suggest that endochondral ossification of articular cartilage accompanied by angiogenesis may occur within the osteochondral unit during aging.

Conclusion: Age-related endochondral ossification of articular cartilage leads to expansion of the non-osteocyte layer of the Subcho.BP. This structural change is strongly associated with radiographic sclerosis and may contribute to the development and progression of OA.

Fig. Effects of aging on osteocytes, chondrocyte, and microstructure of osteochondral unit in the rat knee joint

Fig. Effects of aging on osteocytes, chondrocyte, and microstructure of osteochondral unit in the rat knee joint

Rats' Knee	Growth (1.5~6M)	Aging (6~18M)
Osteocyte density in Subcho.BP	↓	↓
Chondrocyte density in SL	↓	↓
Chondrocyte density in ML	↓	↓
Chondrocyte density in DL	→	↑
HC area	↓	↓
HC lacuna area	↓	↓
Area ratio of HC / HC lacuna	↓	→
Angiogenesis number	-	↑
AC Th	↓	↓
Non-osteocyte layer Th in Subcho.BP	↑	↑
Osteocyte layer Th in Subcho.BP	↑	↑

Abbreviations:
SL, superficial layer; ML, middle layer; DL, deep layer; HC, hypertrophic chondrocyte; AC, articular cartilage; Th, thickness; Subcho.BP, subchondral bone plate; OA, osteoarthritis; OCU, osteochondral unit

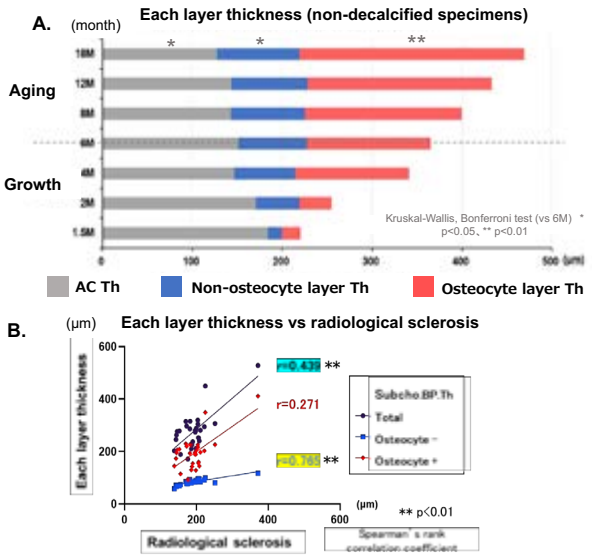

A. The expansion of the non-osteocytic layer associated with endochondral ossification of the AC resulted from osteocyte apoptosis, progression of chondrocyte differentiation, suppression of hypertrophy, and increased angiogenesis in OCU.
B. Strong correlation with non-osteocyte layer Th and radiological sclerosis in OA.

P-19 Claire Acevedo, PhD

From Collagen denaturation to mineral disorganization in dentinogenesis imperfecta

“Shangaya Touraivane1,6, Margot Riou2,3,4, William Woolley6, Muriel de la Dure-Molla2,3,5, Benjamin Fournier2,4,5, Elsa Vennat1, and Claire Acevedo6.
1: Université Paris-Saclay, CentraleSupélec, ENS Paris-Saclay, CNRS, LMPS - Laboratoire de Mécanique Paris-Saclay, 91190, Gif-sur-Yvette, France
2: Université Paris-Cité, Faculté d’Ondotologie, Paris, 75006, France
3: Hôpital Rothschild, Centre de Références des Maladies Rares Orales et Dentaires, Paris, 75013, France
4: INSERM, UMR1333, Oral Health, RHOC Team, Montrouge, 92120,
France 5: Institut Imagine, Bases moléculaires et physiopathologiques des ostéochondrodysplasies, Paris, 75015, France
6: Department of Mechanical and Aerospace Engineering, University of California San Diego, CA 92093, La Jolla, USA

Purpose: Dentinogenesis Imperfecta (DI) associated with Osteogenesis Imperfecta results from variants in COL1A1 or COL1A2 genes and leads to severe dentin fragility. Although collagen mutations are known to affect dentin structure, the mechanisms linking collagen alterations to defects in mineral organization and the tubular network remain poorly understood. This study investigated the relationship between collagen integrity, mineral organization, and dentin microstructure in DI associated with a COL1A2 variant.

Materials and Methods: Four primary teeth from a patient carrying a COL1A2 variant (c.982G>A; p.Gly328Ser - DI group) and eight primary teeth from healthy donors (Control or C group) were analyzed. Collagen denaturation was quantified using trypsin–hydroxyproline assays. Collagen organization was assessed by Second Harmonic Generation (SHG) microscopy. Mineral distribution and density were measured using high-resolution micro-computed tomography (HR micro-CT). The tubular network was characterized in three dimensions using confocal microscopy. The exact sequence of sample preparation and experiments is detailed in Fig. 1.

Results: DI dentin exhibited a threefold increase in denatured collagen compared with controls. SHG imaging revealed pronounced spatial heterogeneities in the collagen scaffold, including localized regions with strongly reduced signal. These regions were associated with mineral disorganization and hypermineralized structures visible in HR micro-CT. Overall mineral density was increased by approximately 30% in DI samples. Confocal imaging further showed extensive occlusion of the tubular network, with reduced porosity and increased numbers of occluded tubules.

Conclusions: This multimodal analysis suggests that collagen denaturation associated with this COL1A2 variant disrupts the collagen scaffold, promoting abnormal mineral deposition and progressive occlusion of the dentinal tubular network. These findings provide new insight into the multiscale structural alterations underlying DI and highlight the value of combining biochemical assays with complementary 3D imaging techniques to investigate mineralized tissue disorders.

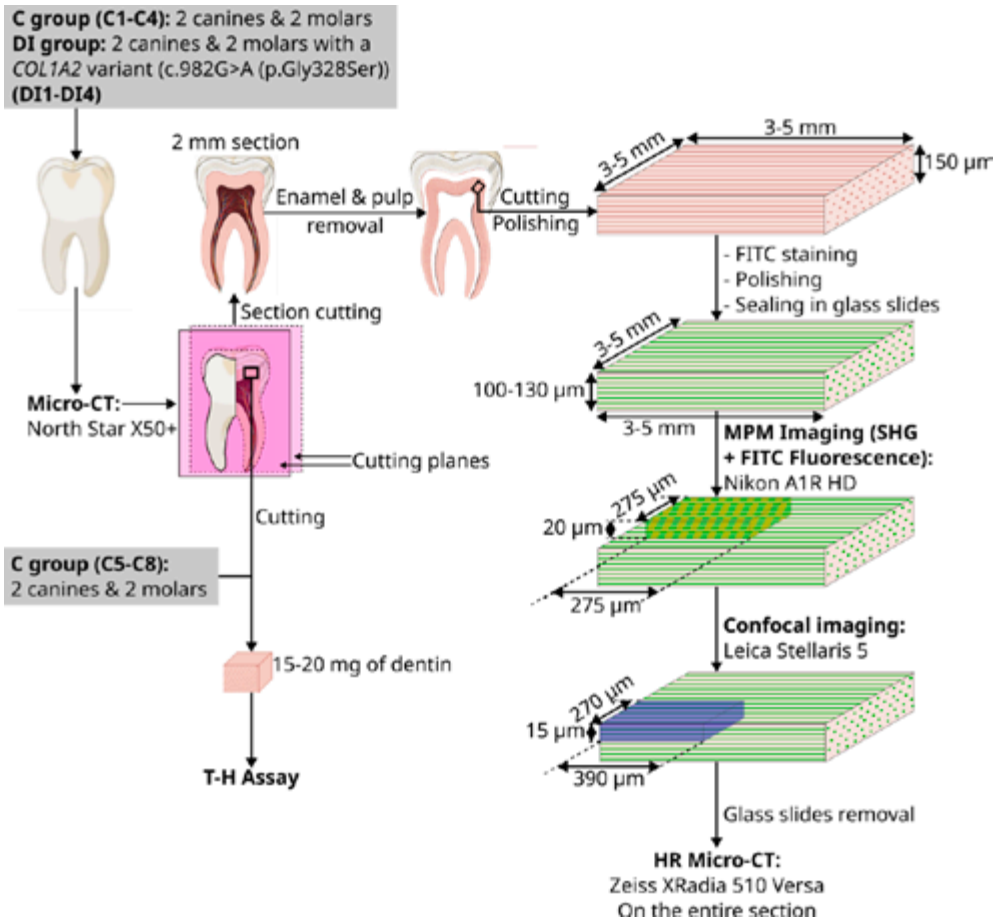

Fig. 1: Sequence of samples preparation and experiments. Samples from both groups were cut into sections sealed in glass slides to perform multi-photon microscopy (MPM) to collect both the second harmonic generation (SHG) signal from the organic matrix and the FITC fluorescence from porosities. Then confocal imaging was performed at a higher resolution to quantify the porous network of samples. Sections were then removed from the glass slides to perform high-resolution micro-computed tomography (HR Micro-CT) on the totality of the sections. Trypsin-hydroxyproline assays (T-H assays) were performed on 15-20 mg fragments of mid-crown dentin sampled independently from the sections for 3D imaging.

P-20 Fatma Younis, BSc

Bone Remodeling Dynamics Within Individual Glucocorticoid-Treated Basic Multicellular Units

Authors: Fatma Younis. Lindsay Loundagin. Kimberly Harrison. David Cooper.

Basic multicellular units (BMU) are temporary structures responsible for continuous renewal and adaptation of the skeleton. They consist of coordinated teams of bone cells—osteoclasts resorbing old bone, and osteoblasts following behind forming new bone. Glucocorticoids (GCs) are steroid hormones widely prescribed to treat inflammation, autoimmune diseases, and cancer. Long term use of GCs disrupts bone remodeling at the level of the BMU by inhibiting osteoblast activity and altering osteoclast behavior, resulting in Glucocorticoid-induced osteoporosis (GIOP), the most common form of secondary osteoporosis. Previous research in our lab demonstrated that GC-treated rabbit BMUs exhibited a 90% reduction in the speed at which they move forward (Linear Erosion Rate; LER) compared to controls. This arrested progression was accompanied by radial expansion of the resorption space rather than the longitudinal progression observed in normal BMUs. This raised the question whether the volume of bone resorbed within individual GC-affected BMUs exceeds that of control BMUs, contributing to increased bone porosity, or whether additional factors were involved in the development of GIOP. We tested the hypothesis that administering GCs uncouples the BMU with increased resorption and decreased formation compared to controls.

Investigated in this study were control and GC-treated rabbits from a larger project in which they received a daily subcutaneous injection of either 0.9% saline or 1.5mg/kg of methylprednisolone sodium succinate, respectively, for 29 days. The distal right tibia of each rabbit was imaged in vivo at the Biomedical Imaging and Therapy beamline at the Canadian Light Source using in-line phase-contrast micro-CT on day 15 and ex vivo after the trial using a SkyScan desktop micro-CT. The scans were co-registered to longitudinally track the LER of individual BMUs and to identify localized resorption and formation volumes within them.

Contrary to our prediction, both mean resorption and formation volumes within individual BMUs were significantly higher in controls compared to in GC-treated animals (resorption: 0.00548 mm3 vs. 0.00355 mm3; formation: 0.00730 mm3 vs. 0.00185 mm3; $p < 0.001$ for both). However, GC-treated BMUs exhibited a marked shift toward net resorption, reflected by a 2.5-fold increase in the ratio of overall mean resorption-to-formation (control: 0.7511; GC: 1.9150). Thus, the effect of GCs at the level of individual BMUs was more nuanced than we hypothesized. A closer look revealed GC-treated BMUs exhibited a great deal of variation in morphology as well as the balance between formation and resorption. The mechanisms underpinning this variation are unclear and warrant further research.v

P-21 Shahak Kuba, MSc

Geometric and mechanical regulation of osteoblast-osteocyte differentiation

Shahak Kuba 1,2 *, Alexandra Tits 2,3, Tarang Janawalkar 1, Richard Weinkamer 2,3, Pascal Buenzli 1,2
1 School of Mathematical Sciences, Queensland University of Technology (QUT), Brisbane, Queensland, Australia
2 Max Planck Queensland Centre for the Materials Science of Extracellular Matrices, Brisbane and Potsdam
3 Department of Biomaterials, Max Planck Institute of Colloids and Interfaces, Potsdam, Germany
* Presenting author

Purpose: Bone formation during cortical pore filling is regulated by mechanics and pore geometry, but it remains challenging to understand how these regulations operate at cellular level. During bone formation, a subset of osteoblasts differentiates into osteocytes, which become embedded in the matrix to form the osteocyte network. We seek to understand how the osteocyte network in bone may provide records of the geometric and mechanical regulation of osteoblasts during bone formation, by comparing numerical simulations of a mathematical model of osteoblast-osteocyte differentiation and experimental analyses of osteocyte positions in osteons.

Materials and methods: We developed a two-dimensional, single-cell-resolution computational model of bone formation incorporating mechanical cell interactions of osteoblasts, bone matrix secretion, and stochastic osteoblast embedment and apoptosis (Figure 1). Various dependences of the embedment rate with the local curvature of the bone surface and the mechanical state of osteoblast can be simulated to understand how these parameters are recorded in osteocyte network imprints. The model tracks osteocyte positions as they form and become embedded within the simulated bone matrix, enabling quantitative comparison with osteon images at cellular resolution.

To analyse experimental data of osteocyte positions in osteons, we reconstructed pseudo-lamellar formation surfaces between the cement line and Haversian canal using a level-set framework. These reconstructions were integrated with three-dimensional confocal scans of human osteons and lacunar spatial data extracted using custom software (TINA [1]) to estimate dynamic osteoblast embedment rates from static experimental data.

P-21 Shahak Kuba, MSc

Geometric and mechanical regulation of osteoblast-osteocyte differentiation

Results: The model generates tissue architectures that resemble histological bone samples. Local osteocyte density is regulated by varying the stochastic embedment probability of osteoblasts Incorporating embedment rates estimated from confocal reconstructions improves agreement between simulated tissue and two-dimensional projections of experimental scans. However, stochastic embedment introduces structural asymmetries between realizations, highlighting the role of probabilistic cell fate decisions in shaping osteonal microstructure.

Conclusions: Our single-cell mathematical model links geometry, mechanics, and stochastic differentiation to osteocyte density and osteonal structure. Integrating surface reconstruction in experimental images with mechanistic modeling provides us with a quantitative basis for developing geometry- and stress-dependent differentiation laws during bone formation.

[1] Repp, F., Kollmannsberger, …, Wagermaier, W. and Weinkamer, R., 2017, Bone Reports 6, 101

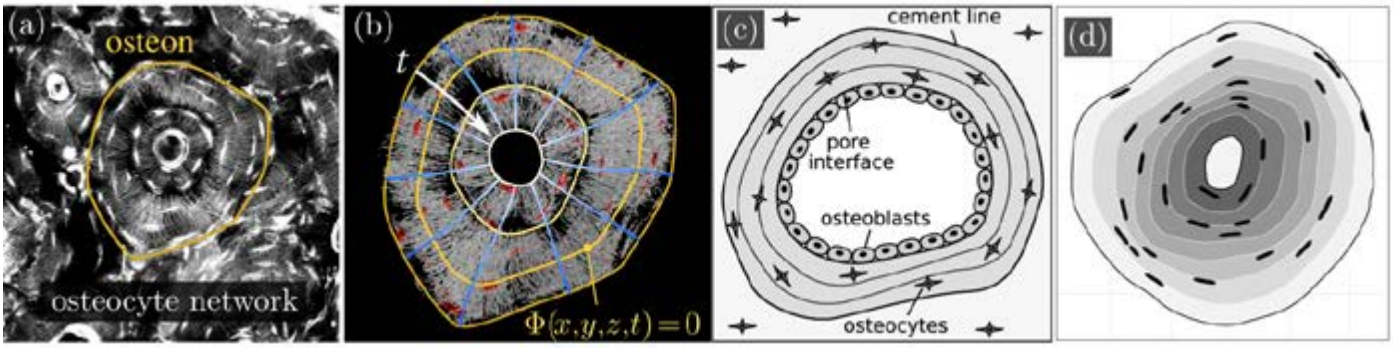

Figure 1: (a) Confocal image of a human osteon with the cement line (orange) and osteocyte lacunae visible. (b) Top-view reconstruction of pseudo-lamellar formation surfaces (yellow) using a level-set description of the pore interface. (c) Schematic of the single-cell computational model showing osteoblasts at the pore interface and embedded osteocytes within the matrix. (d) Example simulated tissue architecture generated by the model.

P-22 Ashlyn Soule, MSc

Site specific and sex dependent effects of minocycline and docycycline on craniofacial and appendicular bone maturation in C57BL/6 mice

Ashlyn Soule1*, Matthew D. Carson1, Chad M. Novince1, J. Ignacio Aguirre2, Caroline Westwater1
1Dept. of Biomedical and Community Health Sciences, College of Dental Medicine, Medical University of South Carolina, Charleston, South Carolina, USA; 2Dept. of Physiological Sciences, College of Veterinary Medicine, University of Florida, Gainesville, Florida, USA.
*Presenting Author.

Purpose: Tetracycline-class antibiotics (TCs) are frequently prescribed during adolescent skeletal maturation, yet their long-term, site-specific effects on bone structure remain poorly understood. We used high-resolution micro-CT to quantify the effects of minocycline (MINO) and doxycycline (DOX) on craniofacial and appendicular skeletal development across sexes, ages, and treatment durations.
Materials and Methods: Sex-matched C57BL/6 mice received MINO or DOX (100 mg/L) via drinking water during the pubertal (6–12 weeks of age) or extended pubertal/post-pubertal phase (6–18 weeks of age). Subgroups were euthanized for tissue collection at 12, 18, or 48 weeks of age (n=5–10/group). Micro-CT scans were acquired at a 6 μm voxel size (55 kVp, 145 μA) to assess the maxilla (cementoenamel-junction to alveolar bone crest (CEJ–ABC) distance and alveolar BV/TV) and the femur (trabecular and cortical parameters). BMD was calibrated to hydroxyapatite phantoms, and groups were compared via two-tailed t-tests.

Results: Following 6 weeks of treatment, both MINO and DOX significantly increased CEJ–ABC distance and reduced alveolar BV/TV across all roots in both sexes; in MINO-treated females, these deficits persisted through 48 weeks. Appendicular responses were sexually dimorphic and drug-specific: at 18 weeks, DOX-treated females exhibited increased trabecular BV/TV and cortical thickness, whereas males showed reductions in these parameters. MINO induced early trabecular loss in both sexes. Long-term evaluation revealed that MINO-induced femoral bone loss remained in females at 48 weeks, whereas further bone loss was arrested in males following the treatment phase.

Conclusions: TCs induce site-specific, sex-dependent skeletal responses dictated by the state of skeletal maturation. The maxilla is the most sensitive site, exhibiting rapid bone loss likely due to its high remodeling rate. Appendicular phenotypes diverge by drug and sex: MINO induces persistent deficits in females, while DOX appears to promote a “”bone-maintenance”” phenotype. These findings suggest that TC-induced shifts in bone volume reflect interference with sex-specific remodeling baselines, emphasizing the need for longitudinal, site-specific analysis when evaluating pharmacologic impacts on the skeleton.

P-22 Ashlyn Soule, MSc

Acknowledgements: We thank Dr. Jessica Hathaway-Schrader for her valuable guidance in micro-CT analysis techniques.

Sources of Support: NIH/NIAMS R01AR081488; NIH/NIDCR T32DE017551”

P-23 Josefin Ewerman, MSc

Correlative EDX And Vibrational Spectroscopy: Toward More Realistic Measurements of Bone Mineral Elemental Composition

“J. Ewerman1*, F.B.G. Zambardino1, H. Ben Amara1, A. Palmquist1, F.A. Shah1
1Department of Biomaterials, Sahlgrenska Academy, University of Gothenburg, Sweden,
*Presenting author

The elemental composition of bone mineral is a heavily debated subject, and it is often incorrectly labelled as “hydroxy(l)apatite” (HAp) [1]. This mislabelling oversimplifies the chemistry of the mineral as it ignores expected ion substitutions, such as carbonate occupying phosphate sites in the apatite crystal lattice (B-type substitution) [2]. Additionally, it places preconceptions on commonly used metrics, e.g., that the calcium to phosphorous ratio (Ca/P) should be ~1.67 in mature bone. Bone mineral is better described as an ion substituted carbonated apatite. We present a simple approach toward more realistic measurements of bone mineral elemental composition by accounting for ion site substitutions [3]. Bovine bone slices were commercially sourced (https://boneslices.com) and systematically deproteinised using 5 % NaOCl at 4 °C for up to 168 h. EDX was used for elemental analysis. Raman spectroscopy was used to monitor deproteinisation. Phosphorous correction was done by accounting for B-type substitution using Raman spectroscopy (1070/960 cm-1) and Fourier transform infrared spectroscopy (FTIR; 872/1020 cm-1 and 1412/1020 cm-1). Backscattered electron scanning electron microscopy (BSE-SEM) was used for imaging. One-way analysis of variance (ANOVA) with post hoc Bonferroni correction was used for statistical analysis of CARs between 0 h, 96 h, and 168 h.

Raman spectroscopy shows a gradual decrease in organic matrix (amide III) in relation to mineral content (v2PO 3-) (Fig. 1A), going from undeproteinised to completely deproteinised after 168 h of NaOCl exposure, further validated by increasing atomic number (Z) contrast on BSE-SEM (Fig. 1C), and decreasing organic matrix content based on inverse mineral-to-matrix ratio (1/MMR) (Fig. 1D-E). EDX reveals that the CARs (Ca/P, Ca+Mg+Na/P) increase from 0 h to 96 h and 168 h ($p < 0.0001$, $p < 0.0001$), and from 96 h to 168 h ($p< 0.0001$). Additionally, phosphorus correction (Pcorr) based on Raman and FTIR spectroscopy generally decreases the overall CAR values (Fig. 1D-E).

P-23 Josefin Ewerman, MSc

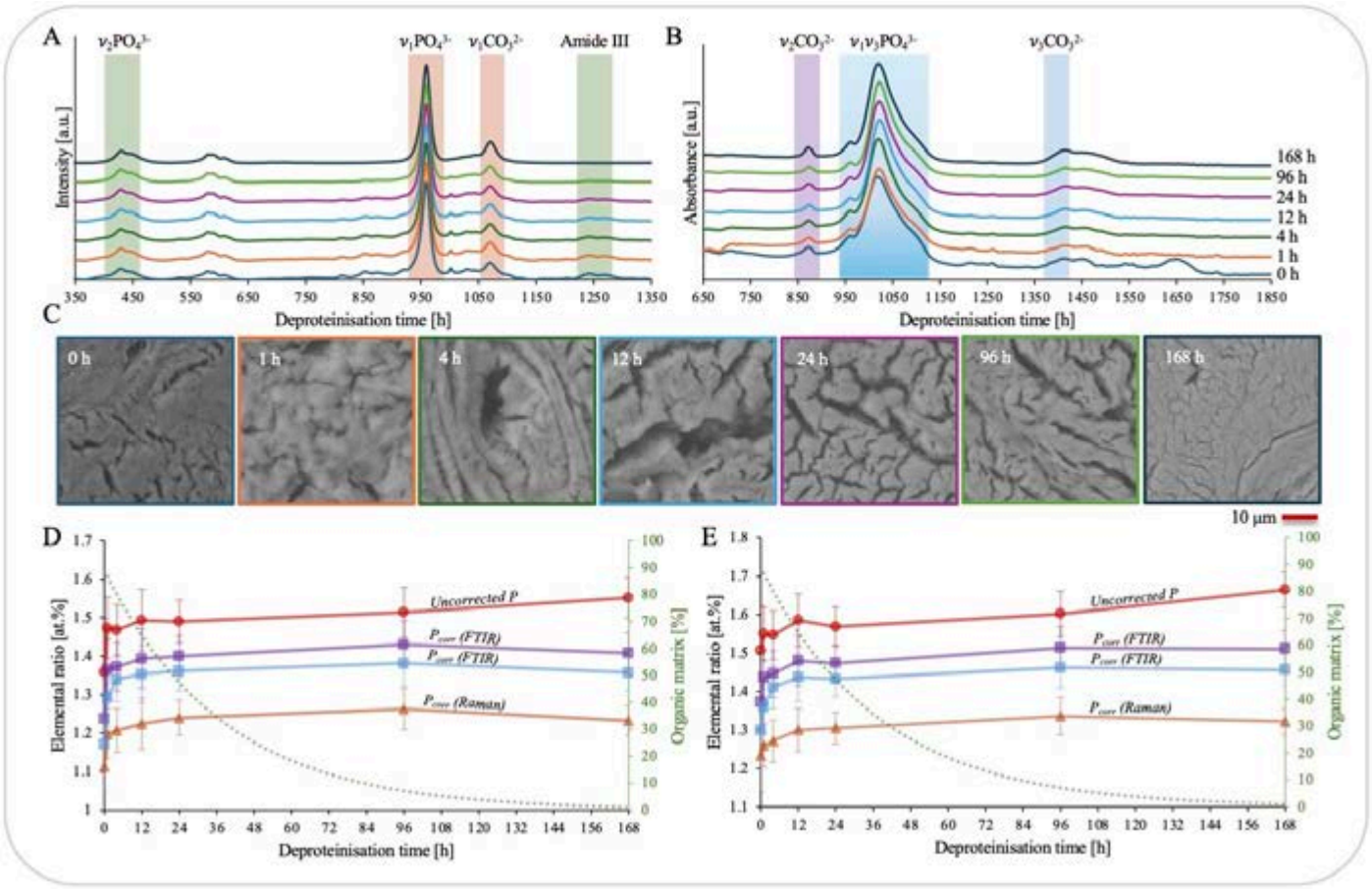

Fig.1: Average (A) Raman spectra (25 measurements per sample; n=3), and (B) FTIR spectra (9 measurements per sample; n=3). (C) BSE-SEM images, showing increased atomic number (Z) contrast from left to right. (D) Ca/P ratios and (E) Ca+Mg+Na/P ratios (mean ± SD) calculated from EDX data (25 measurements per sample; n=3). Secondary y-axes show the organic matrix content based on inverse mineral to matrix ratio (1/MMR) calculated from Raman spectroscopy data.

The increase in CAR values using uncorrected P over deproteinisation time show that they are strongly influenced by the organic matrix, making whole bone inadequate to use for bone mineral elemental composition analysis. Additionally, the decrease in CAR values using Pcorr, for both Raman and FTIR spectroscopy, underscores that uncorrected CAR values are grossly overestimated as the phosphate sites occupied by carbonate ions are ignored. In conclusion, correlative EDX and vibrational spectroscopy on completely deproteinised bone reveals a more realistic view of bone mineral composition as the influence of organic phosphorous is removed and expected ion substitutions are accounted for.

[1] Wopenka B, Pasteris JD. Mat Sci Eng C-Bio S. 2005;25.
[2] Taylor EA, Mileti CJ, Ganesan S, Kim JH, Donnelly E. Calcif Tissue Int. 2021;109.
[3] Shah FA. Acta Biomater. 2025;196.

P-24 Chao Liu, PhD

Harnessing Macrophage Mechanobiology: New Therapeutic Strategies for Bone Regeneration

Authors: Ziyan Wang, Hongzhi Liu, Chao Liu*
Affiliation: Southern University of Science and Technology
*presenting author

Macrophages have emerged as critical mediators of bone repair, integrating mechanical cues with biochemical signaling to orchestrate regeneration. Recent advances reveal two interconnected pathways underpinning this process: Piezo1, a mechanosensitive ion channel that enables macrophages to sense mechanical stimuli, and periostin, a matrix protein that macrophages deploy to regulate osteogenesis. Together, these pathways form a coordinated framework linking macrophage mechanotransduction to skeletal tissue repair. To capture these multi-system interactions with cellular precision, we employed a high-resolution 3D imaging platform that integrates multiplexed confocal and two-photon microscopy, enabling the simultaneous visualization of up to five distinct channels within thick tissue sections. This methodology provides a unique volumetric perspective alongside 3D spatial correlation analysis, which allows for the quantification of the physical proximity and alignment between pro-regenerative macrophages, type H vessels, and osteoprogenitors throughout the regeneration process. Our results indicate that Piezo1 serves as the primary mechanosensing mechanism, where mechanical loading or fluid shear stress activates calcium-dependent signaling in macrophages, driving their polarization toward an anti-inflammatory CD206+ M2 phenotype. This shift enhances type H vessel formation, a specialized vascular network that supports osteoprogenitor cell recruitment and bone mineralization. Periostin acts as a downstream effector, secreted by M2 macrophages in response to mechanical cues. Periostin stabilizes endothelial-osteoblast crosstalk, promotes matrix remodeling, and amplifies TGF-β signaling, thereby sustaining the vascularized osteogenic niche. While Piezo1 initiates the mechanoresponse, periostin propagates the pro-regenerative signaling, ensuring spatial and temporal coordination of bone formation. Disruption of either pathway impairs mechanically-induced benefits in bone regeneration: Piezo1 deletion abrogates mechanical activation of macrophages, stalling angiogenesis and osteogenesis, while periostin deficiency disrupts matrix-mediated growth factor signaling and cell-cell communication. Notably, mechanical activation primes macrophages to upregulate periostin, illustrating their interdependence. This integrated mechanism highlights macrophages as dynamic translators of mechanical forces into biochemical cues to regulate osteogenesis. By coupling immediate mechanosensing (Piezo1) with sustained matrix signaling (periostin), macrophages bridge biomechanical and immunomodulatory processes, offering novel targets to accelerate healing in fractures, osteoporosis, and critical-sized defects.

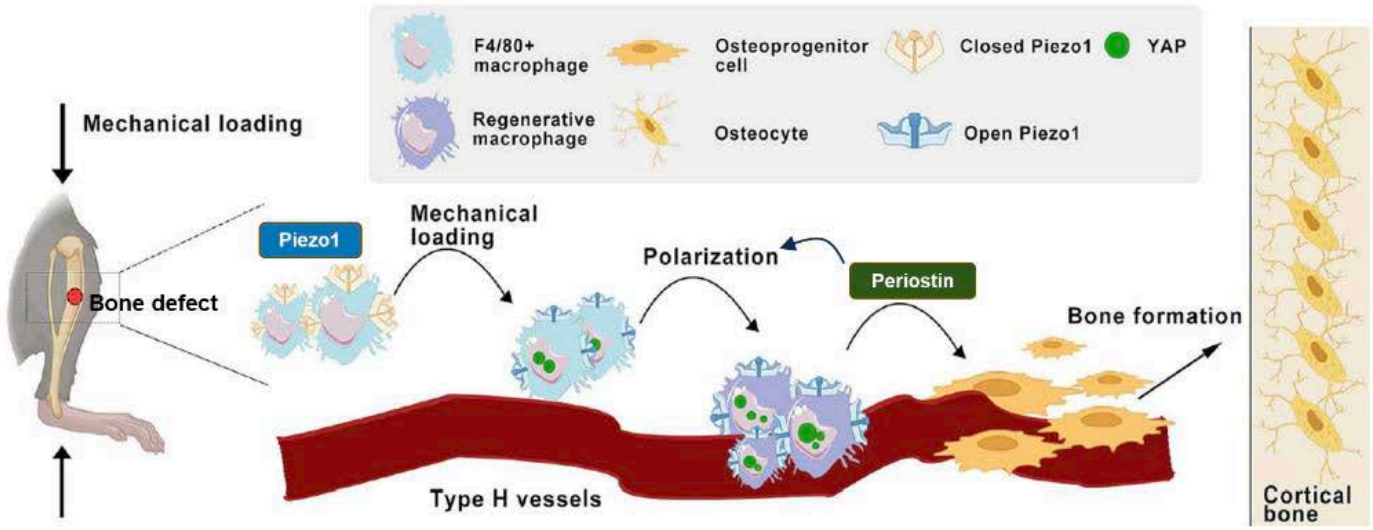

Figure 1. Piezo1 in macrophages senses mechanical stimulation, increases the expression of Periostin, promotes the differentiation of macrophages into M2 pro-regenerative subtype, regulates the coupling of blood vessels and osteogenesis, and promotes bone tissue regeneration.

P-25 Krittikan Chanpaisaeng, PhD

Evaluation of nile tilapia derived biphasic calcium phosphate scaffolds for bone regeneration in a rate calvarial defect model

Authors: Krittikan Chanpaisaeng[1], Ticomporn Luangwattanawilai2, Ruedee Hemstapat2, Amaraporn Wongrakpanich3, Narattaphol Charoenphandhu4, Atchara Khamkongkaeo5

Affiliations: [1]Department of Pharmacology and Physiology, Faculty of Pharmaceutical Sciences, Chulalongkorn University, Bangkok THAILAND; [2] Department of Pharmacology, Faculty of Science, Mahidol University, Bangkok THAILAND; 3Department of Pharmacy, Faculty of Pharmacy, Mahidol University, Bangkok, THAILAND; 4Department of Physiology, Faculty of Science, Mahidol University, Bangkok THAILAND; 5Department of Metallurgical Engineering, Faculty of Engineering, Chulalongkorn University, Bangkok THAILAND.
Presenting Author: Krittikan Chanpaisaeng

Purpose: Critical-sized bone defects resulting from trauma or pathology remain a significant clinical challenge. While autologous bone grafts are the gold standard, their use is limited by donor site morbidity and availability. This study evaluates the osteoregenerative potential of sustainable, fish-bone-derived biphasic calcium phosphate (BCP) scaffolds. By repurposing Nile tilapia (Oreochromis niloticus) aquaculture waste, we aim to develop a cost-effective bone substitute and determine the optimal ratio of hydroxyapatite (HA) to β-tricalcium phosphate (β-TCP) for accelerated healing.

Materials and Methods: Two BCP scaffold formulations derived from Nile tilapia bones were synthesized with varying HA:β-TCP ratios: BCP1 (80-90:10-20) and BCP2 (70-80:20-30). Using an internationally standardized in vivo model, two 5 mm circular non-weight-bearing defects were created in the calvaria of adult male Wistar rats (n=8, 10 weeks old). Defects were randomly assigned to one of two groups: (1) BCP1 scaffold, (2) BCP2 scaffold. Each rat will have one empty defect to serve as a negative control. Bone regeneration and scaffold integration were monitored longitudinally using non-invasive micro-computed tomography (micro-CT) at 0, 4, 8, and 12 weeks post-surgery.

Results: Ongoing micro-CT analysis evaluates longitudinal changes in bone volume fraction (BV/TV), trabecular thickness, and bone mineral density (BMD) within the defect site. Preliminary observations suggest that both BCP formulations support scaffold-tissue integration without significant inflammatory responses. The final presentation will provide a comparative analysis of BCP1 versus BCP2, focusing on the rate of new bone formation and the degradation profile of the scaffolds over the 12-week study period.

P-25 Krittikan Chanpaisaeng, PhD

Conclusions: Tilapia-derived BCP scaffolds represent a promising, sustainable alternative to synthetic or mammalian-derived bone grafts. We anticipate that the results will demonstrate the efficacy of these scaffolds in bridging critical-sized defects. This research provides essential safety and efficacy data for the clinical translation of aquaculture-derived biomaterials, potentially offering a low-cost solution for bone tissue engineering while
promoting environmental sustainability.

P-26 Jodi Dowthwaite, MPhil, PhD

Height adjusted growth curves show advantages in radius periosteal and cortical bone geometry for female gymnasts vs non-gymnasts

Jodi N. Dowthwaite, PhD*1,2; Anna D. Nicotra, BA1; Tim J. Cole, ScD3; Tamara A. Scerpella, MD1,2
1 Department of Orthopedic Surgery, SUNY Upstate Medical University, Syracuse, NY, USA
2 Department of Orthopedics & Rehabilitation, University of Wisconsin-Madison, Madison, WI, USA
3 UCL Great Ormond Street Institute of Child Health, London, UK (*presenter)

Purpose: We aimed to evaluate whether youth mechanical loading yields advantages in total and cortical cross-sectional area, by comparing growth curves for female gymnasts vs. non-gymnasts, at ultradistal, distal, and proximal radius sites. We hypothesized that growth pattern differences would be largest near the hand, where gymnastics applies weight-bearing impacts.

Materials & Methods: In a prospective, longitudinal study of female bone accrual, annual pQCT scans (Stratec XCT2000) measured periosteal and cortical cross-sectional area (pCSA, cCSA: mm2) for the non-dominant radius at 4%, 33%, and 65% of ulnar length. Height measurements (cm), menarche date, and monthly gymnastics participation (gymnastics: calculated annual mean h/wk) were recorded via semi-annual data collection (annual collection after age 18 yrs). Gymnasts (GYM: gymnastics ≥6 h/wk for ≥1 yr, excluding pre-menarcheal quitters) were contrasted against non-gymnasts (NON, standard: gymnastics <6 h/wk). Analysis samples include all individuals with known menarche date and ≥3 measurements for any given metric. SITAR analyses (v1.5.0, R v4.5.2) modeled height growth curves to compare GYM (n=71) vs. NON (n=76) for each growth parameter (SIZE, TIMING, INTENSITY). Individual ages at peak height velocity (PHV) and height “SIZE” were extracted to calculate PHV-centered age and adjust SIZE in bone geometry curves for height SIZE, respectively. Thus, we used SITAR to model height-adjusted, PHV-centered growth curves for pCSA and cCSA to compare SIZE, TIMING, and INTENSITY of growth for GYM (n=53) vs. NON (n=53), across radius sites.

Results: Table 1 presents SITAR results. For height, GYM had lower SIZE & INTENSITY than NON [p≤0.02], with similar TIMING for PHV. Height SIZE was a positive factor in pCSA and cCSA models at all sites [p≤0.008]. GYM had higher height-adjusted SIZE than NON for pCSA and cCSA across sites [p≤0.002; note, GYM effect on SIZE: 65% proximal < 33% distal < 4% ultradistal]. For TIMING, GYM and NON did not differ for any radius outcome [p≥0.14]. For INTENSITY, GYM had higher peak velocity than NON for pCSA (33% & 4%) and for cCSA (65% & 33%) [p<0.03]. SITAR mean curves plotted abrupt decreases in 4% pCSA & cCSA roughly 3 yrs post-PHV (not shown).

Conclusions: As expected, GYM SIZE advantages for larger radius bone geometry were greater with closer proximity to the hand. Higher growth INTENSITY showed GYM geometric advantages increasing via rapid periosteal and cortical expansion, in contrast to lower INTENSITY of GYM height growth. For GYM & NON, decreases in 4% pCSA & cCSA may show metaphyseal in-waisting “catch-up”, after linear growth ceases. Potential limitations include: challenges optimizing scan analyses across growth; partial volume effect concerns for immature bone geometry; variation in metaphysis geometrics if scan positioning is inconsistent; high variability in GYM training & cessation patterns.

Table 1: SITAR Analysis Results for Non-dominant Radius pQCT Bone Geometry

Dependent Variable	Height SIZE on SIZE	GYM status on SIZE	GYM status on TIMING	GYM status on INTENSITY	GYM n (observations)	NON n (observations)
Height (cm: 5 df)	N/A	-4.4 p<0.0001	+0.28 p=0.11	-0.08 p=0.02	71 (1144)	76 (1150)
65% pCSA (mm^2: 2 df)	+0.64 p=0.007	+14.5 p<0.0001	+0.52 p=0.2	+0.07 p=0.6	53 (528)	53 (559)
65% cCSA (mm^2: 6 df)	+0.40 p=0.001	+5.8 p=0.002	-0.30 p=0.2	+0.19 p=0.03	53 (528)	53 (559)
33% pCSA (mm^2: 3 df)	+0.47 p=0.008	+18.2 p<0.0001	-0.07 p=0.8	+0.23 p=0.008	53 (528)	53 (554)
33% cCSA (mm^2: 6 df)	+0.42 p=0.0005	+11.2 p<0.0001	-0.40 p=0.14	+0.25 p=0.002	53 (528)	53 (554)
4% pCSA (mm^2: 3 df)	+1.8 p=0.0001	+44.3 p<0.0001	-0.14 p=0.6	+0.19 p=0.01	53 (524)	53 (552)
4% cCSA (mm^2: 3 df)	+1.9 p=0.0001	+43.9 p<0.0001	-0.15 p=0.6	+0.15 p=0.08	53 (524)	53 (552)

SIZE: super-imposes growth curve magnitude via Y-axis shift, down (-) or up (+).

TIMING: translates earlier or later age at peak growth velocity via X-axis shift, left (-) or right (+).

INTENSITY: rotates growth curve slope for shallower (-) or steeper (+) peak growth velocity (0°-90°).

To optimize model fit, degrees of freedom (df) were selected to minimize Akaike Information Criterion.

pCSA= periosteal cross-sectional area; **cCSA**= cortical cross-sectional area

P-27 Mimi Sammarco, PhD

TrkA+ sensory nerve signaling is required to promote digit regeneration

Emily Busse, Dimitri Sokolowskei, Kyle Berry, Sarah McMahon, Robert J Tower and Mimi C Sammarco

Humans, monkeys, and rodents regenerate the distal end of the digit tip after amputation. After injury, tissue regeneration is coordinated by an intimate structural and functional relationship between fibroblasts and nerve axons, but this process is not well understood. The pan neuronal marker TUBB3 shows extensive innervation prior to amputation along the dorsal and ventral surfaces of the digit. Following amputation, re-innervation occurred along the surfaces of the regenerating bone, eventually extending to the distal tip. ScRNAseq analysis identified the neurotrophin nerve growth factor (NGF) as the primary driver of reinnervation, derived primarily from fibroblasts in early regeneration. To determine the role of nerves in the regenerative process, we used both scRNAseq data derived from the dorsal root ganglia (DRG) (containing the cell bodies of nerves known to innervate the digit), and scRNAseq and spatial transcriptomic data from the regenerating digit. Iterative predictive modeling and histology identified spatial transcriptomic spots likely to contain nerve axons and signaling gradients derived from either all DRG nerves or those derived from nerves expressing TrkA, the high affinity NGF receptor. Consistent with other models, TrkA+ nerves promoted cell proliferation in neighboring fibroblasts. In addition, we also noted expression of WNT activation by TrkA+ nerves in the nailbed, while the absence of TrkA nerves resulted in TGFβ expression and the mechanotransducive Hippo pathway. To determine the role of TrkA+ nerves in regeneration, we TrkAF592A transgenic mice to chemically inhibit NGF/TrkA signaling. TrkA mutant mice showed significantly reduced BV relative to D0 at D17 (CON 0.8342 ± 0.152, TrkA 0.7434 ±0.056, $p<.01$) and D21 (CON 1.081 ± 0.202, TrkA 0.7831 ±0.263, $p<.01$). Analysis using spatial transcriptomics showed reduced TrkA+ nerves, detected by marker gene expression and immunofluorescence, was associated with decreased blastema proliferation and WNT activation. Interestingly, TrkA inhibition resulted in increased innervation of non-peptidergic axons, increasing TGFβ activation and altering mitochondrial morphology through increased fusion and decreased fission, leading to increased expression of transcripts responsive to reactive oxygen species. Our data point to a critical role specifically for TrkA+ sensory nerves and identify molecular cascades regulated by nerve subtypes within the regenerating digit.

P-28 Alexandra Armstrong, DVM, PhD

Digital Pathology of the Femoral Head: Using a Novel RGB-Trichrome Stain for Tissue Quantification using HALO©

Ashton A. Amann1, Ferenc Toth1, Casey P. Johnson1, Alexandra R. Armstrong (presenting author)1
1 Department of Veterinary Clinical Sciences, College of Veterinary Medicine, University of Minnesota, St. Paul, Minnesota, United States
Rolan048@umn.edu

INTRODUCTION: Although several techniques are available for evaluating bone microscopically, there is no reliable method to accurately quantify mineralized versus unmineralized bone in decalcified and formalin-fixed, paraffin-embedded tissue. Hard tissue processing, which is technically challenging and time-consuming, is the gold standard but not practical for many laboratories. A modified alcian-blue/ picrosirius red staining protocol, referred to as RGB-Trichrome (RGBT), shows promise but has not been evaluated in porcine tissues. The objective of this study was to utilize HALO© Software to compare the RGBT stain to an alcian blue-picrosirius red (ABPR) stain to quantify mature bone, osteoid, cartilage, and marrow and to compare RGBT to Gomori's Trichrome (GT) staining for quantification of fibrosis.

METHODS: This study analyzed 13 piglet femoral heads (7 female, 6 male) from a model of Legg-Calvé-Perthes disease that involves osteonecrosis of the hip. Piglets underwent surgical procedure to induce ischemia within the femoral head. Samples were selected based on histological appearance, with samples ranging from no lesions to extensive necrosis and fibrosis of the epiphysis. Femoral heads were harvested 1- or 2-weeks post-operatively. Slides were prepared for histological assessment using three staining techniques: RGBT, ABPR, and GT. RGBT staining followed the same protocol as the ABPR staining, with the addition of 0.04%v Fast Green. The Tissue Classifier algorithm was used to calculate total area and percent composition of marrow, mature bone, cartilage, osteoid, and fibrosis from scanned slides. Osteoid was apparent within a subset of samples. A pathologist with musculoskeletal expertise and experience in the model confirmed 10 example annotations of each tissue type. Mean values (area, percent area) from HALO© were compared by paired T-tests with ABPR and GT treated as the established gold standard.

RESULTS: RGBT demonstrated strong alignment with ABPR for total bone and marrow, with no significant differences in total bone area ($p=0.925$) or percent bone area ($p=0.289$). The staining techniques were strongly correlated for total bone ($r=0.93$ for area, $r=0.79$ for percent area). Uniquely, RGBT was able to provide distinct measurements for the mean area of osteoid and of mature bone, distinguishing osteoid (dark red) from the mature, calcified bone (peach-pale red) [Figure 1].

P-28 Alexandra Armstrong, DVM, PhD

DISCUSSION: RGBT quantified the total bone area comparably to ABPR. RGBT also consistently differentiated osteoid, allowing HALO quantification. With further validation of its specificity in distinguishing new from mature bone, RGBT may allow tissue analysis in the complex context of bone healing and repair. Surprisingly, RGBT detected less fibrosis than GT.
Limitations included a lack of additional validation of osteoid vs. mature bone, such as using traditional hard tissue processing.

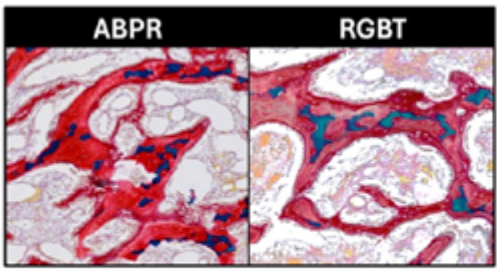

Figure 1: Comparison between ABPR and RGBT, highlighting the more dynamic color range in boney tissues (red) and cartilage (blue). Peach-colored regions on RGBT are consistent with mineralized bone while osteoid (unmineralized) shows up as a darker red.

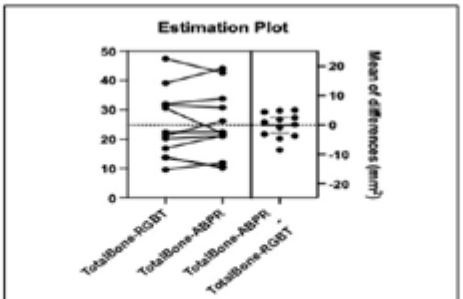

Figure 2: Estimation plot for total bone between RGBT and ABPR. Paired areas of total bone within femoral heads (left) and mean of differences within the 95% CI (right) show consistent total bone when osteoid is included with mature bone from RGBT stains.

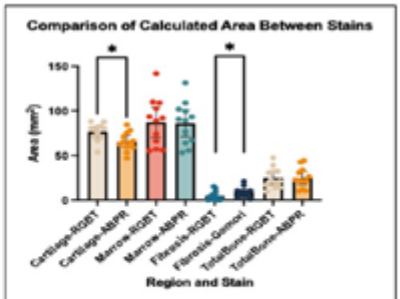

Figure 3: Calculated tissue area differences between RGBT, ABPR and GT. Cartilage and fibrosis were found to be significantly different between stains ($p < 0.05$) while marrow and total bone were similar.

P-29 Alexandra Armstrong, DVM, PhD

DV200 Values in Human and Porcine Formalin-Fixed Paraffin-Embedded (FFPE) Osteochondral Samples

“Alexandra R. Armstrong (presenting author) 1, Ferenc Toth1, Casey P. Johnson1
1University of Minnesota, St. Paul, MN
Rolan048@umn.edu

INTRODUCTION: Formalin-fixation and paraffin-embedding (FFPE) are the standard methods for preparation of samples for histological assessment. While widely used, FFPE preservation is known to interfere with RNA integrity, causing RNA degradation and fragmentation. DV200 testing allows evaluation of RNA integrity prior to pursuing downstream analyses that may have significant associated cost, such as spatial transcriptomics. A DV200 value represents a percentage of RNA fragments >200 nucleotides (nt), and may be decreased by delayed fixation, heat exposure, or decalcification. A DV200 value >30% is recommended for spatial transcriptomics. We hypothesized that DV200 values would be >30% for all decalcified FFPE osteochondral piglet or human samples.

METHODS: We compiled DV200 values from a variety of FFPE samples decalcified with 10% EDTA from several IACUC or IRB-approved experiments. The groups included 6-12 week old piglet femoral or humeral heads that were: 1) collected immediately after euthanasia and bisected before fixation (n=34); 2) kept intact at RT (20C) for 4 hours in PBS prior to bisecting and fixation (n=7); 3) kept intact in PBS and refrigerated (4C) for 24 hours prior to bisecting and fixation (n=6); 4) kept intact in PBS and refrigerated for 72 hours prior to bisecting and fixation (n=6); 5) frozen intact (-20C) prior to bisecting and fixation (n=5); 6) immediately bisected, fixed, decalcified and stored in 70% ethanol >3 months prior to embedding (n=6); 7) immediately bisected, fixed, decalcified, and paraffin embedded samples reembedded after several months of storage in paraffin blocks (n=6); 8) fixed intact at RT for 1 week prior to bisecting (n=5); or 9) fixed intact under refrigeration for 1 week prior to bisecting (n=5). We also assessed human osteochondral samples fixed for 2-4 days and underwent minimal decalcification (group 10; n=10). 4-5 scrolls/sample were evaluated following <2 days storage at -80C (for preservation between cutting and testing). RNA was extracted using the Invitrogen™ PureLink™ FFPE RNA Isolation Kit (ThermoFisher) with DNase I Digestion. For DV200 analysis generated on either an Agilent 2100 Bioanalyzer or Agilent 4200 TapeStation, regions were set from 200-6000nt per protocol and the software calculated a percent of total RNA >200 nt.

P-29 Alexandra Armstrong, DVM, PhD

RESULTS: Welch's ANOVA test was used to assess the equality of variances, and indicated a statistically significant difference between the groups, with W = 9.928, DFn = 9.0000, and DFd = 21.74 (<0.0001). All groups had a mean DV200 value >30. Groups 1, 2, 3, 6, 7, and 10 all had 1-2 samples with a DV200 value <30.
DISCUSSION: DV200 values generally met the >30% cut-off for spatial transcriptomic testing. Given variability within groups, DV200 testing may help guide selection of samples for testing and identify outlier samples with lower RNA integrity.

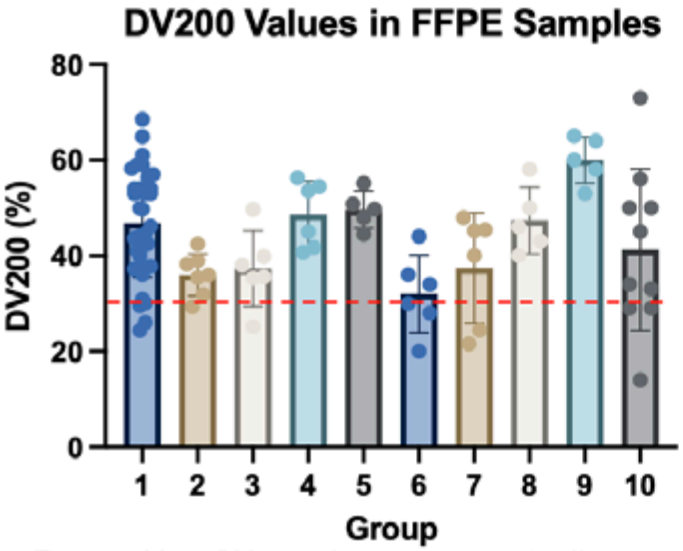

Figure 1. Mean DV200 values were >30% in all groups. Error bars = mean with 95%CI. Red line = 30%DV200.

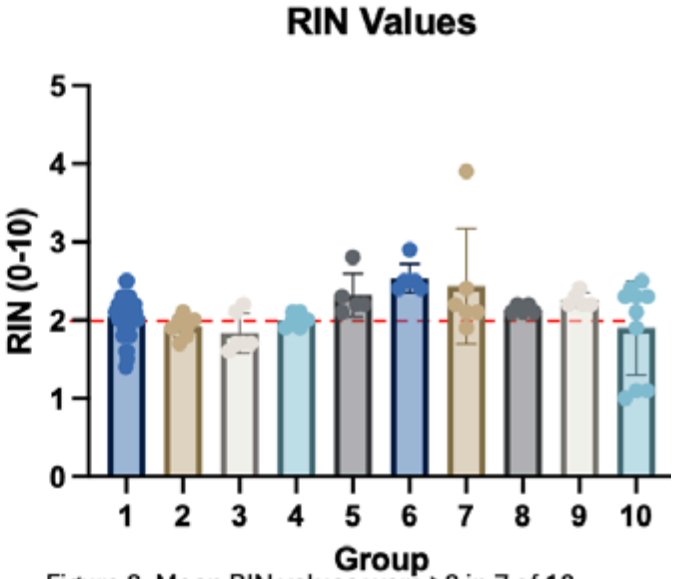

Figure 2. Mean RIN values were >2 in 7 of 10 groups. Error bars = mean with 95%CI. Red line = RIN of 2.

P-30 Kaja Laursen

RNA integrity determination in formalin-fixed paraffiin-embedded human bone tissue for xenium spatial profiling

Kaja Søndergaard Laursen1, Stine Rye Østergaard1, Thomas Levin Andersen1,2,3,4,5, Marta Diaz-delCastillo1,2
1Molecular Bone Histology Team, Dept. of Forensic Medicine, Aarhus University, Aarhus, Denmark.
2Danish Spatial Imaging Consortium, University of Southern Denmark, Odense, Denmark.
3Clinical Cell Biology, Pathology Research Unit, University of Southern Denmark, Odense, Denmark.
4Dept. of Pathology, Odense University Hospital, Odense, Denmark.
5Molecular Bone Histology Team, Dept. of Clinical Research, University of Southern Denmark, Odense, Denmark.

Background: Spatial profiling applications, such as GeoMX, Xenium and CosMX, com-bine multiplex in situ hybridization (ISH) with single-molecule detection in a morpho-logically intact tissue context, and are highly dependent on RNA quality. Thus, devel-oping experimental methods to assess RNA quality in formalin-fixed, paraffin-embed-ded (FFPE) bone tissue is crucial for optimizing the workflow and reducing down-stream costs associated with spatial profiling.
Aim: To determine RNA quality in archival FFPE bone biopsies for downstream Xe-nium High-plex Single cell Spatial Profiling (HSSP), and to create a practical guide for FFPE bone RNA quality assessment for spatial transcriptomics applications.
Methods: We evaluated RNA quality in archival FFPE bone biopsies from patients with monoclonal gammopathies retrieved from Danish pathological biobanks (n=221). To assess RNA quality, tissue sections underwent antigen retrieval and overnight incu-bation with an oligoprobe targeting RUNX2; signal was thereafter developed with Fast Red, and evaluated using the quality scoring system: 0-1= no or minimal RUNX2 ex-pression on bone surface; 2= expression in some bone surface cells and presence of no/few clusters with high intensity; 3= high expression in many (>60%) bone surface cells, presence of few signal clusters with high intensity, and some expression around blood vessels; 4= high expression in all or almost all (>90%) bone surface cells, pres-ence of clusters with high intensity, and high expression around blood vessels.

Results: RUNX2 expression is localized to trabecular bone surface cells in areas of bone formation, and to some extent on bone lining cells, while minimal expression is detected in the bone marrow. Out of 221 bone biopsies, 74 (33.4%) were deemed unsuitable (score 0-1), whereas 147 (66.5%) met the predefined quality criteria for Xenium spatial profiling analysis (score 2-4). Subsequent Xenium HSSP with a 480-target panel demonstrated high transcript decoding in all samples (136.9-533.6 de-coded transcripts per 100 µm2, unpublished) and good morphological correlation of the custom target RUNX2 compared with the single-plex RNA ISH.
Conclusion: RUNX2 ISH and RNAscope quality scoring enabled effective selection of archival FFPE human bone biopsy collected over a decade ago, with most samples meeting the pre-defined Xenium quality criteria. High transcript decoding efficiency and spatial concordance of RUNX2 expression compared with single-plex RNA ISH, emphasizing the importance of tissue quality control and assay optimization upstream of bone spatial profiling applications.”

P-31 Patricia Juarez Camacho, PhD

Development of Bioactive Luminescent Apatites: A Combined In Vitro and In Vivo Study for Enhanced Osteogenesis and Bioimaging

Authors: Lisandra V. Lozano-Barajas1, Ricardo A. González-Sánchez1, Prakhar Sengar2, Maria Marsal3, Gustavo Castro3, Carmen G. Paniagua-Chávez1, Gustavo Hirata-Flores2, Pablo Loza-Alvarez3, Patricia Juarez1.
1 Center for Scien-fic Research and Higher Educa-on.
2. Center of Nanosciences and Nanotechnology-UNAM.
3. The Ins-tute of Photonics Sciences.

Purpose: Bone tissue is a dynamic, highly vascularized structure supported by an inorganic matrix primarily composed of hydroxyapatite (HAp) crystals. Synthetic HAp is a vital bioactive material in nanomedicine, providing a scaffold that mimics the natural bone microenvironment and promotes angiogenesis. In this context, rare-earth dopants such as Eu3+ serve as promising activators for the apatite family, offering stable luminescence for non-invasive bioimaging. This study details the synthesis of specifically engineered europium-doped calcium phosphates produced via optimized hydrothermal and combustion routes. These materials are designed to actively simulate osteogenic differentiation while allowing for high-resolution monitoring through advanced microscopy.

Materials & Methods: Physicochemical properties were characterized using electron microscopy (SEM/TEM), X-ray diffraction (XRD), and spectroscopy (FTIR/EDS/PL/CL). Biological evaluation focused on the differentation potential of MC3T3-E1 pre-osteoblasts, assessing cellular internalization and the material's influence on osteogenic markers. Advanced visualization was achieved using two-photon microscopy to track the distribution and stability of nanoparticles within the MC3T3-E1 cell model. Furthermore, in vivo biocompatibility and systemic integration were evaluated using the zebrafish model.

Results: The synthesized nanoparticles demonstrated target physicochemical characteristics with stable, high-intensity luminescence. In vitro testing confirmed that the materials are highly biocompatible and successfully support the activation of cellular processes associated with early-stage osteoblast differentiation in the MC3T3-E1 line. High-resolution imaging via two-photon microscopy allowed for the precise visualization of the nanoparticles within the pre-osteoblasts, confirming their photostability and safety for real-time monitoring of cell-material interactions without inducing significant oxidative stress. In vivo zebrafish assays demonstrated no significant mortality or developmental malformations, validating the material's safety profile for systemic therapeuetic applications.

Conclusion: These Eu3+-doped materials effectively mimic the mineral phase of natural bone while providing a unique optical signature. The synergy between their osteoinductive potential and their compatibility with two-photon microscopy highlights their potential as a multifunctional plaWorm to simulate bone growth and enable real-time monitoring of the repair process.

P-32 Wanchai Grossrieder, MSc

Quantitative Analysis of Intercellular Connectivity in In Vitro Osteocyte-Like Networks

W. Grossrieder[1], M. Bernero[1], M. Ishmaku[1], M. Escudero[1], X.-H. Qin[1]

[1] *Institute for Biomechanics, ETH Zurich, Zurich, Switzerland*

PURPOSE: Bone is a dynamic tissue in which osteocyte connectivity declines with age. To model age-related changes *in vitro*, we have developed a method to generate artificial osteocyte-like networks with tunable morphologies. We hypothesized that increasing the number of cell-guiding microchannels enhances intercellular connectivity, thereby promoting fluid flow and dendrite elongation under mechanical loading. Fluorescence recovery after photobleaching (FRAP) was used to directly quantify gap junction-mediated molecular exchange within emerging networks, providing a functional measure of connectivity.

METHODS: Gelatin methacryloyl (GelMA) hydrogels were micropatterned by two-photon lithography using different biomimetic computer-aided designs featuring 25 (C25) or 50 (C50) microchannels between cells. Human dermal fibroblasts (HDF) were seeded on the samples and cultured for 11 days. Intercellular connectivity was assessed by live-cell FRAP of Calcein AM-stained cellular networks. Fluorescence recovery was monitored by time-lapsed confocal imaging. The data was fitted to extract the mobile fraction (Mf) and recovery constant (Rc). Gap junction specificity was validated by perturbation using the inhibitor α-glycyrrhetinic acid (AGA, 100 µM).

RESULTS: After 11 days, HDFs successfully formed interconnected cellular networks (**Figure 1a**). FRAP measurements indicated that increasing the number of guidance microchannels enhanced intercellular transport. Inhibition of gap junctions with AGA (C25 neg, C50 neg) resulted in increased recovery constant and reduced mobile fraction, confirming that fluorescence recovery is mediated by functional intercellular coupling. Notably, the mean value of the recovery constant was lower in the C50 condition compared to C25, indicating faster dye exchange between cells (**Figure 1b,c**). In parallel, the mobile fraction was higher in C50 compared to C25, suggesting increased molecular transport. Together, these results confirm that a greater number of guidance microchannels increased functional connectivity between cells. Preliminary data extending this approach to analyze osteocyte-like networks, including FRAP and immunostaining of functional markers, will also be presented.

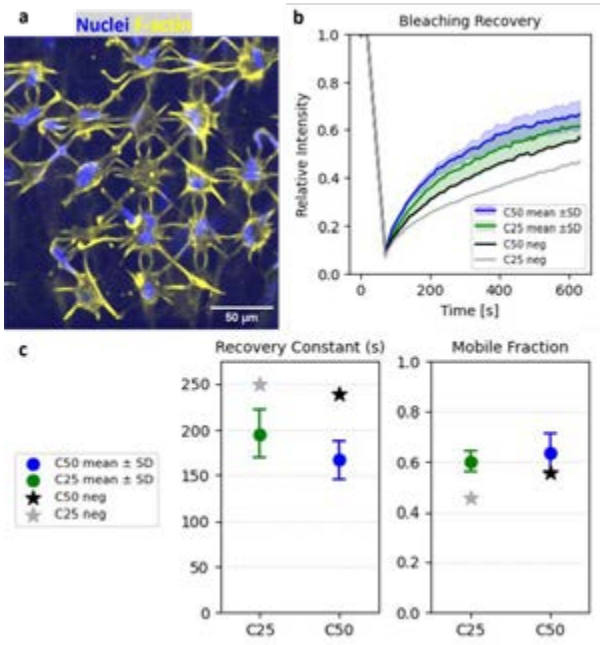

***Figure 1**: **a** HDF network formation on microprinted hydrogels revealed by Nuclei and F-actin staining. **b** Fluorescence recovery of HDFs after photobleaching under different conditions. **c** RC and Mf derived from the mathematical modelling of the recovery curves.*

CONCLUSION: This study demonstrates that cell–cell connectivity can be modulated through spatial confinement. By increasing the number of available microchannels, this platform provides a controllable *in vitro* model to investigate age-related loss of cellular connectivity in osteocyte-like networks and supports bone tissue engineering studies.

ACKNOWLEDGEMENTS: This work was supported by the Swiss National Science Foundation and a SERI-funded ERC Starting Grant.

P-33 Sayaka Ono, DDS, PhD

Cysteine Protease Inhibition Disrupts Quantitative Coupling of Bone Resorption and Formation in a Bone Organoid Imaging System

Authors: Sayaka Ono1, 2, Naoki Tsuji2, 3, 4, Tomoaki Sakamoto2, Shuya Oguchi5, Takashi Nakamura6, Kazuto Hoshi2,
4, 5, Atsuhiko Hikita1, 2
1. Department of Clinical Stem Cell Biology, Graduate School of Medicine, The University of Tokyo
2. Division of Tissue Engineering, The University of Tokyo Hospital
3. Department of Pharmacology, Hokkaido University, Faculty of Dental Medicine/Graduate School of Dental Medicine
4. Department of Oral and Maxillofacial Surgery, Graduate School of Medicine, The University of Tokyo
5. Department of Oral and Maxillofacial Surgery, and Orthodontics, The University of Tokyo Hospital
6. Oral Health Science Center, Tokyo Dental College
*Presenting author: Sayaka Ono

Purpose
Quantitative assessment of bone remodeling requires precise evaluation of the spatial and temporal coupling between bone resorption and formation. While bisphosphonates suppress both processes, the effects of cysteine protease inhibition on the quantitative coordination of remodeling remain unclear. This study aimed to evaluate how cysteine protease inhibition alters the spatial and quantitative coupling of bone resorption and formation using an imaging-based bone organoid system.

Materials and Methods
A bone organoid system was established by co-culturing calcified nodules derived from EGFP-expressing mouse osteoblasts with bone marrow macrophages from Ctsk-Cre;ROSA26-tdTomato mice. Bone remodeling dynamics were visualized longitudinally using two-photon microscopy. Quantitative image analysis was performed to evaluate spatial co-localization and temporal coordination between resorption and formation. The effects of the cysteine protease inhibitor E-64 were compared with those of zoledronic acid (ZOL).

Results
In control conditions, bone resorption and formation exhibited spatial and quantitative coupling, reflecting coordinated remodeling. ZOL partially disrupted this relationship. In contrast, E-64 markedly disrupted both spatial and quantitative coupling, indicating a near-complete decoupling of resorption and formation. This disruption was associated with suppression of spherical osteoblast-like cells at resorption sites, suggesting inhibition of reversal cell emergence.

P-33 Sayaka Ono, DDS, PhD

Cysteine Protease Inhibition Disrupts Quantitative Coupling of Bone Resorption and Formation in a Bone Organoid Imaging System

Conclusions: Cysteine protease inhibition disrupts the quantitative coupling of bone resorption and formation in a bone organoid system. These findings demonstrate distinct effects of antiresorptive agents on bone remodeling dynamics and highlight the importance of quantitative imaging approaches for evaluating skeletal homeostasis.

Keywords
Bone morphometry, Quantitative imaging, Bone remodeling, Resorption–formation coupling, Bone organoid

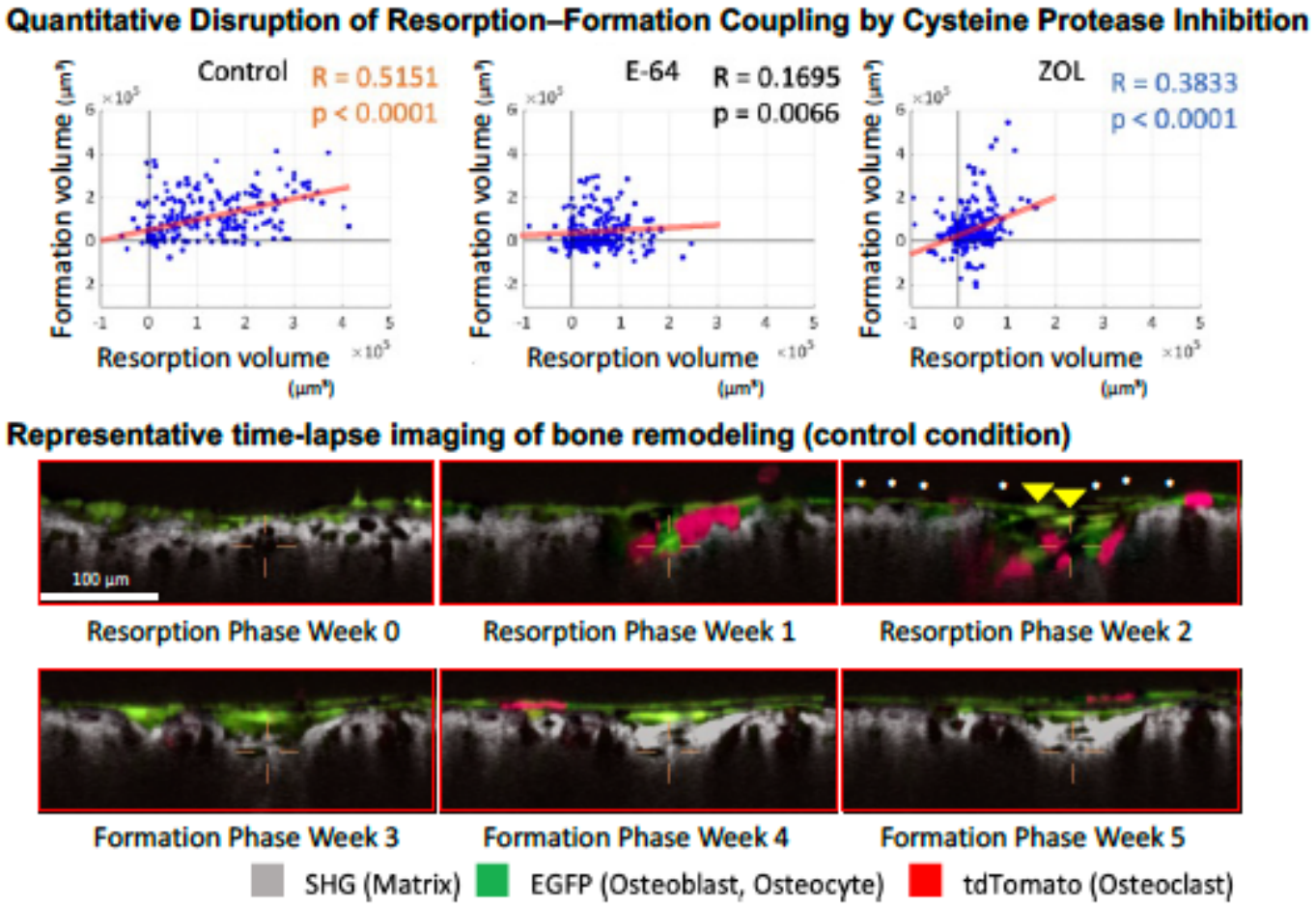

Quantitative disruption of resorption–formation coupling by cysteine protease inhibition. Scatter plots show the relationship between resorption and formation volumes in individual regions ofinterest. In control conditions, a moderate positive correlation indicates spatial and quantitative coupling. Zoledronic acid (ZOL) partially weakens this relationship, whereas E-64 markedly reduces the correlation, indicating near-complete decoupling. Representative two-photon images illustrate the temporal progression of bone remodeling in control samples.

P-34 Kalyan Nannuru, PhD

NPR2 gain-of-function of variants drive increased skeletal growth but causes tibial curvature in mice

THANK YOU TO OUR SPONSORS

REGENERON®

SCANCO MEDICAL

Wonderful Scientific

EVIDENT

LLS ROWIAK LaserLabSolutions

MEDIMAPS We understand bone health

BIOQUANT® image analysis corporation

Lucid concepts

ascendis pharma

www.bonemorphometry.org/isbm-2026